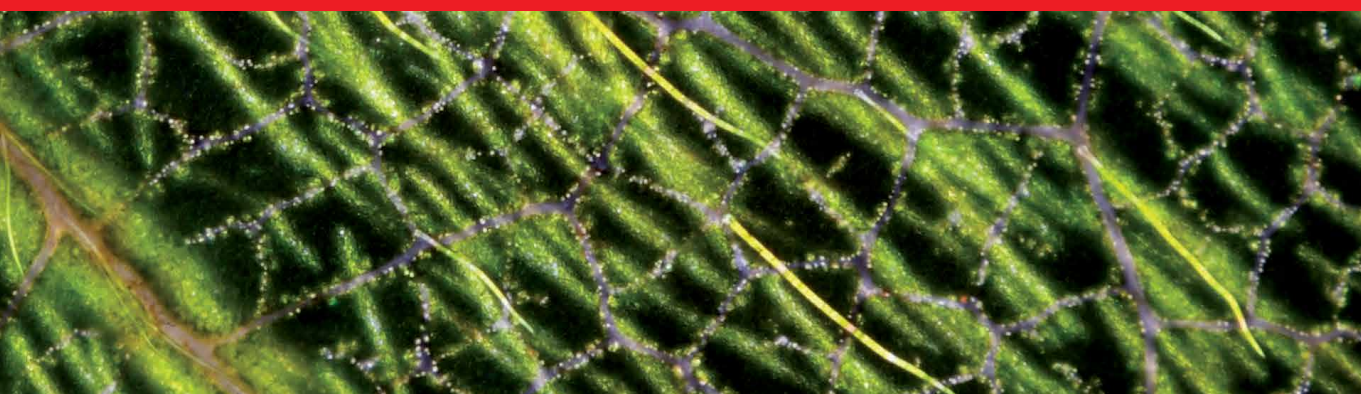


IntechOpen

Photophysics, Photochemical
and Substitution Reactions
Recent Advances

*Edited by Satyen Saha,
Ravi Kumar Kanaparthi and Tanja V. Soldatović*



Photophysics, Photochemical and Substitution Reactions - Recent Advances

*Edited by Satyen Saha, Ravi Kumar
Kanaparthi and Tanja V. Soldatović*

Published in London, United Kingdom



IntechOpen





Supporting open minds since 2005



Photophysics, Photochemical and Substitution Reactions – Recent Advances

<http://dx.doi.org/10.5772/intechopen.77916>

Edited by Satyen Saha, Ravi Kumar Kanaparthi and Tanja V. Soldatović

Contributors

Ataf Ali Altaf, Samia Kausar, Amin Badshah, Muhammad Hamayun, Abdul Razzaq, Robert Melville Metzger, Vu T. Tan, La The Vinh, Tanja V. Soldatovic, Sandip Shinde, Suresh Iyer, Alwar Ramani, Shobha Waghmode, Seda Cetindere, Ravi Kumar Kanaparthi, Akhila M. , Manjeev Singh, Satyen Saha, Zhi-Feng Zhao, Shipra Sagara, Ravi K. Kanaparthi, Manish K. Tiwari, Akira Nishimura

© The Editor(s) and the Author(s) 2021

The rights of the editor(s) and the author(s) have been asserted in accordance with the Copyright, Designs and Patents Act 1988. All rights to the book as a whole are reserved by INTECHOPEN LIMITED. The book as a whole (compilation) cannot be reproduced, distributed or used for commercial or non-commercial purposes without INTECHOPEN LIMITED's written permission. Enquiries concerning the use of the book should be directed to INTECHOPEN LIMITED rights and permissions department (permissions@intechopen.com).

Violations are liable to prosecution under the governing Copyright Law.



Individual chapters of this publication are distributed under the terms of the Creative Commons Attribution 3.0 Unported License which permits commercial use, distribution and reproduction of the individual chapters, provided the original author(s) and source publication are appropriately acknowledged. If so indicated, certain images may not be included under the Creative Commons license. In such cases users will need to obtain permission from the license holder to reproduce the material. More details and guidelines concerning content reuse and adaptation can be found at <http://www.intechopen.com/copyright-policy.html>.

Notice

Statements and opinions expressed in the chapters are these of the individual contributors and not necessarily those of the editors or publisher. No responsibility is accepted for the accuracy of information contained in the published chapters. The publisher assumes no responsibility for any damage or injury to persons or property arising out of the use of any materials, instructions, methods or ideas contained in the book.

First published in London, United Kingdom, 2021 by IntechOpen

IntechOpen is the global imprint of INTECHOPEN LIMITED, registered in England and Wales, registration number: 11086078, 5 Princes Gate Court, London, SW7 2QJ, United Kingdom

Printed in Croatia

British Library Cataloguing-in-Publication Data

A catalogue record for this book is available from the British Library

Additional hard and PDF copies can be obtained from orders@intechopen.com

Photophysics, Photochemical and Substitution Reactions – Recent Advances

Edited by Satyen Saha, Ravi Kumar Kanaparthi and Tanja V. Soldatović

p. cm.

Print ISBN 978-1-83968-223-0

Online ISBN 978-1-83968-224-7

eBook (PDF) ISBN 978-1-83968-225-4

We are IntechOpen, the world's leading publisher of Open Access books Built by scientists, for scientists

5,300+

Open access books available

131,000+

International authors and editors

155M+

Downloads

156

Countries delivered to

Our authors are among the
Top 1%

most cited scientists

12.2%

Contributors from top 500 universities



WEB OF SCIENCE™

Selection of our books indexed in the Book Citation Index
in Web of Science™ Core Collection (BKCI)

Interested in publishing with us?
Contact book.department@intechopen.com

Numbers displayed above are based on latest data collected.
For more information visit www.intechopen.com



Meet the editors



Born in Kolkata (formerly Calcutta) in India, Satyen Saha received his BSc (Chemistry Honors, 1994) and MSc (Chemistry, 1996) from Jadavpur University, Kolkata. He earned his Ph.D. (Photochemistry, 2002) from Hyderabad Central University, Hyderabad, India. Subsequently, he moved to the Department of Chemistry, University of Tokyo, Tokyo, for postdoctoral research (2002–2005) in the group of Prof. Hiro-o Hamaguchi, followed by postdoctoral research work with Prof. Richard Wiess, Georgetown University, Washington DC, USA. He was the recipient of a JSPS postdoctoral fellowship and a JSPS bridge fellowship for a foreign researcher. At present, he is a Professor in the Department of Chemistry, Institute of Science, Banaras Hindu University (Central University), Varanasi, India. His present research interests are synthesis, structure (solid and liquid phase), and interactions in ionic liquids, NIR emitting materials, ionic liquids, and photophysical studies (steady-state and time-resolved) of fluorescent molecules in condensed phases.



Dr. Ravi Kumar Kanaparthi is a senior assistant professor at the Department of Chemistry, the Central University of Kerala, India. His research group focused on material synthesis for harvesting solar energy (dye-sensitized solar cells), optoelectronic devices, and sensors. Besides, he is also working on the fabrication of fluorescent nanomaterials and studying their photophysics. He is an expert in studying photophysics of materials by both steady-state and time-resolved fluorescence techniques, fabrication of DSSCs, synthesis of organic and metal nanoparticles, and optical and electron microscopy techniques. He has successfully completed two major research projects received from SERB, Government of India. He has published over twenty-five international/national research articles in peer-reviewed journals and presented his research findings in various national and international conferences. He teaches Quantum Chemistry, Molecular Spectroscopy, and Instrumental Methods of Analyses to the postgraduate students.



Dr. Tanja V. Soldatović is an associate professor at the Department of Chemical-Technological Sciences at the State University of Novi Pazar. Her scientific focus is on bioinorganic and medicinal inorganic chemistry (studies related to the biological activity and medical application of transition metal antitumor complexes). Dr. Tanja Soldatović is the author and co-author of many peer-reviewed articles and three books. She participated in the realization of three national scientific research projects and an international DAAD project. Also, Dr. Tanja V. Soldatović was a research fellow at the University of Sassari, Department of Chemistry, Sassari-Italy, and the University of Erlangen-Nürnberg, Inorganic Chemistry, Department of Chemistry and Pharmacy,

Erlangen-Germany. Dr. Tanja Soldatović is a member of the following professional societies: the Serbian Chemical Society, the Association for Cancer Research (Serbia), the European Association for Cancer Research, the Serbian Society for Immunology, and the Molecular Oncology and Regenerative Medicine. Currently, she is head of the Department of Chemical-Technological Sciences at the State University of Novi Pazar.

Contents

Preface	XIII
Section 1 Photophysics and Applications	1
Chapter 1 Photophysical Properties of 4-(Dicyanomethylene)-2-Methyl-6-(4-Dimethylaminostyryl)-4H-Pyran (DCM) and Optical Sensing Applications <i>by Ravi Kumar Kanaparthi, Satyen Saha, Manjeev Singh and Akhila M</i>	3
Chapter 2 Photophysics of BODIPY Dyes: Recent Advances <i>by Seda Çetindere</i>	31
Chapter 3 Supramolecular Chemistry and DNA Interaction Studies of Ferrocenyl Ureas and Thioureas <i>by Samia Kausar, Ataf Ali Altaf, Muhammad Hamayun, Amin Badshah and Abdul Razzaq</i>	51
Section 2 Photochemical, Photocatalysis and Applications	71
Chapter 4 CO ₂ Reduction Characteristics of Cu/TiO ₂ with Various Reductants <i>by Akira Nishimura</i>	73
Chapter 5 Recent Progress of Electrocatalysts and Photocatalysts Bearing First Row Transition Metal for Hydrogen Evolution Reaction (HER) <i>by Shipra Sagar, Ravi K. Kanaparthi, Manish K. Tiwari and Satyen Saha</i>	97
Chapter 6 Arsenomolybdates for Photocatalytic Degradation of Organic Dyes <i>by Zhi-Feng Zhao</i>	117

Chapter 7	131
Visible-Light Photocatalysis of Aldehyde and Carbonyl Functionalities, an Innovative Domain <i>by Alwar Ramani, Shobha Waghmode and Suresh Iyer</i>	
Chapter 8	155
Supported-Metal Oxide Nanoparticles-Potential Photocatalysts <i>by Vu T. Tan and La The Vinh</i>	
Chapter 9	179
Ferrocenes as One-Electron Donors in Unimolecular Rectifiers <i>by Robert Melville Metzger</i>	
Section 3	
Substitution Reactions	191
Chapter 10	193
Correlation between HSAB Principle and Substitution Reactions in Bioinorganic Reactions <i>by Tanja Soldatović</i>	
Chapter 11	207
Protic Reaction Media for Nucleophilic Substitution Reactions <i>by Sandip S. Shinde</i>	

Preface

This book entitled “Photophysics, Photochemical and Substitution Reactions - Recent Advances” represents a modern branch of science. Photophysics and photochemical reactions are as old as our world. Working on the principle of light-matter interaction, they are present at the crossroads of several disciplines such as chemistry, physics, material science, biology, and medicines. The same is true for substitution reactions as well. To the best of our knowledge, this fantastic combination of topics, substitution reaction clubbed with reactions initiated by photons (i.e., photochemical reactions), appears for the first time in book literature, representing the importance of gross understanding of organic chemistry, materials science, just a few areas to mention. A combined understanding will also help us to expand the development of new molecules, new materials, as well as understanding new photon-initiated processes. The goal of this book is to familiarize both research scholars and postgraduate students with recent advancements in various fields related to reactions initiated by photons and substitution reactions.

This book is broadly divided into three sections: Section I “Photophysics and Application”; Section II “Photochemical, Photocatalysis and Applications”; and Section III “Substitution Reactions”. Each part provides a unique aspect of its headings.

Section I titled “Photophysics and Applications,” contains three chapters and it starts with an in-depth photophysics details of a popular pyran dye and its application in optical sensing. The second chapter deals with another popular and important dye, BODIPY dye. The DNA interaction studies of ferrocenyl ureas and thioureas have been presented in Chapter 3. Section II of this book comprises six chapters under the heading of “Photochemical, Photocatalysis and Applications”. This section starts with a very important topic, carbon dioxide reduction on Cu/TiO₂, while the second chapter discusses the recent development of hydrogen evolution reaction. Third chapter of this section discusses the photocatalytic degradation of various organic dyes by using arsenomolybdates, while the fourth describes the visible-light-induced photocatalysis of aldehyde. The potential photocatalysis of metal oxide nanoparticles is presented in fifth chapter. The last chapter in this section deals with the ferrocene unimolecular rectifier. The final section of this book consists of two chapters on substitution reactions. Substitution reactions are a type of reaction where one functional group or ligand is substituted by another. They could be electrophilic or nucleophilic, depending upon whether the reagent is involved. However, whether it is organic or inorganic chemistry, there are two mechanisms of substitution reactions: dissociative or SN₁ and associative mechanism or SN₂. Many factors such as solvent, ionic strength, concentration, or hardness of metal ions in inorganic reactions could gain great importance on substitution reactions. The special class of organometallic compounds is ferrocenes. This type of compound, including its derivatives, has shown to be bio-applicable. Two chapters in this book bring us the newest research in this field.

Last but not the least, the future of photophysics, photochemical, and substitution reactions, like any other burgeoning field, is more exciting than the past. This is

particularly due to the increase in the number of young researchers and the development of the instrumentations.

We thank all the contributors for their excellent chapters and the publishing process managers of IntechOpen, especially author service manager, Mr. Josip Knapic, for keeping us on our toes to publish this book on time. It has been another extremely nice experience to work with this dynamic publishing house, IntechOpen.

Satyen Saha

Professor,
Department of Chemistry,
Institute of Science,
Banaras Hindu University,
India

Dr. Ravi Kumar Kanaparthi

Department of Chemistry,
Central University of Kerala,
India

Tanja V. Soldatović

Professor,
Department of Chemical-Technological Sciences,
State University of Novi Pazar,
Serbia

Section 1

Photophysics and Applications

Photophysical Properties of 4-(Dicyanomethylene)-2-Methyl-6-(4-Dimethylaminostyryl)-4H-Pyran (DCM) and Optical Sensing Applications

Ravi Kumar Kanaparthi, Satyen Saha, Manjeev Singh and Akhila M

Abstract

4-(Dicyanomethylene)-2-methyl-6-(4-dimethylaminostyryl)-4H-pyran (DCM) is, commonly known as red dye, an electron donor-acceptor molecule that exhibits very interesting photophysical properties such as high molar absorption coefficients, tunable electronic absorption and fluorescence emission energies, and high fluorescence quantum yields. Several DCM analogous have been synthesized and explored for various practical applications that include solid-state lasers, organic light-emitting diode (OLED), fluorescent sensors, logic gates, photovoltaics, nonlinear optics (NLO), and bioimaging of cells. In recent years, a significant amount of research work has been devoted for developing optical sensors based on DCM dye for detection of various guest analytes. The first part of this book chapter describes comprehensive photophysical properties of the DCM dye which include the results of steady-state and time-resolved absorption and fluorescence studies. The second part of the book chapter summarizes the recent developments of DCM-based optical sensors that exhibit colorimetric, ratiometric, and fluorosensing towards selective detection of metal cations, anions, and neutral species.

Keywords: red dye, electron donor-acceptor molecules, photophysical properties, optical sensors, NIR fluorescence, dicyanomethylene-4H-benzopyran, dicyanomethylene-4H-pyran, chemosensors

1. Introduction

The molecule, 4-(dicyanomethylene)-2-methyl-6-(4-dimethylaminostyryl)-4H-pyran (DCM) belongs to the merocyanine dye category and is well-known in the literature as red fluorescent dye. The DCM dye consists of N,N-dimethylaniline group, electron donor and dicyanomethylene, and electron acceptor which are covalently attached by a π -conjugated moiety, 4H-pyran-4-ylidene, in the form of electron donor-acceptor (D- π -A) architecture. The DCM was first reported by Eastman Kodak Company and initially used as dopant in developing red laser

materials [1]. However, in subsequent years it was found that DCM exhibit high fluorescence quantum efficiency, large Stokes shift, and solvatochromic behavior. Further, the absorption spectrum of DCM dye has minimum overlap with its fluorescence spectrum which was utilized in lasing action, for developing red lasers, and organic light-emitting diode (OLED) materials [2, 3]. Because of their interesting photophysical and optoelectronic properties, several research groups actively involved in developing DCM analogues not only for OLED application but also for logic gates, lasers, bioimaging, sensors, photovoltaics, and NLO applications. Way back in 2004, Chen reviewed how red emitting DCM derivatives have evolved as dopants for OLED device applications [4]. Later in 2012, Tian has published one review article which describes not only OLED applications of DCM-type materials but also fluorescent sensors, logic gates, photovoltaic sensitizers, nonlinear optical materials, bioimaging dyes, etc. [5]. Considering simple synthetic procedures of DCM derivatives [6], many optical sensors were reported based on DCM derivatives for recognizing various guest analytes, and the number of publications is rapidly increasing day by day. However, on the other hand, a comprehensive summary of DCM photophysical behavior has not been reported till date. Moreover, to the best of our knowledge, there is no single report that describes optical sensing behavior of DCM and its derivatives. The book chapter describes both the fundamental photophysics of DCM and recent progress on DCM derivatives as optical sensors.

2. Photophysical properties of DCM

2.1 Absorption

Electronic absorption spectrum of DCM in polar medium, dimethylsulphoxide (DMSO) was reported for the first time by Hammond in 1979 [7]. Later on, the DCM dye absorption spectra in different medium were studied in various contexts, and it is observed that the electronic absorption behavior is quite similar to many charge transfer (CT) dyes [7–16]. The DCM dye has very broad absorption, typically in between 200 and 600 nm, and the nature of the absorption strongly depends upon polarity of the medium (**Figure 1** and **Table 1**) [11, 12, 15, 16]. The DCM exhibits two absorption bands where the longer-wavelength band is found to be more intense than the shorter-wavelength band. In non-polar solvents, the shape of the longer-wavelength band is found to be more structured (vibronic structure) like any other CT dye molecules, and in polar solvents the structured nature disappears [17]. For example, the electronic absorption spectrum of DCM in cyclohexane shows two bands: structured longer-wavelength band with a maximum at 451 nm and shoulder at 340 nm [11]. However, when the same DCM dye is present in highly polar solvent like DMSO, a structureless longer-wavelength band is observed with maxima at 482 nm with a shoulder at 350 nm. Interestingly, the electronic absorption maximum of DCM undergoes a redshift upon increasing with the polarity of the medium which is commonly known as solvatochromic shift of the absorption. The solvatochromic behavior is more prominent in polar aprotic solvents than that of polar protic solvents with that of non-polar solvents. For example, the absorption maxima of DCM in cyclohexane and DMSO in the solvatochromic shift is found to be ~30 nm, which is relatively less (~20 nm) when compared to cyclohexane and ethanol absorption maxima. From the Lippert-Mataga theory [18–20], ground-state dipole moment (μ_a) of the DCM was estimated to be 5.6 D which suggests that the DCM is a dipolar molecule [11]. It is well-known in the literature that an electronic state of a dipolar molecule is more stabilized in polar solvents rather than in less polar or non-polar solvents. So, the observed solvatochromic behavior in different solvents

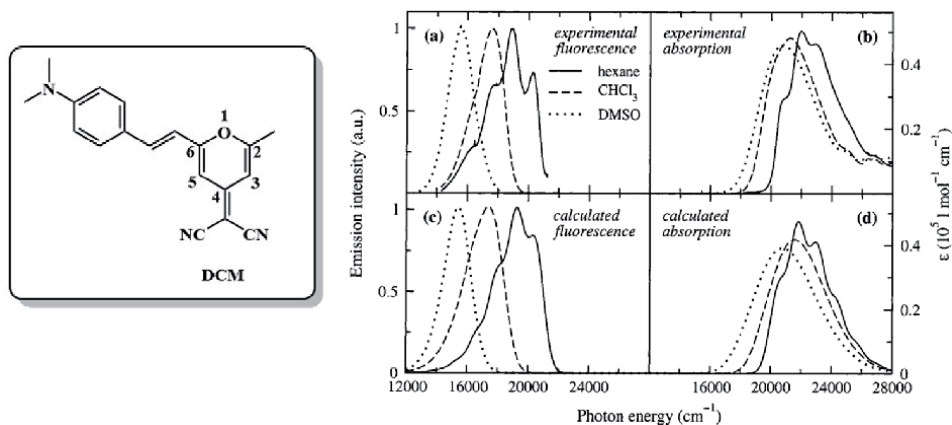


Figure 1. Molecular structure of DCM (left). Right side, experimental (a) fluorescence and (b) absorption spectra of DCM dissolved in hexane (continuous lines), CHCl_3 (dashed lines), and DMSO (dotted lines) and (c) fluorescence and (d) calculated absorption spectra. Reproduced with permission from ACS [16].

Sl. no	Solvent	λ_a (nm)	λ_f (nm)	$\lambda_a - \lambda_f$ (nm)	ϕ_f	τ (ns)
1	n-Hexane	451	530	79	0.05	0.015
2	Cyclohexane	454	533	79	—	—
3	1,4-Dioxane	456	566	100	—	—
4	Toluene	461	567	106	0.08	0.022
5	Chloroform	471	565	94	0.35	—
6	Tetrahydrofuran	—	—	—	0.49	1.24
7	Dichloromethane	468	587	109	—	—
8	Acetonitrile	463	617	154	0.45	1.95
9	DMF	475	626	151	—	—
10	DMSO	481	644	163	0.80	2.25
11	Methanol	466	623	157	0.3	1.36
12	EtOH	470	614	144	—	—
13	n-Propanol	472	614	142	0.57	2.10
14	PMMA	453	550	97	0.76	2.00

λ_a , absorbance maxima (nm); λ_f , fluorescence emission maxima; $\lambda_a - \lambda_f$, Stokes shift; τ , fluorescence lifetime; ϕ_f , fluorescence quantum yield.

Table 1. Photophysical parameters DCM [7–16].

is attributed to the extent of dipole–dipole interactions in the respective solvents. Dipole–dipole interactions are prominent in polar solvents and aromatic solvents, and corresponding energy state will be relatively more stabilized; thereby a red-shift of the absorption maxima is quite obvious. Similarly, the structured longer-wavelength absorption band, observed in non-polar solvents, is primarily due to the vibronic coupling where the vibrational energy levels are well separated and thus their vibrational transitions become prominent. The vibronic coupling is even more prominent at the low-temperature (77 K) experiments and can be attributed to the absence of dipole–dipole interactions [15]. Molar absorption coefficients of DCM in

ethanol are estimated to be $4.2 \times 10^4 \text{ mol}^{-1} \text{ cm}^{-1}$ at its absorption maxima (470 nm) and $1.2 \times 10^4 \text{ mol}^{-1} \text{ cm}^{-1}$ at the shoulder (337 nm).

2.2 Steady-state fluorescence

Fluorescence emission behavior of DCM laser dye in a variety of solvents has been measured [11, 16]. DCM dye molecule exhibits a single structured fluorescence band in non-polar aprotic solvents. For example, the fluorescence maxima of DCM in isooctane and cyclohexane are found to be at 533 nm and 530 nm, respectively (Stokes shift of ~ 80 nm), which shifts its maxima (to 566 nm) upon increasing polarity of the solvent (1,4-dioxane). On the other hand, in dipolar aprotic and protic solvents, the fluorescence maxima shift towards the red region of the visible light, undergo a little change in shape of the band, and are accompanied by a new fluorescence band with its maximum above 610 nm. Similarly, the DCM emits at 635 and 626 nm in DMSO and DMF, respectively, that gives rise to ~ 150 nm Stokes shift. Furthermore, from the systematic fluorescence study, it was observed that the short-wavelength fluorescence intensities depend upon solvent polarity and that the intensity of the longer-wavelength band enhanced monotonically with increasing polarity of the solvent. The structured fluorescence emission band in non-polar solvent is attributed to the Franck-Condon or locally excited (LE) state where the DCM molecular structure/configuration is almost same as the ground-state configuration. The dynamic Stokes shift of the fluorescence emission maxima in polar solvents indicates that the nature of the emitting state is changing to a highly polar state and the solvation of DCM molecules further stabilizing the emitting state. From Stokes shift values obtained in different solvents and by using Lippert-Mataga theory, the excited-state dipole moment (μ_e) was estimated to be 26.3 D [16], which further supports the high dipolar nature of DCM emitting state. A large change in dipole moment (~ 20 D) from ground state to the excited state resulted in a large Stokes shift (~ 150 nm) from non-polar solvents to the polar solvents. The estimated μ_e and large change in dipole moment upon photoexcitation also explain why Stokes shift is more than the solvatochromic shift. Since μ_e is very high, it is likely that the DCM molecule mostly exists in the planar confirmation in charge-transfer (CT) state which will be relatively more stabilized by polar solvents rather than non-polar solvents. Further, it was observed that both the spectral shifts are correlating with Lippert-Mataga solvent parameter, Δf .

In order to understand the nature of the emitting state, titration experiments were carried out in which aliquots of pure ethanol solvent are added gradually to DCM and dioxane solution [9]. It was observed that the original fluorescence band in pure dioxane is redshifted upon gradual addition of ethanol to the DCM-dioxane solution and concurrently produces initially a longer-wavelength fluorescence band with a maximum at 610 nm which reduces its intensity beyond certain ethanol concentration (10^{-4} M) and emerged to a new fluorescence band with a maximum at 630 nm. However, further increase of ethanol concentration beyond this limit did not shift the position of the longer-wavelength fluorescence maximum but increases intensity of fluorescence band despite the fact that there is significant increase in the polarity of the binary solvent mixture. Fluorescence quantum yield (ϕ_f) of DCM highly depends upon the polarity of the solvent. For example, in n-hexane solvent, DCM quantum yield is calculated to be 0.05, and in polar DMSO solvent, quantum yield is estimated to be 0.81 [15]. Therefore, the quantum yield of DCM in non-polar solvents are less and in polar solvents high (**Table 1**). The observed high fluorescence quantum yields in polar solvents can be understood in terms of the CT character of the DCM dye. From the initial steady-state fluorescence studies, it was proposed that the DCM dye molecule emits a single fluorescence, and a three-state model was proposed in order to explain the fluorescence

spectral behavior, and all the solvents and the emitting state would be either LE state. Therefore, solvatochromic behavior of DCM was attributed to the change in their dipole moment of the ground state and excited state where fluorescence spectral shift increases due to an increased dipole moment upon excitation and to the interaction of this dipole with the polar solvent cage.

As can be understood from the molecular structure (**Figure 1**), the DCM dye can present in either cis-confirmation or trans-configuration because of π -spacer. So, the photophysics of cis- and trans-isomerization of DCM were studied by Drake and co-workers [10]. The DCM solutions were analyzed by high-pressure liquid chromatography (HPLC) and nuclear magnetic resonance (NMR), and they found that in the freshly prepared solutions, the DCM exists in trans-configuration (in dark). However, DCM solution when exposed to ambient light, trans-DCM converts in to cis-DCM whose ratio depends on the solvent. From HPLC study, absolute absorption cross sections for both isomers were measured for the first time. The fluorescence quantum yield of trans-isomer is found to be more than that of the cis-isomer because of the less non-radiative rate of the trans-DCM. Temperature dependence of the fluorescence emission spectra of both isomers in methanol, dimethylsulphoxide (DMSO), and lipid bilayers was studied [14]. These results suggest that the fluorescence spectral behavior of the two isomers is almost overlapping while their fluorescence decay times are found to be distinct. Furthermore, cis-DCM fluorescence was measured for the first time in DMSO solvent along with the trans-DCM, and it is observed that the cis-isomer fluorescence quenches to give the trans-DCM.

Based on the steady-state absorption and fluorescence studies in a variety of solvents, a mechanism has been proposed to understand photophysical properties (**Figure 2**) [9]. The DCM dye may be thought of an ionic merocyanine-like electron donor-acceptor (EDA) dye molecule in which an electron-donating N,Ndimethylaniline moiety is covalently connected with a conjugated π -electron spacer and an electron-accepting dicyanomethylene moiety. Electronic excitation of DCM molecules leads to the formation of locally excited (LE) state immediately after photoexcitation. So, the fluorescence emission of DCM in non-polar solvents predominantly occurs from LE state, formed via π - π^* transitions, and has an electronic configuration similar to that of the ground state, which is evident from the vibronic fluorescence emission band. However, in polar solvents, excited DCM molecules emitted from ICT state, which are characterized by a planar molecular conformation, are formed immediately after photoexcitation under the influence of the electric polarization of the surrounding solvent molecules, and it is argued that the short-wavelength fluorescence primarily originated from ICT state. This also explains why

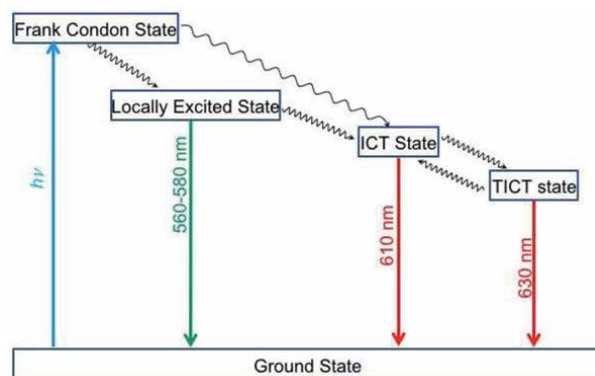


Figure 2. Schematic diagram of the dynamic behavior of low-lying singlet states of DCM.

a gradual shift in the position of the fluorescence band is observed from a non-polar aprotic solvent to a polar solvent. Further, interpretation of the additional long-wavelength fluorescence was not that easy as expected; however, the preliminary fluorescence lifetime data suggest that it is generated from excited DCM in a new ICT state which is formed during the lifetime of the lowest excited singlet state and equilibrates with the ICT state emitting at 610 nm. It was suggested that the dual fluorescence originates from the excited DCM in the ICT state with a twisted conformation formed by internal rotation of the donor moiety with simultaneous ICT from this group to a suitable acceptor orbital. The new state is commonly known as twisted intramolecular charge transfer state (TICT) which was first reported by Grabowski and co-workers [21] to explain dual fluorescence of structurally different compounds such as p-cyano and p-(9-anthryl) derivatives of N,N-dimethylaniline in polar solvents [17, 22]. Typically, the TICT state is characterized by a perpendicular conformation of donor and acceptor moieties which is responsible for dual fluorescence of p-N,N-dimethylaminobenzonitrile (DMABN). However, unlike DMABN molecule, it should be noted that the difference between the short- and long-wavelength maxima of the dual fluorescence of DCM is somewhat smaller than that calculated for DMABN. This may be because the larger separation between the D and A moieties in DCM leads to a smaller fraction of charge transfer than that of DMABN.

Contrary to the above three-state model, a combined experimental and theoretical study revealed quite different results from the measured absorption and steady-state emission spectra of DCM dye upon its comparison with Nile red in a series of aprotic solvents with similar refractive index and different polarity [16]. Unlike many other studies reported earlier, the observed spectral behavior is interpreted to two-state electronic model accounting for the coupling to internal molecular vibrations and to an effective solvation coordinate. This study pointed out that change in band shapes upon varying solvent cannot be accounted as an evidence for two different emitting states and explained all the observed solvatochromic behavior of absorption and fluorescence spectra. Based on the consistency between experimental and calculated spectral data, a two-state model was suggested for understanding DCM photophysical properties which is generally also valid for most of the of the electron donor-acceptor (EDA) molecules.

2.3 Fluorescence lifetimes

Fluorescence lifetimes of DCM were measured in six different solvents for the first time, and it is found that the fluorescence times (τ) depend upon the polarity of the solvent [8]. Later on, wavelength dependent fluorescence decay profiles of DCM in protic-polar solvent (ethanol) and other solvents were measured, and it is found that all the decays profiles are fitting with single exponential function despite the strong overlap between the two fluorescence bands [9]. Moreover, these studies clearly reveal that the fluorescence lifetime value of DCM in a given solvent is independent of the fluorescence wavelength at which the measurement was made. In order to obtain more information about the nature of the emitting states of DCM in polar solvents, the fluorescence spectra of DCM in DMSO were recorded at various times after excitation. From typical time-resolved emission spectral data, it was observed that both short- and long-wavelength fluorescence bands appear within the 0.75 ns after excitation. Further, their relative intensities change with time until a time-independent intensity ratio is reached, at about 2.25 ns. Wavelength-dependent time-resolved fluorescence measurements also suggest that DCM exhibits dual fluorescence in polar solvents which is assigned to the two well-separated different emitting states. Based on the steady-state and time-resolved fluorescence data, Hsing-Kang and co-workers suggested two different intramolecular charge

transfer (ICT) emitting states for DCM which are in dynamic equilibrium with each other, where a short-wavelength emission was assigned to a planar conformation and a longer-wavelength emission to a twisted (TICT) conformation.

Fluorescence decay measurements of *cis*- and *trans*-isomers of DCM were carried out in six solvents using PRA photon counting system [10]. The fluorescence decays of DCM are fitting with mono-exponential despite the presence of two isomers. On the contrary, quite different results were observed when lifetime measurements are carried out using picosecond time-correlated single photon counting technique [23]. The fluorescent decay profiles in methanol, acetonitrile, and chloroform are fitting in bi-exponential. A short component (~25–48 ps) is having longer lifetime in methanol and acetonitrile solvents than that in chloroform. On the other hand, long component has a lifetime (τ) of 1.38 ns in methanol and chloroform solvents and $\tau \sim 1.94$ ns in acetonitrile. Furthermore, fluorescence decay is fitting with single exponential function in DMSO with a lifetime ~ 2.25 ns. Thus, it is proved that solvent plays an important role in the non-radiative decay processes of the DCM in excited state which ultimately changes the fluorescence lifetimes. Bi-exponential nature of DCM clearly suggests the presence of two fluorescent species, and similarly, single exponential decay fitting in DMSO indicates single fluorescence species. The long-lived species are predominant in methanol, and acetonitrile solvent attributed to a *trans*-isomer which is produced while synthesizing DCM. From the relative weight component ratio ($a_2/a_1 + a_2$) analysis at a fixed excitation wavelength, it was observed that the relative contribution of the *cis*-DCM increases in the order methanol, acetonitrile, and chloroform which is inconsistent with the *cis*-DCM percentages obtained by Drake et al. [10] Further, a short component is attributed to *cis*-DCM with fluorescence lifetime in picoseconds and low fluorescence efficiency. The *cis*-DCM is having steric hindrance that inhibits planarity and rigidity of the molecule and thereby favors electronic to vibrational energy conversion. The decay behavior in highly polar DMSO solvent medium is attributed to relaxed fluorescence state from LE state, and it was pointed that TICT model is not necessary to describe single exponential decay [24]. Based on steady-state and time-resolved fluorescence studies, photoisomerization mechanism was suggested as follows: excitation of the *trans*-DCM followed by a nonadiabatic curve crossing process in which a surface crossing leads directly to the photoisomer. Another possible scheme would involve production of an intermediate, twisted internal charge transfer (TICT) state from the excited *trans*-configuration followed by partitioning to the *cis* and *trans* ground state which is similar to the Rullière model [25]. Solvatochromic absorption and emission behavior and the fact that the molecule possesses well-separated donor (amino) and acceptor (cyano) groups are consistent with the well-known charge-transfer properties. Therefore, it is likely that the geometrical configuration is skewed and intermediate between the *cis* and *trans* excited states. On the other hand, non-exponential fluorescence decay of DCM was observed at low temperature (5 and -35°C) in dibutyl ether, and the main fluorescent state was attributed to a TICT state [26].

2.4 Ultra-fast spectroscopic studies of DCM

As described in previous sections, since steady-state absorption and fluorescence studies were not conclusive about the nature of emitting state, one would always ask whether fluorescence emission is from direct charge-transfer state (CT) or relaxed CT state which is originated from locally excited state as shown in **Figure 3**. To answer this question, it is not necessary to have ultra-fast spectroscopy data; in fact simple steady-state fluorescence data would be sufficient to explain the nature of the emitting state. Suppose if it is encountered that the transition dipole moments for absorption ($\text{CT} \leftarrow S_0$) and emission ($\text{CT} \rightarrow S_0$) are the same, one can conclude that the DCM photophysics are involved in two states (ground and CT states) [27]. Further, in such

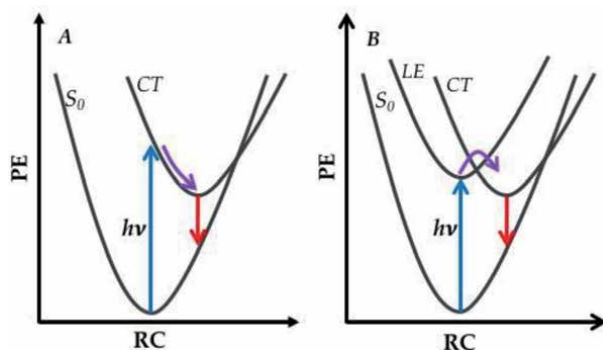


Figure 3.

Potential energy curves against generalized coordinates which include intramolecular and solvent modes for (A) direct vertical excitation to CT -state (B) population of LE state followed by $LE \rightarrow CT$ transition from ground state.

a case, the solvatochromism of absorption and emission should be consistent with ground- and excited-state dipole moments and their difference. On the other hand, if fluorescence anisotropy of DCM is substantially smaller than 0.4, then it is possible that the fluorescence emission could be from a different state than that of populated by photoexcitation, perhaps it is direct indicative of a three-state system (ground, LE , and CT states). Therefore, explicit evidence of such a three-state system can only be obtained by time-resolved spectroscopy through the direct observation of the $LE \rightarrow CT$ transition. However, because of the interference of both population transfer and relaxation (solvent, vibration) in spectral dynamics, the interpretation of the transient spectra can sometimes be sensitive and may lead to confusion. Easter et al. have investigated ultra-fast dynamics of DCM for the first time and observed temporal evolution of its stimulated emission in methanol and ethylene glycol at several wavelengths using sub-picosecond pump-probe spectroscopy [28]. The observed temporal changes of the fluorescence intensity measured during the first 100 ps after excitation were assigned to the dynamic Stokes shift of the fluorescence emission from the CT state following its direct optical excitation. Time-resolved transient absorption spectroscopic studies of DCM solutions in weakly polar and polar were carried out by Martin and co-workers, and corresponding data exhibits an isosbestic point in the net gain spectra within a few picoseconds after excitation which suggest rapid evolution of an emissive intermediate state from the initial excited S_1 state [29]. Solvatochromic behavior of the gain spectral position and its time-resolved redshift in slowly relaxing solvents support the CT character of the emissive intermediate state. Further, the overall intramolecular CT process is observed to take place within 30 ps in all solvents, and solvent relaxation time appears as an important parameter in the observed kinetics. Moreover, it was also found that the time constants associated with these changes depend upon the solvent polarity and vary from 2 ps (in acetonitrile) to 8 ps (in methanol). All these dynamics of DCM were interpreted to a transition that occurs from optically populated LE state to the CT state. However, there was no evidence of the twisted nature of this CT state which was suggested earlier [26].

Population relaxation within the fluorescent state was selectively monitored by Glasbeek and co-workers using femtosecond fluorescent up-conversion technique with a time-resolution of ~ 150 fs which does not permit to probe any influence of the dynamics within the electronic ground state [30]. It has been shown that intramolecular charge separation is taking more than 300 fs after the pulsed excitation. Following the pulsed excitation of the molecule, the integrated intensity of the spontaneous fluorescence decreased to approximately 50% of its initial value within few picoseconds. Moreover, it was observed that a significant portion of the charge

separation trajectory (~30%) is controlled by the solvation process on a picosecond time scale. Therefore, it is inferred that LE and CT states of photoexcited DCM strongly coupled adiabatically in the inverted region where a large extent of the charge separation process occurs on a picosecond time scale controlled by the excited state solvation process. However, subsequent high-resolution (<100 fs) fluorescence up-conversion studies of the DCM dye molecule in methanol and chloroform reveal that there is no change of the integrated spectral intensity during the first 25 ps after vertical excitation for the LE → CT transition [31]. Besides, for all times only one fluorescent excited state was noticeable, and the observed dynamic Stokes shift is attributed to solvent relaxation. Mean position of the time-resolved fluorescence spectrum of DCM in methanol shifts towards the red side with bi-exponential (175 fs and 3.2 ps) behavior, while in chloroform the spectral position remains practically unchanged for all times. The collected time-resolved data concluded that DCM has a single emitting state, which is directly populating upon photoexcitation.

A binodal dynamic Stokes shift was observed with time constants, one is about 100 fs, and another is of few picoseconds, respectively, when DCM is present in highly polar solvent media (methanol, ethylene glycol, ethyl acetate, and acetonitrile) [32]. The initial fast component is attributed to the free streaming motions of the solvent molecules and the second slow time component to the rotational diffusion motions of the solvent molecules. However, from the rapid sub-picosecond rise of the integrated emission intensity, it was suggested that the excited state electron transfer is preferentially taking place within about 100 fs from a higher-lying less emissive state to a lower-lying more emissive CT state. That is, the charge separation process in DCM is completed within about 100 fs. The LE and CT states are pictured as strongly coupled in the inverted region which is already reported earlier by Gustavsson et al. [31], and the gradual charge separation is treated as diffusional motion on the resulting barrierless potential. On the other hand, transient absorption spectra of DCM dye in methanol were measured using pump-supercontinuum probe technique with 40 fs time resolution and also revealed two components [33]. Initially (before 70 fs), a prominent spectral structure is observed which is primarily due to resonance Raman processes. At longer times (>70 fs), the spectrum undergoes a significant redshift, and shape of the band changes with a well-defined isosbestic point, and these observations are quite similar to earlier study done by Martin and co-workers [29]. The early transient component has been assigned to the locally excited state of DCM. Further, it was found that LE → CT transition is much faster than that suggested by Martin et al. and concluded that a substantial fraction of the intramolecular charge separation (≥70%) is completed within 300 fs of the pulsed excitation.

Later, time-resolved visible pump and infrared (IR) probe transient absorption measurements of the DCM and its isotopomer DCM-*d6* were studied by Fleming and co-workers to probe the ultra-fast charge-transfer state formation in polar solvents: dimethylsulphoxide (DMSO) and acetonitrile (MeCN) [34]. Transient infrared absorption bands at both a fingerprint region between 1440 and 1620 cm^{-1} and the CN stretching region, ~2208 cm^{-1} , were probed. The IR band at 1440 cm^{-1} is assigned to the LE state of DCM, while the higher-frequency absorptions (1495, 1520, and 1590 cm^{-1}) are assigned to the CT state. The results reveal that excited-state absorption bands in the fingerprint region (1495 cm^{-1}) are exhibiting a frequency upshift and/or changes in band shape on a few ps time scale (~1–2 ps) which was attributed to the formation of the excited state and charge-transfer state via twisting and pyramidalization of the C–N(Me)₂ group and associated changes in C–C bonding character throughout the molecule. That is the fast rise in the CT bands was assigned to the rapid evolution of the LE state into the CT state.

Excited state non-radiative relaxation dynamics of DCM in hexane have been investigated using femtosecond fluorescence up-conversion technique at three

excitation wavelengths [35]. The S₁ lifetime was observed to be 9.8 ps which is found to be independent of the excitation wavelengths. The observed S₁ lifetime of DCM is less by one order of magnitude as compared to julolidyl DCM dyes DCJT and DCJTb, indicating the significance of the twisting motion of the N,N-dimethylamino group affecting the S₁ non-radiative dynamics. Further, TDDFT calculations suggest that an intersystem crossing is responsible for the observed S₁ dynamics of DCM in non-polar solvent.

2.5 What is understood about DCM dye?

The ground state and dipole moments of DCM are estimated to be very high (5.6 D and 26.6 D) which suggests that the charge is highly polarized even in the ground state. The steady-state absorption and fluorescence spectra of DCM reveal that the molecule exhibit solvatochromic shift and large Stokes shifts depending on the polarity of the solvent [10, 16, 24]. Solvatochromic shift of the electronic absorption is due to high ground-state dipole moment. The dramatic Stokes shift is attributed to the change of the dipole moment upon photoexcitation and fluorescent emitting state to a charge-transfer (CT) state [23, 24]. The fluorescence lifetime of DCM is measured to be of the order of a few nanoseconds, and the solvent relaxation occurs in between sub-picoseconds and picoseconds [9, 10, 23, 28–33]. Both fluorescence lifetime and relaxation depend on the solvent polarity.

Photoexcitation of DCM to its first absorption band put the excited molecule in the S₁/LE state, and subsequently two conformational changes may happen. Firstly, –C=C bond rotation leading to trans and cis isomerization via a phantom singlet state which is a typical photochemical process occurring on trans-stilbene [36] and many olefin molecules [37]. Secondly, twisting of the N,N-dimethylamino group may give rise to a highly polar twisted intramolecular charge-transfer (TICT) state which can be stabilized in polar media like 4-dimethyl-aminobenzonitrile (DMABN) molecule [37, 38]. However, the transition from the LE state to the CT (or TICT) state is under debate, and from both experimental and theoretical calculations [39], the following widely accepted dynamical behavior has been proposed to understand the excited-state dynamics of DCM dye. The potential energy surface (PES) of the LE state (S₁) for twisting motion of the central C=C bond (which bridges N,N-dimethylamino group with pyran group) is calculated to be very small (0.2 eV), and the barrier height is insensitive to the polarity of solvent. However, the shape of excited-state PESs of for the twisting motion of the CN single bond of the N,N-dimethylamino group of DCM is strongly influenced by the polarity of the solvent [39]. Moreover, in a polar media, the energy of the S₁/LE state increases, whereas the energy of the S₂/CT state decreases by twisting the CN single bond of the dimethylamino group and leads to a nonadiabatic curve crossing between the two states. Therefore, the formation of an emissive TICT state along the amino group twisting coordinate is more favored with increasing the polarity of the solvent. Trans and cis isomerization is dominated in polar solvents because of the increased the energy barrier in the TICT state along the torsional coordinate of the C=C double bond when the TICT state is formed at the perpendicular geometry where the energy of the S₁/LE state is higher than that of the S₂/CT state.

3. DCM derivatives as optical sensors

A *chemosensor* can be any organic or inorganic complex molecule that is used for sensing of an analyte to produce a detectable change or a signal [40–43]. Similarly, Cambridge defined the chemical sensor as a ‘miniaturized device that can deliver

real time and online information on the presence of specific compounds or ions in even complex samples'. The chemical sensors employ specific transduction techniques to obtain analyte information. The chemical sensors are widely developed based on optical absorption, luminescence, and redox potential principles. Moreover, sensors based on other optical parameters, such as refractive index and reflectivity are also frequently reported in the literature [44].

Any chemosensor consists of three components: a *chemical receptor* which is capable of recognizing the analyte/guest of interest; a *transducer* or *signaling unit* that converts recognition event into a measurable physical change; and finally a method of measuring change and converting it to useful signal/information. An ideal chemosensor is expected to have high selectivity, sensitivity, prompt response, and low cost. Various approaches have been developed in the recent past years by various groups for designing chemosensors and broadly classified in to three different approaches [45], which only differ in the arrangement of receptor and signaling unit:

- Binding site-signaling approach
- Displacement approach
- Chemodosimeter approach

These approaches only differ in the arrangement of two units (receptor and signaling) with respect to each other. In the 'binding site-signalling subunit' approach, two parts are linked through a covalent bond. The interaction of the analyte/guest with the binding site induces changes in the electronic properties of the signaling subunit that results sensing of the target anion. The displacement approach is based on the formation of molecular assemblies of binding site-signaling subunit, which in coordination of a certain anion with the binding site results in the release of the signaling subunit into the solution with a concomitant change in their optical properties. In the chemodosimeter approach, a chemical reaction results in an optical signal when a specific anion approaches the receptor. Depending on the type of signals that are produced upon the recognition event, chemosensors are classified into two categories: optical sensors and electronic sensors. While the former sensors change optical signals, the latter change electrochemical properties. Based on the type of optical signal, the optical sensors further can be classified into two categories.

Chromogenic chemosensors change the color upon the recognition event (binding of analyte/guest into the receptor subunit) and thus show variation in absorption of signaling unit. Since the color of parent solution is changing after recognition, these are also known as colorimetric sensors.

Fluorogenic chemosensors change the fluorescence of the signaling unit upon the recognition event. These are also called fluorosensors.

It has been demonstrated that the colorimetric sensors are simple and low-cost and offer both qualitative and quantitative information without any need of sophisticated spectroscopic instrumentation, and most often the colorimetric response can be visualized with the naked eye. On the other hand, the fluorescence measurement is a bit expensive but relatively more sensitive and versatile and offers micro- to nanomolar estimation of guest species. A wide variety of optical chemosensors have been reported for the cation, anion, and neutral molecules. Based on the nature of analyte being detected, irrespective of the photophysical phenomenon the receptors follows, the chemosensors may be broadly classified into three categories: cations sensors, anions sensors, neutral sensors.

The ICT mechanism has been exploited quite extensively in ion sensing and molecular switching applications [45, 46]. A fluorosensor is generally designed to

have two units: a signaling unit typically a fluorophore and a receptor (recognition unit) which are covalently connected with a π -spacer for rendering the recognition event to the fluorophore that ultimately changes fluorescence signal. A group of fluorogenic sensors which has either weak fluorescence or no fluorescence (off state) by nature and that becomes fluorescent (on state) upon the receptor recognizes the analyte/guest molecule, and this type of fluorogenic sensors are called as off–on sensors. Similarly, on–off sensors can also be designed, where a sensor initially exhibits fluorescence (on state) and after the recognition event, the sensor becomes nonfluorescent/weakly fluorescent (off state). A schematic representation of off–on fluorogenic sensors is shown in **Figure 4**.

As discussed in the previous section, the DCM molecule and its derivatives are having unique advantages in terms of their photophysical properties such as red light emission, high quantum yield, and highly tunable fluorescence that is sensitive not only by solvent polarity but also structure modification. Unlike visible light fluorogenic sensors, red and NIR fluorogenic sensors (600–950 nm) have received considerable interest due to minimum fluorescence background, less light scattering, and less photodamage and are having certain advantages in bioimaging applications of live cells. Therefore, in recent years, there is a consistent growth of the colorimetric and fluorogenic sensors based on DCM and its analogues (**Figure 5**) for sensing cations, anions, and neutral species, which are summarized below.

3.1 DCM derivatives as metal sensors

Valeur and Bourson designed a DCM derivative, **DCM1**, which contains a receptor macrocycle (monoaza-15-crown-5) unit that is covalently attached to the electron-donating substituent (N,N-dimethylaniline unit) [47]. It was found that the resulting fluorosensor **DCM1** has almost identical photophysical properties to that of DCM. However, upon complexation with alkaline earth metal cations such as Li, Na, Mg, and Ca, the absorption spectra of **DCM1** undergo either hypsochromic shift or hypochromic shift. Similarly, with addition of alkaline metal cations, a substantial decrease in the fluorescence emission intensity and quantum yield was also observed. It is interesting to note that the fluorescence

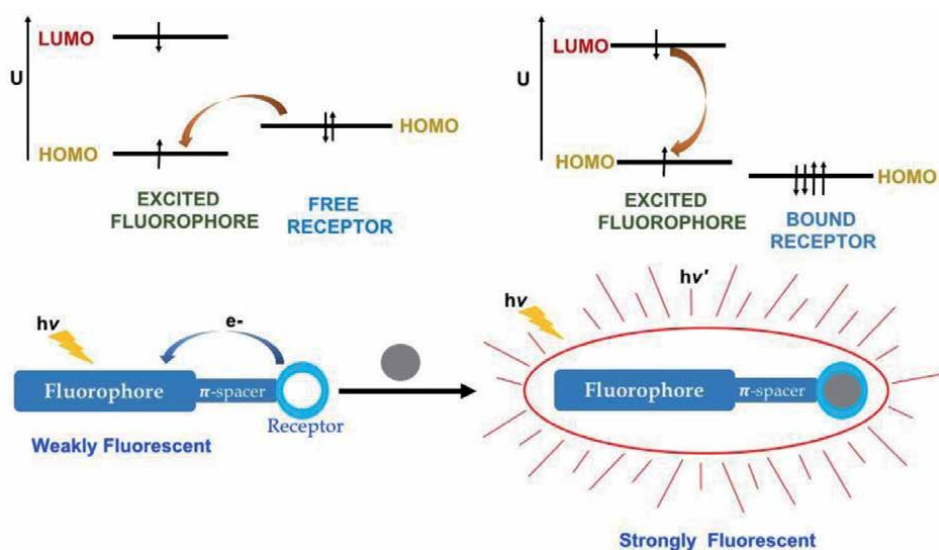


Figure 4. Schematic diagram of OFF–ON fluorogenic sensing mechanism [45, 46].

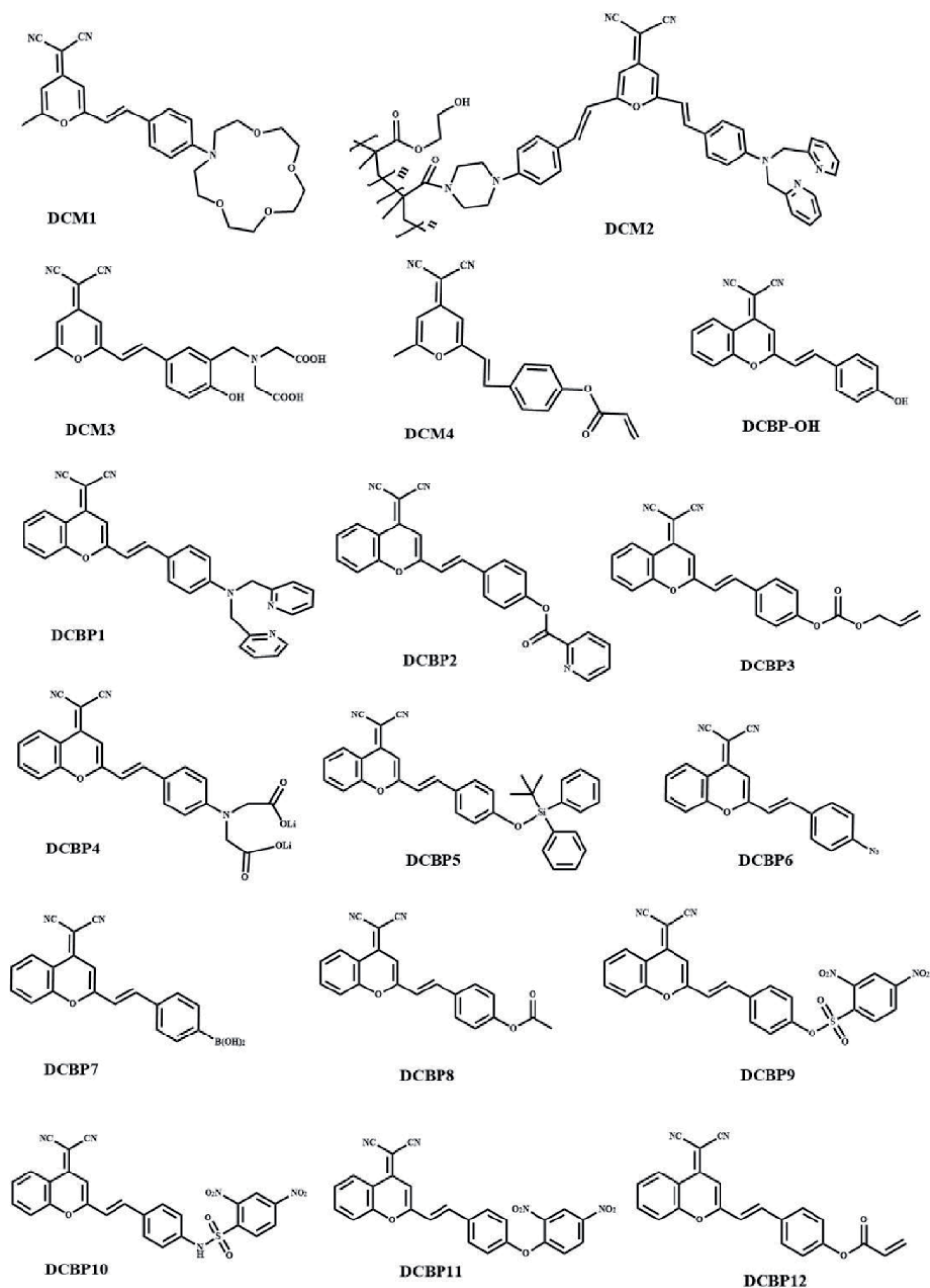


Figure 5.
Molecular structures of DCM and its derivatives as optical sensors for various analytes.

emission is slightly blueshifted and corresponding fluorescence lifetime is almost unchanged. It is well established that the ICT from the electron donor to the electron acceptor can be diminished if the electron-donating character of the donor moiety is reduced. In the **DCM1** fluorosensor, the nitrogen atom belongs to the crown, and therefore, upon complexation with cations, the donating ability is reduced and thus hinders the ICT character which more or less depends upon on the nature of the cation. From the observed sensing changes, it is understood that the charge transfer of the cation plays a key role and the reduction of

charge-transfer efficiency from a nonemissive locally excited state to an emissive relaxed intramolecular charge-transfer state (RICT).

A red fluorosensor (**DCBP1**) was designed by replacing N,N-dimethylamine of **DCM** with bis(2-pyridylmethyl) amine (DPA) moiety and benzopyran backbone [48]. Screening of various alkaline and transition metals reveals that the **DCBP1** has more binding affinity towards Cu^{2+} ions than that of any other cations. The binding affinity is evident not only from the absorption spectrum but also colorimetric response where light pink color of free **DCBP1** solution changes to yellow color after coordinating with copper ions (**DCBP1-Cu2+**), which is visible even to the naked eye. Free **DCBP1** shows a characteristic emission band around 650 nm (with fluorescence high quantum efficiency, $\phi_{\text{DCBP1}} = 0.40$) which is redshifted 55 nm as compared to fluorescence emission of **DCM** ($\lambda_{\text{em}} = 595$ nm) due to insertion of a conjugated benzene unit onto the dicyanopyran backbone. Fluorescence behavior of **DCBP1** in presence of various metal ions was studied in a mixture of ethanol-water (60:40, v/v), and it is observed that only the addition of Cu^{2+} to **DCBP1** causes a significant decrease in fluorescence intensity. Surprisingly, when pyrophosphate (PPi) anion is added to the in situ generated **DCBP1** metal complex (**DCBP1-Cu2+**), the absorption at 505 nm increases with a isobestic point at 447 nm, and the color of the solution also changes from pale yellow to pink (original color of **DCBP1**). Similarly, fluorescence emission of the **DCBP1-Cu2+** is turned on, and fluorescence emission intensity at 650 nm is also enhanced. From the fluorescence measurements, it is observed that **DCBP1** forms a 1:1 complex with pyrophosphate (PPi) anion, and association constant (K_a) is estimated to be very high at 4.6×10^5 M. Further, an investigation of a series of other anions reveals that the **DCBP1** probe molecule is highly selective and sensitive only towards PPi anion. The observed colorimetric response and on-off fluorescence response of **DCBP1** were attributed to the inhibition of the ICT because of decreased the electron-donating ability of the amino group upon binding with Cu^{2+} ion. On the other hand, turn-on fluorescence is due to electrostatic interaction between PPi and **DCBP1-Cu2+**. Since, the two oxygen atoms of PPi somewhat strongly coordinated with the copper, and the nitrogen-copper bond gets weakened which restores the ICT; thereby fluorescence emission is enhanced. Therefore, the **DCBP1** molecule is demonstrated as both fluorescence on-off and off-on sensor when it is binding with Cu^{2+} ions and PPi, respectively.

In general, most of the fluorosensors exhibit on-off sensing behavior in solution phase because quenching of fluorescence emission is quite easy. However, developing off-on fluorosensor with processible technology is relatively a tedious and challenging task. Such fluorescence off-on sensors can be tailored to meet the specific needs via rational design approaches and have been paid much attention in recent years due to growing demand of various chemical and biological species detection by exploiting energy transduction principles such as radiant, electrical, mechanical, and thermal processes [49, 50]. Tian and co-workers have extended their previous research work [48] and developed a polymeric **DCM2** sensor based on a hydrophilic copolymer bearing the **DCM** moiety in the form of a fluorescent film which senses Cu^{2+} and PPi anion works based on off-on fluorescence mechanism (**Figure 6**) [51]. The sensor **DCM2** is decorated with a hydrophilic copolymer, poly(2-hydroxyethyl methacrylate) (PHEMA), that exhibits high hydrophilicity but insoluble in water. The hydrophilic chain segment was chosen mainly to improve the permeability of ions into the polymer backbone, and the **DCM** fluorophore is also grafted into the polymer backbone as metal ion-sensing units. The copolymer **DCM2** and the corresponding metal complex, **DCM2-Cu2+**, exhibit turn-off fluorescence for the selective targeting of Cu^{2+} (**Figure 6**). However, interestingly, upon adding PPi anion, the fluorescence of the copolymer is turned on with high sensitivity both in solution and in thin film over other anions such as AMP, ADP, ATP, and phosphate (Pi). Furthermore, the low-cost

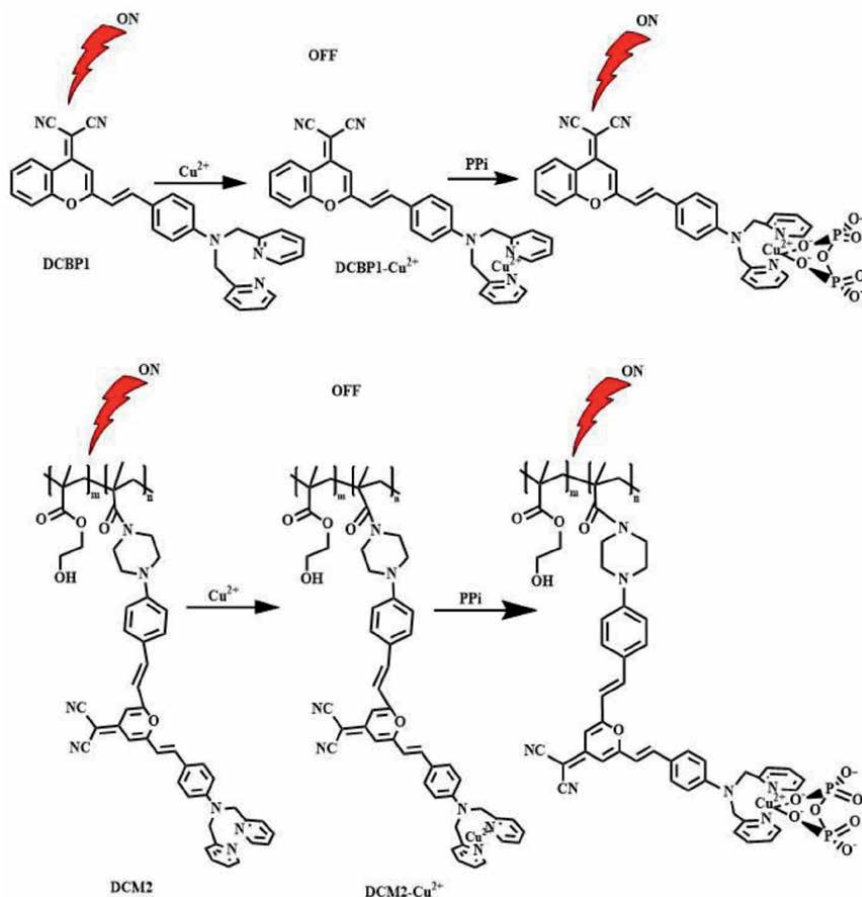


Figure 6. Fluorescence on-off and off-on mechanism of DCBP1 (above) DCM2 copolymer (below).

hydrophilic copolymer film of **DCM2-Cu²⁺** on a quartz plate shows a very rapid response towards PPI anion with turn-on orange-red fluorescence due to high permeability of its side chains. Recently, a new **DCM**-based NIR fluorescent probe (E)-4-(2-(4-(dicyanomethylene)-4H-chromen-2-yl)vinyl) phenyl picolinate (**DCBP2**) was designed and synthesized for Cu^{2+} ions with improved performance [52]. As shown in **Chart 5**, the sensor molecule **DCBP2** consists of **DCBP-OH** as a fluorophore and electron-withdrawing 2-pyridinecarbonyl group as the receptor for Cu^{2+} ions. The reaction between **DCM-OH** and 2-pyridinecarbonyl gives rise to picolinoyl ester of the **DCM**. Since 2-pyridinecarbonyl group is covalently anchored to the fluorophore, the ICT is blocked, and no fluorescence can be observed. At this stage when Cu^{2+} is added to the probe, the copper ions coordinate with nitrogen and oxygen atoms of 2-pyridinecarbonyl group fluorescence emission quenches. However, upon hydrolysing **DCBP2** with water, Cu^{2+} releases from coordination, and subsequently a phenolate ion (**DCBPO⁻**) is produced, which is a better electron-donating group and thus restores its ICT property which ultimately leads to a dramatic increase in fluorescence intensity at 676 nm. The sensing behavior of the probe **DCBP2** towards Cu^{2+} ions can also be conveniently followed by naked eye inspection and measuring absorption under mild conditions. The color of the solution appears yellow in absence of copper ions, which, however, changes to pink color upon adding copper ions and clearly visible to the naked eye. The free **DCBP2** gives absorption 558 nm upon, and binding with copper ions, the absorption shifts 415 nm (blueshift). Furthermore, this probe was

successfully applied for the quantitative estimation of Cu^{2+} in various types of water samples and also demonstrated its utility in imaging living cells.

DCBP3 is designed based on the Pd(0)-catalyzed Tsuji-Trost allylic oxidative insertion reaction and dicyanomethylene benzopyran moiety [53]. Photophysical properties revealed that the probe **DCBP3** exhibits high sensitivity and selectivity towards the detection of both Pd(0) and Pd(II) under reducing conditions. The probe **DCBP3** shows a major absorption band with a maximum at 450 nm, and after treating with palladium, another new absorption peak started appearing around 560 nm. On the other hand, **DCBP3** displays no fluorescence at 700 nm when excited at 560 nm. However, upon the addition of palladium, the fluorescence emission peak at 700 nm increases gradually. Additionally, marked color changes were also noticed. All the photophysical properties have been explained based on palladium-triggered cleavage reaction that produced a free **DCBP-OH**. Moreover, the probe **DCBP3** is little affected with pH variation and has low cytotoxicity.

3.2 DCM derivatives as anion sensors

As discussed in Section 3.1, the molecules **DCBP1** and **DCM2** form copper complexes (**DCBP1 Cu²⁺** and **DCBP1-Cu²⁺**), and their fluorescence emission quenches drastically [48, 51]. In situ generated **DCBP1 Cu²⁺** and **DCBP1-Cu²⁺** recognize PPI anion which can be tracked from spectrophotometrically and fluorescence measurements. Later, the molecule **DCBP1** was modified by decorating with a lithium iminodiacetate group in place of N-aryl group [54]. The synthesized NIR fluorophore, **DCBP4**, selectively binds with Cu^{2+} ions because of lithium iminodiacetate receptor and found to have very good solubility in aqueous water. The photophysical properties of metallated fluorophore (**DCBP4-Cu²⁺**) were found to be modified upon interacting selectively with pyrophosphate (PPI) anion. When PPI is gradually added to the solution of **DCBP4-Cu²⁺**, a new redshifted peak at 503 nm appeared and increased gradually with an isosbestic point at 450 nm. The absorption spectral changes are very much evident to the naked eye where the pale brown color of the **DCBP4-Cu²⁺** solution changes to red color. On the other hand, simultaneously turned on fluorescence and emission intensity in the NIR region (675 nm) are enhanced gradually and stabilized upon the addition of 15 equiv. of PPI. The fluorescence off-on switching and the colorimetric response of **DCBP4-Cu²⁺** are interpreted in terms of ICT variations upon sensing the receptor.

A near-infrared (NIR) fluorescent chemosensor, **DCBP5**, was developed on the basis of dicyanomethylene-4H-benzopyran derivative for detecting fluoride anions [55]. Chemodosimeter **DCBP5** was synthesized by the Knoevenagel condensation of 4-dicyanomethylene-2-methyl-4H-pyran and 4-(tert-butyl)diphenylsilyloxy benzaldehyde. With the addition of F^- ions to the **DCBP5** sensor, absorption band centered at 447 nm slowly decreases, and at lower F^- concentration ($<30 \mu\text{M}$), a new absorption emerges at 454 nm gradually. When the F^- concentration was further increased beyond $50 \mu\text{M}$, the new absorption band at 454 nm decreases, and a concomitant increase of a new band at 645 nm was observed with an isosbestic point at 510 nm. The large redshift (190 nm) is also noticeable to the naked eye in which the initial pale yellow color of the **DCBP5** solution changes to blue color upon adding fluoride ions. It should also be noted that the sensing process is very fast, and within 30 s the sensing is noticeable to the naked eye. The observed isosbestic point of **DCBP5** sensor upon addition of the F^- ions clearly indicates formation of a new species which is attributed to phenolate group generation due to Si-O cleavage. Similar supporting results were also observed from fluorescence measurements. The **DCBP5** molecule is non-fluorescent due to the presence of silyl group. However, the sensor **DCBP5** turn-on fluorescence with gradual addition of

F⁻ ion which is evident from the fluorescence emission measurements in which a new fluorescent band started emerging in the NIR region (at 718 nm). Since the in situ generated phenolate group is a much stronger electron-donating group than the silyl group, the ICT efficiency restored after **DCBP5** interaction with that of F⁻ ions. Further, the results also revealed that the **DCBP5** is not just an off-on fluorescent sensor, but it is also a ratiometric and colorimetric sensor which is the ideal characteristic of any sensor.

3.3 DCM derivatives for detection of neutral species

3.3.1 Hydrogen sulphide (H₂S)

Hydrogen sulphide (H₂S) is involved as a signaling molecule in various physiological processes that include modulation of neuronal transmission, regulation of release of insulin, relaxation of the smooth muscle, and reduction of the metabolic rate [56, 57]. From the animal model study of critical illness, it was realized that the H₂S donor protect from lethal hypoxia and reperfusion injury and exert anti-inflammatory effects [58]. Physiological H₂S concentration is estimated to vary from nano- to millimolar levels [59], and once this limit is crossed, the cells release H₂S that can cause certain diseases, such as Alzheimer, Down syndrome, diabetes, and other diseases of mental deficiency [60]. Hence, a reliable in vivo study is essential to measure accurately H₂S concentration thereby preventing deceases. A NIR probe, **DCBP6**, that comprises dicyanobenzopyran and 4-azidostyryl group as receptor was developed for selective detection of H₂S [61]. The probe **DCBP6** selectively reacts with H₂S and reduces the azido group (-N₃) to amine (-NH₂), and the corresponding molecule becomes highly fluorescent than the parent **DCBP6**. Upon H₂S detection, the **DCBP6** probe solution changes which is visible to the naked eye and causes a large Stokes shift (>100 nm in different solvents). Besides, the reduced probe **DCBP6NH2** exhibit two-photon absorption (TPA) which is having more advantages than traditional one-photon absorption probes in fluorescence microscopy such as less phototoxicity, better three-dimensional spatial localization, deeper penetration depth, and lower self-absorption. Further, the probe molecule **DCBP6** was successfully used as fluorescent probe for monitoring H₂S in living cells and tissues and in vivo in mice via fluorescence bioimaging investigations. More or less at the same time, Xu and co-workers have reported the same molecular probe for in vivo detection of H₂S [62].

3.3.2 Dopamine

A catecholamine compound dopamine is known as a neurotransmitter that regulates a wide range of cognitive functions such as behavior, learning, motivation, and memory [63–65]. The dopamine content in the human brain is an important factor that can cause various diseases that include Parkinson's disease, and in fact it is used as a marker in the diagnosis of several conditions related to neurotransmitters. Therefore, there is a strong quest for developing efficient and rapid methods that can selectively determine and continuously sense the dopamine levels on a real-time basis. The DCM fluorosensor (**DCM3-Fe²⁺**) was developed for selective detection of dopamine based on on-off sensing mechanism [66]. The electron-donor part of DCM fluorophore is modified with a ligand, diethyliminodiacetic acid, such that it selectively complexes with iron(II) ions. In the absence of dopamine, the sensor molecule **DCM3-Fe²⁺** is weakly fluorescent due to inhibition of ICT because of Fe²⁺ complexation with the donor moiety (off-state fluorescence). However, a much stronger fluorescence emission was observed upon gradual addition of dopamine owing to the release of Fe²⁺ from DCM complex. A good linear relationship was

observed between the dopamine concentration and the fluorescence intensity. That means the observed fluorescence enhancement which is observed after addition of dopamine serves as an indicator to monitor dopamine content in a given sample. Besides, the fluorosensor does show any fluorescence response against other foreign substances, thereby allowing selective detection of dopamine.

3.3.3 Hydrogen peroxide (H_2O_2)

Zhang et al. have synthesized a new NIR and colorimetric fluorescent molecular probe, **DCBP7**, by covalently attaching dicyanomethylene-4*H*-benzopyran and phenylboronic acid for rapid detection of H_2O_2 [67]. The boronic acid functional group is attached primarily to have NIR fluorescence off-on switching. The sensing of H_2O_2 was successfully demonstrated by UV-visible absorption and fluorescence measurements. **DCBP7** exhibit a structured absorption band at 450 nm, and its solution appears pale yellow in color. However, with gradual addition of H_2O_2 (>20 equiv.), apparently, the absorption at 450 nm decreases, and a new absorption band starts evolving at 560 nm. Due to the large redshift (110 nm) of the absorption, the color of the solution (yellow) changed to purple, and colorimetric detection of H_2O_2 is visible even to the naked eye. The fluorescence measurements were also carried out to confirm the H_2O_2 sensing behavior of the probe molecule. The free probe molecule is non-fluorescent primarily because of phenylboronic group. However, after adding H_2O_2 , the boronic acid group gets cleaved and generate a phenolate ion which is evident from the new fluorescent emission band at 670 nm. The Stokes shift (110 nm) of the phenolate band in the NIR region has been exploited further for detecting H_2O_2 and imaging live cells. Unlike the most conventional fluorescent probes, the developed **DCBP7** has been shown to have unique advantages such as deeper tissue penetration ability, lower background autofluorescence, and less damage to biological samples which ultimately allowed to in vivo studies of live cells.

3.3.4 Hydrazine (N_2H_4)

Hydrazine is used as a common precursor in synthetic chemistry of many polymers, pharmaceutical intermediates, hydrazine fuel cells in power generation sector, and materials science [68, 69]. It is often used in rocket propulsion systems as an important propellant for its flammable and detonable characteristics. Moreover, hydrazine serves as an important metal corrosion inhibitor because of its strong reducing properties; hydrazine scavenges oxygen in water boilers that are used for feed and heating systems. However, hydrazine and its aqueous solutions are highly toxic to all living organisms when inhaled or in contact. It has been shown that hydrazine is mutagenic and carcinogenic which causes serious damage to the human central nervous system, kidneys, liver, and lungs [70]. Therefore, it is of great interest and importance to develop a reliable method for hydrazine detection with selectivity and sensitivity. With a view to develop efficient DCM-based NIR fluorophore for selective detection of hydrazine, a phenyl ring bearing *O*-acetyl moiety was introduced onto the into dicyanomethylene-4*H*-benzopyran backbone and synthesized **DCBP8** [71]. The absorption and fluorescence properties of **DCBP8** were measured in PBS solution (pH = 7.4) containing 50% of ethanol. **DCBP8** has absorption in between 300 and 450 nm region with a maximum at 434 nm. After treatment of **DCBP8** with N_2H_4 , gradually new absorption peaks started appearing at 551 nm at the expense of 434 nm absorption band. The absorption maximum shifted from 434 nm to 551 nm which indicates the efficiency of **DCBP8** for colorimetric detection of N_2H_4 when absorption intensity ratio (A_{551}/A_{434}) and concentration of N_2H_4 ranging from 0 to 40 μ M are plotted against each other, there is a

good linearity suggesting a ratiometric response. On the other hand, free DCBP8 is almost no fluorescent upon excitation at 560 nm, which showed a dramatic fluorescence enhancement at 680 nm upon addition of N₂H₄. The fluorescence enhancement is found to be more than 110-fold. Mass spectrometry data along with photophysical properties revealed that the N₂H₄-mediated acetyl deprotection of DCBP8 generates **DCBP8-O-**, a highly fluorescent product because of ICT character.

3.4 DCM derivatives for sensing biothiols and selcysteine

3.4.1 Biothiols

There is quest for developing molecular probes for rapid, selective, and sensitive detection of the highly toxic thiophenols which are of great importance in both environmental and biological science. James and co-workers have developed a novel near-infrared (NIR) and colorimetric fluorescent molecular probe, **DCBP9**, based on a dicyanomethylene-4H-pyran chromophore for selective detection of glutathione in living cells [72]. The molecular probe **DCBP9** was synthesized by Michael's addition of 2-(2-(4-hydroxystyryl)-4H-chromen-4-ylidene) malononitrile and 2,4-dinitrobenzene-1-sulphonyl chloride (DNBS) in the presence of pyridine at room temperature. Molecular probe has an intense absorption centred at 414 nm in a DMSO-PBS buffer solution; upon the addition of glutathione (GSH), the color of the solution turned to pink from slight yellow and clearly visible to the naked eyes. In addition, a new absorption band emerged at 560 nm with an isosbestic point at 446 nm which is assigned to the specific O-S cleavage, and the generation of phenolate ion with a distinct 146 nm redshift in absorbance is observed. Since the phenolate group is a much stronger electron donor than the sulphonate group, the ICT efficiency is significantly enhanced by the interaction of **DCBP9** with GSH and thus shifts the absorption to a longer wavelength region. Subsequent fluorescence experiments showed that the molecular probe alone is nonemissive (turn-off) in absence of GSH. However, when the probe is excited at 560 nm in presence of GSH, turn-on fluorescence and the intensity at 690 nm were dramatically enhanced. The turn-on fluorescence is due to the release of electron-withdrawing DNBS moiety via a GSH-induced O-S bond cleavage and produces phenolate ion, which possesses a strong ICT character and induces a turn-on NIR fluorescence. Having known chemical properties of thiophenols that are able to cleave sulphonamide selectively and efficiently under mild conditions, a dicyanomethylene-benzopyran-based NIR fluorescent probe **DCBP10** is designed for detection of thiophenols [73]. Upon adding thiophenols to the **DCBP10** solution, the DNBS moiety is cleaved and forms amine (-NH₂) functional group at the phenyl ring. Since the amine is an electron-donating group, the ICT of the fluorophore is restored, and as a result, absorption and fluorescence emission properties of the probe were changed. This probe features remarkable large Stokes shift and shows a rapid, highly selective, and sensitive detection process for thiophenols with significant NIR turn-on fluorescent response. Therefore, **DCBP10** was successfully demonstrated as a potential NIR fluorescent probe that can be mitigated not only for quantitative detection of thiophenol in real water samples but also fluorescence imaging of thiophenol in living cells [73].

Slightly similar molecular structure **DCBP11** is redesigned by Li et al. that consists of dicyanomethylene-benzopyran scaffold and 2,4-dinitrophenyl (DNP) connected by ether linkage for probing for thiophenols [74]. It was demonstrated that **DCBP11** shows both colorimetric and rapid turn-on fluorescence sensing process for thiophenols with high selectivity and better sensitivity (DL = 70 nm). Moreover, it should be noted that a dual colorimetric and selective NIR fluorescence sensing phenomenon is also visual to the 'naked eye' without the need of advanced

instrumentation. In addition, quantitative detection of thiophenol in real water samples and fluorescent imaging of thiophenol in living cells and zebrafish were successfully demonstrated which suggests that this probe has a great potential for in vitro and in vivo applications. Another NIR probe, which contains a conjugated dicyanomethylene-benzopyran moiety as the NIR fluorophore **DCBP12** and an acrylate moiety as a receptor, is found to be promising for biothiols: cysteine (Cys), homocysteine (Hcy), and glutathione (GSH) detection. **DCBP12** itself almost non-fluorescent due to alkene-induced quenching of photoinduced electron-transfer (PET) process; however, it becomes fluorescent upon sensing biothiols. It has been proven that the NIR fluorescence enhancement of **DCBP12** is due to Cys sensing originating from cleavage of acryloyl group of **DCBP12** that simultaneously releases a NIR fluorescent DCM-OH. A feasible sensing mechanism was proposed to understand the sensing process of Cys. The reaction of Cys with **DCBP12** involves two steps. Initially, a Michael addition reaction of the thiol functional group of Cys with the acryloyl group has taken place and then followed by a spontaneous intramolecular cyclization to release the NIR fluorescent, phenolate ion (**DCMO⁻**). Further, the detection limit for Cys was estimated to be 81 nM. In addition, imaging of biothiols by **DCBP12** was also successfully demonstrated in living cells which indicates that this probe is suitable for imaging biological samples [75]. Therefore, **DCBP12** shows rapid response and high-selectivity and high-sensitivity biothiols particularly for Cys and Hcy, accompanied by distinct color changes seen by the naked eye and significant NIR turn-on fluorescence responses.

Recently, a red-emitting fluorescent probe **DCM4** was developed for selective detection of cysteine (Cys) over glutathione (GSH) and homocysteine (Hcy) by incorporating acryloyl group as the recognition unit into the 2-(2-(4-hydroxystyryl)-6-methyl-4H-pyran-4-ylidene) malononitrile (P-OH) fluorophore [76]. Selective detection of Cys is very important because, among biothiols, Cys is considered as the most significant biothiols of living organisms and plays a crucial role in multiple physiological processes that include mitochondrial protein turnover, protein biosynthesis, detoxification administration, and metabolism regulation [77]. Further, because of crucial physiological and pathological significance of Cys in biological systems, it is essential to develop a rapid and promising analytical tool for selective detection of Cys so as to unravel hidden physiological processes of Cys and understand the specific pathogenesis of Cys-related diseases. Basically, the probe design is almost similar with **DCBP12** used for thiol detection and **DCBP3** used for palladium detection. The **DCM4** molecule is almost non-fluorescent due to acryloyl group that blocks ICT and promotes non-radiative processes. Upon the addition of Cys, **DCM4** undergoes Michael addition of Cys and the acryloyl group to afford a transient intermediate, followed by the intramolecular cyclization to give highly fluorescent oxide anion. Therefore, accordingly by monitoring fluorescence intensity variations before and after the addition, the Cys can be detected. The fluorosensor **DCM4** has certain advantages. Firstly, probe **DCM4** has good selectivity for Cys over Hcy and GSH. Secondly, the probe senses Cys in the solution and responds in a short time (4 min) towards Cys. Thirdly, this probe exhibits high signal-to-noise ratio (~147-fold) and ultralow detection limit (41.696 nM). Thus, the **DCM4** was successfully demonstrated as off-on fluorosensor to monitor the Cys level in living cells with low cytotoxicity.

3.4.2 Selenocysteine

Selenocysteine (Sec) is a cysteine (Cys) analogue which consists of selenol group in place of the thiol group in Cys and considered as a major form of biological selenium and known as the 21st proteinogenic amino acid that is specifically

incorporated into selenoproteins (SePs). More than 50 human proteins are known to contain Sec [78]. Therefore, detection of Sec in physiological conditions is very important. In order to achieve NIR turn-on fluorescent detection of Sec selectively, the molecule **DCBP11** was designed which was originally used for thiol detection [74]. **DCBP11** senses the presence of Sec and shows colorimetric and NIR turn-on fluorescence response upon cleavage of ether bond and subsequent formation of **DCM-OH** [79]. Similar to many other DCM-based ICT molecules, **DCBP11** also shows a remarkable large Stokes shift at 146 nm. Besides, **DCBP11** is highly sensitive to Sec and exhibits a very small detection limit of 62 nM over a wide linear range (0.2–80 μ M) of selenocysteines which allows quantitative estimation of the Sec. Moreover, it was further demonstrated that this NIR fluorescent probe can be employed to image both exogenous and endogenous Sec in living cells, indicating that **DCBP11** has great potential for biological applications.

3.5 DCM derivatives as pH sensor

A pH-sensitive fluorescent chemosensor, **DCBP-OH**, was designed based on dicyanomethylene-4H-benzopyran scaffold by employing D- π -A architecture [80]. At neutral pH, the **DCBP-OH** shows absorption at 450 nm which is attributed to the typical ICT band of DCM chromophore and very weak fluorescent (~ 574 nm). Interestingly, as the pH of the solution increases (from 7.15 to 11.00), the weak fluorescence emission band at 574 nm decreases, and simultaneously a new band at 692 nm started increasing. The evolution of new fluorescence band at 692 nm is assigned to the increase of the ICT process from the oxygen anion of phenolate group. That means the strong change in fluorescence intensity is a clear indication for determining pH of any solution from 7 to 11. Acid dissociation constant pK_a value is calculated to be 7.21. Moreover, it was found that the fluorescence signal ratio (I_{692}/I_{574}) is found to be ratiometric induced by a large Stokes shift of about 118 nm. Furthermore, from the absorption and fluorescence measurements, it was proved that the pH response of **DCBP-OH** is reversible which makes **DCBP-OH** a simple naked-eye sensitive NIR fluorescent chemosensor for pH measurement. In a very recent work, the **DCBP-OH** probe has been slightly modified with triphenylphosphate and shown as NIR sensor for lysozyme detection in urine sample [81].

3.6 DCM derivatives as polarity sensor

Kwak et al. developed different types of copolymers by decorating with the DCM moiety into a certain polymer chain which are sensible to external environment and useful to probe dye molecules [82]. The photophysical properties in solution, solid film, and aggregation revealed that ICT characteristics of the copolymers are modifying. More interestingly, it was observed that the fluorescent properties of DCM-type dyes within the polymers are significantly dependent upon the polarity of the polymer matrix. Three copolymers (P(St-*co*-2), P(MMA-*co*-2), and P(AN-*co*-2)) have shown quite unusual photophysical properties which are completely different from the corresponding DCM-type monomer. The copolymers show a blueshift in fluorescence emission relative to the monomer. The aggregates of copolymers prepared in polar medium (DMF) by adding methanol showed a significant blueshift in fluorescence emission, and aggregates prepared from non-polar medium (1,4-dioxan)/methanol exhibit a prominent redshift. Similarly, it was also observed that the fluorescence intensity of P(St-*co*-2) and P(MMA-*co*-2) decreased by aggregation while that of P(AN-*co*-2) increased. Such interesting solvatochromism and unusual aggregation behavior of the three copolymers were exploited further for selective sensing of volatile organic compounds (VOC).

Acknowledgements

RKK acknowledges the Science and Engineering Research Board (SERB), New Delhi, for the research funding (EEQ/2016/000736).

Author details


Ravi Kumar Kanaparthi^{1*}, Satyen Saha², Manjeev Singh¹ and Akhila M¹

1 Department of Chemistry, Central University of Kerala, Kasaragod, Kerala, India

2 Department of Chemistry, Faculty of Science, Banaras Hindu University, Varanasi, India

*Address all correspondence to: rkchem@cukerala.ac.in

IntechOpen

© 2020 The Author(s). Licensee IntechOpen. This chapter is distributed under the terms of the Creative Commons Attribution License (<http://creativecommons.org/licenses/by/3.0>), which permits unrestricted use, distribution, and reproduction in any medium, provided the original work is properly cited. 

References

- [1] Webster GF, McColgin WC. Arylidene dye lasers. US Patent: 3852683; 1974
- [2] Marason EG. Laser dye DCM: CW, synchronously pumped, cavity pumped and single frequency performance. *Optics Communications*. 1981;**37**(1):56-58
- [3] Mau AW-H. Broadband tunability of dye lasers. *Optics Communications*. 1974;**11**(4):356-359
- [4] Chen C-T. Evolution of red organic light-emitting diodes: Materials and devices. *Chemistry of Materials*. 2004;**16**:4389-4400
- [5] Guo Z, Zhu W, Tian H. Dicyanomethylene-4H-pyran chromophores for OLED emitters, logic gates and optical chemosensors. *Chemical Communications*. 2012;**28**:6073-6084
- [6] Zarins E, Vembris A, Kokars V, Muzikante I. Chapter 8: Synthesis and physical properties of red luminescent glass forming pyranilidene and isophorene fragment containing derivatives. In: Singh J, editor. *Organic Light Emitting Devices*. Croatia: IntechOpen; 2012. pp. 197-232
- [7] Hammond PR. Laser dye DCM, its spectral properties, synthesis and comparison with other dyes in the red. *Optics Communications*. 1979;**29**(3):331-333
- [8] Lesiecki M, Asmar F, Drake JM, Camaioni DM. Photoproperties of DCM. *Journal of Luminescence*. 1984;**31&32**:546-548
- [9] Hsing-Kang Z, Ren-Lan M, Er-Pin N, Chu G. Behaviour of the laser dye 4-dicyanomethylene-2-methyl-6-dimethylaminostyryl-4h-pyran in the excited single state. *Journal of Photochemistry*. 1985;**29**:397-404
- [10] Drake JM, Lesiecki ML, Camaioni DM. Photophysics and Cis-trans isomerization of DCM. *Chemical Physics Letters*. 1985;**113**(6):530-534
- [11] Meyer M, Mialocq JC. Ground state and singlet excited state of laser dye DCM: Dipole moments and solvent induced spectral shifts. *Optics Communications*. 1987;**64**(3):264-269
- [12] Bourson J, Doizi D, Lambert D, Sacaze T, Vaveur B. A derivative of laser dye DCM highly soluble in alcohols. *Optics Communications*. 1989;**72**(6):367-370
- [13] Meyer J-C. Photophysical properties of the DCM and DFSBO styryl dyes consequence for their laser properties. *Laser Chemistry*. 1990;**10**:277-296
- [14] Birch DJS, Hungerford G, Imhof RE, Holme AS. The fluorescence properties of DCM. *Chemical Physics Letters*. 1991;**178**(2,3):177-184
- [15] Bondarev SL, Knyukshto VN, Stepuro VI, Stupak AP, Turban AA. Fluorescence and electronic structure of the laser dye DCM in solutions and in polymethylmethacrylate. *Journal of Applied Spectroscopy*. 2004;**71**(2):194-201
- [16] Boldrini B, Cavalli E, Painelli A, Terenziani F. Polar dyes in solution: A joint experimental and theoretical study of absorption and emission band shapes. *Journal of Physical Chemistry A*. 2002;**106**:6286-6294
- [17] Grabowski ZR, Rotkiewicz K, Rettig W. Structural changes accompanying intramolecular electron transfer: Focus on twisted intramolecular charge-transfer states and structures. *Chemical Reviews*. 2003;**103**(10):3899-4031
- [18] Mataga N, Kaifu Y, Kolzumi M. Solvent effects upon fluorescence

- spectra and the dipole moments of excited molecules. Bulletin of the Chemical Society of Japan. 1956;**29**(4):465-470
- [19] Lippert VE. Dipolmoment und elektronenstruktur von angeregten molekülen. Zeitschrift für Naturforschung A. 1955;**10a**:541-545
- [20] Lippert VE. Spektroskopische bestimmung des dipolmomentes aromatischer verbindungen im ersten angeregten singulettzustand. Zeitschrift für Elektrochemie. 1957;**61**(8):962-975
- [21] Rotkiewicz K, Grellmann KH, Grabowski ZR. Reinterpretation of the anomalous Fluorescence of p-N,N-Dimethylaminobenzonitrile. Chemical Physics Letters. 1973;**19**:315-318
- [22] Kanaparthi RK, Sarkar M, Samanta A. Probing the aggregated state of 4-(9-anthryl)-N,N-dimethylaniline by UV-Vis absorption and fluorescence spectroscopy, microscopy, and crystallography. Journal of Physical Chemistry B. 2009;**113**:15189-15195
- [23] Meyer M, Mialocq JC, Rougee M. Fluorescence lifetime measurements of the two isomers of the laser dye DCM. Chemical Physics Letters. 1988;**150**(6):484-490
- [24] Meyer M, Mialocq J-C, Perly B. Photoinduced intramolecular charge transfer and trans-cis isomerization of the DCM styrene dye. Picosecond and nanosecond laser spectroscopy, high-performance liquid chromatography, and nuclear magnetic resonance studies. Journal of Physical Chemistry. 1990;**94**:98-104
- [25] Rullière C. Laser action and photoisomerisation of 3,3'-diethyl oxadiazocyanine iodide (DODCI): Influence of temperature and concentration. Chemical Physics Letters. 1976;**43**(2):303-308
- [26] Rettig W, Majenz W. Competing adiabatic photoreaction channels in Stilbene derivatives. Chemical Physics Letters. 1989;**154**(4):335-341
- [27] Kumpulainen T, Lang B, Rosspeintner A, Vauthey E. Ultrafast elementary photochemical processes of organic molecules in liquid solution. Chemical Reviews. 2017;**117**:10826-10939
- [28] Easter DC, Baronavski AP. Ultrafast relaxation in the fluorescent state of the laser dye DCM. Chemical Physics Letters. 1993;**201**:153-158
- [29] Martin MM, Plaza P, Meyer YH. Ultrafast intramolecular charge transfer in the Merocyanine dye DCM. Chemical Physics. 1995;**192**:367-377
- [30] Zhang H, Jonkman AM, Meulen PVD, Glasbeek M. Femtosecond studies of charge separation in photo-excited DCM in liquid solution. Chemical Physics Letters. 1994;**224**(5-6):551-556
- [31] Gustavsson T, Baldacchino G, Mialocq JC, Pommeret S. A femtosecond fluorescence up-conversion study of the dynamic Stokes shift of the DCM dye molecule in polar and non-polar solvents. Chemical Physics Letters. 1995;**236**:587-594
- [32] Meulen PVD, Zhang H, Jonkman AM, Glasbeek M. Subpicosecond solvation relaxation of 4-(dicyanomethylene)-2-methyl-6-(p-(dimethylamino)styryl)-4h-pyran in polar liquids. Journal of Physical Chemistry. 1996;**100**:5367-5373
- [33] Kovalenko SA, Ernsting NP, Ruthmann JF. Femtosecond hole-burning spectroscopy of the dye DCM in solution: The transition from the locally excited to a charge-transfer state. Chemical Physics Letters. 1996;**258**:445-454

- [34] Van Tassel AJP, Fleming GR. Investigation of the excited state structure of DCM via ultrafast electronic pump/vibrational probe. *Journal of Physical Chemistry B*. 2006;**110**:18989-18995
- [35] Chang C-W, Kao Y-T, Diao EW-G. Fluorescence lifetime and nonradiative relaxation dynamics of DCM in nonpolar solvent. *Chemical Physics Letters*. 2003;**74**:110-118
- [36] Baskin JS, Banares L, Pedersen S, Zewail AH. Femtosecond real-time probing of reactions. 20. Dynamics of twisting, alignment, and IVR in the trans-Stilbene isomerization reaction. *Journal of Physical Chemistry*. 1996;**100**:11920-11933
- [37] Klessinger M, Michl J. *Excited States and Photochemistry of Organic Molecules*. New York: VCH Publishers; 1995
- [38] Grabowski ZR, Dobkowski J. Twisted intramolecular charge transfer (TICT) excited states: Energy and molecular structure. *Pure and Applied Chemistry*. 1983;**55**:245
- [39] Marguet S, Mialocq JC, Millie P, Berthier G, Momicchioli F. Intramolecular charge transfer and trans-cis isomerization of the DCM styrene dye in polar solvents. A CS INDO MRCI study. *Chemical Physics*. 1992;**160**(2):265-279
- [40] Wu D, Sedgwick AC, Gunnlaugsson T, Akkaya EU, Yoon J, James TD. Fluorescent chemosensors: The past, present and future. *Chemical Society Reviews*. 2017;**46**(23):7105-7123
- [41] Wang B, Anslyn EV. *Chemosensors: Principles, Strategies, and Applications*. Hoboken, New Jersey: John Wiley & Sons; 2011
- [42] Rice AP et al. Signaling recognition events with fluorescent sensors and switches. *Chemical Reviews*. 1997;**97**(5):1515-1566
- [43] Bissell RA, Silva APD, Gunaratne HQN, Lynch PLM, Maguire GEM, Sandanayake KRAS. Molecular fluorescent signalling with 'fluor-spacer-receptor' systems: approaches to sensing and switching devices via supramolecular photophysics. *Chemical Society Reviews*. 1992;**21**:187-195
- [44] McDonagh C, Burke CS, MacCraith BD. Optical chemical sensors. *Chemical Reviews*. 2008;**2**:400-422
- [45] Martínez-Mañez R, Sancenón F. Fluorogenic and chromogenic chemosensors and reagents for anions. *Chemical Reviews*. 2003;**103**(11):4419-4476
- [46] Callan FJ, Silva APD, Magri CD. Luminescent sensors and switches in the early 21st century. *Tetrahedron*. 2005;**61**(36):8551-8588
- [47] Bourson J, Valeur B. Ion-responsive fluorescent compounds. 2. Cation-steered intramolecular charge transfer in a crowned merocyanine. *Journal of Physical Chemistry*. 1989;**93**:3871-3876
- [48] Huang X, Guo Z, Zhu W, Xiea Y, Tian H. A colorimetric and fluorescent turn-on sensor for pyrophosphate anion based on a dicyanomethylene-4H-chromene framework. *Chemical Communications*. 2008;**44**:5143-5145
- [49] Liu Y, Schanze KS. Conjugated polyelectrolyte-based real-time fluorescence assay for alkaline phosphatase with pyrophosphate as substrate. *Analytical Chemistry*. 2008;**80**:8605-8612
- [50] Zhao X, Liu Y, Schanze KS. A conjugated polyelectrolyte-based fluorescence sensor for pyrophosphate.

Chemical Communications.
2007;**43**:2914-2916

[51] Guo Z, Zhu W, Tian H. Hydrophilic copolymer bearing dicyanomethylene-4H-pyran moiety As fluorescent film sensor for Cu²⁺ and pyrophosphate anion. *Macromolecules*. 2010;**43**:739-744

[52] Gu B, Huang L, Xu Z, Tan Z, Hu M, Yang Z, et al. A reaction-based, colorimetric and near-infrared fluorescent probe for Cu²⁺ and its applications. *Sensors and Actuators B*. 2018;**273**(10):118-125

[53] Wang P, Xia J, Gu Y. A novel NIR fluorescent probe for palladium detection based on Pd(0) mediated reaction. *Tetrahedron Letters*. 2015;**56**:6491-6494

[54] Zhu W, Huang X, Guo Z, Wu X, Yu H, Tian H. A novel NIR fluorescent turn-on sensor for the detection of pyrophosphate anion in complete water system. *Chemical Communications*. 2012;**48**:1784-1786

[55] Cao J, Zhao C, Zhu W. A near-infrared fluorescence chemodosimeter for fluoride via specific Si-O cleavage. *Tetrahedron Letters*. 2012;**53**(16):2107-2110

[56] Kimura H. Hydrogen sulfide: Its production, release and functions. *Amino Acids*. 2011;**41**:113-121

[57] Blackstone E, Morrison M, Roth MB. H₂S induces a suspended animation-like state in mice. *Science*. 2005;**308**:518

[58] Wallace JL. Hydrogen sulfide-releasing anti-inflammatory drugs. *Trends in Pharmacological Sciences*. 2007;**28**:501-504

[59] Han Y, Qin J, Chang X, Yang Z, Du J. Hydrogen sulfide and carbon monoxide are in synergy with each

other in the pathogenesis of recurrent febrile seizures. *Cellular and Molecular Neurobiology*. 2006;**26**:101-107

[60] Eto K, Asada T, Arima K, Makifuchi T, Kimura H. Brain hydrogen sulfide is severely decreased in Alzheimer's disease. *Biochemical and Biophysical Research Communications*. 2002;**293**:1485-1488

[61] Sun W, Fan J, Hu C, Cao J, Zhang H, Xiong X, et al. A two-photon fluorescent probe with near-infrared emission for hydrogen sulfide imaging in biosystems. *Chemical Communications*. 2013;**49**:3890-3892

[62] Zheng Y, Zhao M, Qiao Q, Liu H, Lang H, Xu Z. A near-infrared fluorescent probe for hydrogen sulfide in living cells. *Dyes and Pigments*. 2013;**98**:367-371

[63] Gingrich JA, Caron MG. Recent advances in the molecular biology of dopamine receptors. *Annual Review of Neuroscience*. 1993;**16**:299-321

[64] Tritsch NX, Sabatini BL. Dopaminergic modulation of synaptic transmission in cortex and striatum. *Neuron*. 2012;**76**:33-50

[65] Vandecasteele M, Glowinski J, Deniau J-M, Venance L. Chemical transmission between dopaminergic neuron pairs. *Proceedings of the National Academy of Sciences*. 2008;**105**:4904-4909

[66] Suzuki Y. Design and synthesis of fluorescent reagents for selective detection of dopamine. *Sensors and Actuators B*. 2017;**239**:383-389

[67] Zhang X, Zhang L, Liu Y, Bao B, Zang Y, Li J, et al. A near-infrared fluorescent probe for rapid detection of hydrogen peroxide in living cells. *Tetrahedron*. 2015;**71**(29):4842-4845

[68] Serov A, Kwak C. Direct hydrazine fuel cells: A review. *Applied Catalysis B: Environmental*. 2010;**98**(1-2):1-9

- [69] Ragnarsson U. Synthetic methodology for alkyl substituted hydrazines. *Chemical Society Reviews*. 2001;**30**:205-213
- [70] Reilly CA, Aust SD. Peroxidase substrates stimulate the oxidation of hydralazine to metabolites which cause single-strand breaks in DNA. *Chemical Research in Toxicology*. 1997;**10**:328-334
- [71] Ma J, Fan J, Li H, Yao Q, Xia J, Wang J, et al. Probing hydrazine with a near-infrared fluorescent chemodosimeter. *Dyes and Pigments*. 2017;**138**:39-46
- [72] Li M, Wu X, Wang Y, Li Y, Zhu W, James TD. A Near-infrared colorimetric fluorescent chemodosimeter for the detection of glutathione in living cells. *Chemical Communications*. 2014;**50**:1751-1753
- [73] Yu D, Huang F, Ding S, Feng G. Near-infrared fluorescent probe for detection of thiophenols in water samples and living cells. *Analytical Chemistry*. 2014;**86**(17):8835-8841
- [74] Yu D, Zhai Q, Yang S, Feng G. A colorimetric and near-infrared fluorescent turn-on probe for in vitro and in vivo detection of thiophenols. *Analytical Methods*. 2015;**7**(18):7534-7539
- [75] Dehuan Yu QZ, Ding S, Feng G. A colorimetric and near-infrared fluorescent probe for biothiols and its application in living cells. *RSC Advances*. 2014;**4**:46561-46567
- [76] Qian M, Zhang L, Wang J, Peng X. A red-emitting fluorescent probe with large Stokes shift for real-time tracking of cysteine over glutathione and homocysteine in living cells. *Spectrochimica Acta Part A: Molecular and Biomolecular Spectroscopy*. 2019;**214**:469-475
- [77] Weerapana E, Wang C, Simon GM, Richter F, Khare S, Dillon MBD. Quantitative reactivity profiling predicts functional cysteines in proteomes. *Nature*. 2010;**468**:790-795
- [78] Romagné F, Santesmasses D, White L, Sarangi GK, Mariotti M, Hübler R, et al. SelenoDB 2.0: Annotation of selenoprotein genes in animals and their genetic diversity in humans. *Nucleic Acids Research*. 2014;**42**(D1):D437-D443
- [79] Li M, Feng W, Zhai Q, Feng G. Selenocysteine detection and bioimaging in living cells by a colorimetric and near-infrared fluorescent turn-on probe with a large Stokes shift. *Biosensors and Bioelectronics*. 2017;**87**(15):894-900
- [80] Yang J, Li M, Zhu W-H. Dicyanomethylene-4H-pyran based NIR fluorescent ratiometric chemosensor for pH measurement. *Research on Chemical Intermediates*. 2018;**44**:3959-3969
- [81] Yang Y, Wang L, Xu M, Chen J, Qu Y. Triphenyl phosphate end-capped dicyanomethylene-4H-pyran as a near infrared fluorescent sensor for lysozyme in urine sample. *Sensors and Actuators B: Chemical*. 2019;**284**:553-561
- [82] Kwak G, Kim H, Kang I-K, Kim S-H. Charge transfer dye in various polymers with different polarity: Synthesis, photophysical properties, and unusual aggregation-induced fluorescence changes. *Macromolecules*. 2009;**42**(5):1733-1738

Photophysics of BODIPY Dyes: Recent Advances

Seda Çetindere

Abstract

BODIPY dyes are unique fluorophores that can be used in numerous application areas because of their interesting photophysical properties such as high molar absorptivity, tunable absorption and emission energies, and high fluorescence quantum yields. They show impressive photophysical property changes upon substitution of functional groups on the main core structure. Exchange of the meso-carbon on dipyrin core with nitrogen produces an analog class of BODIPY called aza-BODIPY. Up to now, various kinds of BODIPY and aza-BODIPY derivatives have been developed and applied in science and industry. In this chapter, recent studies on photophysical properties of BODIPY derivatives are summarized.

Keywords: BODIPY, aza-BODIPY, fluorescence, fluorophore, photophysical property

1. Introduction

In the constantly expanding multi-disciplinary science world, fluorescent dyes attract the attention of researchers. 4,4-Difluoro-4-bora-3a,4a-diaza-s-indacene (abridged as BODIPY) dyes are compounds that are rapidly increasing in importance among fluorescent organic dyes [1]. BODIPY core is formed from the complexation of a dipyrromethene ligand with a disubstituted boron moiety, typically in the form of BF_2 [1–4]. The first BODIPY was synthesized by Treibs and Kreuzer in 1968 by accident through the combining of 2,4-dimethylpyrrole and acetic anhydride in the presence of $\text{BF}_3 \cdot \text{OEt}_2$ [5]. Although the basic procedure for the synthesis of BODIPY core usually starts from a simple pyrrole condensation with a highly electrophilic carbonyl compound (e.g., aldehyde, acid anhydride, and acyl chloride), the three major routes of BODIPY synthesis are from pyrroles and acid chlorides or pyrroles and aldehydes or ketopyrroles [1]. BODIPY derivatives absorb strongly visible region, have relatively sharp emission peaks, possess high fluorescence quantum efficiencies (Φ ca. 0.5–0.8), high molar absorption coefficients ($\epsilon > 7 \times 10^4 \text{ M}^{-1} \text{ cm}^{-1}$), and have relatively small Stokes' shift (around 10 nm) [1–4]. Besides, most BODIPY dyes indicate thermal and photostability in solid and solution phases are highly soluble in most organic solvents and are insensible to solvent polarity and pH [6, 7]. The BODIPY core (see the core structure and numbering in **Figure 1**) can be easily modified to bear desired functionalities at α -, β -, and meso-positions as well as through substitution of the fluorine. The addition of functional groups to the BODIPY core can have varying effects depending upon the placement and symmetry of the substituent [8, 9]. Symmetrical BODIPYs (substitution from 1,7- or 3,5-positions) appear to produce more red-shifted absorptions compared

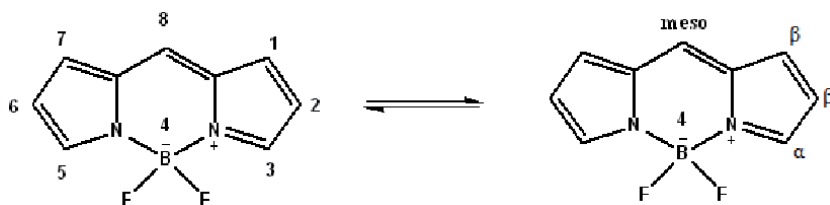


Figure 1.
Chemical structure and numbering of BODIPY core.

to either equally substituted asymmetric counterpart (substitution from 1,3- or 5,7-positions). However, the greater substitution of the BODIPY core does not necessarily produce a larger bathochromic shift, as depicted upon the comparison of the penta-substituted BODIPY (substitution from 1,3,5,7- and 8-positions) to the tetra-substituted BODIPY (substitution from 1,3,5,7-positions) [8, 9]. Red to near infrared (NIR) shifts are generally attained owing to the straightforward modification to the BODIPY core with the extension of the degree of π -delocalization. Also, the emissive behavior of BODIPY fluorophores is much affected by steric and electronic interactions of substituent moieties. Rotation of pendant components as well as their electron-donating or withdrawing effects on the conjugated core greatly influences both the brightness and absorptive and emissive properties of BODIPY [10].

Due to these excellent photophysical characteristics, BODIPY dyes increase their potential using in different applications such as fluorescent labels for biomolecules and cellular imaging [11–15], light-emitting devices [16–18], drug delivery agents [19–21], photosensitizers [22–24], fluorescent switches [25], chemosensors [26–29], energy transfer cassettes [30–33], and solar cells [34–37]. In this chapter, general photophysical properties of BODIPY and aza-BODIPY derivatives and recent studies on the photophysical properties of these dyes are presented.

2. Photophysical properties of BODIPY dyes

BODIPY dyes possess interesting photophysical properties such as high fluorescence quantum yields and narrow emission bandwidths with high peak intensities, elevated photostability, relatively high absorption coefficients, and the extra feature of excitation/emission wavelengths in the visible region. The absorption and fluorescence properties of BODIPY dyes are highly influenced by the extent of electron delocalization around the core and through conjugated substituents, and as such, may be tuned to have photophysical characteristics. BODIPY dyes show a strong, narrow absorption band in the visible region signifying the S_0 - S_1 (π - π^*) transition with a shoulder of high energy around 480 nm assigned to the 0–1 vibrational translation. A broad, much weaker band around 350 nm denotes the S_0 - S_2 (π - π^*) transition [38]. Upon excitation to either the S_1 or S_2 states, an equally narrow emission band of mirror image to the absorption spectra is observed from the S_1 state. Most of the BODIPY dyes emit at wavelengths less than 600 nm, routinely providing yellow to green emissions (500–590 nm) [2, 39]. The fluorescence emission wavelength of BODIPY can be controlled by suitable substitution of chemical fragments such as aliphatic carbon, aromatic ring, pi-bond conjugation, halogens, and electron-withdrawing or donating groups. The pi-bond prolongation on 3 and 5 positions of BODIPY core gives the red-shifted fluorescence emission wavelength [1]. On the other hand, the substitution of electron-donating groups such as amine or alkoxy groups on the 8-position (so-called meso-position) of BODIPY gives

the blue-shifted fluorescence emission wavelength [1]. Unsubstituted BODIPY typically absorbs near 500 nm and emits around 510 nm. Small Stokes' shifts are routinely seen and indicate a modest change in the core structure following S_0 - S_1 transition and vibrational relaxation [40].

The groups that substituted onto the BODIPY scaffold can adjust the photophysical properties of BODIPYs [1]. The addition of functionality at any position of the aromatic core alters the photochemical profile to varying degrees, dependent upon the groups added. BODIPY based dyes containing methyl groups at positions 3- and 5- can be functionalized with aromatic compounds with the help of the Knoevenagel reaction [41]. The 2,6-positions of the BODIPY core tend to give an electrophilic substitution reaction. Decorating the BODIPY skeleton from 3,5-positions generally produces a greater bathochromic shift (ca. 50–100 nm) than adding conjugation through the 2,6-positions, displaying the greatest shift when all four methyls have converted to styryl groups [42]. Although the tetra-styryl BODIPY has been synthesized by activation and subsequent condensation of the 1,3,5,7-methyls [43], an extension of π -conjugation and addition of functionality is most frequently accomplished through the 3,5-methyls. Thus, the visible region of different BODIPY derivatives can be largely scanned, resulting in a wider range of use.

From past to present, many research groups have been studying BODIPY and its derivatives. Consequently, there are many reported papers about the photophysical properties of BODIPY derivatives, especially in recent years. In 2014, Majumdar et al. [44] reported the synthesis of four styryl-BODIPY-containing Ir(III) complexes which show strong NIR absorption (644–729 nm), strong NIR fluorescence (700–800 nm), and long-lived triplet excited states (92.5–156.5 μ s). Investigations of the photophysical properties of these complexes showed that they were strongly fluorescent, although the p-conjugation is present between the BODIPY ligands and the Ir(III) coordination center. Moderate intersystem crossing (ISC) was observed for the complexes, proved by the population of the long-lived intraligand triplet excited state (3 IL) and the singlet oxygen (1 O₂) photosensitizing property. Based on the property of NIR absorption/fluorescence and the reasonable 1 O₂ quantum efficiency, the complexes were used as multi-functional materials as luminescent bioimaging reagents and in intracellular photodynamic studies. Also, they reported that their results are useful for the preparation of NIR absorbing cyclometalated Ir(III) complexes, and the relevant application of these complexes as multi-functional materials such as a luminescent bioimaging reagent, in photodynamic therapy (PDT) and photocatalysis. At the same year, a 2,6-distyryl-substituted BODIPY dye and a new series of 2,6-p-dimethylaminostyrene isomers containing both α - and β -position styryl substituents were reported by Gai et al. [45]. They used styrene and p-dimethylaminostyrene with an electron-rich diiodo-BODIPY in the synthesis of these compounds. They indicated that the absorption spectra contain red-shifted absorbance bands due to conjugation between the styryl moieties and the main BODIPY fluorophore. Besides, very low fluorescence quantum yields, and significant Stokes shifts were observed for 2,6-distyryl-substituted BODIPYs, concerning like 3,5-distyryl- and 1,7-distyryl-substituted BODIPYs. In spite of the fluorescence of the compound with β -position styryl substituents on both pyrrole fragments and one with both β - and α -position substituents was fully quenched, the compound with only α -position substituents displays weak emission in polar solvents, but strong emission with a quantum yield of 0.49 in hexane. They enounced that 2,6-p-dimethylaminostyrene isomers can be used as sensors for changes in pH. Two novel azomethine-BODIPY dyads were reported by Pan et al. [46]. These two dyads have been synthesized by covalent tethering of tautomeric ortho-hydroxy aromatic azomethine moieties including N-salicylideneaniline (SA) and N-naphthylideneaniline (NA) to a BODIPY fluorophore. Both two dyads showed

enol-imine (OH) structures dominating in the crystalline state. For the first dyad, in the enol state is the most stable form at room temperature in most environments, while enol-keto prototropic tautomerism of the NA fragment in solution is maintained in the second dyad, which can be reversibly modified between enol and keto forms in the environment's polarity. Visible lighting of the second dyad in the enol case excites selectively the BODIPY moiety and then counteracts radiatively by emitting green light in the form of fluorescence, while the emission intensity of the second dyad in the keto case is quenched based on the proton-coupled photo-induced electron transfer (PCPET) mechanism. This permits to large fluorescence modulation among the two states of the second dyad and creates a new tautomerisable fluorescent switch. Photophysical properties of a pyrene-based tetramethyl difluoroborondipyrromethane (PYBDP) were investigated by Yang et al. [47]. The PYBDP showed a higher fluorescence quantum efficiency and Stokes shift than other phenyl-substituted laser dyes in the green region. Under transversal pumping conditions, this new dye exhibited highly effective and stable emissions centering at 531 nm. The PYBDP dye exhibited a maximum narrow band amplified spontaneous emission (ASE) lasing yield of 10.86% with an extensive adjustable range (525–560 nm) under demanding transversal pumping at 355 nm in toluene. The lasing efficiency remains unaffected in 1 h but a dramatic decrease or even the loss of the laser action is observed in intermediate or highly polar solvents. The combination of excellent photostability and tunability of ASE makes PYBDP a potentially green-emitting laser dye in the green-orange region. In a reported study from our working group [48] was about the treatment of boron (III) subphthalocyanine chloride with borondipyrromethene derivatives containing either one or two [4-(N,N-dimethylamino)phenyl]ethenyl groups in toluene gave the corresponding axially substituted boron(III) subphthalocyanine dyes (**Figure 2**). Methyl groups on 3- and 5-positions have acidic hydrogens due to electron-withdrawing property of heterocyclic BODIPY ring. This acidic property can be taken advantage of, in the synthesis of other BODIPY fluorophores for example with aromatic aldehydes. For this reason, N,N-dimethyl-4-aminobenzaldehyde was reacted with BODIPY, resulting in extension of conjugation in our study. This extension of conjugation allowed us to shift the absorption and emission spectra to longer wavelengths. The reaction was performed in a solution containing acetic acid and piperidine. The solvent was toluene because any water forming in the reaction should be removed. Dean-Stark apparatus is a good choice because water can be removed azeotropically during reflux. The photophysical properties of these compounds were examined utilizing absorption and fluorescence spectroscopy in dilute benzene solutions. They

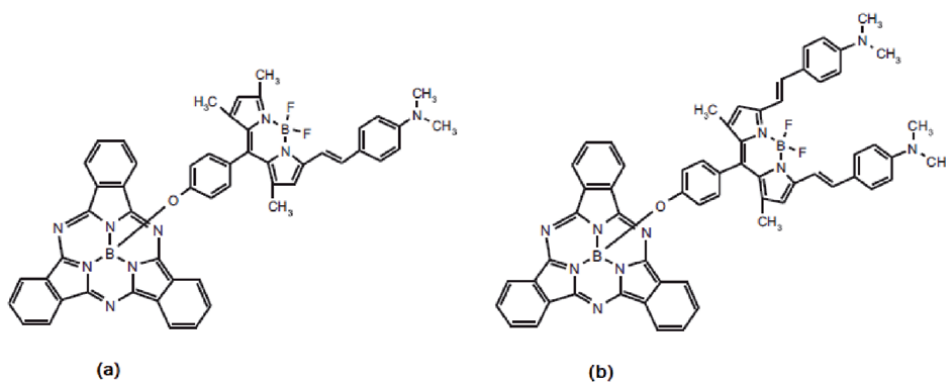


Figure 2. Chemical structure of (a) mono-styryl and (b) distyryl-BODIPY substituted subphthalocyanines.

exhibited a highly efficient energy transfer process from the excited subphthalocyanine (SubPc) unit to the BODIPY unit. Increased $^1\text{O}_2$ production was noted for BODIPY substituted SubPc compounds relative to their BODIPY precursors; a feature that may be useful for PDT application of these dyes.

The effect of the substituent side groups like phenyl (Ph), phenylethynyl (Ethyne) and styryl moiety at the 2-, 3- or 8- position of the BODIPY scaffold was reported by Orte et al. [49]. A large number of solvents (methanol, acetonitrile, diethyl ether, acetone, ethyl acetate, 2-propanol, isobutyronitrile, dibutyl ether, tetrahydrofuran, 1-pentanol, 1,4-dioxane, dichloromethane, cyclohexane, 1-octanol, chloroform, cyclohexanone, toluene, chlorobenzene) were used for investigation of the photophysical properties of these compounds. A substitution from 3-position is beneficial for producing BODIPYs with sharp absorption bands and high fluorescence quantum yields. Contrarily, substitution at the 2-position yielded BODIPY dyes with large Stokes shifts and broad bands. Substitution at the meso-position produced dyes with features like the 3-substituted ones, except for meso-phenyl BODIPY (8-Ph). Between the phenyl-substituted BODIPY dyes, some differences in absorption behavior were observed. The presence of the p-tert-butylphenyl moiety shifts the absorption maximum, $\lambda_{\text{abs}}(\text{max})$ from 516 to 530 nm when this group is at the 2-position (2-Ph) to 513–527 nm and when it is at the 3-position (3-Ph). In these two statuses, $\lambda_{\text{abs}}(\text{max})$ is more red-shifted in the more polarizable solvents toluene and chlorobenzene. Conversely, the values of $\lambda_{\text{abs}}(\text{max})$ of 8-Ph are blue-shifted concerning those of 2-Ph and 3-Ph and are close to those of unsubstituted BODIPY [50, 51], ranging from 489 nm in acetonitrile to 497 nm in toluene and chlorobenzene. This absorption energy range is in good agreement with that of other BODIPYs substituted at the meso-position with a weak electron acceptor or donor [52, 53]. For the phenylethynyl BODIPYs, the absorption spectra show also the characteristic properties of typical BODIPYs. 2-Ethyne possessed an absorption maximum between 503 and 525 nm, whereas the $\lambda_{\text{abs}}(\text{max})$ of 3-Ethyne changes between 525 and 545 nm. For the two dyes, the lowest $\lambda_{\text{abs}}(\text{max})$ value was founded in acetonitrile and the highest in cyclohexane. The influence of the substitution positions (2 vs. 3) on $\lambda_{\text{abs}}(\text{max})$ is much higher for the phenylethynyl fragment than for the phenyl moiety and moving the p-tert-butylphenyl substituent from the 2-Ph to the 3-Ph causes a 3 nm blue shift of $\lambda_{\text{abs}}(\text{max})$, while the similar change from 2-Ethyne to 3-Ethyne results in a ca. 20 nm red shift of $\lambda_{\text{abs}}(\text{max})$. 8-Ethyne is bathochromically shifted for 2-Ethyne and 3-Ethyne, with $\lambda_{\text{abs}}(\text{max})$ ranging from 537 to 547 nm which is parallel with an increasing refractive index [54]. Styryl-substituted BODIPYs (2-Styryl, 3-Styryl and 8-Styryl) displayed different absorption properties. The $\lambda_{\text{abs}}(\text{max})$ values range from 549 to 561 nm, with a typical redshift from acetonitrile to chlorobenzene. The extended conjugation ensured by the styryl functional group reasons an extra bathochromic shift of around 20 nm for 3-Ethyne, and ca. 30 nm for 3-Ph. Conversely, 2-Styryl and 8-Styryl show clear dual-band absorption and emission behavior. The photophysical reaction of two BODIPY-based D–A and A–D–A molecules, where D is the donor and A is the acceptor was reported by Hendel et al. [55]. A BODIPY fragment was given as the A component and was attached through the meso position using a 3-hexylthiophene linker to an N-(2-ethylhexyl) dithieno[3,2-b:2',3'-d] pyrrole (DTP), which was given as the D component. An A–D–A molecule was compared to its corresponding D – A dyad counterpart. This showed a potential advantage to the A–D–A molecule over the D–A dyad in creating longer-lived excited states. A–D–A possess slightly longer excited-state lifetimes, 42 ps nonradiative decay, and 4.64 ns radiative decay compared to those of D–A, 24 ps nonradiative decay, and 3.95 ns radiative decay. These results show a full picture of the electronic and photophysical properties of D–A and A–D–A that provide contextualization for structure–function relationships between molecules

and organic photovoltaic (OPV) devices. A type of fluorescent chemosensor based on tethered hexa-borondipyrromethene cyclotriphosphazene platform (HBTC) (**Figure 3**) linked via triazole groups reported by our working group [56]. Its sensing behavior toward metal ions was investigated. Addition of a Fe^{2+} ion to a tetrahydrofuran (THF) solution of HBTC gave a visual color change as well as a significantly quenched fluorescence emission, while other tested 19 metal ions (Fe^{2+} , Al^{3+} , Ba^{2+} , Ca^{2+} , Co^{2+} , Ag^+ , Cd^{2+} , Cr^{3+} , Cs^+ , Cu^{2+} , Fe^{3+} , Hg^{2+} , K^+ , Li^+ , Mg^{2+} , Mn^{2+} , Na^+ , Ni^{2+} , Pb^{2+} , and Zn^{2+}) induced no color or spectral changes. This compound was found to be highly selective and sensitive for Fe^{2+} with a low limit of detection ($2.03 \mu\text{M}$). HBTC is a potential selective and sensitive fluorescence chemosensor for imaging Fe^{2+} in the living cells.

A synthetic approach for palladium-catalyzed direct $\text{C}(\text{sp}^3)\text{-H}$ arylation of the methyl group at the 8-position of BODIPY reported by Chong et al. [57]. This approach permitted attaching electron-donating/withdrawing, halogen-substituted aryls and a heteroaryl with a yield running from 55 to 99%. Novel pH sensors, which in the lack of acid demonstrated the photoinduced electron transfer (PET), were synthesized by linking dimethylaniline to the methyl at the C8-position of BODIPY. The reference compounds with dimethylaniline directly linked to the C8-position were also synthesized and PET showed a charge-transfer emission. Addition of trifluoroacetic acid (TFA) onto toluene and ethanol, the fluorescence intensity was at least an order of magnitude more effective with the synthesized sensors compared to the traditional reference sensors. The developed sensibility of these BODIPY-based pH sensors was connected to less effective proton-coupled electron transfer of the protonated types. This approach could pave a new way for the convenient syntheses of functional BODIPY molecules. Two

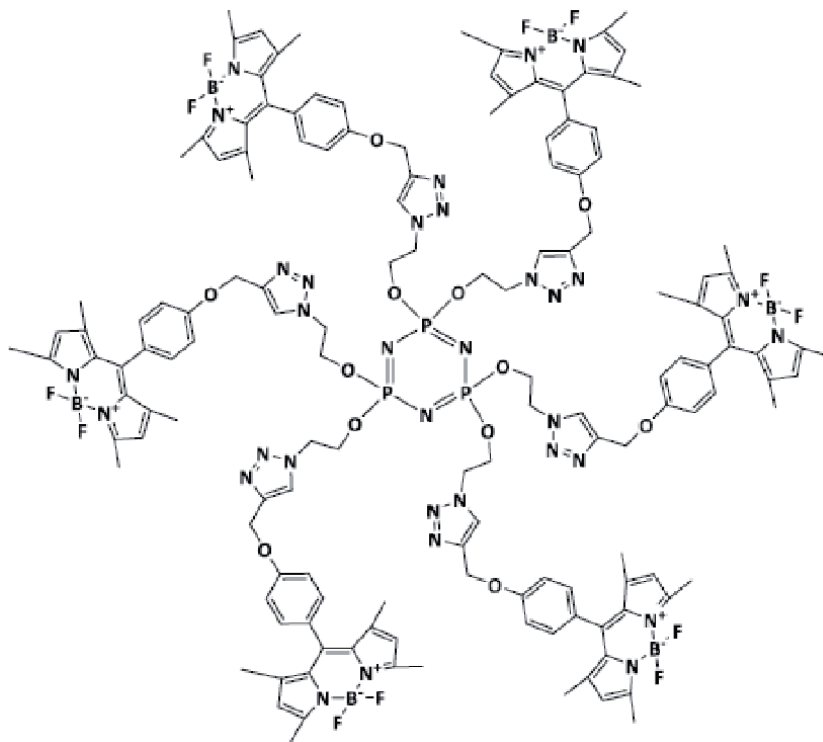


Figure 3.
Chemical structure of HBTC.

cyclotriphosphazene compounds bearing mono- and distyryl BODIPY substituents reported in 2017 (**Figure 4**) [58]. The photophysical properties of these cyclotriphosphazene compounds were examined in THF solutions. All these heavy atom free compounds indicated very limited fluorescence emission and $^1\text{O}_2$ generation owing to the internal charge transfer (ICT) that occurred between BODIPY core and dimethylaminobenzyl groups. These properties were also investigated by the protonation of the studied compounds. Fluorescence emission and $^1\text{O}_2$ generation attitudes of these compounds were dramatically increased after the addition of acid because the ICT effect was blocked owing to the protonation of the nitrogen atoms on the dimethylamine groups. These compounds can be used as potential photosensitizers that can be used as efficient singlet oxygen generators.

Six different molecules including 3,5-distyryl-BODIPY backbones were reported by Kang et al. [59] and the $^1\text{O}_2$ photosensitizing experiments of dibromo substituted BODIPY compounds and two boronic acid ester substituted BODIPY compounds were investigated. The $^1\text{O}_2$ quantum yields of dibromo substituted BODIPYs were calculated as 0.075 and 0.44 and the $^1\text{O}_2$ quantum yields of boronic acid ester substituted BODIPYs were not more than 0.07. It was indicating that halogenation on the benzene rings of 3,5 distyryl-BODIPYs or boronate esterification of BODIPY had no positive effect on $^1\text{O}_2$ production, while halogenation on the 2/6 position resulted in seemingly increased $^1\text{O}_2$ efficiencies. The results would enrich the research of BODIPYs and would provide a useful envision for the preparation of powerful BODIPYs drugs for the PDT process. An excited-state intramolecular proton transfer (ESIPT) meso linked BODIPY dyad (Bn-OH-BDY) was reported by Mallah et al. [60]. The fluorescence lifetime of Bn-OH-BDY dyad was recorded 5.71 ns. A large shift of 255 nm has been monitored between excitation and emitted light. Excitation ($\lambda_{\text{exc}} = 290$ nm) of the Bn-OH-BDY dyad leads to emission ($\lambda_{\text{emi}} = 545$ nm) directed by the BODIPY subunits pointing to excitation energy transfer (EET) from the ESIPT to BODIPY core. Two cyclotriphosphazene (Cpz) compounds bearing mono- and distyryl(pyrene) BODIPY dyes (**Figure 5**) reported in 2019 [61]. These compounds indicated intense fluorescence emission even at very low concentrations. In accordance with absorption and emission spectra of Cpz compounds, di-styryl pyrene BODIPY containing Cpz indicated redshift more than

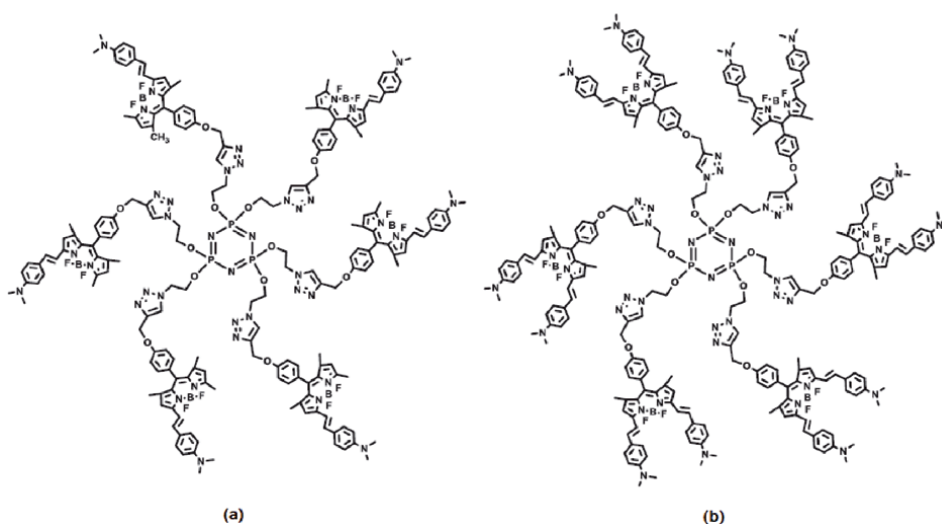


Figure 4.
Chemical structures of (a) mono-styryl and (b) distyryl-BODIPY substituted cyclophosphazenes.

mono-styryl pyrene BODIPY containing Cpz because of mono- and di-styryl bonding positions of pyrene molecules. These Cpz compounds revealed different color and spectral changes throughout reduction and oxidation reactions as compared to BODIPY derivatives and newly synthesized BODIPY molecules, which might have potential applications for electrochromic materials. Extreme properties of these compounds also illustrated probable utilization of these as functional materials for use in electrochemical and photovoltaic applications.

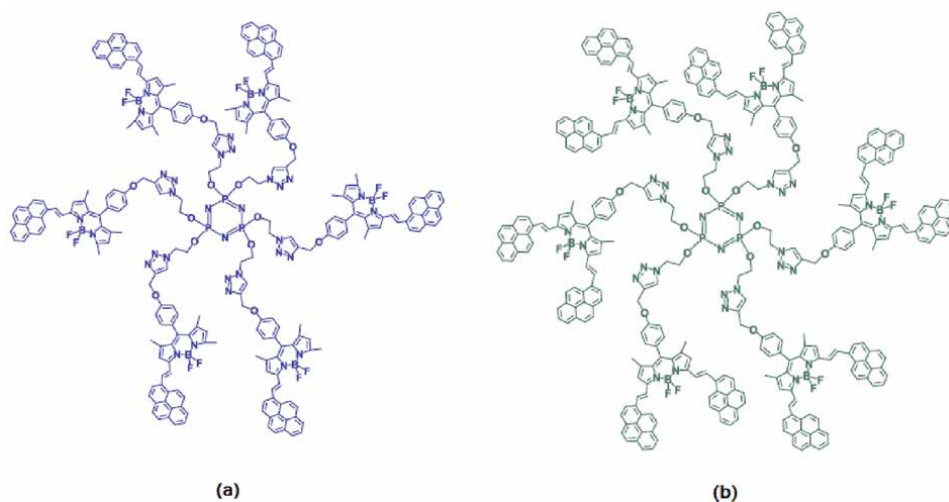


Figure 5. Chemical structures of (a) mono-styryl and (b) distyryl-pyrene BODIPY substituted cyclophosphazenes.

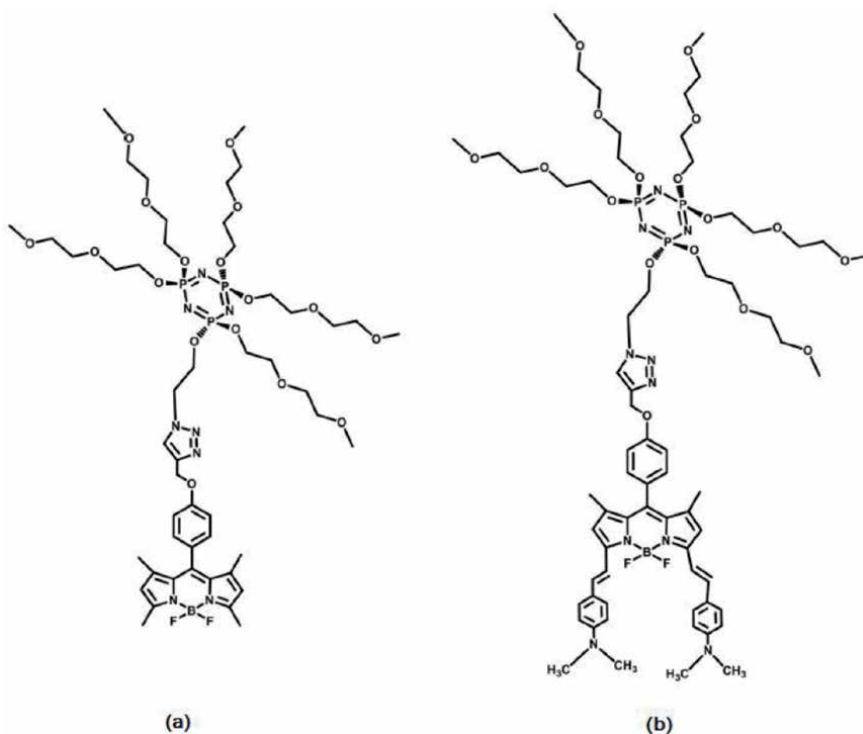


Figure 6. Chemical structures of (a) BODIPY and (b) distyryl-BODIPY substituted cyclophosphazenes.

Synthesis, photophysics, and photobiological activities of a series of neutral heteroleptic cyclometalated iridium (III) complexes including BODIPY substituted N-heterocyclic carbene (NHC) ligands reported by Liu et al. [62]. The effect of the substitution position of BODIPY on the NHC ligands, either on C4 of the phenyl ring or C5 of the benzimidazole unit, and its linker type on the photophysical properties was investigated. All complexes showed BODIPY-localized intense ^1IL (intraligand)/ $^1\text{MLCT}$ (metal-to-ligand charge transfer) absorption at 530–543 nm and $^1,^3\text{IL}/^1,^3\text{CT}$ (charge transfer) emission at 582–610 nm. However, the lowest triplet excited state of these complexes is the BODIPY-localized $^3\pi,\pi^*$ states. It was demonstrated that the position of the BODIPY pendant on the NHC ligand impacted both the $^1\text{IL}/^1\text{MLCT}$ absorption and $^1,^3\text{IL}/^1,^3\text{CT}$ emission bands. This study indicated that the substitution position of BODIPY on the NHC ligand plays an important role in the cytotoxicity and photocytotoxicity of this new type of complexes. BODIPY-substitution at C5 of benzimidazole compared to C4-phenyl substitution leads to lower $^1\text{O}_2$ quantum efficiencies but more efficient phototoxic effects. The effect of BODIPY substitution position at the NHC ligand is more cleared on the photobiological activities than on the photophysical properties. Two water-soluble cyclotriphosphazene derivatives by “click” reactions between cyclotriphosphazene derivative with hydrophilic glycol side groups and BODIPY's (**Figure 6**) were reported in 2019 [63]. The photophysical properties of these compounds were examined inside the water and many organic solvents such as acetone, THF, dichloromethane, dimethyl sulfoxide, etc., and the results were compared with each other. These compounds have good solubility in many different organic solvents and especially acetone: water systems that are suitable to use in environmental and biological applications.

3. Photophysical properties of aza-BODIPY dyes

Replacement of the meso-carbon with nitrogen creates a similar class of compounds mentioned as aza-BODIPYs (**Figure 7**). In contrast to the well-known BODIPYs, aza-BODIPYs have not been extensively studied. Aza-BODIPY skeletons are generally prepared from nitromethane adducts to the corresponding chalcone, but butanol, rather than methanol or solvent-free conditions, are the preferred medium. The syntheses are completed by adding $\text{BF}_3\cdot\text{OEt}_2$ at room temperature [1]. Like BODIPY derivatives, aza-BODIPY derivatives also have high molar extinction coefficients and moderate fluorescence quantum yields (ca. 0.20–0.40). The addition of the lone pair on the nitrogen properly affects the HOMO-LUMO energy gap owing to stabilization [1]. This improved stability causes a red-shift in the absorption and emission profiles into the 650–850 nm range [64]. Aza-BODIPY core offers several advantages including ease of synthesis and an inherent bathochromic shift in the absorption maxima in comparison to the carbon analog. Aza-BODIPY dyes have a marked red shift of the absorption and emission bands relative to traditional BODIPY dyes can be accomplished without modifying the key properties of BODIPY dyes, such as their high molar absorption coefficients, narrow and structured absorption and emission bands, small Stokes shifts, high fluorescence quantum yields, and photostability. The UV absorption maxima of the aza-BODIPY dyes are comparatively insensitive to solvent polarity; only small blue shifts tend to be observed (6–9 nm) when switching solvents from toluene to ethanol. Their absorptions are strong, with a full width at a half-maximum height changing from 51 to 67 nm in aqueous solution and 47–57 nm in chloroform indicating that the dyes do not aggregate under those conditions. The extinction coefficients range from 7.5×10^4 to $8.5 \times 10^4 \text{ M}^{-1} \text{ cm}^{-1}$. Fluorescence emission spectra of the aza-BODIPY

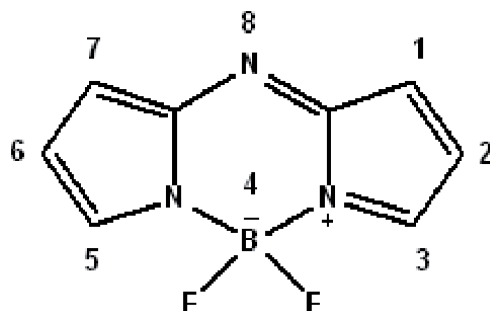


Figure 7.
Chemical structure and numbering of aza-BODIPY core.

dyes are also relatively insensitive to the solvent polarity [1]. Aza-BODIPYs are of great interest due to their appealing optical properties of strong absorbance and emission in the NIR region and easy structural modification. For this reason, this class of BODIPY has found use as photosensitizers [65, 66], near-IR emitting chemosensors and imaging probes [67–70], and as fluorescent labels [71, 72].

The synthesis and photophysical properties of a NIR absorbing acenaphtho-fused aza-BODIPY dye with using 1,2-dicyanoacetophenylene as a precursor [73] were reported by Majumdar et al. [74]. In contrast with its naphtho-fused analog [75], a stable complex was obtained due to the differing effects of the fused ring moieties on the energies of the frontier π molecular orbitals (MOs). The Φ_F values obtained for this aza-BODIPY are comparatively low in a set of solvents with different polarities, limiting the benefit of this compound for sensor and bioimaging applications, but the comparatively broad absorption band at the red end of the visible region may make the compound appropriate for use in solar cells. The synthesis and photophysical properties of two NIR absorbing conjugates based on orthogonally arranged rhodium (III) tetrakis-4-tolylporphyrin [$\text{Rh}^{\text{III}}(\text{ttp})$] and BF_2 -chelated aza-BODIPY linked by a covalent $\text{Rh}-\text{C}(\text{aryl})$ bond were reported by Zhou et al. in 2016 [76]. These conjugates display intense absorption and moderate fluorescence bands around 700 nm, which do not correspond with those of their aza-BODIPY precursors, due to the strong ground-state interaction between the aza-BODIPY and metal porphyrin moieties. Minor changes in the linkage position on the aza-BODIPY moiety can alter the relative energies of MOs and hence have a significant impact on the optical and photophysical properties. This study sheds light on the actual role of the heavy atom in excited-state processes that cannot be separated from its ligands. Besides, this approach gives promise as a strategy for overcoming the two main problems that have been encountered throughout dye research in the NIR region: the first one is the relatively weak absorption of transition-metal porphyrins in this spectral region, and the second one is the relatively weak $^1\text{O}_2$ yields of organic fluorophores. The influence of halogen atom substitution (Br and I), in different amounts and positions on an aza-BODIPY skeleton, was investigated by De Simone et al. The heavy atom effect on excitation energies, singlet-triplet energy gaps and spin-orbit matrix elements has been investigated. The maximum absorption within the therapeutic window has been approved for all the aza-BODIPY derivatives. Possible intersystem spin crossing pathways for the population of the lowest triplet state, which will depend on the values of the spin-orbit matrix elements, the energy gaps as well as the orbital combination of the concerned states have been found to most likely concern the S_1 and T_1 or T_2 states. The potential therapeutic use of these compounds as photosensitizers in PDT was reported [77]. The comparison of optical and electrochemical properties

of aza-BODIPY dyes that differ under the substituents at 1,7- and 3,5-positions of the aza-BODIPY backbone was reported by Gut et al. [78]. Especially, the influence of highly electron-withdrawing nitro substituents on these properties was investigated. The aza-BODIPYs studied display a broad absorption band extending from ca. 600 nm to ca. 700 nm, a spectral region that is highly searched after for biomedical applications, and have high molar absorption coefficients (ϵ) ranging from 6.4×10^4 ($M^{-1} \text{ cm}^{-1}$) to 8.5×10^4 ($M^{-1} \text{ cm}^{-1}$) in THF. These compounds were weakly emissive as non-radiative decay is the overpowering route of the excited state energy spreading. The fluorescence quantum efficiencies (Φ_f) measured in THF was between 0.03 and 0.06 for the aza-BODIPYs. Transient absorption experiments divulged $T_1 \rightarrow T_n$ absorption extend from ca. 400 nm to ca. 600 nm and allowed determination of the triplet state lifetimes. The estimated triplet lifetimes (τ_T) in deaerated THF ranged from 77 to 130 μs . As predicted by the CV/DPV measurements, all aza-BODIPYs displayed one irreversible oxidation and two quasi-reversible reductions. Prediction of the E_{HOMO} gave a value of ca. 5.8 eV while the E_{LUMO} was found to be located at ca. 4.5 eV. Exceptionally high photostability and thermal durability up to near 300°C were found for the nitro-substituted aza-BODIPYs.

In 2019, Obloza et al. [79] reported a series of aza-BODIPY dyes substituted with meta-(dimethylamino) phenyl groups. Highly attractive photophysical and photochemical properties were induced in meta-(Me₂N) Ph-substituted aza-BODIPY by bromination of the aromatic rings at the 3 and 5 positions. High values of ¹O₂ quantum yields were measured, ranging from 0.36 to 0.58. The photosensitized oxygenation process of a sample compound, diphenylisobenzofuran (DPBF), continuous over a Type II mechanism for the di-bromo derivative, while for the tetra-bromo derivative a mixed mechanism including both ¹O₂ and other forms of oxygen formation (Type I and/or Type III) was assigned. Nanosecond laser photolysis (NLP) experiments of the brominated aza-BODIPYs divulged $T_1 \rightarrow T_n$ absorption extending between ca. 350 nm and ca. 510 nm with τ_T ranged between 15.6 and 26.0 μs . The brominated aza-BODIPYs studied displayed an absorption band therein so-called “therapeutic window”, with λ_{abs} placed among 620 and 636 nm. As predicted by cyclic voltammetry (CV)/ differential pulse voltammetry (DPV) measurements, the meta-(Me₂N) Ph-substituted aza-BODIPYs studied displayed a multi-electron oxidation process at a relatively low oxidation potential (E_{ox}), pointing to the very good electron-donating features of these molecules. These compounds showed high photo- and thermal stability. The synthesis of a series of aza-BODIPY dyes substituted with p-(dimethylamino) phenyl groups was also reported by Obloza et al. [80]. Especially, the effect of p-(Me₂N) Ph-moieties on these characteristics was of importance. For two aza-BODIPYs studied, a near-IR absorption band was monitored at ca. $\lambda_{\text{abs}} = 796$ nm. Owing to the prominent ICT applied by the existence of strongly electron-donating p-(Me₂N) Ph-substituents, the compounds studied were weakly emissive with the singlet lifetimes (τ_S) in the picosecond range. NLP experiments of the brominated aza-BODIPYs divulged $T_1 \rightarrow T_n$ absorption extending between ca. 350 nm and ca. 550 nm with τ_T ranged between 6.0 and 8.5 μs . The optical features of the aza-BODIPYs studied were pH-sensitive. Upon protonation of the dimethylamino groups with TFA in toluene, a stepwise extinction of the NIR absorption band at $\lambda_{\text{abs}} = 790$ nm was monitored with the accompanying view of a blue-shifted absorption band at $\lambda_{\text{abs}} = 652$ nm, which was accompanied by an important emission band at $\lambda_{\text{emi}} = 680$ nm. The conversion from a non-emissive to an emissive compound is concerned with the prevention of the ICT. CV/DPV measurements were showed that these aza-BODIPYs displayed two irreversible oxidation and two quasi-reversible reduction processes. All these studied compounds displayed extremely high photo and thermal stability.

4. Conclusion


In this chapter, the basic photophysical properties of BODIPY and aza-BODIPY derivatives are introduced briefly. Unsubstituted BODIPY absorbs near 500 nm and emits around 510 nm. Substitution of amino- or alkoxy-moieties at the meso-position of BODIPY core is expected to provide a shorter excitation and emission wavelength at the blue region with high quantum yields. Substitution of styryl- or distyryl moieties from 3,5-positions is expected to produce more red-shifted emissions. Aza-BODIPY derivatives also show red-shift in the absorption and emission profiles, because of the lone pair on the nitrogen. According to the recent advances on BODIPY dyes, it has been seen that they have many application areas especially on bioimaging, laser-dyes, OPV devices, chemosensors, and PDT, because of their superior photophysics. It seems that BODIPY derivatives still will remain popular in the future.

Author details

Seda Çetindere
Department of Chemistry, Faculty of Science, Gebze Technical University,
Gebze, Kocaeli, Turkey

*Address all correspondence to: sdemirer@gtu.edu.tr

IntechOpen

© 2020 The Author(s). Licensee IntechOpen. This chapter is distributed under the terms of the Creative Commons Attribution License (<http://creativecommons.org/licenses/by/3.0>), which permits unrestricted use, distribution, and reproduction in any medium, provided the original work is properly cited. 

References

- [1] Loudet A, Burgess K. BODIPY dyes and their derivatives: Syntheses and spectroscopic properties. *Chemical Reviews*. 2007;**107**:4891-4932. DOI: 10.1021/cr078381n
- [2] Ulrich G, Ziessel R, Harriman A. The chemistry of fluorescent bodipy dyes: Versatility unsurpassed. *Angewandte Chemie, International Edition*. 2008;**47**:1184-1201. DOI: 10.1002/anie.200702070
- [3] Ziessel R, Ulrich G, Harriman A. The chemistry of Bodipy: A new El Dorado for fluorescence tools. *New Journal of Chemistry*. 2007;**31**:496-501. DOI: 10.1039/B617972J
- [4] Descalzo AB, Xu HJ, Shen Z, Rurack K. Red/near-infrared boron-dipyrromethene dyes as strongly emitting fluorophores. *Annals of the New York Academy of Sciences*. 2008;**1130**:164-171. DOI: 10.1196/annals.1430.016
- [5] Treibs A, Kreuzer FH. Difluoroboryl-Komplexe von Di- und Tripyrrylmethenen. *Justus Liebigs Annalen der Chemie*. 1968;**718**:208-223. DOI: 10.1002/jlac.19687180119
- [6] Li L, Nguyen B, Burgess K. Functionalization of the 4,4-difluoro-4-bora-3a, 4a-diazas-indacene (BODIPY) core. *Bioorganic & Medicinal Chemistry Letters*. 2008;**18**:3112-3116. DOI: 10.1016/j.bmcl.2007.10.103
- [7] Thivierge C, Bandichhor R, Burgess K. Spectral dispersion and water solubilization of BODIPY dyes via palladium-catalyzed C-H functionalization. *Organic Letters*. 2007;**9**:2135-2138. DOI: 10.1021/ol0706197
- [8] Wael EV, Pardo JA, Koevering JA, Lugtenburg J. Pyrromethene-BF₂ complexes (4,4'-difluoro-4-bora-3a,4a-diaza-s-indacenes). *Synthesis and luminescence properties*. *Physical-Organic Chemistry*. 1977;**96**:306-309. DOI: 10.1002/recl.19770961205
- [9] Bandichhor R, Thivierge C, Bhuvanesh NSP, Burgess K. 4,4-difluoro-1,3,5,7-tetramethyl-4-bora-3a,4a-diaza-s-indacene. *Acta Crystallographica Section E*. 2006;**62**:o4310-o4311. DOI: 10.1107/S1600536806032235
- [10] Hu R, Lager E, Aguilar-Aguilar A, Liu J, Lam JWY, Sung HHY, et al. Twisted intramolecular charge transfer and aggregation-induced emission of BODIPY derivatives. *Journal of Physical Chemistry C*. 2009;**113**:15845-15853. DOI: 10.1021/jp902962h
- [11] Kalai T, Hideg K. Synthesis of new, BODIPY-based sensors and labels. *Tetrahedron*. 2006;**62**:10352-10360. DOI: 10.1016/j.tet.2006.08.079
- [12] Karolin J, Johansson LBA, Strandberg L, Ny T. Fluorescence and absorption spectroscopic properties of dipyrrometheneboron difluoride (BODIPY) derivatives in liquids, lipid-membranes, and proteins. *Journal of the American Chemical Society*. 1994;**116**:7801-7806. DOI: 10.1021/ja00096a042
- [13] Ehrenschwender T, Wagenknecht HA. 4,4-Difluoro-4-bora-3a,4a-diaza-s-indacene as a bright fluorescent label for DNA. *The Journal of Organic Chemistry*. 2011;**76**:2301-2304. DOI: 10.1021/jo102519k
- [14] Giessler K, Griesser H, Goehringer D, Sabirov T, Richert C. Synthesis of 3'-BODIPY-labeled active esters of nucleotides and a chemical primer extension assay on beads. *European Journal of Organic Chemistry*. 2010;**19**:3611-3620. DOI: 10.1002/ejoc.201000210

- [15] Kim D, Ma D, Kim M, Jung Y, Kim NH, Lee C, et al. Fluorescent labeling of protein using blue-emitting 8-amino-BODIPY derivatives. *Journal of Fluorescence*. 2017;**27**:2231-2238. DOI: 10.1007/s10895-017-2164-5
- [16] Baysec S, Minotto A, Klein P, Poddi S, Zampetti A, Allard S, et al. Tetraphenylethylene-BODIPY aggregation-induced emission luminogens for near-infrared polymer light-emitting diodes. *Science China: Chemistry*. 2018;**61**:932-939. DOI: 10.1007/s11426-018-9306-2
- [17] Zampetti A, Minott A, Squeo BM, Gregorius VG, Allard S, Scherf U, et al. Highly efficient solid-state nearinfrared Organic light-emitting diodes incorporating A-D-A dyes based on α,β -unsubstituted "BODIPY" moieties. *Scientific Reports*. 2011;**7**:1611-1617. DOI: 10.1038/s41598-017-01785-2
- [18] Gao H, Gao Y, Wang C, Hu D, Xie Z, Liu L, et al. Anomalous effect of intramolecular charge transfer on the light emitting properties of BODIPY. *ACS Applied Materials & Interfaces*. 2018;**10**:14956-14965. DOI: 10.1021/acsami.7b13444
- [19] Liu X, Chen B, Li X, Zhang L, Xu Y, Liu Z, et al. Self-assembly of BODIPY based pH-sensitive near infrared polymeric micelles for drug controlled delivery and fluorescence imaging applications. *Nanoscale*. 2015;**7**:16399-16416. DOI: 10.1039/C5NR04655F
- [20] Quan L, Liu S, Sun T, Guan X, Lin W, Xie Z, et al. Near-infrared emitting fluorescent BODIPY nanovesicles for in vivo molecular imaging and drug delivery. *ACS Applied Materials & Interfaces*. 2014;**6**:16166-16173. DOI: 10.1021/am5042115
- [21] De la Torre B, Hornillos V, Luque-Ortega JR, Abengozar MA, Amat-Guerri F, Acun AU, et al. A BODIPY-embedding miltefosine analog linked to cellpenetrating Tat(48-60) peptide favors intracellular delivery and visualization of the antiparasitic drug. *Amino Acids*. 2014;**46**:1047-1058. DOI: 10.1007/s00726-013-1661-3
- [22] Filatov MA. Heavy-atom-free BODIPY photosensitizers with intersystem crossing mediated by intramolecular photoinduced electron transfer. *Organic & Biomolecular Chemistry*. 2020;**18**:10-27. DOI: 10.1039/C9OB02170A
- [23] Wang L, Bai J, Qian Y. Synthesis of a triphenylamine BODIPY photosensitizer with D-A configuration and its application in intracellular simulated photodynamic therapy. *New Journal of Chemistry*. 2019;**43**:16829-16834. DOI: 10.1039/C9NJ04166D
- [24] Wang C, Qian Y. A novel BODIPY-based photosensitizer with pH-active singlet oxygen generation for photodynamic therapy in lysosomes. *Organic & Biomolecular Chemistry*. 2019;**17**:8001-8007. DOI: 10.1039/C9OB01242G
- [25] Bill NL, Lim JM, Davis CM, Bahrng S, Jeppesen JO, Kim D, et al. π -Extended tetrathiafulvalene BODIPY (ex-TTF-BODIPY): a redox switched "on-off-on" electrochromic system with two near-infrared fluorescent outputs. *Chemical Communications*. 2014;**50**:6758-6761. DOI: 10.1039/C4CC02567A
- [26] Haldar U, Sharma R, Ruidas B, Lee H. Toward rapid and selective detection of hypochlorous acid in pure aqueous media and its application to cell imaging: BODIPY-derived water-soluble macromolecular chemosensor with high sensitivity. *Dyes and Pigments*. 2020;**172**:107858. DOI: 10.1016/j.dyepig.2019.107858
- [27] Gao J, Chen X, Chen S, Meng H, Wang Y, Li C, et al. The BODIPY-based

chemosensor for fluorometric/
colorimetric dual channel detection of
RDX and PA. *Analytical Chemistry*.
2019;**91**:13675-13680. DOI: 10.1021/acs.
analchem.9b02888

[28] Li S, Cao D, Hu Z, Li Z, Meng X,
Hana X, et al. A chemosensor with a
paddle structure based on a BODIPY
chromophore for sequential recognition
of Cu²⁺ and HSO₃. *RSC Advances*.
2019;**9**:34652-34657. DOI: 10.1039/
C9RA08345F

[29] Xue Z, Liu T, Liu H. Naked-
eye chromogenic and fluorogenic
chemosensor for mercury (II) ion
based on substituted distyryl BODIPY
complex. *Dyes and Pigments*.
2019;**165**:65-70. DOI: 10.1016/j.
dyepig.2019.01.061

[30] Spiege JD, Lyskov I,
Kleinschmidt M, Marian CM. Charge-
transfer contributions to the excitonic
coupling matrix element in BODIPY-
based energy transfer cassettes.
Chemical Physics. 2017;**482**:265-276.
DOI: 10.1016/j.chemphys.2016.10.004

[31] Bag S, Tseng JC, Rochford J. A
BODIPY-luminol chemiluminescent
resonance energy-transfer (CRET)
cassette for imaging of cellular
superoxide. *Organic & Biomolecular
Chemistry*. 2015;**13**:1763-1767. DOI:
10.1039/C4OB02413C

[32] Zhao Y, Zhang Y, Lv X, Liu Y,
Chen M, Wang P, et al. Through-bond
energy transfer cassettes based on
coumarin-Bodipy/distyryl Bodipy
dyads with efficient energy efficiencies
and large pseudo-Stokes' shifts. *Journal
of Materials Chemistry*. 2011;**21**:13168-
13171. DOI: 10.1039/C1JM12503F

[33] Wan CW, Burghart A, Chen J,
Bergström F, Johansson LBA,
Wolford MF, et al. Anthracene-BODIPY
cassettes: Syntheses and energy
transfer. *Chemical European Journal*.

2003;**9**:4430-4441. DOI: 10.1002/
chem.200304754

[34] Ortiz A. Triarylamine-BODIPY
derivatives: A promising building
block as hole transporting materials
for efficient perovskite solar cells. *Dyes
and Pigments*. 2019;**171**:107690. DOI:
10.1016/j.dyepig.2019.107690

[35] Shah MF, Mirloup A,
Chowdhury TH, Alexandra S,
Hanbazazah AS, Ahmed A, et al.
A near-infrared thienyl-BODIPY
co-sensitizer for high-efficiency
dye-sensitized solar cells. *Sustainable
Energy & Fuels*. 2019;**3**:2983-2989. DOI:
10.1039/C9SE00300B

[36] Hualme Q, Aumaitre C,
Kontkanen OV, Beljonne D, Sutter A,
Ulrich G, et al. Functional panchromatic
BODIPY dyes with near-infrared
absorption: Design, synthesis,
characterization and use in dye-
sensitized solar cells. *Beilstein Journal of
Organic Chemistry*. 2019;**15**:1758-1768.
DOI: 10.3762/bjoc.15.169

[37] Dos Santos JM, Jagadamma LK,
Latif NM, Ruseckas A, Samuel IVD,
Cooke G. BODIPY derivatives with near
infra-red absorption as small molecule
donors for bulk heterojunction solar
cells. *RSC Advances*. 2019;**9**:15410-
15423. DOI: 10.1039/C9RA01750J

[38] Meng G, Velayudham S,
Smith A, Luck R, Liu HY. Color tuning
of polyfluorene emission with
BODIPY monomers. *Macromolecules*.
2009;**42**:1995-2001

[39] Bonardi L, Ulrich G, Ziesel R.
Tailoring the properties of boron-
dipyrrromethene dyes with acetylenic
functions at the 2,6,8 and 4-B
substitution positions. *Organic Letters*.
2008;**10**:2183-2186

[40] Benniston AC, Copley G. Lighting
the way ahead with boron
dipyrrromethene (Bodipy) dyes.

Physical Chemistry Chemical Physics. 2009;**11**:4124-4131

[41] Galangau O, Dumas-Verdes C, Méallet-Renault R, Clavier G. Rational design of visible and NIR distyryl-BODIPY dyes from a novel fluorinated platform. *Organic & Biomolecular Chemistry*. 2010;**8**:4546-4553. DOI: 10.1039/C004812G

[42] Niu SL, Massif C, Ulrich G, Ziesel R, Renard PY, Romieu A. Water solubilisation and bio-conjugation of a red-emitting BODIPY marker. *Organic & Biomolecular Chemistry*. 2011;**9**:66-69. DOI: 10.1039/C00B00693A

[43] Bura T, Retailleau P, Ulrich G, Ziesel R. Highly substituted Bodipy dyes with spectroscopic features sensitive to the environment. *The Journal of Organic Chemistry*. 2011;**76**:1109-1117. DOI: 10.1021/jo102203f

[44] Majumdar P, Yuan X, Li S, Le Guennic B, Ma J, Zhang C, et al. Cyclometalated Ir(III) complexes with styryl-BODIPY ligands showing near IR absorption/emission: Preparation, study of photophysical properties and application as photodynamic/ luminescence imaging materials. *Journal of Materials Chemistry B*. 2014;**2**:2838-2854. DOI: 10.1039/C4TB00284A

[45] Gai L, Mack J, Lu H, Yamada H, Kuzuhara D, Lai G, et al. New 2,6-distyryl-substituted BODIPY isomers: Synthesis, photophysical properties, and theoretical calculations. *Chemical European Journal*. 2014;**20**:1091-1102. DOI: 10.1002/chem.201303291

[46] Pan ZH, Zhou JW, Luo GG. Experimental and theoretical study of enol-keto prototropic tautomerism and photophysics of azomethine-BODIPY dyads. *Physical Chemistry Chemical Physics*. 2014;**16**:16290-16301. DOI: 10.1039/C4CP02151G

[47] Yang Y, Zhang L, Gao C, Xua L, Baia S, Liu X. Pyrene-based BODIPY: Synthesis, photophysics and lasing properties under UV-pumping radiation. *RSC Advances*. 2014;**4**:38119-38123. DOI: 10.1039/C4RA04759A

[48] Cetindere S, Cosut B, Yesilot S, Durmus M, Kilic A. Synthesis and properties of axially BODIPY conjugated subphthalocyanine dyads. *Dyes and Pigments*. 2014;**101**:234-239. DOI: 10.1016/j.dyepig.2013.10.015

[49] Orte A, Debroye E, Ruedas-Ram J, Garcia-Fernandez E, Robinson D, Crovetto L, Talavera EM, et al. Effect of the substitution position (2, 3 or 8) on the spectroscopic and photophysical properties of BODIPY dyes with a phenyl, styryl or phenylethynyl group. *RSC Advances* 2016;**6**:102899-102913. DOI:10.1039/C6RA22340K

[50] Schmitt A, Hinkeldey B, Wild M, Jung G. Synthesis of the core compound of the BODIPY dye class: 4,4'-difluoro-4-bora-(3a,4a)-diazas-indacene. *Journal of Fluorescence*. 2009;**19**:755-758. DOI: 10.1007/s10895-008-0446-7

[51] Groves BR, Crawford SM, Lundrigan T, Matta CF, Sowlati-Hashjin S, Thompson A. Synthesis and characterisation of the unsubstituted dipyrin and 4,4-dichloro-4-bora-3a,4a-diazas-indacene: Improved synthesis and functionalisation of the simplest BODIPY framework. *Chemical Communications*. 2013;**49**:816-818. DOI: 10.1039/C2CC37480C

[52] Qin W, Baruah M, Van der Auweraer M, De Schryver FC, Boens N. Photophysical properties of borondipyrromethene analogues in solution. *The Journal of Physical Chemistry. A*. 2005;**109**:7371-7384. DOI: 10.1021/jp052626n

[53] Qin W, Baruah M, Stefan A, Van der Auweraer M, Boens N. Photophysical

properties of BODIPY-derived hydroxyaryl fluorescent pH probes in solution. *ChemPhysChem*. 2005;**6**:2343-2351. DOI: 10.1002/cphc.200500341

[54] Boens N, Wang L, Leen V, Yuan P, Verbelen B, Dehaen W, et al. 8-HaloBODIPYs and their 8-(C, N, O, S) substituted analogues: Solvent dependent UV-Vis spectroscopy, variable temperature NMR, crystal structure determination, and quantum chemical calculations. *Journal of Physical Chemistry A*. 2014;**118**:1576-1594. DOI: 10.1021/jp412132y

[55] Hendel SJ, Poe AM, Khomein P, Bae Y, Thayumanavan S, Young ER. Photophysical and electrochemical characterization of BODIPY containing dyads comparing the influence of an A-D-A versus D-A motif on excited-state photophysics. *Journal of Physical Chemistry A*. 2016;**120**:8794-8803. DOI: 10.1021/acs.jpca.6b06590

[56] Cetindere S, Tümay SO, Kilic A, Durmus M, Yesilot S. Hexa-BODIPY linked-triazole based on a cyclotriphosphazene core as a highly selective and sensitive fluorescent sensor for Fe²⁺ ions. *Journal of Fluorescence*. 2016;**26**:1173-1181. DOI: 10.1007/s10895-016-1797-0

[57] Chong H, Fron E, Liu Z, Boodts S, Thomas J, Harvey JN, et al. Acid-sensitive BODIPY dyes: Synthesis through Pd-catalyzed direct C(sp³)-H arylation and photophysics. *Chemical European Journal*. 2017;**23**:4687-4699

[58] Cetindere S, Tümay SO, Kilic A, Durmus M, Yesilot S. Synthesis and physico-chemical properties of cyclotriphosphazene-BODIPY conjugates. *Dyes and Pigments*. 2017;**139**:517-523. DOI: 10.1016/j.dyepig.2016.12.035

[59] Kang H, Si Y, Liu Y, Zhang X, Zhang W, Zhao Y, et al. Photophysical/chemistry properties of distyryl-BODIPY derivatives: An experimental

and density functional theoretical study. *The Journal of Physical Chemistry. A*. 2018;**122**:5574-5579. DOI: 10.1021/acs.jpca.8b02656

[60] Mallah R, Sreenath MC, Subramaniyan C, Joe IH, Sekar N. Excitation energy transfer processes in BODIPY based donor-acceptor system—Synthesis, photophysics, NLO and DFT study. *Optical Materials*. 2018;**84**:795-806. DOI: 10.1016/j.optmat.2018.08.007

[61] Cetindere S, Tümay SO, Senocak A, Kilic A, Durmus M, Demirbas E, et al. Novel pyrene-BODIPY dyes based on cyclotriphosphazene scaffolds: Synthesis, photophysical and spectroelectrochemical properties. *Inorganica Chimica Acta*. 2019;**494**:132-140. DOI: 10.1016/j.ica.2019.05.022

[62] Liu B, Monro S, Javed MA, Cameron CG, Colón KL, Xu W, et al. Neutral iridium(III) complexes bearing BODIPY-substituted N-heterocyclic carbene (NHC) ligands: Synthesis, photophysics, in vitro theranostic photodynamic therapy, and antimicrobial activity. *Photochemical & Photobiological Sciences*. 2019;**18**:2381-2396. DOI: 10.1039/C9PP00142E

[63] Cetindere S, Okutan E, Tümay SO, Yesilot S, Kilic A. Novel water-soluble cyclotriphosphazene-Bodipy conjugates: Synthesis, characterization and photophysical properties. *Journal of Fluorescence*. 2019;**29**:1143-1152. DOI: 10.1007/s10895-019-02424-x

[64] McDonnell SO, O'Shea DF. Near-infrared sensing properties of imethylaminosubstituted BF₂-azadipyromethenes. *Organic Letters*. 2006;**8**:3493-3496. DOI: 10.1021/ol061171x

[65] Gresser R, Hartmann H, Wrackmeyer M, Leo K, Riede M. Synthesis of thiophenesubstituted aza-BODIPYs and their optical

- and electrochemical properties. *Tetrahedron*. 2011;**67**:7148-7155. DOI: 10.1016/j.tet.2011.06.100
- [66] Adarsh N, Avirah RR, Ramaiah D. Tuning photosensitized singlet oxygen generation efficiency of novel Aza-BODIPY dyes. *Organic Letters*. 2010;**12**:5720-5723. DOI: 10.1021/ol102562k
- [67] Zhao WL, Carreira EM. Conformationally restricted aza-bodipy: A highly fluorescent, stable, near-infrared-absorbing dye. *Angewandte Chemie, International Edition*. 2005;**44**:1677-1679. DOI: 10.1002/anie.200461868
- [68] Li Y, Dolphin D, Patrick BO. Synthesis of a BF₂ complex of indol-2-yl-isoindol-1-ylidene-amine: A fully conjugated azadipyromethene. *Tetrahedron Letters*. 2010;**51**:811-814. DOI: 10.1016/j.tetlet.2009.12.003
- [69] Loudet A, Bandichhor R, Burgess K, Palma A, McDonnell SO, Hall MJ, et al. B, O-chelated azadipyromethenes as near-IR probes. *Organic Letters*. 2008;**10**:4771-4774. DOI: 10.1021/ol8018506
- [70] Loudet A, Bandichhor R, Wu L, Burgess K. Functionalized BF₂ chelated azadipyromethene dyes. *Tetrahedron*. 2008;**64**:3642-3654. DOI: 10.1016/j.tet.2008.01.117
- [71] Palma A, Tasior M, Frimannsson DO, Vu TT, Meallet-Renault R, O'Shea DF. New on-bead near-infrared fluorophores and fluorescent sensor constructs. *Organic Letters*. 2009;**11**:3638-3641. DOI: 10.1021/ol901413u
- [72] Yoshii R, Nagai A, Chujo Y. Highly near-infrared photoluminescence from Aza-borondipyromethene-based conjugated polymers. *Journal of Polymer Science Part a-Polymer Chemistry*. 2010;**48**:5348-5356. DOI: 10.1002/pola.24335
- [73] Herold DA, Rieke RD. Synthesis of 1,2-disubstituted acenaphthylenes. *Journal of Organic Chemistry*. 1979;**44**:1359
- [74] Majumdar P, Mack J, Nyokong T. Synthesis, characterization and photophysical properties of an acenaphthalene fused-ring-expanded NIR absorbing aza-BODIPY dye. *RSC Advances*. 2015;**5**:78253-78258. DOI: 10.1039/C5RA14916A
- [75] Lu H, Mack J, Yang Y, Shen Z. Structural modification strategies for the rational design of red/NIR region BODIPYs. *Chemical Society Reviews*. 2014;**43**:4778-4823. DOI: 10.1039/C4CS00030G
- [76] Zhou J, Gai L, Mack J, Zhou Z, Qiu H, Chan KS, et al. Synthesis and photophysical properties of orthogonal rhodium(III)-carbon bonded porphyrin-aza-BODIPY conjugates. *Journal of Materials Chemistry C*. 2016;**4**:8422-8428. DOI: 10.1039/C6TC03130G
- [77] De Simone BC, Mazzone G, Pirillo J, Russo N, Sicilia E. Halogen atom effect on the photophysical properties of substituted aza-BODIPY derivatives. *Physical Chemistry Chemical Physics*. 2017;**19**:2530-2536. DOI: 10.1039/C6CP07874E
- [78] Gut A, Łapok L, Jamróz D, Gorski A, Solarzski J, Nowakowska M. Photophysics and redox properties of aza-BODIPY dyes with electron-withdrawing groups. *New Journal of Chemistry*. 2017;**41**:12110-12122. DOI: 10.1039/C7NJ02757E
- [79] Obłóza M, Łapok L, Pędziński T, Nowakowska M. A beneficial effect of bromination on the photophysical and photochemical properties of

Aza-BODIPY dyes with electron-donating groups. *Asian Journal of Organic Chemistry*. 2019;**8**:1879-1892.
DOI: 10.1002/ajoc.201900385

[80] Obłozka M, Łapok L, Pędziński T, Stadnicka KM, Nowakowska M. Synthesis, photophysics and redox properties of Aza-BODIPY dyes with electron-donating groups. *ChemPhysChem*. 2019;**20**:2482-2497.
DOI: 10.1002/cphc.201900689

Supramolecular Chemistry and DNA Interaction Studies of Ferrocenyl Ureas and Thioureas

Samia Kausar, Ataf Ali Altaf, Muhammad Hamayun, Amin Badshah and Abdul Razzaq

Abstract

In this chapter, we have discussed the characteristics and bioapplicabilities of different ferrocene derivatives, for example, amides, amines, sulfonamide, and polymers, focusing mainly on urea and thiourea derivatives due to their autonomous and widespread spectroscopic action and bioactivities. Supramolecular chemistry of ferrocenyl ureas and thioureas is described owing to exploring their mode of interactions within and among the molecules and the role of these supramolecular structures in enhancing the DNA intercalation. DNA interaction studies of these ferrocenyl-based ureas and thioureas are explored with approaches like electrochemical study, viscosity measurements, molecular docking, electronic spectroscopy, dynamic light scattering (DLS), and radical scavenging activity. Attachment of ferrocene moiety to ureas and thioureas closer to DNA is very promising strategy which most possibly boosts the probability of DNA damage and cell apoptosis which is responsible for enormous biological activities.

Keywords: thioureas, ferrocene, medicinal chemistry, supramolecular chemistry, ureas, DNA interaction

1. Introduction

Soon after discovery of ferrocene in 1951 [1], the main focus of scientists was to determine its accurate structure. Its correct elucidation was carried out individually by Fischer and Hafner and Wilkinson et al. [2, 3]. Woodward et al. termed this iron-containing compound as ferrocene due to resemblance of its reactivity with benzene [4]. The structural determination of ferrocene proved a revolutionary discovery and a progressive revelation in the historical backdrop of chemistry which directed new dimensions in organometallic chemistry. Today, terms like metallocenes and sandwich compounds are used for ferrocene and ferrocenyl derivatives due to significantly more extensive scope of these compounds that assimilate other metals also [5].

Due to impressive stability of ferrocene in aerobic medium and water, its promising electrochemical properties and openness of an extensive assortment of subordinates have made ferrocenyl derivative compounds widespread molecules for biological applicabilities [6–8]. The promising applications of ferrocene in the field of medicine proved a vigorous research area nowadays [9]. Many reports have revealed that some ferrocenyl derivatives are extremely active in vivo and in vitro,

against various diseases, for example, bacterial and fungal contagions [10, 11], malaria [12], cancer [13], and human immunodeficiency virus (HIV) [14].

2. Ferrocene derivatives

Extensive applications of ferrocene and its derivative compounds in material science, homogeneous catalysis [15], nonlinear optics [16], and molecular sensors are observed [17]. Furthermore, an unexpected biological activity is often witnessed upon incorporating a fragment of ferrocene into a molecule of an organic compound [18]. Many ferrocene derivative compounds exhibit stimulating cytotoxic, antimalarial, antitumor, antioxidant, antifungal, and DNA-cleaving activity [19–21].

The anticancer [22] perspective of ferrocenyl derivative compounds was first premeditated around the 1970s. Brynes and collaborators explored the counter tumor action of ferrocenyl compounds containing amide or amine moieties against leukemia P-388 of the lymphocytic system [23]. They administered these derivative compounds to mice intraperitoneally using either water or surfactant with water as Tween-80: water. The anti-tumor action of these compounds was considerable enough to show that the incorporation of the ferrocenyl moiety into an appropriate bearer could provide a drug with elevated antitumorous activity (**Figure 1**) [23].

Extensive study is carried out about ferrocene and its derivative compounds as efficient chemotherapeutic agents [24]. Stability, electroactivity, and extraordinary spectroscopic actions of ferrocene-incorporated organometallics are reasoned for being auspicious contenders for various biological applicabilities [25–27]. With reversible redox characteristics and elevated cell penetrability owing to its extensive lipophilicity, ferrocenyl moiety is responsible for pronounced characteristics of ferrocenyl derivative

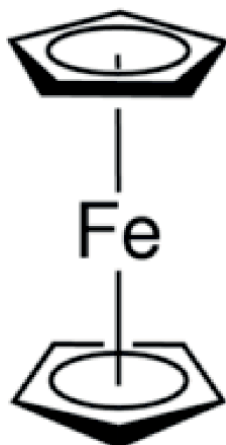


Figure 1.
Structure of ferrocene.

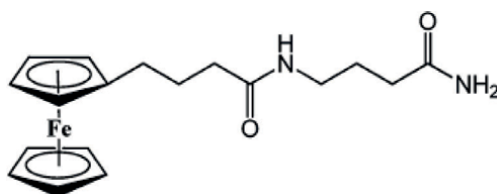


Figure 2.
Ferrocenyl derivative verified against lymphocytic leukemia P-388.

compounds [28]. For example, enhanced anticancer activity was observed when ferrocene was incorporated into tamoxifen which is a potent anticancer drug i.e. Ferrocenyl derivative verified against lymphocytic leukemia P-388 (**Figure 2**) [29].

3. Ferrocenyl ureas and thiourea

Among the various ferrocenyl derivative compounds are i.e. amides, amines, polyacids, polymers, ureas, thioureas, and sulfonamide derivatives [30]. A lot of work is happening on the applications of ferrocenyl urea and thiourea compounds due to their pronounced interactions, supramolecular chemistry, electrochemical characteristics, and DNA interactions. Following are some examples of ferrocenyl urea and thiourea derivative compounds checked for their various activities depicted in **Figure 3** [30].

3.1 Ferrocenyl ureas

Urea ($R_1R_2NC=ONR_3R_4$) is a striking building block in consequence of its widespread bioactivities and extensive bioavailability from natural products [31]. Among the urea derivative compounds, urea derivatives having aromaticity in them such as N-phenyl-N-(2-chloroethyl)urea and heterocyclic urea derivatives illustrate potential anticancer activities because of their efficient inhibitory effect against the receptor tyrosine kinases (RTKs) [32].

Urea is ascertained to be an appealing building obstruct for receptors of anion as it contributes two comparatively robust H-bonding positions [33]. The two N—H groups in urea are able to make a bond with the only acceptor atom to form a ring structure comprising six-membered chelate or bind with two nearby oxygen atoms in an oxy-anion to give a ring structure consisting of eight-membered chelate as

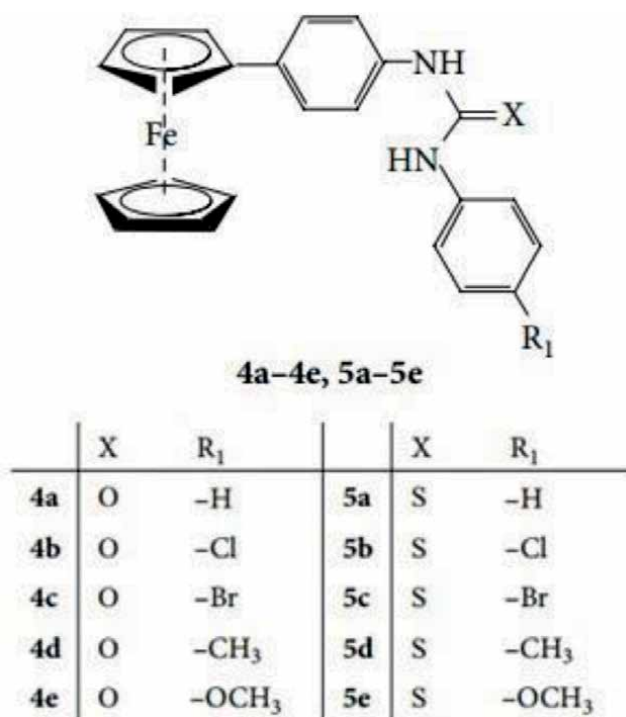


Figure 3.
Some representative ferrocenyl ureas and thioureas.

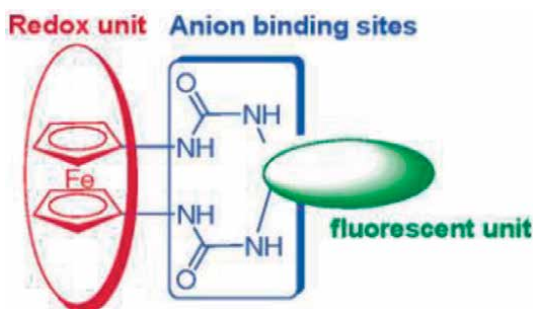


Figure 4.
Ferrocenyl urea [34].

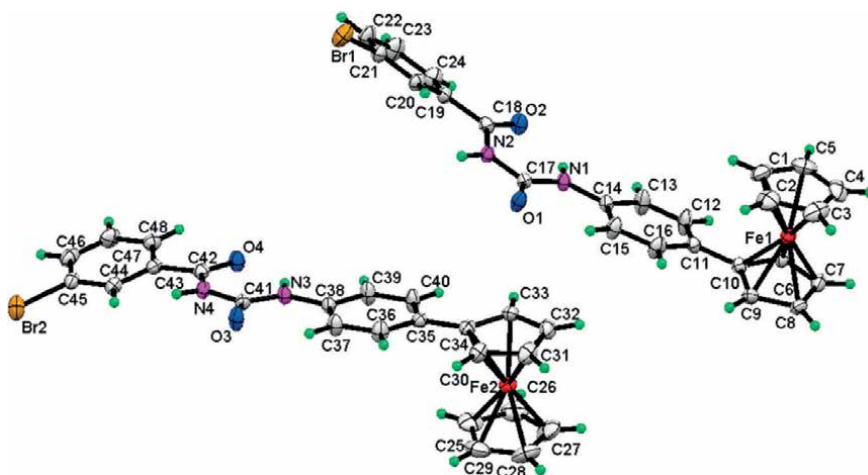


Figure 5.
Molecular structure of 1-(3-bromobenzoyl)-3-(4-ferrocenylphenyl)urea.

depicted in (Figure 4). These N-H groups are modified to supplement target anion and minimal intramolecular H-bonding to observe strong and selective binding characteristics [34] (Figure 4).

Over the past few years, assortment of urea-based hosts comprising one or more than one urea subunits is premeditated and tested for anion recognition and for being capable of sensing [35]. New perceptions into characteristics of interactions between urea and anionic moiety providing structural measures for considered designing of novel anion-selective receptors which contain two or additional urea binding groups have also been discovered in recent times [36]. On the other hand, there are few instances of ferrocenyl urea derivatives as redox active anionophores [37]. The molecular structure of a representative ferrocenyl urea derivative is presented in Figure 5 [38].

3.2 Ferrocenyl thioureas

Replacement of an oxygen atom in urea moiety by a sulfur atom results in thio-urea formation, the characteristics of which are significantly diverged than those of urea due to the variation in electronegative character among sulfur and oxygen atoms [39]. Thiourea-based compounds and complexes have also been explored for several biological activities because of the thio-carbonyl group, which influences biochemical activity by lipophilic or hydrophilic character and electronic properties of derivative compounds [40].

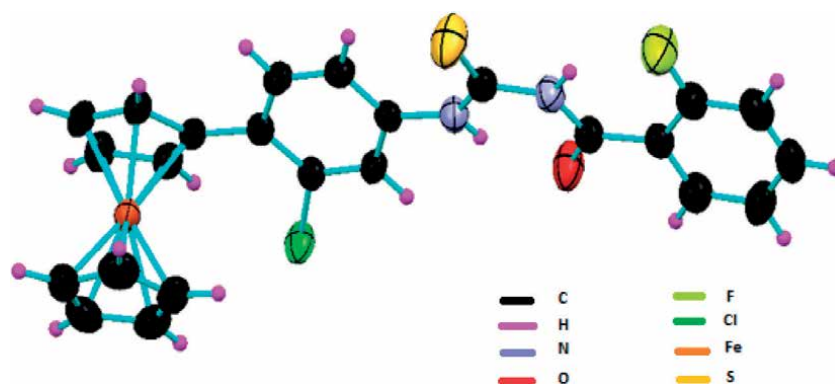


Figure 6.
Molecular structure of 1-(2-florobenzoyl)-3-(2-chloro,4-ferrocenylphenyl)thiourea.

The lipophilicity/hydrophilic characters and the electronic properties of thiourea derivative compounds are greatly inclined due to the presence of thio-carbonyl moiety which in turn affects the labile nature of leaving substituents, hence regulating the biochemical activity. Various ferrocenyl thiourea derivative compounds have been discovered, which are significantly important for various features of antitumorous agents due to their inhibitory rejoiner against receptor tyrosine kinases (RTKs), protein tyrosine kinases (PTKs), and NADH oxidases [41, 42]. Various thiourea derivatives exhibited bioactivities against different infectious diseases, leukemias, and solid tumors, for example, aroylthioureas, diarylsulphonylureas, N-nitrosoureas, and benzoylureas [43]. The molecular structure of a representative ferrocenyl urea derivative compound is depicted in **Figure 6** [40].

4. Supramolecular chemistry of ferrocenyl ureas and thioureas

4.1 Supramolecular chemistry

Supramolecular chemistry [44] focuses on the design and synthesis of “Supramolecular Entities” [45], i.e., compound elements held together by noncovalent connections including hydrogen bonding, bonds with halogens, forces of coordination, or π - π connections (**Figure 7**) [46]. Research in supramolecular chemistry and crystal engineering is principally centered around host-guest arrangements, binding of anion and cation, coordination polymers, developments of self-assembly networks, biological simulators, gels, fibers, liquid polymers, crystals, and other various types of materials [47].

Supramolecular chemistry objects to the considerations of interactions between molecules and packing patterns in molecular crystals and, consequently, usage of information spawned for potential novel material designing gathered with targeted structures and proficient characteristics [48–50]. From this objective, one can consider assembling molecular crystals having a multitude of noncovalent interactions among which a prominent position is occupied by H-bonds owing to their noticeable directionalities and reasonably high strength [51]. Hydrogen bonds are characteristically much weaker in comparison to covalent bonds though and hence have minimum predictability, which often destabilizes the crystal designing process utilizing these interactions [52].

While considering the molecular synthesis, synthetic schemes are confidently planned by researchers for molecules comprising very complex framework. In synthesizing crystalline organic solids, the term engineering can be invoked infrequently in its true sense. Taking from supramolecular structure to design a crystal

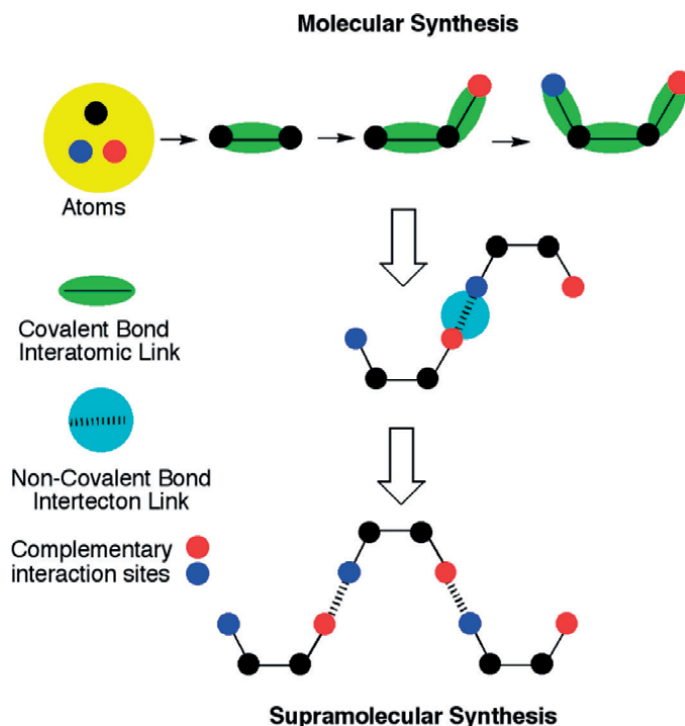


Figure 7.
Noncovalent interactions in supramolecular synthesis.

structure, the whole process considers experiential observations and a posteriori structure of crystal and analytical measurement [53].

4.2 Supramolecules of ureas and thioureas

Urea group is one such powerful building obstruct that formulates obstinate chains that bind through hydrogen bonding in various surroundings, from solutions [54] to gels and fibrous materials [55], also with crystals [47]. An approach that has been comprehensively discovered since the initial research in crystallography of disubstituted ureas in the late 1960s is the use of symmetrical or asymmetrical N,N'-di-substituted ureas that can deliver widespread multiple building congers for designing of organic solids of crystalline nature. N,N'-di-substituted ureas have the ability to act as H-bond donors by using their two N—H protons, and play the role of acceptors through utilizing the presence of the lone electron pairs of CO group [36]. Robust one-dimensional hydrogen bonded chains having self-association reinforced promising complementarity between both groups (**Figure 8**) [56], which have been reconnoitered for developing the crystalline networks repeatedly.

Nanostructured materials on the basis of cylindrical or columnar constructions have been innovated more recently. Thioureas, despite the fact that they can also practice comparatively robust H-bonded motifs [57], have not been as much searched out for the coherent assemblage of solids of crystalline nature as compared to ureas [58, 59].

4.2.1 Example illustrating the supramolecular interactions of ferrocenyl thiourea

Dr. Bhajan Lal Bhatia and coworkers synthesized ferrocenyl-based thiourea compounds, i.e., 1-benzoyl-3-(4-ferrocenylphenyl)thiourea (**B16**) and

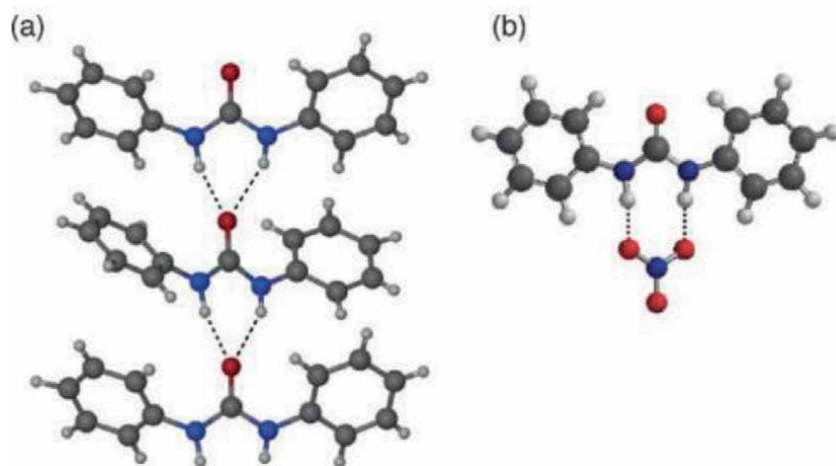


Figure 8.
The contrast of N,N'-disubstituted ureas functioning as: (a) building blocks for the assemblage of H-bonded chains, as depicted by the crystal structure of di-phenylurea [59] or (b) anion binding groups, as represented by calculated di-phenylurea:nitrate complex, optimized with DFT at B₃LYP/6-31G level [56].*

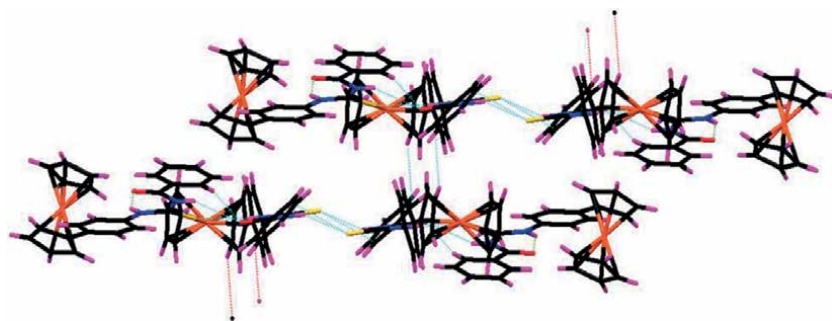


Figure 9.
Supramolecular structures of B16 intervened by secondary bonding.

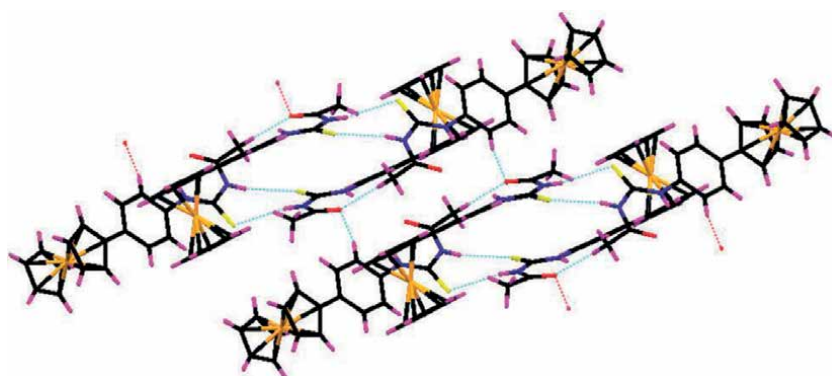


Figure 10.
Supramolecular structures of B3 intervened by secondary bonding.

1-acetyl-3-(4-ferrocenylphenyl)thiourea (**B3**) [60]. Finding displayed two self-regulating molecules which are present in an asymmetrical component in structures of B16 and B3 linked interchangeably to each other through intermolecular NH...O and NH...S types of hydrogen bonding and secondary interactions

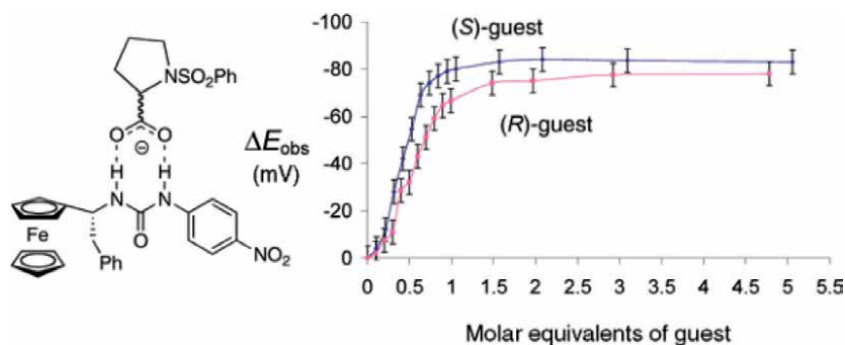


Figure 11. Novel redox active ferrocenyl urea receptors for the purpose of binding and sensing the chiral carboxylate anions and their molar equivalents of (S)-(blue) (R)-(pink) [66].

non-covalent in nature ($\pi \cdots \text{H}$), which intervene supramolecular structures for B16 and B3 as shown in **Figures 9** and **10** [60].

Determination of some important biological activities usually depends upon these types of secondary nonbonding interactions between the molecules. Greater ability of compounds to associate with macromolecules such as DNA and proteins is observed due to having an ability to make stronger nonbonding interactions [61]. Among the compounds studied, B16 was reported to be associated with more secondary interactions that were apparent from H-bonding data and formation of a supramolecular structure. Therefore, it can be predictable that B16 can have better strapping interaction with DNA that will transform into more elevated biological activities [60].

4.3 Chiral recognition of ferrocenyl derivatives

Now a days, main focus in supramolecular chemistry is chiral recognitions [62] hence designing of enantioselective sensors growing quickly. The encouragement directed us to search for appropriate ways of ascertaining one enantiomer of a specific chiral target board regarding its mirror image [63–65] (**Figure 11**).

The productions of chiral urea's series attached to the ferrocene group which is redox active are discovered [62]. These are able to bind through hydrogen bonding interactions with chiral carboxylates in organic solvents confirmed by spectroscopic and cyclic voltammetric measurements. Cyclic voltammetric measurements have shown that these guests can be sensed via electrochemical approaches in solution. For example, enantioselective nature is prominent enough in the association of protected amino acid, i.e., N-benzenesulfonylproline, through a ferrocenyl-benzyl host that permits the contrary enantiomers to be distinguished in an electrochemical way as depicted in (**Figure 11**) [66].

5. DNA interaction of ferrocenyl ureas and thioureas

DNA is relatively the key target within cells for research work having small molecular entities important biologically, i.e., steroids, cancer-causing agents and other various modules of drugs [67]. The exploration of interactions of drug with DNA is far more imperative for consideration of characteristic molecular drug action mechanisms to its peculiar target and for fabrication of definite DNA-targeted drugs [68]. Usually, three binding approaches, intercalative mode of binding, groove binding, and electrostatic type of interactions, are involved in the noncovalent interactions

of small molecules with DNA [69]. The intercalative binding mode is resilient than the other two modes of binding due to the surface of intercalating molecule, which is sandwiched among aromatic and heterocyclic DNA base pairs [70–72].

5.1 Activity of ferrocenyl moiety

The introduction of a ferrocenyl group to molecules like urea and thiourea that bind with DNA is an auspicious strategy to take the ferrocene moiety in close proximity of DNA which most possibly boosts the probability of DNA damage and cell apoptosis. The above-discussed anticancer character of ferrocenyl derivatives is found to be reliant on mainly oxidation state of Fe in ferrocene moiety as approximate results clearly exhibited that the Fe(II) ferrocenyl derivative compound is found to have more activity than Fe(III)-containing compounds [73].

One of the Fe(II) compounds, ferrocifen, performs its action by altering the conformation of protein having receptor site as indicated by the results of the study carried out [74]. Binding of ferrocifen to estrogen receptor (ER β) is considered to result in its dimerization, which is followed by attachment of the dimerized species to a particular targeted area of DNA. Reactive oxygen species (ROS), such as hydroxyl radicals (\bullet OH) produced as a result of electron transfer reactions, result in in-vivo formation of ferrocenium ion or formation of ferrocifen-ER β complex. ROS produced can be responsible to damage DNA [75, 76] and may also control the anticancer activity by forming the radical metabolites that carry the biological impairment in cancerous regions [77].

5.2 DNA binding studies through cyclic voltammetry

To demonstrate the approach of interaction and the DNA binding constraints, different techniques are employed. Cyclic voltammetry is proved to be one of the most sophisticated and sensitive techniques to carry out DNA binding studies. Investigation of mode of interaction between DNA and derivative compounds is determined through shift in peak potential. Indication of intercalation of derivative compounds into double helix structured DNA comes from slightly positive shift of the peak potential. The ratio of binding of oxidized and reduced molecules is calculated using the following equation Eq. (1) [78, 79]:

$$E_b^\circ - E_f^\circ = 0.05916 \log \left(\frac{K_{red}}{K_{oxd}} \right) \quad (1)$$

where E_b° and E_f° are proper potentials of bound and free drug candidates, correspondingly. Positive shift is indicative for intercalation of derivative compounds with DNA. The formation of a supramolecular complex due to drug diffusion into DNA results in dropping of current in electrochemical analysis. Drop off in current is observed depending upon the number of transferred electrons, which is decreased upon formation of a supramolecular complex. Binding constant is calculated using the following equation Eq. (2) [80]:

$$\frac{1}{[DNA]} = \frac{K[(1 - A)]}{1 - i/i_o} - K \quad (2)$$

where K is the binding constant, i and i_o represent peak currents in the presence and absence of DNA, and A is the proportionality constant. The plot of $1/[DNA]$ versus $1 - i/i_o$ produces binding constants.

Following are the examples of cyclic voltammetric results in **Figures 12** and **13** for the characteristic ferrocenyl thioureas discussed in Section 3.2 and their molecular structures in **Figures 9** and **10**.

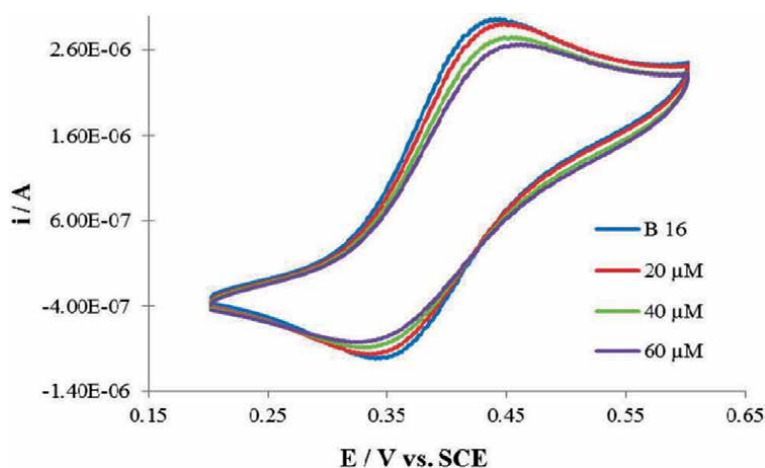


Figure 12.

Cyclic voltammograms of 1 mM B16 at a 0.05 V s^{-1} potential sweep rate on a glassy-carbon electrode at 298 K with and without incorporation of 1 mL of CT-DNA by its increasing concentrations (i.e. 10, 20, and 60 μM) in a 20% aq. DMSO buffer at pH 6.0; supporting electrolyte 0.1 M TBAP [60].

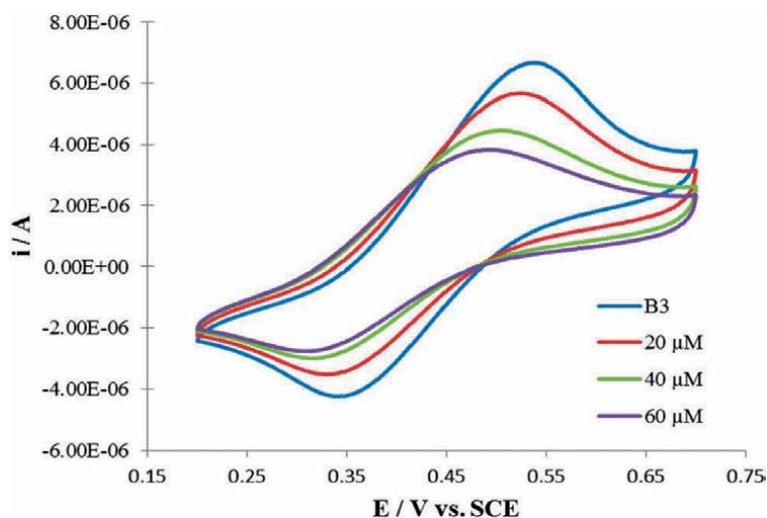


Figure 13.

Cyclic voltammograms of 1 mM B3 at a 0.05 V s^{-1} potential sweep rate on a glassy-carbon electrode at 298 K with and without incorporation 1 mL of CT-DNA by its increasing concentrations (i.e. 10, 20, and 60 μM) in a 20% aq. DMSO buffer at pH 6.0; supporting electrolyte 0.1 M TBAP [60].

Cyclic voltammetric analysis of 1 mM of B16 and B3 was carried out incorporating and without incorporating calf-thymus DNA (CT-DNA). After the addition of CT-DNA, an obvious positive shift in formal potential was observed for B16, which indicated the intercalative mode of interaction, whereas for B3, a formal potential shift toward negative side was observed, which is credited to electrostatic interactions among compound and DNA [60].

5.3 DNA binding studies through viscometry

Viscosity measurement is another beneficial technique to demonstrate intercalation of derivative compounds with DNA. It is sensitive to change in DNA length as base pair active pockets are broadened to provide lodging to binding molecule that ultimately results in lengthening of DNA helix. This technique is considered

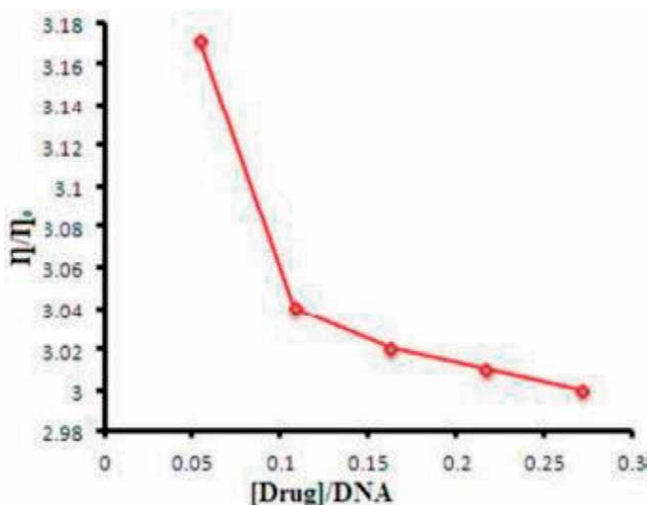


Figure 14.
Relative viscosity versus $[\text{Drug}]/[\text{DNA}]$ representative plot for mode of interaction determination.

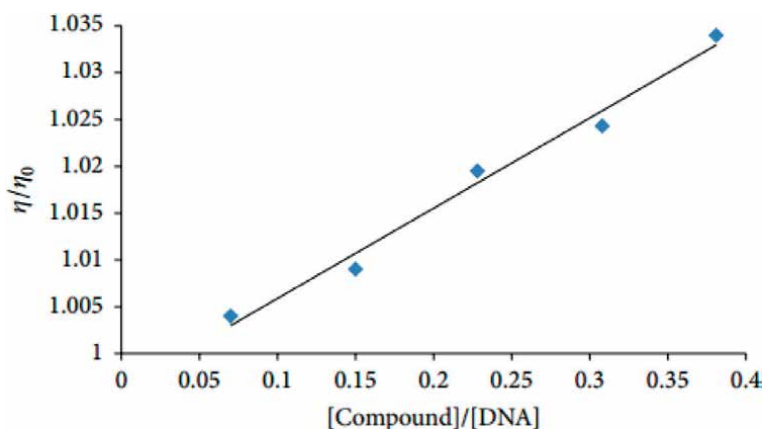


Figure 15.
Effect of increasing concentration of compound 1,1'-(4,4'-di-ferrocenyl)di-phenylthiourea on relative viscosity of DNA at 25°C. $[\text{DNA}] = 30 \mu\text{M}$ and $[\text{compound}] = 5\text{--}25 \mu\text{M}$.

as a least abstruse and utmost precarious test for binding mode determination in solution phase under suitable conditions, i.e., constant temperature at $25.0 \pm 0.1^\circ\text{C}$ in a thermostatic bath [81].

Following is the representative plot (**Figure 14**) [82] which exhibits the relative viscosity (η/η_0) against $[\text{compound}]/[\text{DNA}]$ concentrations to examine the mode of interaction. Derivative compounds have shown that upon increasing binding ratio, relative viscosity decreases which is a representative for electrostatic interactions [82].

Figure 15 [81] is another example of a viscosity measurement result of a ferrocenyl urea derivative compound that shows the consequence of increment in concentration of derivative compound on viscosity [81].

5.4 Molecular docking

Molecular docking approach is one of the most frequently employed approaches in structure-based drug designing, owing to its capability to predict conformation

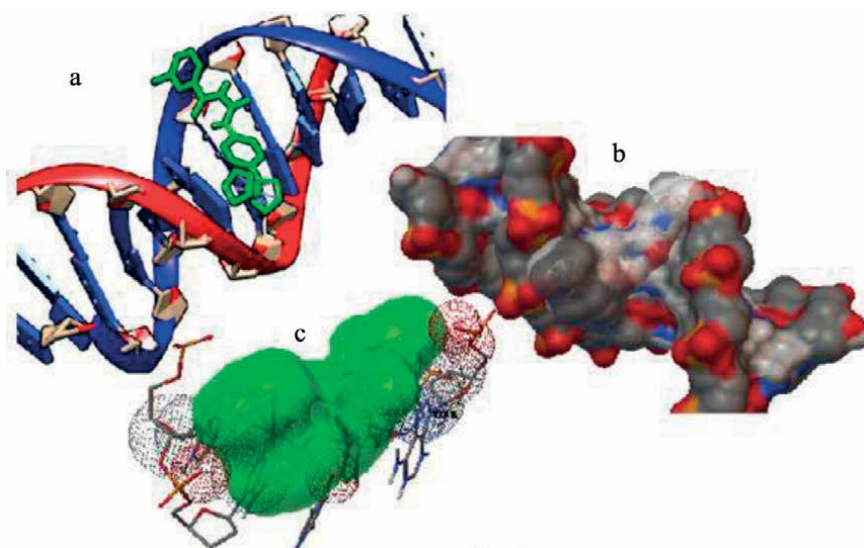


Figure 16.

(a) Docked conformation of representative P₃Cl compound with 1-BNA; P₃Cl is shown in green color while 1-BNA exhibited a ribbon structure, (b) surface outlook of docked-P₃Cl with 1-BNA (color code: grey-carbon, red-oxygen, and blue-nitrogen) and (c) 3D-model representing interactions of P₃Cl and DNA [82].

responsible for binding of small molecular entities, i.e., ligands to a suitable target active binding site [83].

The example illustrated in **Figure 16(a)** exhibits the representative docked conformation of compound 1-(3-chlorobenzoyl)-3-(4-ferrocenylphenyl)urea (P₃Cl) with DNA attributed to have the lowest binding energy, recommended by AutoDock [84], whereas **Figure 16b** depicts the surface view of docked conformation of the represented compound and it is clearly indicated from **Figure 16b** that ferrocenyl group of docked P₃Cl is in close interaction with O-atom which is linked to sugar phosphate DNA backbone. This, in another way, suggested that electrostatic interaction force exist among Fe and O-atoms of sugar and phosphate backbone [82]. **Figure 16c** is the close view of DNA atoms that clearly interact with the active surface of the P₃Cl compound, and O-atom of the sugar-phosphate backbone can be seen, which prevails among deoxyadenosine (DA)-18 and DA-17, showing electrostatic interactions with ferrocenyl group [85]. The presence of hydrogen bond is also observed in the structure among one of the O atoms of P₃Cl and H-atom attached to N-atom of DA5 [86].

5.5 Dynamic light scattering (DLS)

Dynamic light scattering (DLS) approach is employed to govern size distribution of small particles in suspension or polymers in solution. This method is used in medicine to detect molecular changes in the cornea in biology to measure the rate of diffusion on proteins, and in material science to study the orientational fluctuation in the liquid crystals [87].

DLS is, in principle, capable of distinguishing whether a protein is a monomer or dimer; it is much less accurate for distinguishing small oligomers than is classical light scattering or sedimentation velocity. The advantage of using dynamic scattering is the possibility to analyze samples containing broad distributions of species of widely differing molecular masses (e.g. a native protein and various sizes of aggregates), and to detect very small amounts of the higher mass species (<0.01% in many cases) [88].

For example, expansion of DNA helix occurs upon intercalation of a small molecule into DNA helix, as cavities are created to lodge small molecules between the bases which minimize the hydrodynamic radius (R_h) as shown in **Figure 17** [61].

5.6 UV-vis spectroscopy

UV-vis spectroscopy is used frequently for studying ferrocene and ferrocenyl derivative compounds owing to their fairly high stability under visible irradiation, and hence, they are widely used in luminescent systems. They are classical quenchers of excited states. Both energy and electron transfer may be involved, depending on the nature of the excited species [89]. The color of the ferrocene greatly changes upon oxidation, hence permitting spectroscopic measurements in the visible range. UV-vis spectroscopy is proved to be an effective approach for calculation of binding strength of DNA with derivative compounds. **Figure 18** depicts a representative UV-vis plot of ferrocenyl urea depicting a noticeable hypochromic and a slender blue peak shift representing adducts of drug-DNA comparative to free drug entities, which approves the electrostatic nature of interactions (**Figure 18a**) [38].

5.7 Free radical scavenging activity

Substantial binding of derivative compounds with DNA can be observed via electrostatic type of interactions and remarkable free-radical scavenging capability [90].

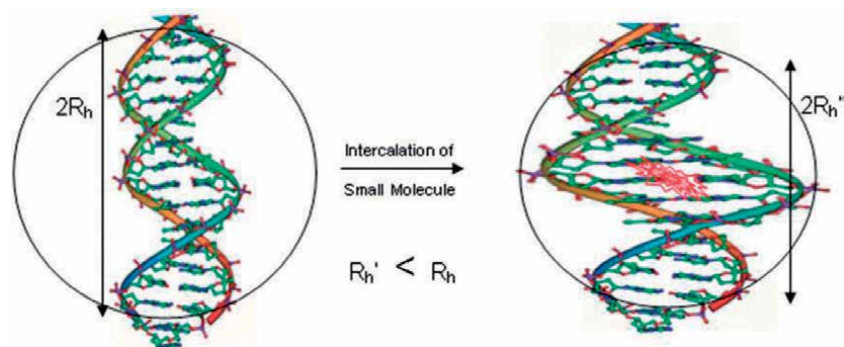


Figure 17. Decrease in hydrodynamic radius (R_h) upon intercalation of complex in DNA helix.

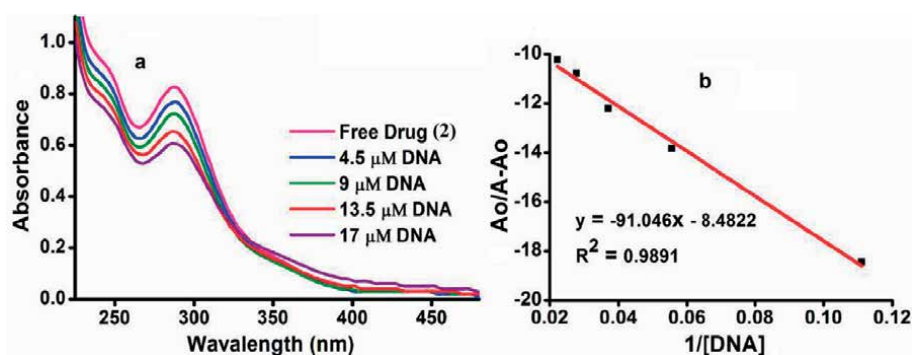


Figure 18. (a) Representative plots of absorbance versus wavelength of $25 \mu\text{M}$ 1-(3-bromobenzoyl)-3-(4-ferrocenylphenyl) urea in ethanol with DNA's increasing concentration from (4.5–17 μM) and (b) plot of A^0/A^∞ versus $1/[\text{DNA}]$ for determining binding constant of DNA attached to the compound [38].

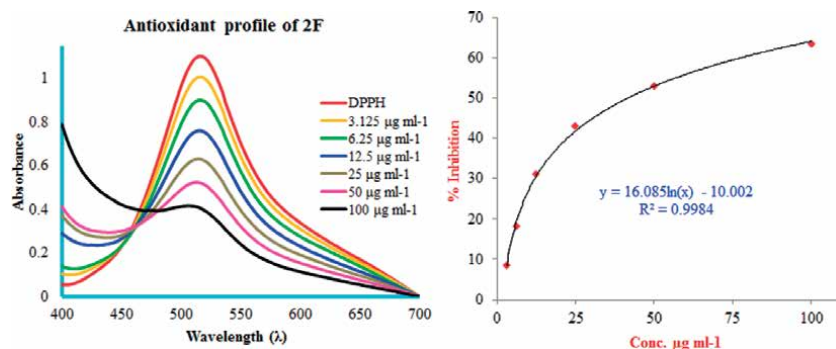


Figure 19. Electronic absorption spectra of [1-(2-florobenzoyl)-3-(2-chloro, 4-ferrocenylphenyl)thiourea (2F)] ($3.125\text{--}100\ \mu\text{g mL}^{-1}$) representing free-radical scavenging outline.

The free-radical scavenging activity of compound [1-(2-florobenzoyl)-3-(2-chloro, 4-ferrocenylphenyl)thiourea (2F)] molecular structure is given in Section 3.2 in **Figure 6**, which exhibits a sheer increment in % inhibition by increment in its concentration. It had been found that with increasing concentration of ferrocenyl thioureas, the % inhibitory activity is increased as depicted in the representative plot in **Figure 19** [40].

Author details

Samia Kausar¹, Ataf Ali Altaf^{1*}, Muhammad Hamayun¹, Amin Badshah² and Abdul Razzaq³


¹ Department of Chemistry, University of Gujrat, Gujrat, Pakistan

² Department of Chemistry, Quaid-i-Azam University, Islamabad, Pakistan

³ Department of Chemistry, Government Postgraduate College, Sahiwal, Pakistan

*Address all correspondence to: atafali.altaf@uog.edu.pk

IntechOpen

© 2020 The Author(s). Licensee IntechOpen. This chapter is distributed under the terms of the Creative Commons Attribution License (<http://creativecommons.org/licenses/by/3.0>), which permits unrestricted use, distribution, and reproduction in any medium, provided the original work is properly cited. 

References

- [1] Kealy T, Pauson P. A new type of organo-iron compound. *Nature*. 1951;**168**(4285):1039
- [2] Fischer E, Hafner W. *Zeitschrift für Naturforschung. B: Anorganische Chemie, organische Chemie, Biochemie, Biophysik, Biologie*. 1962;**17**:774-775
- [3] Wilkinson G et al. The structure of iron bis-cyclopentadienyl. *Journal of the American Chemical Society*. 1952;**74**(8):2125-2126
- [4] Woodward R, Rosenblum M, Whiting M. A new aromatic system. *Journal of the American Chemical Society*. 1952;**74**(13):3458-3459
- [5] Rosenblum M. *Chemistry of the Iron Group Metallocenes: Ferrocene, Ruthenocene, Osmocene*. Vol. 1. Interscience Publishers; 1965
- [6] Van Staveren DR, Metzler-Nolte N. Bioorganometallic chemistry of ferrocene. *Chemical Reviews*. 2004;**104**(12):5931-5986
- [7] Allardyce CS et al. Development of organometallic (organo-transition metal) pharmaceuticals. *Applied Organometallic Chemistry*. 2005;**19**(1):1-10
- [8] Hillard EA, Vessieres A, Jaouen G. Ferrocene functionalized endocrine modulators as anticancer agents. In: *Medicinal Organometallic Chemistry*. Springer; 2010. pp. 81-117
- [9] Fouda MF et al. On the medicinal chemistry of ferrocene. *Applied Organometallic Chemistry*. 2007;**21**(8):613-625
- [10] Biot C et al. Synthesis and antifungal activity of a ferrocene-fluconazole analogue. *Bioorganic & Medicinal Chemistry Letters*. 2000;**10**(8):839-841
- [11] Zhang J. Preparation, characterization, crystal structure and bioactivity determination of ferrocenyl-thiazoleacylhydrazones. *Applied Organometallic Chemistry*. 2008;**22**(1):6-11
- [12] Delhaes L et al. Novel ferrocenic artemisinin derivatives: Synthesis, in vitro antimalarial activity and affinity of binding with ferroprotoporphyrin IX. *Bioorganic & Medicinal Chemistry*. 2000;**8**(12):2739-2745
- [13] Ornelas C. Application of ferrocene and its derivatives in cancer research. *New Journal of Chemistry*. 2011;**35**(10):1973-1985
- [14] Kondapi AK, Satyanarayana N, Saikrishna A. A study of the topoisomerase II activity in HIV-1 replication using the ferrocene derivatives as probes. *Archives of Biochemistry and Biophysics*. 2006;**450**(2):123-132
- [15] Andrieux C et al. Determination of the lifetimes of unstable ion radicals by homogeneous redox catalysis of electrochemical reactions. Application to the reduction of aromatic halides. *Journal of the American Chemical Society*. 1980;**102**(11):3806-3813
- [16] Pal SK et al. Schiff base linked ferrocenyl complexes for second-order nonlinear optics. *Journal of Organometallic Chemistry*. 2000;**604**(2):248-259
- [17] Nieto D et al. Pt (II)-activated coupling of aminoethylferrocene with benzonitrile. A facile access route to a new redox-active bis (ferrocenyl-amidine) anion sensor. *Chemical Communications*. 2011;**47**(37):10398-10400
- [18] Chohan ZH et al. Organometallic-based antibacterial and antifungal

- compounds: Transition metal complexes of 1, 1'-diacetylferrocene-derived thiocarbohydrazone, carbohydrazone, thiosemicarbazone and semicarbazone. *Journal of Enzyme Inhibition and Medicinal Chemistry*. 2005;**20**(1):81-89
- [19] dos Santos L et al. Synthesis of new 1-phenyl-3-{4-[(2E)-3-phenylprop-2-enoyl] phenyl}-thiourea and urea derivatives with anti-nociceptive activity. *Bioorganic & Medicinal Chemistry*. 2008;**16**(18):8526-8534
- [20] Sharma B et al. A quantitative structure-activity relationship study of novel, potent, orally active, selective VEGFR-2 and PDGFR α tyrosine kinase inhibitors: Derivatives of N-phenyl-N'-(4-(4-quinolyloxy) phenyl) urea as antitumor agents. *Journal of Enzyme Inhibition and Medicinal Chemistry*. 2008;**23**(2):168-173
- [21] Corry AJ et al. Synthesis, characterization and in vitro anti-cancer activity of N-(ferrocenyl) benzoyl tri- and tetrapeptide esters. *Inorganica Chimica Acta*. 2009;**362**(9):2957-2961
- [22] Neuse EW. Macromolecular ferrocene compounds as cancer drug models. *Journal of Inorganic and Organometallic Polymers and Materials*. 2005;**15**(1):3-31
- [23] Fiorina VJ, Dubois RJ, Brynes S. Ferrocenyl polyamines as agents for the chemoimmunotherapy of cancer. *Journal of Medicinal Chemistry*. 1978;**21**(4):393-395
- [24] Sacht C, Datt M. Synthesis and characterisation of mixed-ligand platinum (II)-sulfoxide complexes, [PtCl (DMSO)(L)], for potential use as chemotherapeutic agents (HL= N, N-dialkyl-N'-(3-R-benzoyl) thiourea). *Polyhedron*. 2000;**19**(11):1347-1354
- [25] Osella D et al. On the mechanism of the antitumor activity of ferrocenium derivatives. *Inorganica Chimica Acta*. 2000;**306**(1):42-48
- [26] Abd-Elzaher MM, Hegazy WH, Gaafar AEDM. Synthesis, characterization and biological studies of ferrocenyl complexes containing thiophene moiety. *Applied Organometallic Chemistry*. 2005;**19**(8):911-916
- [27] Lal B et al. Miscellaneous applications of ferrocene-based peptides/amides. *Applied Organometallic Chemistry*. 2011;**25**(12):843-855
- [28] Neidle S. 3 the molecular basis for the action of some DNA-binding drugs. In: *Progress in Medicinal Chemistry*. Elsevier; 1979. p. 151-221
- [29] Pigeon P et al. The replacement of a phenol group by an aniline or acetanilide group enhances the cytotoxicity of 2-ferrocenyl-1, 1-diphenyl-but-1-ene compounds against breast cancer cells. *Journal of Organometallic Chemistry*. 2009;**694**(6):895-901
- [30] Yavuz S, Yildirim H. Ferrocene derivatives carrying urea, thiourea, and sulfonamide moieties: Synthesis and evaluation of antibacterial and antifungal activities. *Journal of Chemistry*. 2013;**2013**
- [31] Khan KM et al. Unsymmetrically disubstituted urea derivatives: A potent class of antiglycating agents. *Bioorganic & Medicinal Chemistry*. 2009;**17**(6):2447-2451
- [32] Li H-Q et al. Urea derivatives as anticancer agents. *Anti-Cancer Agents in Medicinal Chemistry (Formerly Current Medicinal Chemistry-Anti-Cancer Agents)*. 2009;**9**(4):471-480
- [33] Fan E et al. Molecular recognition: Hydrogen-bonding receptors that function in highly competitive solvents. *Journal of the American Chemical Society*. 1993;**115**(1):369-370
- [34] Otón F et al. Ferrocene-based ureas as multisignaling receptors for anions.

The Journal of Organic Chemistry.
2006;**71**(12):4590-4598

[35] Otón F et al. Heteroditopic ferrocene-based ureas as receptors for anions and cations. Dalton Transactions. 2006;**0**(30):3685-3692

[36] Hay BP, Firman TK, Moyer BA. Structural design criteria for anion hosts: Strategies for achieving anion shape recognition through the complementary placement of urea donor groups. Journal of the American Chemical Society. 2005;**127**(6):1810-1819

[37] Pratt MD, Beer PD. Anion recognition and sensing by mono- and bis-urea substituted ferrocene receptors. Polyhedron. 2003;**22**(5):649-653

[38] Asghar F et al. Bioactivity of new ferrocene incorporated N, N'-disubstituted ureas: Synthesis, structural elucidation and DFT study. Inorganica Chimica Acta. 2016;**439**:82-91

[39] Saeed A et al. Synthesis, crystal X-ray diffraction structure, vibrational properties and quantum chemical calculations on 1-(4-(4-Fluorobenzamido) phenyl)-3-(4-fluorobenzoyl) thiourea. Journal of Molecular Structure. 2010;**984**(1):240-245

[40] Lal B et al. Synthesis, Crystal structure, spectral and electrochemical characterization, DNA binding and antioxidant studies of 1-(2-fluorobenzoyl)-3-(2-chloro, 4-ferrocenylphenyl) thiourea. International Journal of Electrochemical Science. 2016;**11**:1632-1639

[41] Lv P-C et al. Synthesis and biological evaluation of pyrazole derivatives containing thiourea skeleton as anticancer agents. Bioorganic & Medicinal Chemistry. 2010;**18**(13):4606-4614

[42] Li H-Q et al. Synthesis and structure-activity relationships of N-benzyl-N-(X-2-hydroxybenzyl)-N'-phenylureas and thioureas as antitumor agents. Bioorganic & Medicinal Chemistry. 2010;**18**(1):305-313

[43] Altaf AA. Synthesis, Characterization and Biological Studies of Ferrocenyl Ureas & Thioureas. Quaid-i-Azam University Islamabad; 2012

[44] Atwood JL, Steed JW. Encyclopedia of Supramolecular Chemistry. Vol. 1. CRC Press; 2004

[45] Dunitz JD. Thoughts on Crystals as Supermolecules. Vol. 2. JM Lehn; 1996

[46] Jouaiti A, Hosseini MW, Kyritsakas N. Molecular tectonics: Design of 1-D coordination networks based on pyrene-bearing pyrazolyl units. European Journal of Inorganic Chemistry. 2003;**2003**(1):57-61

[47] Desiraju GR. The Crystal as a Supramolecular Entity. Vol. 18. John Wiley & Sons; 2008

[48] Lehn J-M. From supramolecular chemistry towards constitutional dynamic chemistry and adaptive chemistry. Chemical Society Reviews. 2007;**36**(2):151-160

[49] Lehn J-M. Towards complex matter: Supramolecular chemistry and self-organization. European Review. 2009;**17**(2):263-280

[50] Stang PJ, Olenyuk B. Self-assembly, symmetry, and molecular architecture: Coordination as the motif in the rational design of supramolecular metallacyclic polygons and polyhedra. Accounts of Chemical Research. 1997;**30**(12):502-518

[51] Ward MD. Design of crystalline molecular networks with charge-assisted hydrogen bonds. Chemical Communications. 2005;**0**(47):5838-5842

- [52] Custelcean R. Crystal engineering with urea and thiourea hydrogen-bonding groups. *Chemical Communications*. 2008;**0**(3):295-307
- [53] Crawford PC et al. Synthetic crystallography: Synthon mimicry and tecton elaboration in metallate anion salts. *CrystEngComm*. 2004;**6**(70):419-428
- [54] Lortie F, Boileau S, Bouteiller L. N, N'-disubstituted ureas: Influence of substituents on the formation of supramolecular polymers. *Chemistry—A European Journal*. 2003;**9**(13):3008-3014
- [55] de Loos M et al. Tripodal tris-urea derivatives as gelators for organic solvents. *European Journal of Organic Chemistry*. 2000;**2000**(22):3675-3678
- [56] Custelcean R et al. Anion coordination in metal–organic frameworks functionalized with urea hydrogen-bonding groups. *Crystal Growth & Design*. 2006;**6**(2):555-563
- [57] Pratt RC et al. Exploration, optimization, and application of supramolecular thiourea–amine catalysts for the synthesis of lactide (co) polymers. *Macromolecules*. 2006;**39**(23):7863-7871
- [58] Dove AP et al. Thiourea-based bifunctional organocatalysis: Supramolecular recognition for living polymerization. *Journal of the American Chemical Society*. 2005;**127**(40):13798-13799
- [59] Dannecker W, Kopf J, Rust H. N, N'-Diphenylurea, C₁₃H₁₂N₂O. *Crystal Structure Communications*. 1979;**8**(2):429-432
- [60] Lal B et al. Synthesis, characterization and antitumor activity of new ferrocene incorporated N, N'-disubstituted thioureas. *Dalton Transactions*. 2012;**41**(48):14643-14650
- [61] Javed F et al. New supramolecular ferrocenyl amides: Synthesis, characterization, and preliminary DNA-binding studies. *Journal of Coordination Chemistry*. 2012;**65**(6):969-979
- [62] Westwood J et al. Binding and electrochemical recognition of barbiturate and urea derivatives by a regioisomeric series of hydrogen-bonding ferrocene receptors. *Organometallics*. 2004;**23**(5):946-951
- [63] Heo J, Mirkin CA. Pseudo-allosteric recognition of mandelic acid with an enantioselective coordination complex. *Angewandte Chemie*. 2006;**118**(6):955-958
- [64] Abbott AP et al. Electrochemical recognition of chiral species using quaternary ammonium binaphthyl salts. *Analytical Chemistry*. 2002;**74**(16):4002-4006
- [65] Dai Z, Xu X, Canary JW. Rigidified tripodal chiral ligands in the asymmetric recognition of amino compounds. *Chirality*. 2005;**17**(S1):S227-S233
- [66] Willener Y et al. An exploration of ferrocenyl ureas as enantioselective electrochemical sensors for chiral carboxylate anions. *The Journal of Organic Chemistry*. 2008;**73**(4):1225-1233
- [67] Sahoo BK et al. Studies on the interaction of diacetylcurcumin with calf thymus-DNA. *Chemical Physics*. 2008;**351**(1-3):163-169
- [68] Asghar F et al. Facile synthesis of fluoro, methoxy, and methyl substituted ferrocene-based urea complexes as potential therapeutic agents. *Bioorganic Chemistry*. 2017;**72**:215-227
- [69] Tjahjono DH et al. Cationic porphyrins bearing diazolum rings: Synthesis and their interaction with calf thymus DNA. *Biochimica et Biophysica Acta (BBA)-General Subjects*. 1999;**1472**(1-2):333-343

- [70] Strekowski L, Wilson B. Noncovalent interactions with DNA: An overview. *Mutation Research/ Fundamental and Molecular Mechanisms of Mutagenesis*. 2007;**623**(1):3-13
- [71] He X-Q et al. Synthesis, characterization and DNA-binding studies on La (III) and Ce (III) complexes containing ligand of N-phenyl-2-pyridinecarboxamide. *Spectrochimica Acta Part A: Molecular and Biomolecular Spectroscopy*. 2007;**68**(1):184-190
- [72] Verheijen JC et al. Transition metal derivatives of peptide nucleic acid (PNA) oligomers synthesis, characterization, and DNA binding. *Bioconjugate Chemistry*. 2000;**11**(6):741-743
- [73] Cowan DO et al. Organic solid state. VIII. Mixed-valence ferrocene chemistry. *Accounts of Chemical Research*. 1973;**6**(1):1-7
- [74] Kashanian S et al. Interaction of diazinon with DNA and the protective role of selenium in DNA damage. *DNA and Cell Biology*. 2008;**27**(6):325-332
- [75] Sun Y et al. The potential trauma of three kinds of carbamate pesticides to DNA. *Journal of Agro-environment Science*. 2004;**23**(3):464-466
- [76] Top S et al. Studies on organometallic selective estrogen receptor modulators (SERMs) dual activity in the hydroxy-ferrocifen series. *Journal of Organometallic Chemistry*. 2001;**637**:500-506
- [77] Liu J-Z et al. Synthesis and in vitro study of pseudo-peptide thioureas containing α -aminophosphonate moiety as potential antitumor agents. *European Journal of Medicinal Chemistry*. 2010;**45**(11):5108-5112
- [78] Bian C-L et al. Voltammetric studies of the interaction of rutin with DNA and its analytical applications on the MWNTs-COOH/Fe₃O₄ modified electrode. *Sensors and Actuators B: Chemical*. 2011;**156**(2):615-620
- [79] Ibrahim M. Voltammetric studies of the interaction of nogalamycin antitumor drug with DNA. *Analytica Chimica Acta*. 2001;**443**(1):63-72
- [80] Raman N, Pothiraj K, Baskaran T. DNA interaction, antimicrobial, electrochemical and spectroscopic studies of metal (II) complexes with tridentate heterocyclic Schiff base derived from 2'-methylacetoacetanilide. *Journal of Molecular Structure*. 2011;**1000**(1-3):135-144
- [81] Ali S et al. Ferrocene-based bioactive bimetallic thiourea complexes: Synthesis and spectroscopic studies. *Bioinorganic Chemistry and Applications*. 2015;**2015**
- [82] Asghar F et al. Synthesis, structural characterization, DNA binding and antioxidant potency of new ferrocene incorporated acyl ureas. *Journal of Organometallic Chemistry*. 2015;**797**:131-139
- [83] Gul R et al. Ferrocene-based guanidine derivatives: In vitro antimicrobial, DNA binding and docking supported urease inhibition studies. *European Journal of Medicinal Chemistry*. 2014;**85**:438-449
- [84] Namasivayam V, Günther R. PSO@AUTODOCK: A fast flexible molecular docking program based on swarm intelligence. *Chemical Biology & Drug Design*. 2007;**70**(6):475-484
- [85] Hussain RA et al. Synthesis, chemical characterization, DNA binding and antioxidant studies of ferrocene incorporated selenourea. *Journal of Molecular Structure*. 2013;**1048**:367-374
- [86] Österberg F et al. Automated docking to multiple target structures:

Incorporation of protein mobility and structural water heterogeneity in AutoDock. *Proteins: Structure, Function, and Bioinformatics*. 2002;**46**(1):34-40

[87] El Hadji Mamour Sakho EA, Oluwafemi OS. Dynamic light scattering (DLS). In: *Thermal and Rheological Measurement Techniques for Nanomaterials Characterization*. Vol. 3. 2017. p. 37

[88] Ferré-D'Amaré AR, Burley SK. Use of dynamic light scattering to assess crystallizability of macromolecules and macromolecular assemblies. *Structure*. 1994;**2**(5):357-359

[89] Caballero A et al. Electroactive thiazole derivatives capped with ferrocenyl units showing charge-transfer transition and selective ion-sensing properties: A combined experimental and theoretical study. *Inorganic Chemistry*. 2007;**46**(3):825-838

[90] Arjmand F, Sayeed F, Muddassir M. Synthesis of new chiral heterocyclic Schiff base modulated Cu (II)/Zn (II) complexes: Their comparative binding studies with CT-DNA, mononucleotides and cleavage activity. *Journal of Photochemistry and Photobiology B: Biology*. 2011;**103**(2):166-179

Section 2

Photochemical,
Photocatalysis and
Applications

CO₂ Reduction Characteristics of Cu/TiO₂ with Various Reductants

Akira Nishimura

Abstract

Cu-doped TiO₂ (Cu/TiO₂) film photocatalyst was prepared by combination of sol-gel and dip-coating process and pulse arc plasma method. The effect of Cu/TiO₂ photocatalyst on CO₂ reduction performance with reductants of H₂O and H₂ or NH₃ was investigated. In addition, the overlapping two Cu/TiO₂ coated on netlike glass discs were also investigated. The CO₂ reduction performance of Cu/TiO₂ film was tested under illumination of Xe lamp with or without ultraviolet (UV) light, respectively. As to the condition of CO₂/H₂/H₂O, the best CO₂ reduction performance has been achieved under the condition of CO₂/H₂/H₂O = 1:0.5:0.5 with UV light illumination as well as without UV light illumination. The theoretical molar ratio of CO₂/H₂O or CO₂/H₂ to produce CO is 1:1. Since the molar ratio of CO₂/H₂/H₂O = 1:0.5:0.5 can be regarded as the molar ratio of CO₂/total reductants = 1:1, it is believed that the results of this study follow the reaction scheme of CO₂/H₂O and CO₂/H₂. On the other hand, as to the condition of CO₂/NH₃/H₂O, the best CO₂ reduction performance has been achieved under the condition of CO₂/H₂/H₂O = 1:1:1 with UV light illumination as well as without UV light illumination.

Keywords: CO₂ reduction, Cu/TiO₂ photocatalyst, reductants combination, visible light, overlapping effect

1. Introduction

Paris Agreement adopted in 2015 sets the goal that the increase in average temperature in the world from the industrial revolution by 2030 should be kept less than 2 K. However, due to the increase in the averaged concentrations of CO₂ in the atmosphere to 410 ppmV in December 2019 [1], CO₂ reduction or utilization technologies to recycle CO₂ are urgently required.

There are six vital CO₂ conversions: chemical conversions, electrochemical reductions, biological conversions, reforming, inorganic conversions, and photochemical reductions [2, 3]. Recently, artificial photosynthesis or the photochemical reduction of CO₂ to fuel has become an attractive route due to its economically and environmentally friendly behavior [2].

The application of CO₂ as a raw material can produce chemicals and energy to diminish the CO₂ accumulation in the atmosphere [2]. If we consider energy producing possibilities, one possibility is the photochemical conversion of CO₂ into value-added chemicals which could be used as fuel [4].

The most widely used photocatalyst for the photocatalytic reactions is TiO₂ due to its availability, chemical stability, low cost, and resistance to corrosion [5]. It is

well known that CO₂ can be reduced into fuels, e.g., CO, CH₄, CH₃OH, H₂, etc. by using TiO₂ as the photocatalyst under ultraviolet (UV) light illumination [6–9]. However, pure TiO₂ has the limitation. It is only active when irradiated by UV light, which is not effective under sunlight. Since the solar spectrum only consists of about 4% of UV light, sunlight is not able to activate the TiO₂ effectively for photocatalytic reaction. In addition, TiO₂ has a high electron/hole pair recombination rate compared to the rate of chemical interaction with the absorbed species for redox reactions [10].

Recently, studies on CO₂ photochemical reduction by TiO₂ have been carried out from the viewpoint of performance promotion by extending absorption wavelength toward visible region. It was reported that a transition metal doping is useful technique for extending the absorbance of TiO₂ into the visible region [11–15]. Noble metal doping such as Pt, Pd, Au and Ag [11], Au, Pd-three dimensionally ordered macroporous TiO₂ [12], composition materials formed by GaP and TiO₂ [13], nanocomposite CdS/TiO₂ combining two different band gap photocatalysts [14], and carbon-based AgBr nanocomposited TiO₂ [15], had been attempted to overcome the shortcomings of the pure TiO₂. They could improve the CO₂ reduction performance; however, the concentrations in the products achieved in all the attempts so far were still low, ranging from 1 to 150 μmol/g-cat [11–16].

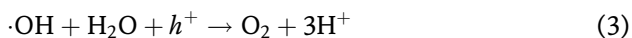
Though various metals have been used for doping [11–16], Cu is considered as a favorite candidate. Cu can extend the absorption band to 600–800 nm [17, 18], which covers the whole visible light range. Cu-decorated TiO₂ nanorod thin film performed 10 times yield as large as TiO₂ for C₂H₅OH production [19]. Cu-loaded N/TiO₂ also showed the good performance which yielded eight times as large as TiO₂ for CH₄ production [20]. Noble metals such as Pt and Au are too expensive to be used in industrial scale. Therefore, Cu is the best candidate because of its high efficiency and low cost compared to noble metals. Due to its availability as well as above described characteristics, Cu is selected as the dopant in this study.

Since a reductant is necessary for CO₂ reduction to produce fuel; H₂O and H₂ are usually used as reductants according to the review papers [7, 9]. To promote the CO₂ reduction performance of photocatalyst, it is important to select the optimum reductant which provides the proton (H⁺) for the reaction scheme of CO₂ reduction with H₂O is as follows [21–23]:

<Photocatalytic reaction>



<Oxidization>



<Reduction>



The reaction scheme of CO₂ reduction with H₂ is as follows [24]:

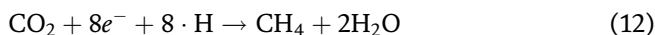
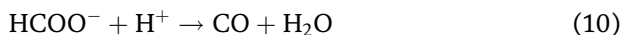
<Photocatalytic reaction>



<Oxidization>



<Reduction>



The reaction scheme to reduce CO₂ with NH₃ can be summarized as shown below [24, 25]:

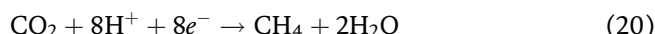
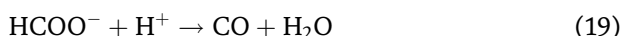
<Photocatalytic reaction>



<Oxidization>



<Reduction>



There are some reports on CO₂ reduction with either H₂O or H₂ [7, 9]. However, the effect of using H₂O and H₂ or NH₃ together as reductants is not investigated well. Though a few studies using pure TiO₂ under CO₂/H₂/H₂O condition were reported [24, 26], the effect of ratio of CO₂, H₂ and H₂O or NH₃ as well as the effect of Cu doping with TiO₂ on CO₂ reduction performance of photocatalyst were not investigated previously.

Consequently, the purpose of this chapter is to clarify the effect of molar ratio of CO₂ to H₂O and H₂ or NH₃ on the performance of CO₂ reduction with Cu/TiO₂. The CO₂ reduction performance with H₂O and H₂ or NH₃ using Cu/TiO₂ coated on netlike glass fiber as photocatalyst under the condition of illuminating Xe lamp with or without UV light was investigated. Cu is loaded on TiO₂-coated netlike glass fiber by pulse arc plasma method which can emit nanosized Cu particles by applying high electron potential difference. The amount of loaded Cu can be controlled by the pulse number. Cu/TiO₂ prepared was characterized by Scanning Electron Microscope (SEM) and Electron Probe Micro Analyzer (EPMA), Transmission Electron Microscope (TEM), Energy Dispersive X-ray Spectrometry (EDX), and Electron Energy Loss Spectrum (EELS) analysis. The CO₂ reduction performance with H₂O and H₂ or NH₃ under the condition of illuminating Xe lamp with or without UV

light was investigated. The molar ratio of $\text{CO}_2/\text{H}_2/\text{H}_2\text{O}$ was changed for 1:1:1, 1:0.5:1, 1:1:0.5, 1:0.5:0.5 to clarify the optimum combination of $\text{CO}_2/\text{H}_2/\text{H}_2\text{O}$ for CO_2 reduction with Cu/TiO_2 . According to the reaction scheme to reduce CO_2 with H_2O or NH_3 as shown above, the theoretical molar ratio of $\text{CO}_2/\text{H}_2\text{O}$ to produce CO or CH_4 is 1:1 or 1:4, respectively, while that of CO_2/NH_3 to produce CO or CH_4 is 3:2, 3:8, respectively. Therefore, this study assumes that the molar ratio of $\text{CO}_2/\text{NH}_3/\text{H}_2\text{O} = 3:2:3$ and $3:8:12$ are theoretical molar ratio to produce CO and CH_4 , respectively. Moreover, the effect of overlapping two layers of Cu/TiO_2 -coated netlike glass fiber on CO_2 reduction performance with H_2 and H_2O was investigated.

2. Experiment

2.1 Preparation of Cu/TiO_2 film

The combination of sol-gel and dip-coating process was used for preparing TiO_2 film. TiO_2 sol solution was made by mixing $[(\text{CH}_3)_2\text{CHO}]_4\text{Ti}$ (purity of 95 wt%, Nacalai Tesque Co.) of 0.3 mol, anhydrous $\text{C}_2\text{H}_5\text{OH}$ (purity of 99.5 wt%, Nacalai Tesque Co.) of 2.4 mol, distilled water of 0.3 mol, and HCl (purity of 35 wt%, Nacalai Tesque Co.) of 0.1 mol. Netlike glass fiber was cut like a disc, and its diameter and thickness were 50 mm and 1 mm, respectively. The netlike glass fiber disc was dipped into TiO_2 sol solution at the speed of 1.5 mm/s and pulled up at the fixed speed of 0.2 mm/s. Then, it was dried out and fired under the controlled firing temperature (FT) and firing duration time (FD), resulting that TiO_2 film was fastened on the netlike glass fiber. FT and FD were set at 623 K and 180 s, respectively. Cu was loaded on TiO_2 film by pulse arc plasma method. The pulse arc plasma gun device (ULVAC, Inc., ARL-300) having Cu electrode whose diameter was 10 mm was applied for Cu loading. After the netlike glass fiber coated with TiO_2 was set in chamber of the pulse arc plasma gun device which was vacuumed, the nanosized Cu particles were emitted from Cu electrode with applying the electrical potential difference of 200 V. The pulse arc plasma gun can evaporate Cu particle over the target in the circle area whose diameter is 100 mm when the distance between Cu electrode and the target is 160 mm. Since the difference between Cu electrode and TiO_2 film was 150 nm in the present study, Cu particle can be evaporated over TiO_2 film uniformly. The amount of loaded Cu was controlled by the pulse number. In the present study, the pulse number was set at 100. Since the netlike glass fiber is transparent, the light can pass through the netlike glass fiber. The present study has also investigated if two layers of two Cu/TiO_2 coated on netlike glass fiber put on the top of the other (with certain distance, i.e., overlapping), what impact/improvement would be on the CO_2 reduction performance. The overlapping two layers of Cu/TiO_2 coated on netlike glass fiber is expected to utilize the light effectively as well as to increase the amount of photocatalyst used for CO_2 reduction.

2.2 Characterization of Cu/TiO_2 film

The structure and crystallization characteristics of Cu/TiO_2 film were evaluated by SEM (JXS-8530F, JEOL Ltd.), EPMA (JXA-8530F, JEOL Ltd.), TEM (JEM-2100/HK, JEOL Ltd.), EDX (JEM-2100F/HK, JEOL Ltd.), and EELS (JEM-ARM2007 Cold, JEOL Ltd.). Since these measurement instruments use electron for analysis, the sample should be an electron conductor. Since netlike glass disc was not an electron for analysis, the carbon vapor deposition was conducted by the dedicated device (JEE-420, JEOL Ltd.) for Cu/TiO_2 coated on netlike glass disc before analysis. The thickness of carbon deposited on sample was approximately 20–30 nm.

The electron probe emits the electrons to the sample under the acceleration voltage of 15 kV and the current of 3.0×10^{-8} A, when the surface structure of sample is analyzed by SEM. The characteristic X-ray is detected by EPMA at the same time, resulting that the concentration of channel element is analyzed according to the relationship between the characteristic X-ray energy and the atomic number. The spatial resolutions of SEM and EPMA are 10 μ m. The EPMA analysis helps not only to understand the coating state of prepared photocatalyst but also to measure the amount of doped metal within TiO₂ film on the base material.

The electron probe emits the electron to the sample under the acceleration voltage of 200 kV, when the inner structure of sample is analyzed by TEM. The size, thickness, and structure of loaded Cu were evaluated. The characteristic X-ray is detected by EDX at the same time, resulting that the concentration distribution of chemical element toward thickness direction of the sample is analyzed. In the present study, the concentration distribution of Ti and Cu were analyzed.

EELS can be applied not only for element detection but also determination of oxidation states of some transition metals. The EELS characterization was performed by JEM-ARM200F equipped with GIF Quantum having 2048 ch. The dispersion of 0.5 eV/ch can be achieved for the full width at half maximum of the zero loss peak.

2.3 CO₂ reduction experiment

Figure 1 [27, 28] shows the experimental set-up of the reactor composing of stainless tube (100 mm (H.) \times 50 mm (I.D.)), Cu/TiO₂ film coated on netlike glass disc (50 mm (D.) \times 1 mm (t.)) located on the Teflon cylinder (50 mm (H.) \times 50 mm (D.)), a quartz glass disc (84 mm (D.) \times 10 mm (t.)), a sharp cut filter cutting off the light whose wavelength is below 400 nm (SCF-49.5C-42 L, SIGMA KOKI CO. LTD.), a 150 W Xe lamp (L2175, Hamamatsu Photonics K. K.), mass flow controller, and CO₂ gas cylinder. The volume of reactor to charge CO₂ is 1.3×10^{-4} m³. The light of Xe lamp which is located inside the stainless tube illuminates Cu/TiO₂ film coated on the netlike glass disc through the sharp cut filter and the quartz glass disc that are at the top of the stainless tube. The wavelength of light from Xe lamp is ranged from 185 to 2000 nm. Since the sharp cut filter can remove UV components of the light from the Xe lamp, the wavelength of light from Xe lamp is ranged from 401 to 2000 nm with the filter. **Figure 2** [29] shows the performance of the sharp cut filter to cut off the wavelength is below 400 nm. The

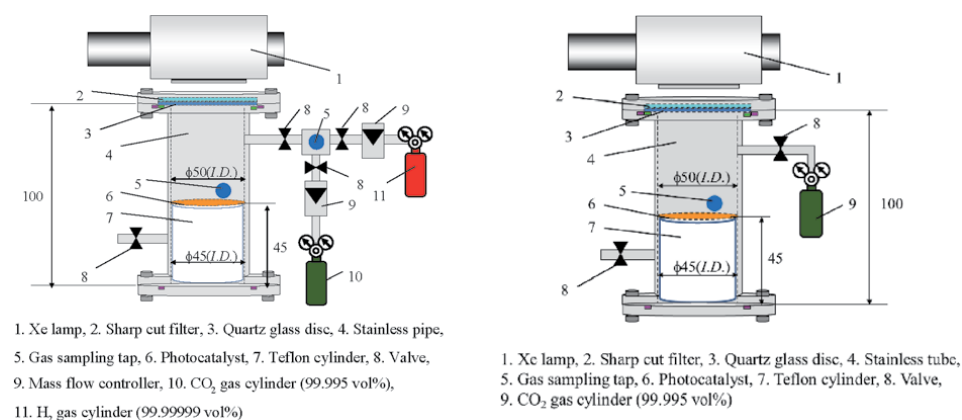


Figure 1. Schematic drawing of CO₂ reduction experimental set-up (left: CO₂/H₂/H₂O system; right: CO₂/NH₃/H₂O system).

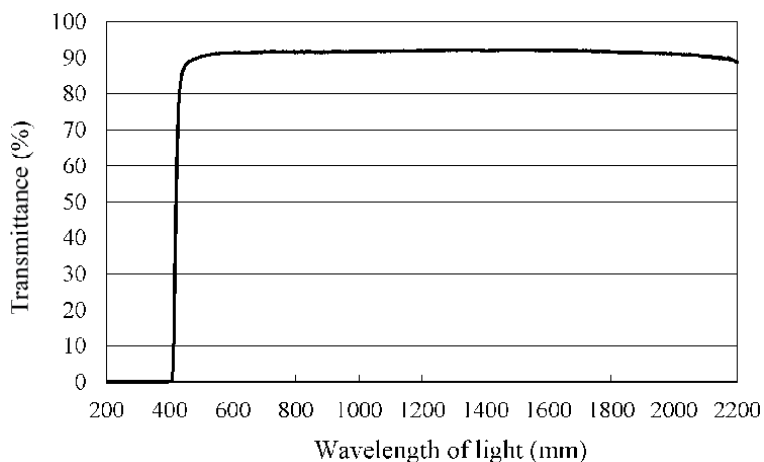


Figure 2.
Light transmittance data of sharp cut filter.

average light intensity of Xe lamp without and with the sharp cut filter is 58.2 and 33.8 mW/cm², respectively.

In the CO₂ reduction experiment with H₂ and H₂O, CO₂ gas with the purity of 99.9 vol% which were controlled by mass flow controller was mixed in the buffer chamber and introduced into the reactor which was pre-vacuumed by a vacuum pump. The mixing ratio of CO₂ and H₂ was confirmed by TCD gas chromatograph (Micro GC CP4900, GL Science) before introducing into the reactor. After confirming the mixing ratio of CO₂ and H₂, the distilled water was injected into the reactor through a gas sampling tap by syringe and Xe lamp illumination was turned on the same time. The amount of injected water was measured and controlled by the syringe. The injected water vaporized completely in the reactor. The molar ratio of CO₂/H₂/H₂O was set at 1:1:1, 1:0.5:1, 1:1:0.5, 1:0.5:0.5. Due to the heat of Xe lamp, the temperature in reactor was attained at 343 K within an hour and kept an approximately 343 K during the experiment.

In the CO₂ reduction experiment with NH₃ and H₂O, after purging the reactor with CO₂ gas of 99.9 vol% purity introduced in the reactor, which was pre-vacuumed by a vacuum pump, for 15 minutes, the valves located at the inlet and the outlet of reactor were closed. After confirming the pressure and gas temperature in the reactor at 0.1 MPa and 298 K, respectively, the NH₃ aqueous solution (NH₃; 50 vol%), which was changed according to the planed molar ratio, was injected into the reactor through gas sampling tap, and Xe lamp illumination was turned on the same time. The NH₃ aqueous solution injected was vaporized completely in the reactor. Due to the heat of Xe lamp, the temperature in the reactor was attained at 343 K within an hour and kept at approximately 343 K during the experiment. The molar ratio of CO₂/NH₃/H₂O was set at 1:1:1, 1:0.5:1, 1:1:0.5, 1:0.5:0.5, 3:2:3, 3:8:12, respectively. The gas in the reactor was sampled every 24 hours during the experiment. The gas samples were analyzed by FID gas chromatograph (GC353B, GL Science). Minimum resolution of FID gas chromatograph and methanizer is 1 ppmV.

3. Results and discussion

3.1 Characterization analysis of Cu/TiO₂ film

Figure 3 shows SEM image of Cu/TiO₂ film coated on netlike glass disc [28]. The SEM image was taken at 1500 times magnification. **Figure 4** shows EPMA image of

Cu/TiO₂ film coated on netlike glass disc [28]. EPMA analysis was carried out for SEM images taken by 1500 times magnification. In EPMA image, the concentration of each element in observation area is indicated by the different colors. Light colors, for example, white, pink, and red indicate that the amount of element is large, while dark colors like black and blue indicate that the amount of element is small.

From these figures, it can be observed that TiO₂ film was coated on netlike glass fiber. During firing process, the temperature profile of TiO₂ solution adhered on the netlike glass disc was not even due to the different thermal conductivities of Ti and SiO₂. Their thermal conductivities of Ti and SiO₂ at 600 K are 19.4 and 1.8 W/(m·K) [30], respectively. Due to thermal expansion and shrinkage around netlike glass fiber, it can be considered that thermal crack is formed on the TiO₂ film.

In addition, it is observed from **Figure 4** that nanosized Cu particles are loaded on TiO₂ uniformly, resulted from that the pulse arc plasma method can emit nanosized Cu particles.

To evaluate the amount of loaded Cu within TiO₂ film quantitatively, the observation area, which is the center of netlike glass disc, of diameter of 300 μm is analyzed by EPMA. The ratio of Cu to Ti is counted by averaging the data obtained in this area. As a result, the weight percentages of elements of Cu and Ti in the Cu/TiO₂ film are 0.6 and 99.4 wt%, respectively.

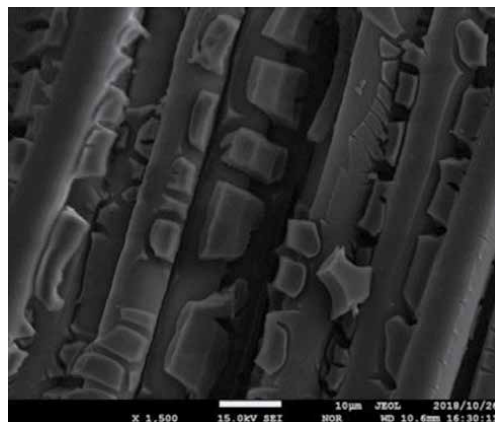


Figure 3.
SEM image of Cu/TiO₂ film coated on netlike glass disc.

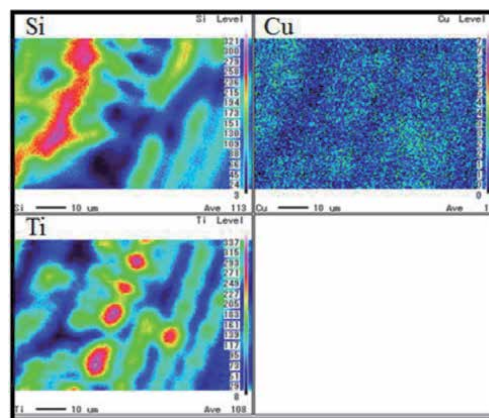


Figure 4.
EPMA image of Cu/TiO₂ film coated on netlike glass disc.

Figures 5 and 6 show TEM and EDX images of Cu/TiO₂ film, respectively [27]. ESX analysis was carried out using TEM image taken by 150,000 times magnification. According to **Figure 6**, it is observed that Cu particles are distributed in TiO₂ film. Though many Cu particles are loaded on the upside of TiO₂ film, it is not confirmed that the Cu layer is formed.

Figure 7 shows EELS spectra of Cu in Cu/TiO₂ film [27]. From this figure, the peaks at around 932 and 952 eV can be observed. Compared to the report investigating peaks of Cu, Cu₂O, and CuO [31], the EELS spectra of Cu₂O matches with **Figure 7**. Therefore, Cu in Cu/TiO₂ prepared in this study exists as Cu⁺ ion in Cu₂O. It was reported that the heterojunctions between CuO and TiO₂ contributed to the promotion of the photoactivity [32]. In addition, it was reported that Cu⁺ was more active than Cu²⁺ [33]. Therefore, it is expected that Cu⁺ would play a role to enhance the CO₂ reduction performance in this study. **Figure 8** shows EELS spectra of TiO₂ referred from EELS data base [34]. Comparing **Figure 8** with **Figure 7**, EELS spectra of TiO₂ is very different from EELS spectra of Cu in Cu/TiO₂.

3.2 Effect of molar ratio of CO₂, H₂, and H₂O on CO₂ reduction characteristics

Figures 9 and 10 show the concentration changes of CO and CH₄ produced in the reactor along the time under the illumination of Xe lamp with UV light,

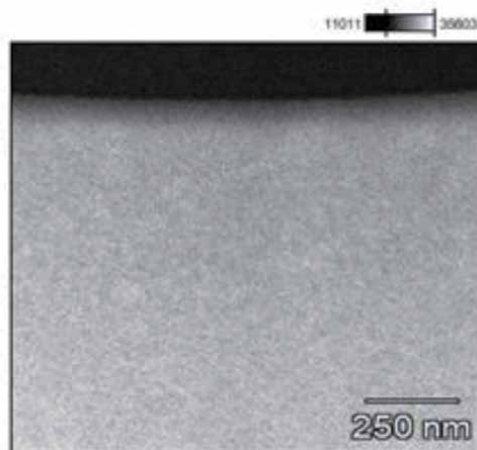


Figure 5.
TEM image of Cu/TiO₂ film.

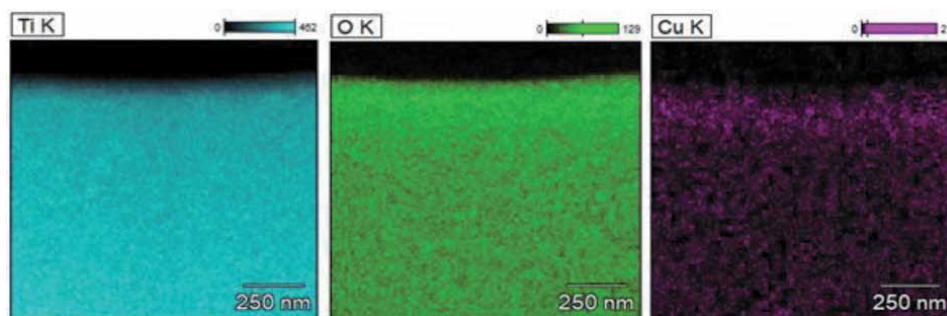


Figure 6.
EDX images of Cu/TiO₂ film.

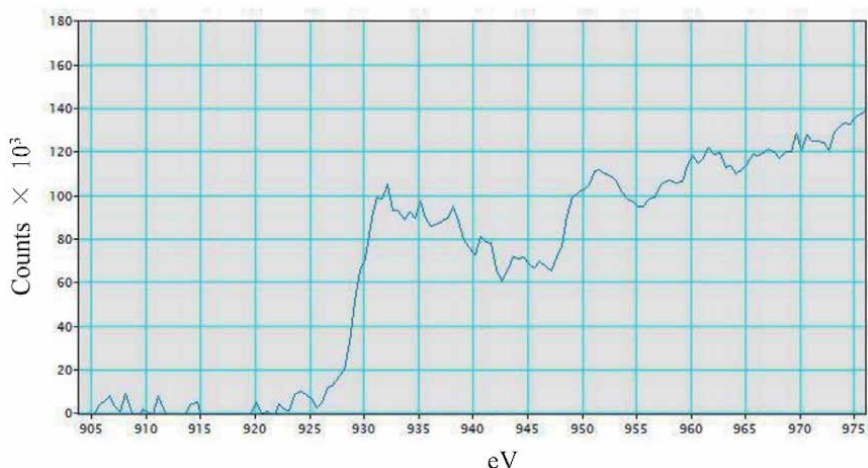


Figure 7.
 EELS spectra of Cu in Cu/TiO₂.

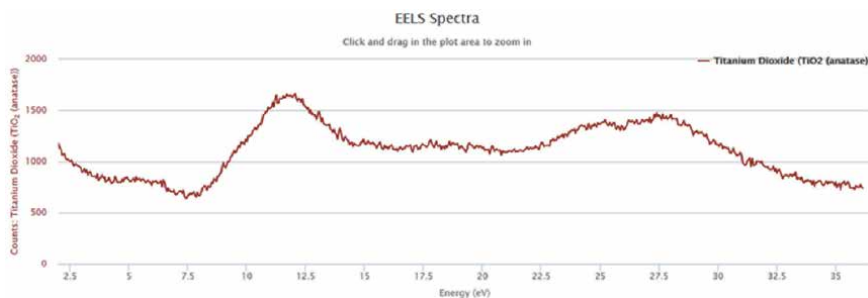


Figure 8.
 EELS spectra of TiO₂ referred from EELS data base [34].

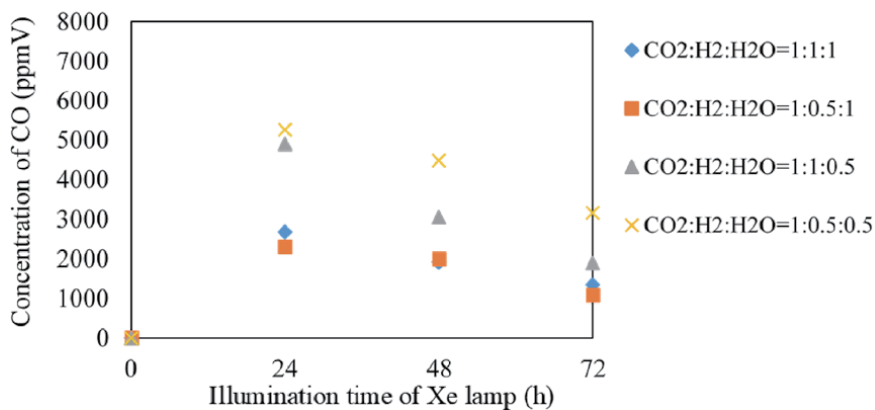


Figure 9.
 Change of concentration of CO with time for several molar ratios of CO₂/H₂/H₂O under illumination condition with UV light.

respectively. **Figures 11** and **12** show the molar quantities of CO and CH₄ per weight of photocatalyst in the reactor along the time under the illumination of Xe lamp with UV light, respectively. The amount of Cu/TiO₂ is 0.2 g. In this experiment, a blank test, that was running the same experiment without illumination of Xe lamp,

had been carried out to set up a reference case. No fuel was produced in the blank test as expected.

According to **Figures 9–12**, the CO₂ reduction performance is the highest for the molar ratio of CO₂/H₂/H₂O = 1:0.5:0.5. Since the reaction scheme of CO₂/H₂/H₂O is not fully understood, this study refers to the reaction scheme of CO₂/H₂O and CO₂/H₂ as shown by Eqs. (1)–(12). It is known from the reaction scheme that the theoretical molar ratio of CO₂/H₂O and CO₂/H₂ to produce CO is 1:1. On the other hand, the theoretical molar ratio of CO₂/H₂O and CO₂/H₂ to produce CH₄ is 1:4. Since the molar ratio of CO₂/H₂/H₂O = 1:0.5:0.5 can be regarded as the molar ratio of CO₂/total reductants = 1:1, it is believed that the results of this study follow the reaction scheme presented in Eqs. (1)–(12). Comparing the CO production with the CH₄ production, CO is produced first. According to Eq. (5), it is believed that some CO might be converted into CH₄. Therefore, the start of CH₄ production is slower than that of CO production. Producing CH₄ needs four times H⁺ and electrons as many as producing CO needs. Therefore, it is revealed that the optimum molar ratio

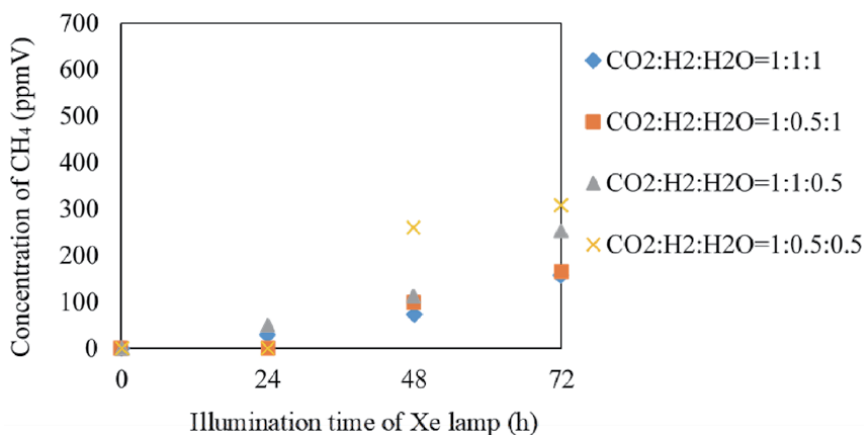


Figure 10. Change of concentration of CH₄ with time for several molar ratios of CO₂/H₂/H₂O under illumination condition with UV light.

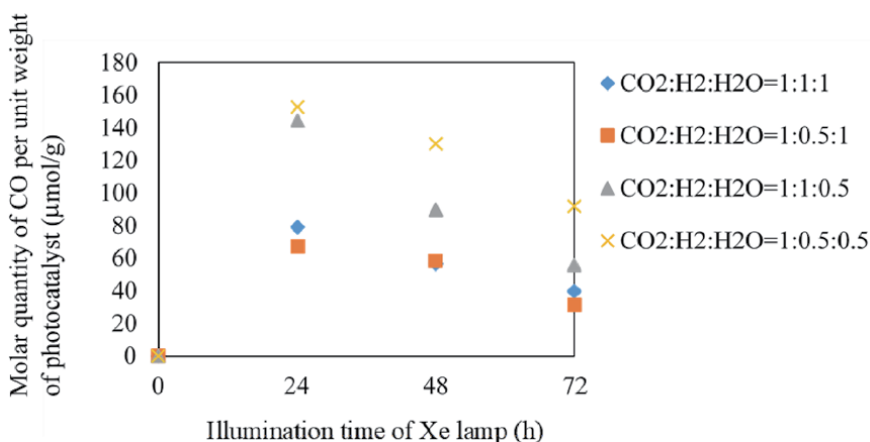


Figure 11. Change of molar quantity of CO per unit weight of photocatalyst with time for several molar ratios of CO₂/H₂/H₂O under illumination condition with UV light.

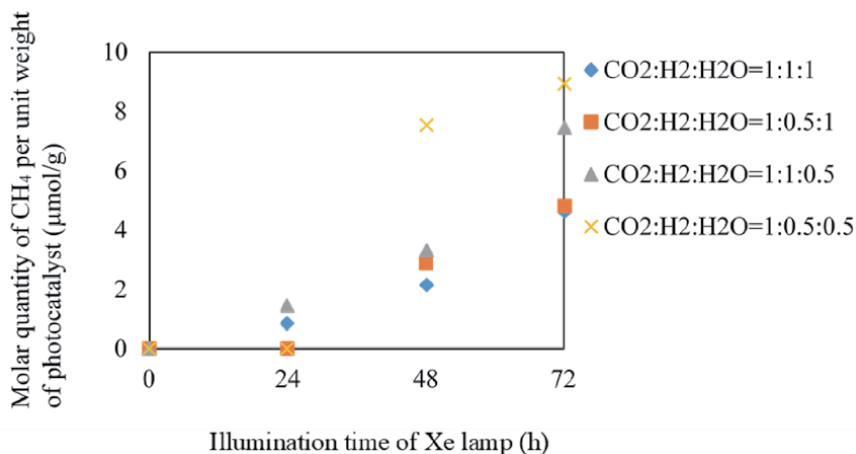


Figure 12. Change of molar quantity of CH₄ per unit weight of photocatalyst with time for several molar ratios of CO₂/H₂/H₂O under illumination condition with UV light.

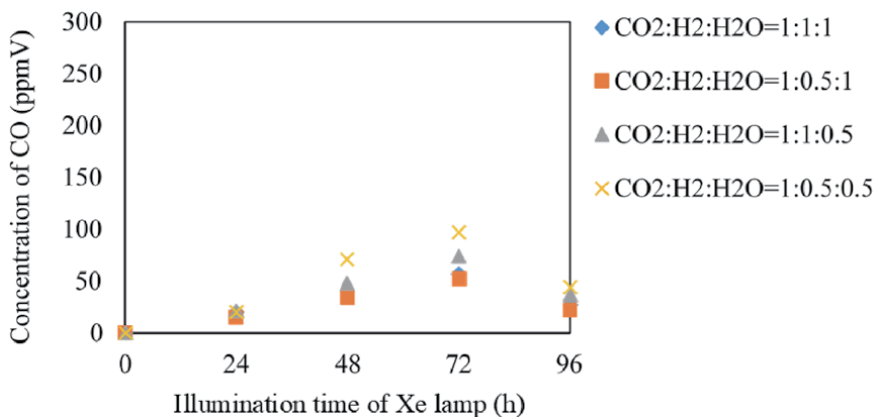


Figure 13. Change of concentration of CO with time for several molar ratios of CO₂/H₂/H₂O under illumination condition without UV light.

of CO₂/H₂/H₂O is decided by the CO production scheme. Though CO decreases after reaching the peak, CH₄ increases gradually.

According to Hinojosa-Reyes et al. [35], TiO₂ and Cu₂O formation leads to the photocatalytic activity since Cu₂O is a semiconductor with small band gap energy. In addition, Cu performs to avoid the electron and hole recombination and promotes the charge transfer. In this study, it seems that the effect of Cu and Cu₂O on photoactivity is performed.

Figures 13 and **14** show the concentration changes of CO produced and the molar quantity of CO per weight of photocatalyst in the reactor under the illumination of Xe lamp without UV light, respectively. In this experiment, CO is the only fuel produced from the reactions.

According to **Figures 13** and **14**, the CO₂ reduction performance is also the highest for the molar ratio of CO₂/H₂/H₂O = 1:0.5:0.5 in this case. It is considered that the same reaction mechanism as mentioned above is conducted. The CO₂ reduction performance of Cu/TiO₂ under the illumination condition without UV

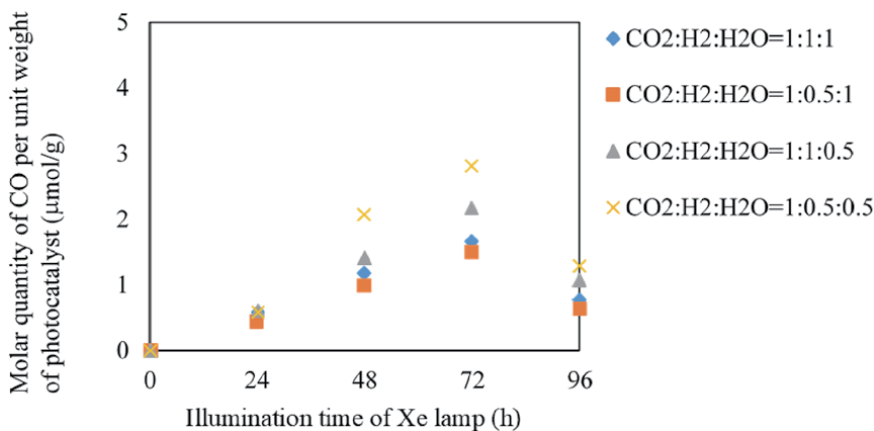


Figure 14. Change of molar quantity of CO per unit weight of photocatalyst with time for several molar ratios of CO₂/H₂/H₂O under illumination condition without UV light.

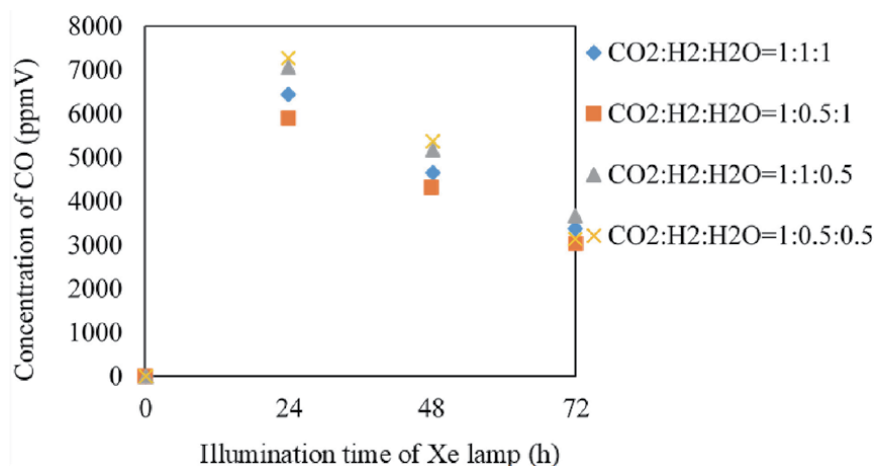


Figure 15. Change of concentration of CO for Cu/TiO₂ overlapped with time for several molar ratios of CO₂/H₂/H₂O under illumination condition with UV light.

light is lower than that under the illumination condition with UV light. Therefore, it can be claimed that Cu/TiO₂ obtains the main photoenergy from UV light.

3.3 Effect of overlapping of Cu/TiO₂ film with H₂ and H₂O on CO₂ reduction characteristics

Figures 15 and 16 show the concentration change of CO and CH₄ produced in the reactor under the illumination of Xe lamp with UV light, with two Cu/TiO₂ films coated on netlike glass discs overlapped, respectively. The photocatalyst is coated on both upper and lower surfaces of the top disc and only the upper surface of the bottom disc.

Figures 17 and 18 show the molar quantities of CO and CH₄ per weight of photocatalyst in the reactor along the time under the Xe lamp with UV light, respectively. The total amount of Cu/TiO₂ on two discs is 0.4 g.

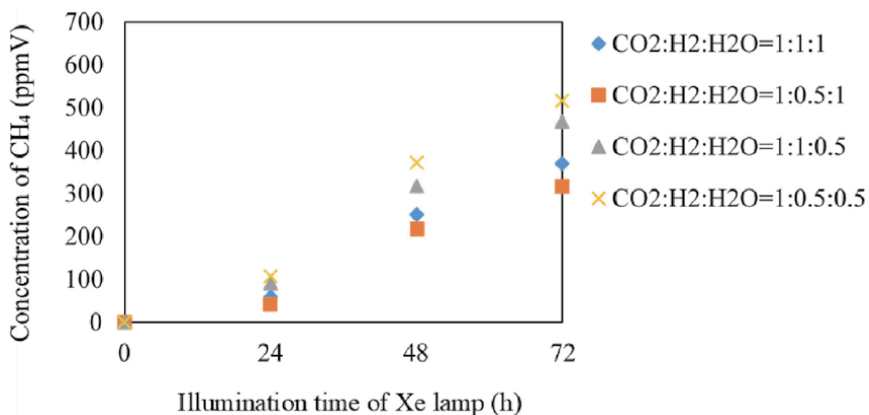


Figure 16. Change of concentration of CH₄ for Cu/TiO₂ overlapped with time for several molar ratios of CO₂/H₂/H₂O under illumination condition with UV light.

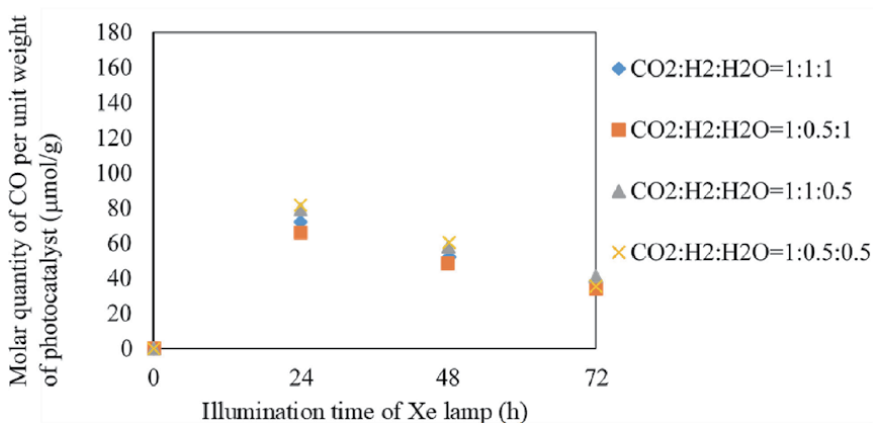


Figure 17. Change of molar quantity of CO per unit weight of photocatalyst for Cu/TiO₂ overlapped with time for several molar ratios of CO₂/H₂/H₂O under illumination condition with UV light.

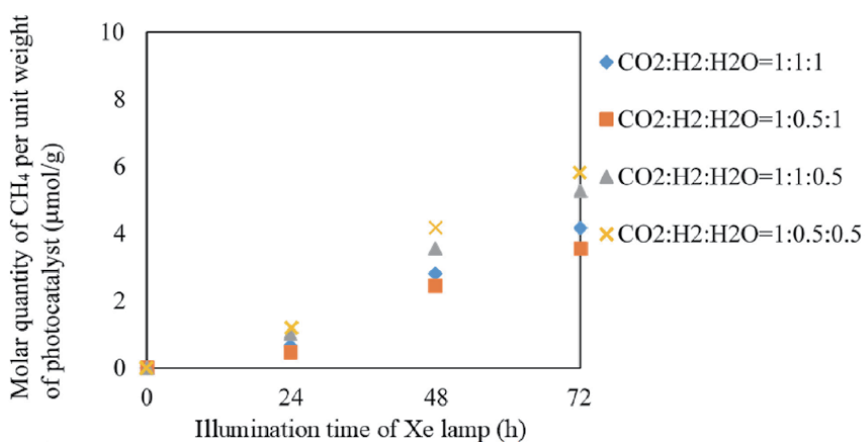


Figure 18. Change of molar quantity of CH₄ per unit weight of photocatalyst for Cu/TiO₂ overlapped with time for several molar ratios of CO₂/H₂/H₂O under illumination condition with UV light.

According to **Figures 15–18**, the CO₂ reduction performance is the highest for the molar ratio of CO₂/H₂/H₂O = 1:0.5:0.5, the same as that in the case of single Cu/TiO₂ disc. In addition, the order of CO₂ reduction performance of Cu/TiO₂ overlapped is the same as that of single Cu/TiO₂. However, comparing **Figures 15 and 16** with **Figures 9 and 10**, the concentrations of CO and CH₄ for two Cu/TiO₂ discs overlapped are higher than those for single Cu/TiO₂ disc under every molar ratio of CO₂/H₂/H₂O. The highest concentration of CO for Cu/TiO₂ overlapped is 7273 ppmV, which is 1.4 times as large as that for single Cu/TiO₂. On the other hand, the highest concentration of CH₄ for Cu/TiO₂ overlapped is 516 ppmV, which is 1.7 times as large as that for single Cu/TiO₂. In the case of two discs overlapped, the following things are believed: (i) the amount of photocatalyst used for photocatalysis reaction is increased, (ii) the electron transfer between two Cu/TiO₂ films promotes the activity of photocatalysis reaction, and (iii) the lower positioned Cu/TiO₂ disc utilizes the light passing through the top disc.

However, comparing **Figures 17 and 18** with **Figures 11 and 12**, the molar quantities of CO and CH₄ per weight of photocatalyst in two discs case are lower than those for single Cu/TiO₂ disc case under every molar ratio of CO₂/H₂/H₂O. The highest molar quantity of CO per weight of photocatalyst in two discs overlapped case is 82 μmol/g, which is 54% of that in single disc case. Similarly, the highest molar quantity of CH₄ per weight of photocatalyst in two discs overlapped case is 5.8 μmol/g, which is 65% of that in single disc case. The reasons of this result are considered to be: (i) some parts of the Cu/TiO₂ film on the lower positioned disc cannot receive the light, (ii) if the produced fuel remains in the space between two discs, the reactants of CO₂, H₂, and H₂O would be blocked to reach the surface of photocatalyst, resulting that the photochemical reaction could not be carried out well even though the light is illuminated for photocatalyst.

Figures 19 and 20 show the concentration changes of CO produced and the molar quantity of CO per weight of photocatalyst in the reactor with two overlapped Cu/TiO₂ film coated on netlike glass disc under the illumination of Xe lamp without UV light, respectively. In this experiment, CO is the only produced from the reactions.

According to **Figures 19 and 20**, the CO₂ reduction performance in two discs case is the highest for the molar ratio of CO₂/H₂/H₂O = 1:0.5:0.5 which is the same as

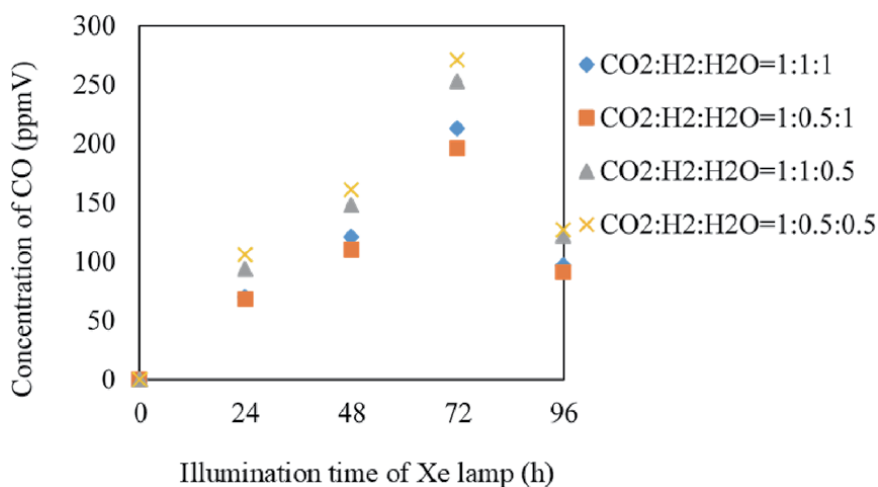


Figure 19. Change of concentration of CO for Cu/TiO₂ overlapped with time for several molar ratios of CO₂/H₂/H₂O under illumination condition without UV light.

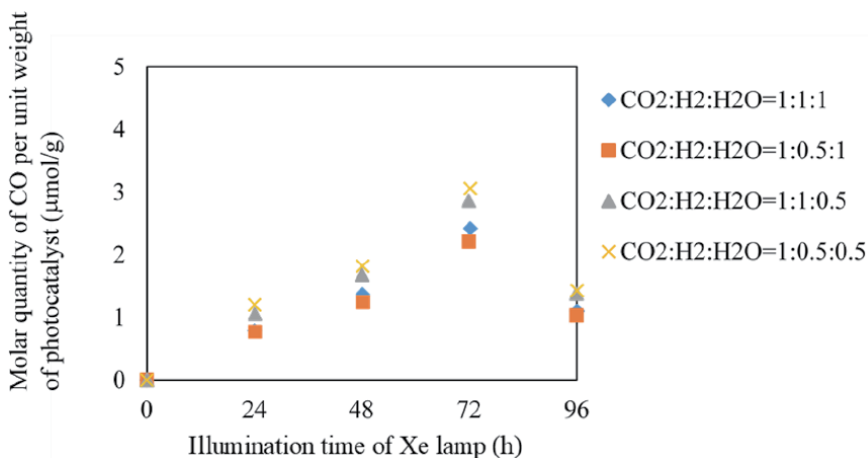


Figure 20. Change of molar quantity of CO per unit weight of photocatalyst for Cu/TiO₂ overlapped with time for several molar ratios of CO₂/H₂/H₂O under illumination condition without UV light.

that in the single disc case. The order of CO₂ reduction performance in two discs is the same as that in the single disc case. However, comparing **Figure 19** with **Figure 13**, the concentrations in two discs case are higher than those in single case under every molar ratio of CO₂/H₂/H₂O. The highest concentration of CO in two discs case is 271 ppmV, which is 2.8 times as large as that in single disc case. The same reasons explained in the case of illumination with UV light can be thought to cause the results.

In addition, comparing **Figure 20** with **Figure 14**, the molar quantity of CO per weight of photocatalyst in two Cu/TiO₂ discs overlapped case is singly higher than that in the single disc case under every molar ratio of CO₂/H₂/H₂O. The highest molar quantity of CO per weight of photocatalyst is 3.1 μmol/g in two disc cases, which is 1.1 times as large as that in the single disc case. Though the effect of overlapping layout is not obtained under the illumination condition with UV light, the effect of overlapping layout is confirmed under the illumination condition without UV light. Since the photochemical reaction rate and the amount of produced fuel are small under the no-UV illumination condition compared to that with UV light, it would be beneficial to the mass transfer between produced fuels and reactants of CO₂, H₂, and H₂O on the surface of photocatalyst in no-UV cases [36]. As a result, the mass transfer and photochemical reaction are carried out effectively in no-UV cases. Therefore, the effect of overlapping layout is obtained in no-UV cases. According to the previous reports [37, 38], the mass transfer is an inhibition factor to promote the CO₂ reduction performance of photocatalyst, and it is necessary to control the mass transfer rate to meet the photochemical reaction rate. **Figure 21** illustrates the comparison of mass and electron transfer within overlapped two photocatalysts in UV and no-UV illumination cases [27].

3.4 Effect of molar ratio of CO₂, NH₃ and H₂O on CO₂ reduction characteristics

Figures 22 and **23** show the concentration changes of formed CO and CH₄, along the time under the Xe lamp with UV light, respectively. The amount of Cu/TiO₂ on the netlike glass disc is 0.1 g. Before the experiments, a blank test, which was running the same experiment without illumination of Xe lamp, had been carried out to set up a reference case. No fuel was produced in the blank test as expected.

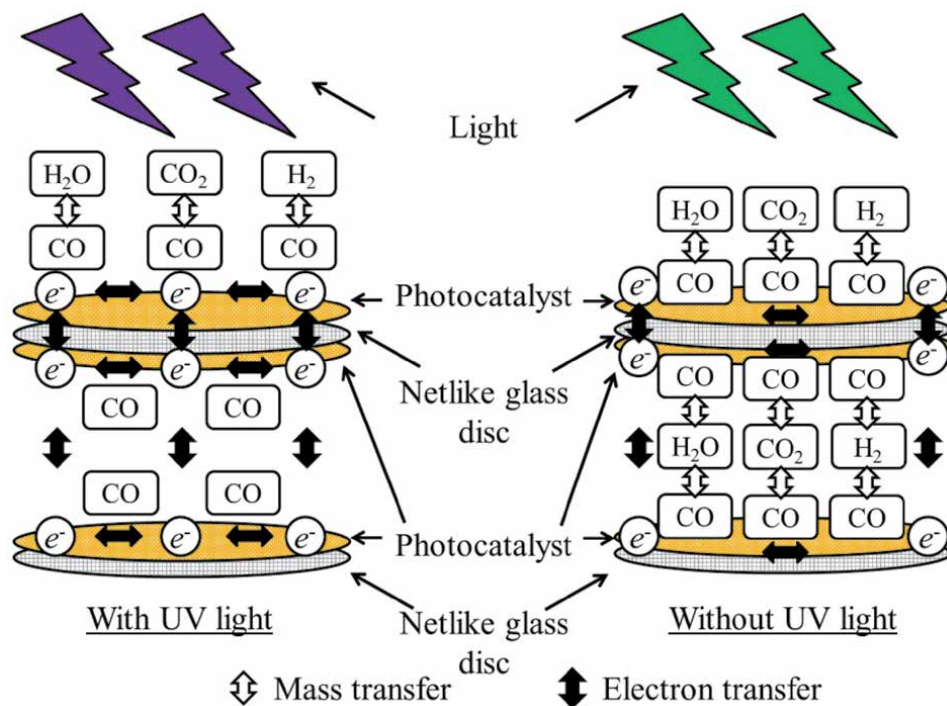


Figure 21. Comparison of mass and electron transfer within overlapped two photocatalysts between the illumination condition with UV light and without UV light.

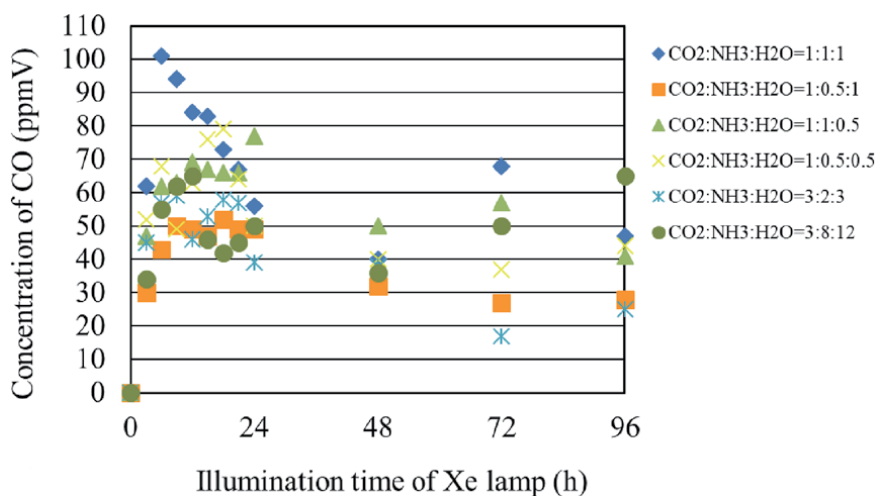


Figure 22. Comparison of concentration of formed CO among several molar ratios of $CO_2/NH_3/H_2O$ under the illumination condition with UV light.

According to **Figures 22** and **23**, the CO_2 reduction performance is the highest for the molar ratio of $CO_2/NH_3/H_2O = 1:1:1$.

According to the reaction scheme to reduce CO_2 with H_2O or NH_3 as shown by Eqs. (1)–(5), (13)–(20), the theoretical molar ratio of CO_2/H_2O to produce CO or CH_4 is 1:1 or 1:4, respectively, while that of CO_2/NH_3 to produce CO or CH_4 is 3:2,

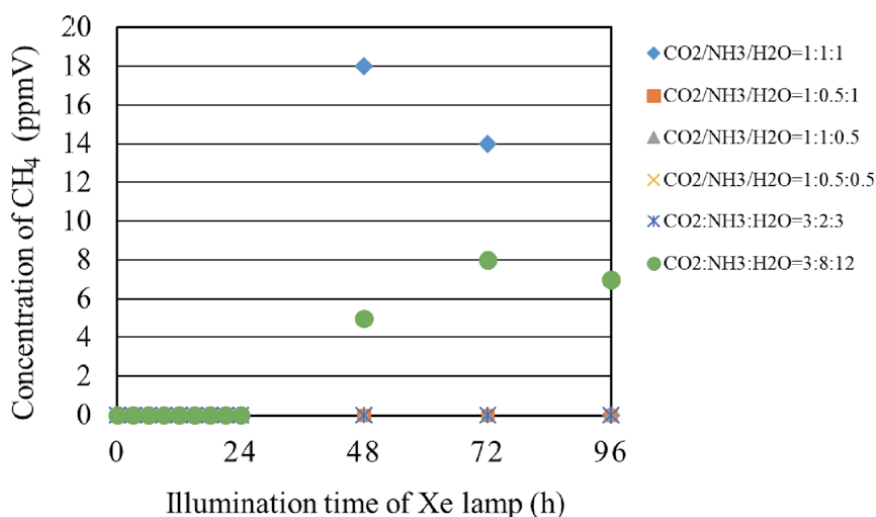


Figure 23.
Comparison of concentration of formed CH₄ among several molar ratios of CO₂/NH₃/H₂O under the illumination condition with UV light.

3:8, respectively. Therefore, this study assumes that the molar ratio of CO₂/NH₃/H₂O = 3:2:3 and 3:8:12 is theoretical molar ratio to produce CO and CH₄, respectively. However, the molar ratio of CO₂/NH₃/H₂O = 1:1:1 is not matched with these theoretical molar ratios to produce CO and CH₄. Since the ionized Cu doped with TiO₂ provides free electron for the reduction reaction process [39], the reductants of NH₃ and H₂O which are less than the values indicated in the theoretical scheme are enough for producing CO and CH₄ in this study. The highest molar quantities of CO and CH₄ per weight of photocatalyst in the reactor, which are obtained for the molar ratio of CO₂/NH₃/H₂O = 1:1:1, are 10.2 and 1.8 μmol/g, respectively.

In addition, it is confirmed from **Figure 22** that the concentration of formed CO is increased from the start of illumination of Xe lamp and decreased after attaining the peak concentration. However, the concentration of formed CO increases again after 48 hours. It is believed that the decrease in the concentration of formed CO is resulted from the oxidization reaction between CO and O₂ which is by-product as shown in Eq. (3) [40]. Since the produced CO might be remained near the photocatalyst due to high absorption performance of netlike glass fiber, this oxidization reaction is thought to be occurred. The increase in the concentration of formed CO after 48 hours might be due to the difference in reaction rates between CO₂/H₂O and CO₂/NH₃ condition. It is also revealed that the maximum concentration of formed CO is higher when the molar of NH₃ is higher than that of H₂O. Since the number of H⁺ which can be provided is 3 and 2 for NH₃ and H₂O, respectively, it is considered that NH₃ is effective for promoting the reduction performance of Cu/TiO₂. Furthermore, it is found from **Figures 22** and **23** that the concentration of formed CH₄ starts to increase after the decreasing of CO concentration. According to the reaction schemes, the more H⁺ and electron are needed to produce CH₄, resulting that the production of CH₄ starts later.

Figure 24 shows the concentration changes of formed CO along the time under the Xe lamp without UV light. In this experiment, CO is the only fuel produced from the reactions, that is, no CH₄ was detected. Before the experiments, a blank test, which was running the same experiment without illumination of Xe lamp, had been carried out to set up a reference case. No CO or CH₄ was produced in the blank test as expected. According to **Figure 24**, the CO₂ reduction performance is the best

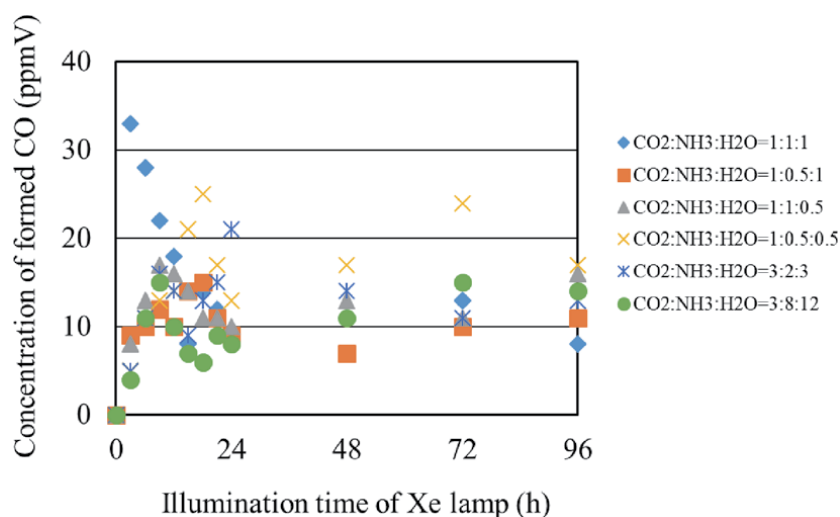


Figure 24.

Comparison of concentration of formed CO among several molar ratios of CO₂/NH₃/H₂O under the illumination condition without UV light.

for the molar ratio of CO₂/NH₃/H₂O = 1:1:1. In addition, it is confirmed from **Figure 24** that the concentration of formed CO is increased from the start of illumination of Xe lamp and decreased after reaching the maximum concentration. However, the concentration of formed CO is increased gradually again after a while. It can be considered that the same reaction mechanism under the illumination condition with UV light as mentioned above occurred.

3.5 Proposal to improve the CO₂ reduction performance with H₂O and H₂ or NH₃

Under the condition of CO₂/H₂/H₂O, the highest molar quantity of CO per weight of photocatalyst is 153 μmol/g in a single disc case with UV light illumination. The CO production performance achieved in this study is approximately 500 times as large as that reported in [24, 26] which is owing to Cu doping. The CH₄ production performance achieved in this study is almost the same as that reported in [24]. Since the doped Cu provides the free electron preventing recombination of electron and hole produced as well as the improvement of the light absorption effect, the big improvement of CO₂ reduction performance is obtained in this study.

One way to further promote the CO₂ reduction performance may be that different metals should be doped on the higher and the lower positioned photocatalysts discs. The co-doped such as PbS-Cu/TiO₂, Cu-Fe/TiO₂, Cu-Ce/TiO₂, Cu-Mn/TiO₂, and Cu-CdS/TiO₂ would promote the CO₂ reduction performance of TiO₂ under the CO₂/H₂O condition [7, 9]. When the combination of CO₂/H₂/H₂O is considered, the ion number of dopant is important to match the number of electron emitted from the dopant with H⁺ as shown by the reaction schemes of CO₂/H₂O and CO₂/H₂. The same number of electron and H⁺ are necessary for fuel production. Though Cu⁺ ion is applied to promote the CO₂ reduction performance with TiO₂ in this study, it is expected that the co-doping of Cu and the other metal having larger positive ion might have positive effect for CO₂ reduction with H₂ and H₂O. In addition, the dopant like Fe, which can absorb the shorter wavelength light than Cu [17, 41, 42], should be used at the higher positioned layer. The wavelength of light becomes long

after penetrating the higher positioned photocatalyst [36]. Therefore, it may be an effective way for utilization of wide wavelength range light that the higher positioned Fe/TiO₂ which absorbs the shorter wavelength light and the lower positioned Cu/TiO₂ which absorbs the longer wavelength light are overlapped. This idea is similar to the concept of hybridizing two photocatalysts having different band gaps [13, 42, 43].

On the other hand, under the condition of CO₂/NH₃/H₂O, the highest molar quantities of CO and CH₄ per weight of photocatalyst in the reactor, which are obtained for the molar ratio of CO₂/NH₃/H₂O = 1:1:1, are 10.2 and 1.8 μmol/g, respectively. Compared to the previous research on CO₂ reduction with H₂ and H₂O over pure TiO₂, the CO₂ reduction performance of photocatalyst prepared in this study is approximately 35 times as large as that reported in Refs. [24, 39], which is owing to not only Cu doping but also the combination of NH₃ and H₂O. The CO production performance over the Cu/TiO₂ prepared in this study is approximately 3 times as large as that reported in the reference [44]. However, the CH₄ production performance of Cu/TiO₂ prepared in this study is one twentieth as large as that of Cu/TiO₂ reported in the other reference [45]. Therefore, it is necessary to promote the conversion from NH₃ into H₂ in order to improve the reduction performance according to the reaction scheme to reduce CO₂ with NH₃. One way to promote the conversion from NH₃ into H₂ is thought to be using Pt as a dopant. It was reported that Pt/TiO₂ was effective to dissolve NH₃ aqueous solution into N₂ and H₂ [25].

4. Conclusions

The conclusions on this chapter are as follows:

- i. Cu in Cu/TiO₂ prepared by this study exists in the form of Cu⁺ ion in Cu₂O.
- ii. Under the condition of CO₂/H₂/H₂O, the highest concentrations of CO and CH₄ produced as well as the highest molar quantities of CO and CH₄ per weight of photocatalyst for Cu/TiO₂ are obtained for CO₂/H₂/H₂O ratio of 1:0.5:0.5. Since the molar ratio of CO₂/H₂/H₂O = 1:0.5:0.5 can be regarded as the molar ratio of CO₂/total reductants = 1:1, it is believed that the results of this study follow the reaction scheme of CO₂/H₂O and CO₂/H₂.
- iii. Under the condition of CO₂/H₂/H₂O, the highest concentration of CO in two discs case is 1.4 times as large as that in the single disc case, while the highest concentration of CH₄ is 1.7 times with UV light illumination. Under the illumination condition without UV light, the highest concentration of CO with two Cu/TiO₂ disc is 2.8 times as large as that with single Cu/TiO₂ disc.
- iv. Under the condition of CO₂/H₂/H₂O, the highest molar quantity of CO per weight of photocatalyst with two Cu/TiO₂ discs overlapped is 54% of that with single Cu/TiO₂ disc with UV light illumination. The highest molar quantity of CH₄ per weight of photocatalyst with two Cu/TiO₂ discs overlapped is 65% of that with single Cu/TiO₂ disc.
- v. Under the condition of CO₂/H₂/H₂O, the molar quantity of CO per weight of photocatalyst with two Cu/TiO₂ discs overlapped is slightly (1.1 times) higher than that with single Cu/TiO₂ disc without UV light illumination.

- vi. Under the condition of CO₂/NH₃/H₂O, the molar ratio of CO₂/NH₃/H₂O is 1:1:1 under the illumination condition with UV as well as without UV. The highest molar quantities of CO and CH₄ per weight of photocatalyst obtained in this study are 10.2 and 1.8 μmol/g, respectively.

Acknowledgements


The authors would like to gratefully thank from JSPS KAKENHI Grant Number 16K06970 for the financial support of this work.

Author details

Akira Nishimura
Mie University, Tsu, Japan

*Address all correspondence to: nisimura@mach.mie-u.ac.jp

IntechOpen

© 2020 The Author(s). Licensee IntechOpen. This chapter is distributed under the terms of the Creative Commons Attribution License (<http://creativecommons.org/licenses/by/3.0>), which permits unrestricted use, distribution, and reproduction in any medium, provided the original work is properly cited. 

References

- [1] Greenhouse Gases Observing Satellite GOAST “IBUSUKI” [Internet]. 2020. Available from: <http://www.goast.nies.go.jp/en/> [Accessed: 17 March 2020]
- [2] Das S, Daud WMAW. Photocatalytic CO₂ transformation into fuel: A review on advances in photocatalyst and photoreactor. *Renewable and Sustainable Energy Reviews*. 2014;**39**: 765-805
- [3] Adachi K, Ohta K, Mizuno T. Photocatalytic reduction of carbon dioxide to hydrocarbon using copperloaded titanium dioxide. *Solar Energy*. 1994;**53**:187-190
- [4] Tahir M, Amin NS. Photocatalytic reduction of carbon dioxide with water vapor over montmorillonite modified TiO₂ nanocomposites. *Applied Catalysis B: Environmental*. 2015;**162**:98-109
- [5] Tahir M, Amin NS. Indium-doped TiO₂ nanoparticles for photocatalytic CO₂ reduction with H₂O vapors to CH₄. *Applied Catalysis B: Environmental*. 2015;**162**:98-109
- [6] Abdulah H, Khan MMR, Ong HR, Yaakob Z. Modified TiO₂ photocatalyst for CO₂ photocatalytic reduction: An overview. *Journal of CO₂ Utilization*. 2017;**22**:15-32
- [7] Sohn Y, Huang W, Taghipour F. Recent progress and perspectives in the photocatalytic CO₂ reduction of Ti-oxide-based nanomaterials. *Applied Surface Science*. 2017;**396**:1696-1711
- [8] Neatu S, Macia-Agullo JA, Garcia H. Solar light photocatalytic CO₂ reduction: General considerations and selected benchmark photocatalysts. *International Journal of Molecular Sciences*. 2014;**15**: 5246-5262
- [9] Tahir M, Amin NS. Advances in visible light responsive titanium oxide-based photocatalysts for CO₂ conversion to hydrocarbon fuels. *Energy Conversion and Management*. 2013;**76**:194-214
- [10] Ola O, Maroto-Valer MM. Review of material design and reactor engineering on TiO₂ photocatalysis for CO₂ reduction. *Journal of Photochemistry and Photobiology*. 2015;**24**:16-42
- [11] Tan LL, Ong WJ, Chai SP, Mohamed AR. Noble metal modified reduced graphene oxide/TiO₂ ternary nanostructures for efficient visible-light-driven photoreduction of carbon dioxide into methane. *Applied Catalysis B: Environmental*. 2015;**167**:251-259
- [12] Jiao J, Wei Y, Zhao Y, Zhao Z, Duan A, Liu J, et al. AuPd/3DOM-TiO₂ catalysts for photocatalytic reduction of CO₂: High efficient separation of photogenerated charge carriers. *Applied Catalysis B: Environmental*. 2017;**209**: 228-239
- [13] Marci G, Garcia-Lopez EI, Palmisano L. Photocatalytic CO₂ reduction in gas- solid regime in the presence of H₂O by using GaP/TiO₂ composite as photocatalyst under simulated solar light. *Catalysis Communications*. 2014;**53**:38-41
- [14] Beigi AA, Fatemi S, Salehi Z. Synthesis of nanocomposite CdS/TiO₂ and investigation of its photocatalytic activity of CO₂ reduction to CO and CH₄ under visible light irradiation. *Journal of CO₂ Utilization*. 2014;**7**:23-29
- [15] Fang Z, Li S, Gong Y, Liao W, Tian S, Shan C, et al. Comparison of catalytic activity of carbon-based AgBr nanocomposites for conversion of CO₂ under visible light. *Journal of Saudi Chemical Society*. 2014;**18**:299-307
- [16] Nagaveni K, Hegde MS, Madras G. Structure and photocatalytic activity of Ti_{1-x}M_xO_{2±δ} (M = W, V, Ce, Zr, Fe, and

- Cu) synthesized by solution combustion method. *The Journal of Physical Chemistry B*. 2004;**108**:20204-20212
- [17] Yoong LS, Chong FK, Dutta BK. Development of copper-doped TiO₂ photocatalyst for hydrogen production under visible light. *Energy*. 2009;**34**: 1652-1661
- [18] Cheng M, Yang S, Chen R, Zhu X, Liao Q, Huang Y. Copper-decorated TiO₂ nanorod thin films in optofluidic planer reactors for efficient photocatalytic reduction of CO₂. *International Journal of Hydrogen Energy*. 2017;**42**:9722-9732
- [19] Khalid NR, Ahmed E, Niaz NA, Nabi G, Ahmad M, Tahir MB, et al. Highly visible light responsive metal loaded N/TiO₂ nanoparticles for photocatalytic conversion of CO₂ into methane. *Ceramics International*. 2017;**43**:6771-6777
- [20] Tan JZY, Fernandez Y, Liu D, Maroto-Valer M, Bian J, Zhang X. Photoreduction of CO₂ using copper-decorated TiO₂ nanorod films with localized surface plasmon behavior. *Chemical Physics Letters*. 2012;**531**: 149-154
- [21] Goren Z, Willner I, Nelson AJ, Frank AJ. Selective photoreduction of CO₂/HCO₃⁻ to formate by aqueous suspensions and colloids of Pd-TiO₂. *The Journal of Physical Chemistry*. 1990;**94**:3784-3790
- [22] Tseng IH, Chang WC, Wu JCS. Selective photoreduction of CO₂ using sol-gel derived titania and titania-supported copper catalyst. *Applied Catalysis B: Environmental*. 2002;**37**: 37-38
- [23] Nishimura A, Sugiura N, Fujita M, Kato S, Kato S. Influence of preparation conditions of coated TiO₂ film on CO₂ reforming performance. *Kagaku Kogaku Ronbunshu*. 2007;**33**:146-153
- [24] Lo CC, Hung CH, Yuan CS, Wu JF. Photoreduction of carbon dioxide with H₂ and H₂O over TiO₂ and ZrO₂ in a circulated photocatalytic reactor. *Solar Energy Materials & Solar Cells*. 2007;**33**: 146-153
- [25] Nemoto J, Goken N, Ueno H. Photodecomposition of ammonia to dinitrogen and dihydrogen on platinumized TiO₂ nanoparticles in an aqueous solution. *Journal of Photochemistry and Photobiology A: Chemistry*. 2007;**185**: 295-300
- [26] Jensen J, Mikkelsen M, Krebs FC. Flexible substrates as basis for photocatalytic reduction of carbon dioxide. *Solar Energy Materials & Solar Cells*. 2011;**95**:2949-2958
- [27] Nishimura A, Toyoda R, Tatematsu D, Hirota M, Koshio A, Kokai F, et al. Optimum reductants ratio for CO₂ reduction by overlapped Cu/TiO₂. *Materials Science*. 2019;**6**:214-233
- [28] Nishimura A, Sakakibara Y, Inoue T, Hirota M, Koshio A, Kokai F, et al. Impact of molar ratio of NH₃ and H₂O on CO₂ reduction performance over Cu/TiO₂ photocatalyst. *Physics & Astronomy International Journal (PAIJ)*. 2019;**3**:176-182
- [29] Nishimura A, Tatematsu D, Toyoda R, Hirota M, Koshio A, Kokai F, et al. Effect of overlapping layout of Fe/TiO₂ on CO₂ reduction with H₂ and H₂O. *MOJ Solar and Photoenergy Systems (MOJSP)*. 2019;**3**:1-8
- [30] Japan society of mechanical engineering. *Heat Transfer Hand Book*. 1st ed. Maruzen; 1993. pp. 367-369
- [31] Yang G, Cheng S, Li C, Zhong J, Ma C, Wang Z, et al. Investigation of the oxidation states of Cu additive in colored borosilicate glasses by electron energy loss spectroscopy. *Journal of Applied Physiology*. 2014;**116**. DOI: 10.1063/1.4903955

- [32] Qin S, Xin F, Liu Y, Yin X, Ma W. Photocatalytic reduction of CO₂ in methanol to methyl formate over CuO-TiO₂ composite catalysts. *Journal of Colloid and Interface Science*. 2011;**356**: 257-261
- [33] Liu L, Gao F, Zhao H, Li Y. Tailoring Cu valence and oxygen vacancy in Cu/TiO₂ catalysts for enhanced CO₂ photoreduction efficiency. *Applied Catalysis B: Environmental*. 2013; **134-135**:349-358
- [34] EELS data base [Internet]. 2020. Available from: <https://eesdb.eu/spectra/titanium-dioxide-2/> [Accessed: 18 March 2020]
- [35] Hinojosa-Reyes M, Camposeco-Solis R, Zanella R, Zanella R, Gonzalez VR. Hydrogen production by tailoring the brookite and Cu₂O ratio of sol-gel Cu-TiO₂ photocatalysts. *Chemosphere*. 2017;**184**:992-1002
- [36] Nishimura A, Zhao X, Hayakawa T, Ishida N, Hirota M, Hu E. Impact of overlapping Fe/TiO₂ prepared by sol-gel and dip-coating process on CO₂ reduction. *International Journal of Photoenergy*. 2016;**2016**. DOI: 10.1155/2016/2392581
- [37] Nishimura A, Komatsu N, Mitsui G, Hirota M, Hu E. CO₂ reforming into fuel using TiO₂ photocatalyst and gas separation membrane. *Catalysis Today*. 2009;**148**:341-349
- [38] Nishimura A, Okano Y, Hirota M, Hu E. Effect of preparation condition of TiO₂ film and experimental condition on CO₂ reduction performance of TiO₂ photocatalyst membrane reactor. *International Journal of Photoenergy*. 2011;**2011**. DOI: 10.1155/2011/305650
- [39] Paulino PN, Salim VMM, Resende NS. Zn-Cu promoted TiO₂ photocatalyst for CO₂ reduction with H₂O under UV light. *Applied Catalysis B: Environmental*. 2016;**185**:362-370
- [40] Tahir M, Amin NAS. Photo-induced CO₂ reduction by hydrogen for selective CO evolution in dynamic monolith photoreactor loaded with Ag-modified TiO₂ nanocatalyst. *International Journal of Hydrogen Energy*. 2017;**42**: 15507-15522
- [41] Ambrus Z, Balazs N, Alapi T, Wittmann G, Sipos P, Dombi A, et al. Synthesis, structure and photocatalytic properties of Fe(III)-doped TiO₂ prepared from TiCl₃. *Applied Catalysis B: Environmental*. 2008;**81**:27-37
- [42] Navio JA, Colon G, Litter MI, Bianco GN. Synthesis, characterization and photocatalytic properties of iron-doped titania semiconductors prepared from TiO₂ and iron (III) acetylacetonate. *Journal of Molecular Catalysis A: Chemical*. 1996;**106**:267-276
- [43] Song G, Xin F, Chen J, Yin X. Photocatalytic reduction of CO₂ in cyclohexanol on CdeS-TiO₂ heterostructured photocatalyst. *Applied Catalysis A: General*. 2014;**473**:90-95
- [44] Aguirre ME, Zhou R, Engene AJ, Guzman MI, Grela MA. Cu₂O/TiO₂ heterostructures for CO₂ reduction through a direct Z-scheme: Protecting Cu₂O from photocorrosion. *Applied Catalysis B: Environmental*. 2017;**217**: 485-493
- [45] Ambrozova N, Reli M, Sihor M, Kustrowski P, Wu JCS, Koci K. Copper and platinum doped titania for photocatalytic reduction of carbon dioxide. *Applied Surface Science*. 2018; **430**:475-487

Recent Progress of Electrocatalysts and Photocatalysts Bearing First Row Transition Metal for Hydrogen Evolution Reaction (HER)

Shipra Sagar, Ravi K. Kanaparthi, Manish K. Tiwari and Satyen Saha

Abstract

The design and modification of metal–organic complexes for hydrogen (H_2) gas production by water splitting have been intensively investigated over the recent decades. In most reported mechanistic pathways, metal hydride species are considered as crucial intermediates for H_2 formation where the metal present at the active site plays an imperative role in the transfer of electron and proton. In the last few decades, much consideration has been done on the development of non-precious metal–organic catalysts that use solar energy to split water into hydrogen (H_2) and oxygen (O_2) as alternative fossil fuels. This review discussed the design, fabrication, and evaluation of the catalysts for electrocatalytic and photocatalytic hydrogen production. Mechanistic approach is addressed here in order to understand the fundamental design principle and structural properties relationship of electrocatalysts and photocatalysts. Finally, we discuss some challenges and opportunities of research in the near future in this promising area.

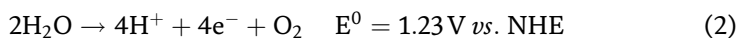
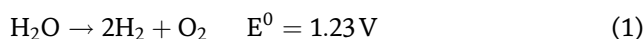
Keywords: redox-active-ligand, first-row transition metals, hydrogen evolution, catalytic cycle, electrocatalyst, photocatalyst

1. Introduction

Climate change and increasing energy demand have emphasized research on sustainable energy source [1, 2]. Day-by-day increase of human population and global requirements has compelled researchers to develop new renewable sustainable energy sources in replacement of hydrocarbon deposits [3]. Renewable sources such as solar power, wind, and water, storage of these energies for on-demand utilization, and transportation are the major challenges for researchers. To develop a clean and eco-friendly environment, splitting of water into hydrogen and oxygen is a tremendous way to produce sustainable energy. Hydrogen gas emerged as a green energy fuel due to its high-energy density and zero carbon dioxide (CO_2) emission [4–6]. In this regard, electrocatalytic and photocatalytic H_2 generation

from water has been considered as one of the most striking approaches [7–9]. In recent years, a substantial number of artificial photosynthesis have been developed, exploited solar power as electron and proton source to make a clean renewable fuel [10–14]. Light-induced splitting of water is a suitable process because the production of hydrogen is used as green fuel in future and even used for the synthesis of other chemicals [15–18].

Literature reports suggested more than 500 billion cubic meters (44.5 million tons) of hydrogen gas is produced yearly worldwide [19, 20]. In the current scenario, steam methane refining, coal gasification, and water electrolysis are the major way for hydrogen production. Nowadays 95% hydrogen gas is produced from steam methane reforming and coal gasification, however only 4% hydrogen from water electrolysis. Steam methane is a high-energy-intensive process maintained at high temperature with the formation of carbon dioxide and carbon monoxide: (i) $\text{CH}_4 + \text{H}_2\text{O} = \text{CO} + 3\text{H}_2$ (ii) $\text{CO} + \text{H}_2\text{O} = \text{CO}_2 + \text{H}_2$. Hence, it is not an eco-friendly method for hydrogen production. Water electrolysis is the most sustainable and clean approach for hydrogen production because its source is abundant. Since the most suitable way of light-driven energy conversion is water electrolysis, artificial photosynthesis (PS II) has been considered as primary goal to produce electron and proton [21, 22]. Water splitting is a redox reaction in which aqueous protons are reduced into H_2 at cathode and water is oxidized to O_2 at anode [23]. Both H_2 (HER) and O_2 (OER) reactions are rigorously coupled, which may lead to the formation of explosive H_2/O_2 mixtures due to gas crossover [24–26]. By far, only a few stable metal complexes as catalysts are achieved that can decompose water into H_2 and O_2 [27–31]. Water-splitting reactions are split into two half-reactions: water oxidation to O_2 evolution and water reduction to H_2 production:



The limitation of OER is that it takes place after the successive accumulation of four oxidized electrons and protons in Kok cycle (catalytic cycle of the water oxidation in PS II) that require much higher overpotential input than that of HER [32]. Thermodynamic potential is different for H^+/H_2 (0 V vs. NHE) and OH^-/O_2 (1.23 V vs. NHE), and the overall solar energy conversion efficiency is only ~15% in OER [33]. The hydrogen evolution reaction (HER, $2\text{H}^+ + 2\text{e}^- = \text{H}_2$) is the cathodic reaction with the two-electron transfer in one catalytic intermediate and offers the potential to hydrogen production. However, hydrogen production technology requires proficient electrocatalysts and photocatalysts which support two key electrode reactions (OER and HER) at lower overpotentials.

Moreover discussion on the mechanism of HER, H^+ adsorption on the hydrogen evolution catalyst surface is the first step, known as Volmer step, followed by Heyrovsky or Tafel steps shown in **Figure 1**. A suitable HER catalyst always binds H^+ very fast and releases the product. Hence, electrochemical hydrogen evolution reaction (HER) facilitates for H_2 production on large-scale.

Afterwards, H_2 evolution may occur via two different reaction mechanisms depending on the action of catalyst [34]. Hydronium cation (H_3O^+) is the proton source in acidic solution, and in alkaline condition H_2O is the proton source. In Volmer-Tafel mechanism, two protons absorbed on the catalytic surface can combine to form H-H bond to yield H_2 . In Heyrovsky reaction route, a second electron and another proton from the solution are transferred to the catalyst surface which reacts with the absorbed H atom and generate H_2 . This is an electrochemical

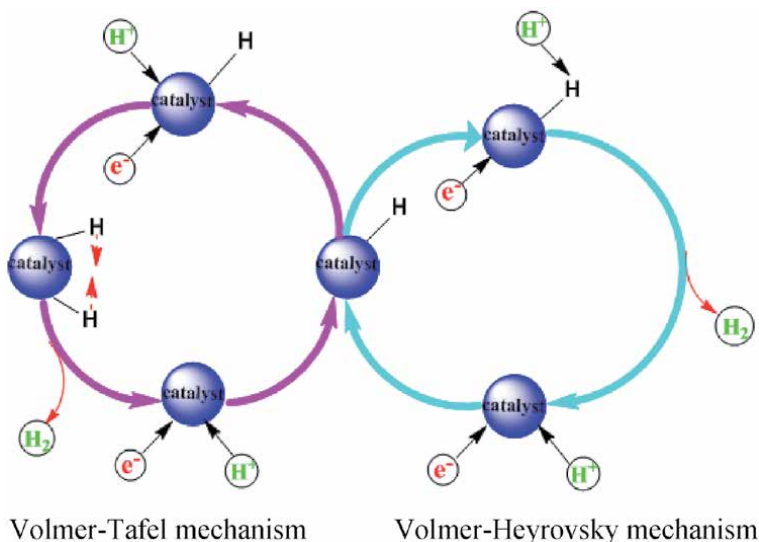


Figure 1.
 The inside mechanism of H_2 evolution of electrocatalyst in acidic solution.

desorption pathway. Precious metal like Pt-based electrocatalysts is highly reactive for HER and is usually pursuing Volmer-Tafel mechanism. Lately few literatures [35–37] have been reported on Ni-based electrocatalysts which follows Volmer-Heyrovsky path.

1.1 Fundamental aspects of photocatalytic and electrocatalytic hydrogen production process

Electrocatalytic water splitting is driven by passing the electric current through the water; conversion of electrical energy to chemical energy takes place at electrode through charge transfer process. During this process, water reacts at the anode form O_2 and hydrogen (proton) produce at the cathode as we mentioned earlier. Suitable electrocatalysts can maximally reduce the overpotential which is highly desirable for driving a specific electrochemical reaction. However, the process of surface catalytic reactions in electrocatalysis is very similar to photocatalysis [38]. Photocatalytic is a simple water-splitting reaction in which H_2 and O_2 are produced from water by utilizing the energy of sunlight. **Figure 2(a)** shows the process of photocatalysis in which a metal catalyst contains chromophores that

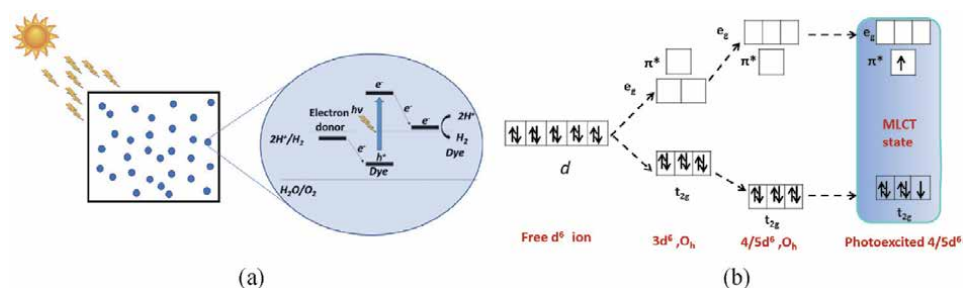


Figure 2.
 (a) Photocatalyst system for water splitting. (b) Molecular orbital diagram for d^6 metal complex chromophores.

immersed solar energy and triggered the electron transfer reaction. The most important criteria for the solar-driven water-splitting reaction are electronic band gap matching of the photosensitive material to the redox potential of water [39]. Metal complexes act as chromophore associated with mainly three types of electron transfer: metal center (MC), ligand center (LC), and metal–ligand center transition (MLCT). The MLCT state of the metal complex plays a crucial role in photocatalytic reactions. In octahedral complexes with conjugated ligand system, the highest occupied molecular orbital (HOMO) corresponds to the metal-localized t_{2g} -orbitals, and the lowest unoccupied molecular orbital (LUMO) is associated with anti-bonding π^* -orbital localized on the ligands. On the absorption of UV–visible light, an electron is promoted from one of the metal-centered t_{2g} orbitals to a ligand-centered π^* orbital, resulting in the MLCT state shown in **Figure 2(b)**. As a result, the redox properties of the metal complexes are dramatically changed. The excited metal complexes behave as better oxidants and better reductants than their electronic ground state and can hold more thermodynamic driving force for the charge transfer reactions. Based on the photo-induced redox potential changes and the long-lived lifetime of the excited state, many metal complexes have been intensively investigated as chromophores for this photocatalytic H_2 production purpose [40]. Zou and coworkers have described various photocatalytic systems for H_2 production, which exposed that most of the photocatalytic systems suffer photodecomposition and instability [40]. Hence, for long-term use, it is imperative to build up highly proficient H_2 generation systems with long lifetimes and high durability. Many reviews have been published on solar H_2 evolution systems based on photocatalysts [41–44].

1.2 Mechanistic pathway

So far, extensive theoretical study has been revealed, the possible mechanistic process of proton reduction to hydrogen evolution through transition metal molecular catalyst. A generalized mechanistic scheme depicting the homolytic and heterolytic path is shown in **Figure 3**. The homolytic mechanism involves bimetallic route, where a metal hydride species ($[M^{n+}-H]$) react with another metal hydride to release one H_2 via reductive elimination. Instead, heterolytic is a monometallic

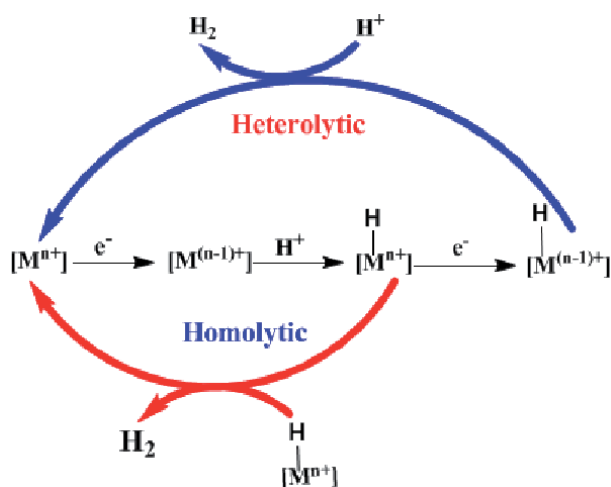


Figure 3. Proposed homolytic and heterolytic mechanisms for H_2 evolution via the formation of a metal hydride (M-H) intermediate.

pathway, where the metal hydride $[M^{n+}-H]$ is further reduce and protonated for H_2 evolution [45]. Both pathways function simultaneously, two protons and two electrons are delivered to the metal center, and in few cases, the pH, catalytic concentration, and proton source decide the dominant route [46]. During the past decade, a number of review articles emphases on the structural property relationship and mechanistic study [45, 47–49]. Among all research on catalyzed H_2 evolution, the mechanistic investigation on proton reduction catalysis is essential because it can give us a significant idea to design better molecular catalyts in the future [49].

1.3 Metal and redox-active ligands for HER

Here we start by describing the fundamental concept of metal and organic ligand system which gives a strong influence on the performance of H_2 evolution. Transition metal cations with partial filled d-electronic configurations are considered as catalyst. The characteristic feature of this type of catalyst is that the metal ions can exist in higher oxidation state [44]. There are several literatures reported with partially filled d-orbital which show high stability toward water-splitting reactions [50–53]. However, the most catalytic system requires very high temperature and precious metal at the active site; therefore, it will be a challenge for researchers to develop a photocatalytic and electrocatalytic system at low temperature with low-cost metal [54–57]. Indeed, first-row transition metal complexes (Co, Ni, Cu, Zn) have been exploited in the last few decades for this purpose. Beyond the reactivity of metal, the redox activity of organic ligands has also received continuous attention. The redox-active ligand works as electron sink in the complexes and maintains the metal in its original oxidation state. Redox-active ligands convey a novel reactivity to the complex by loss or gain of electrons [58]. In addition, the redox-active property of the ligand can also be influenced by the modification of the substituents by σ and π donating ability, π accepting ability, and conjugation [59]. A highly conjugated system such as bpy, porphyrins, and ortho-phenylenediamine (opda) having anti-bonding π^* -orbital localized on the ligands is considered for hydrogen production due to its multielectron or multiproton pooling ability which is responsible for dramatically changing the potential of redox properties [60, 61]. Substituents attached to redox-active ligands, electron density, and charge on the metal ions also effect the standard electrode potential.

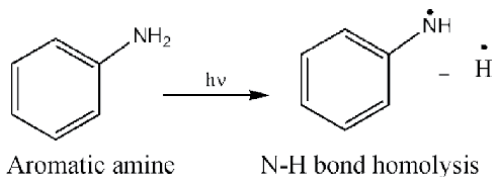
So far, considerable advancement has been done in the field of electrocatalytic and photocatalytic water-splitting reaction for hydrogen production, and several advance review papers have been reported by scientists [40, 51, 62–64]. However, very limited comprehensive tutorial has published on only first-row transition metal-based catalysts. This chapter describes electrocatalytic as well photocatalytic properties of inorganic catalysts and their structural and mechanistic features. Here we put an effort elucidate the direction of fundamental mechanistic aspects during electrocatalytic and photocatalytic hydrogen (H_2) production reaction (HER).

2. Photochemical hydrogen production from a series of 3D transition metal complexes bearing o-phenylenediamine ligand

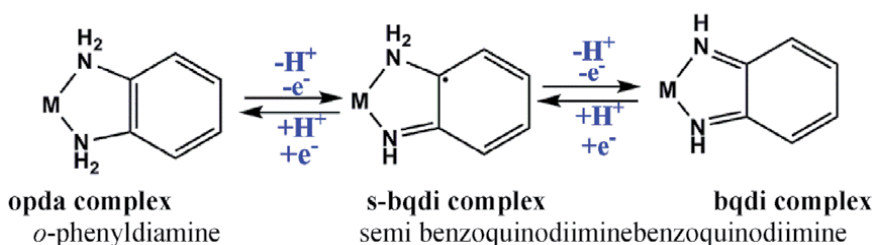
Masaki Yoshida et al. [65] developed a series of 3D-transition metal complexes with *o*-phenylenediamine (opda) ligands for hydrogen production due to the following properties: (a) aromatic amine undergoes homolytic N-H bond cleavage by photoexcitation [66] which is applicable for hydrogen production under mild condition, and (b) opda complexes have extensively been obsessed as reversible multielectron or multiproton pooling ability because of its multistep redox

processes between *o*-phenylenediamine (opda), semibenzoquinodiamine (s-bqdi), and *o*-benzoquinodiamine (bqdi) which is useful for reversible hydrogen production. $[M(\text{opda})_3]$, $M = \text{Mn}^{2+}$, Fe^{2+} , Co^{2+} , Ni^{2+} , and Zn^{+2} complexes (1-5) shown in **Table 1** have photochemical hydrogen production ability.

a. Photochemistry of aromatic amine (opda)



b. Redox properties of opda complex



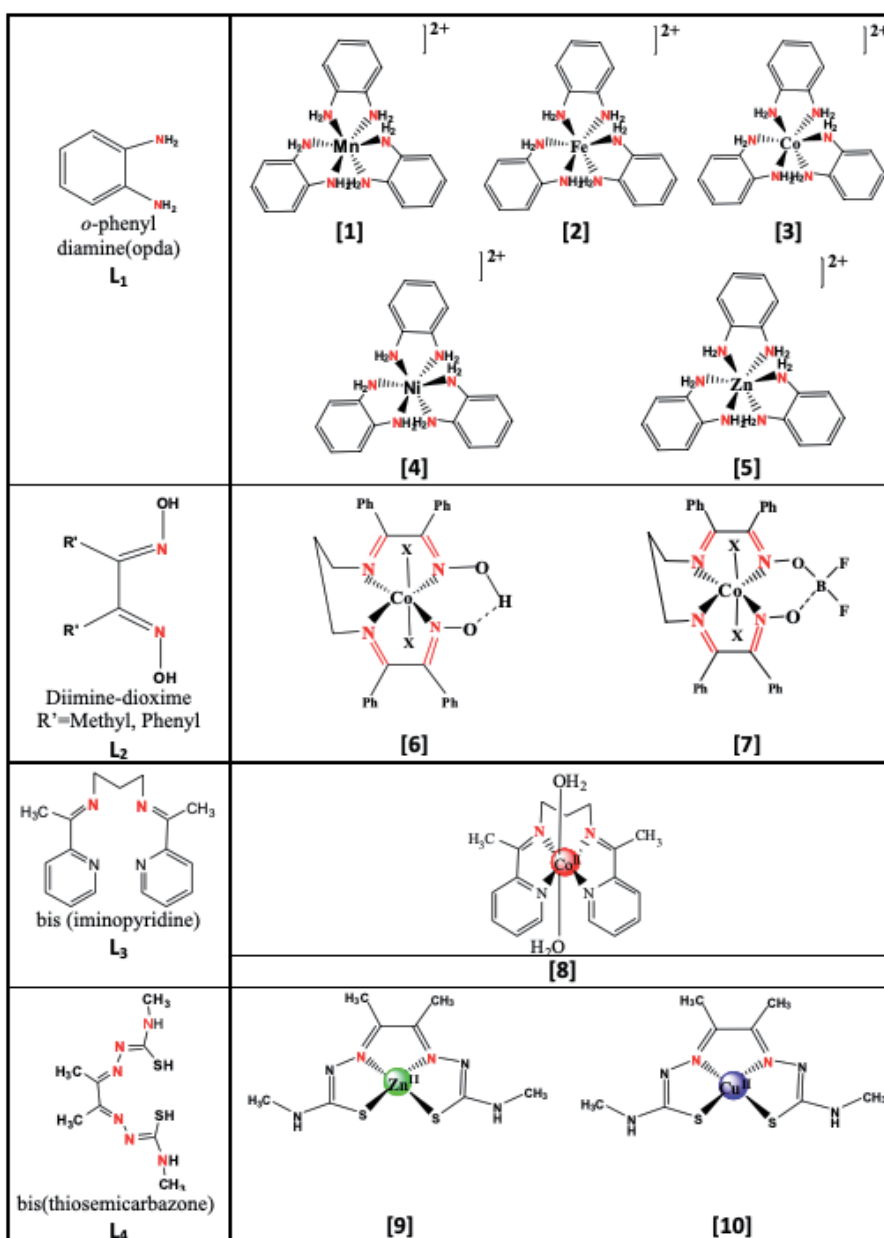
In the past M. Yoshida and coworkers proposed $[\text{Fe-opda}]$ for photochemical HER mechanism at photoirradiation of $\lambda = 298 \text{ nm}$; $\pi\pi^*$ excitation occurred in complex with N-H bond homolysis process, followed by H_2 elimination [67]. After this process, the opda ligands in the complex were partially oxidized to bqdi or s-bqdi ligands. This mechanism is based on the deep-rooted photochemical N-H bond activation of aromatic amines. Theoretical study and ultrafast spectroscopic studies of amino benzene support that the photochemical N-H fission occurs by the photo-excitation to higher-lying $\pi\pi^*$ level which leads to the formation of the $\pi\sigma^*$ state [68]. Photochemical mechanism for HER of all complexes is shown in **Figure 4**.

All opda-based metal complexes display photochemical HER activities with the formation of almost one equivalent of H_2 gas. However, the HER was not observed at all in the dark in all complexes, which suggests that the HER was obsessed by photochemical reaction. Moreover, they observed remarkable decrease in hydrogen evolution reaction, while the ligand is replaced with aromatic amines. This experiment suggested that the photo-induced HER activities of the complexes in this case are weakly dependent on the central metal ion and strongly dependent on the redox-active ligand. Further to check the metal ion dependency, examine the catalytic hydrogen production in the presence of hydroquinone (HQ; 10 equiv) as a sacrificial electron-proton donor. The photochemical H_2 production from $[\text{M-opda}]$ ($7.98 \times 10^{-2} \text{ mmol}$) with HQ ($7.98 \times 10^{-1} \text{ mmol}$) in THF (4 mL) under an N_2 atmosphere at 20°C for 190 h turns over the number for all the complexes given in **Table 2**. Difference in TON may be caused by the stability of each complexes.

2.1 Cobalt diimine-dioxime complexes for HER

V. Artero and coworker synthesized cobalt diimine-dioxime complexes as molecular catalysts for H_2 evolution [69, 70]. This synthesized ligand (N^2 , N^2 -propanediylbis-butan-2-imine-3-oxime) has emerged many years ago through

Schiff base condensation of butanedione-monoximeon diamine compounds but not widely used for HER. Cobalt diimine-dioxime catalysts are active for H₂ evolution in aqueous solution, both after immobilization on electrode materials and in light-driven homogeneous conditions. The electrocatalytic activity of complexes (6) and (7) for hydrogen evolution was supported gas chromatography and by cyclic voltammetry study illustrated in **Figure 5** with the appearance of an irreversible wave. In the case of the BF₂-associated complex (7), the electrocatalytic wave which developed toward negative potentials corresponds to the Co^{II}/Co^I couple in contrast to the H-bridged complex (6), electrocatalytic H₂ evolution occurs at potentials positively shifted with regard to the Co^{II}/Co^I couple.



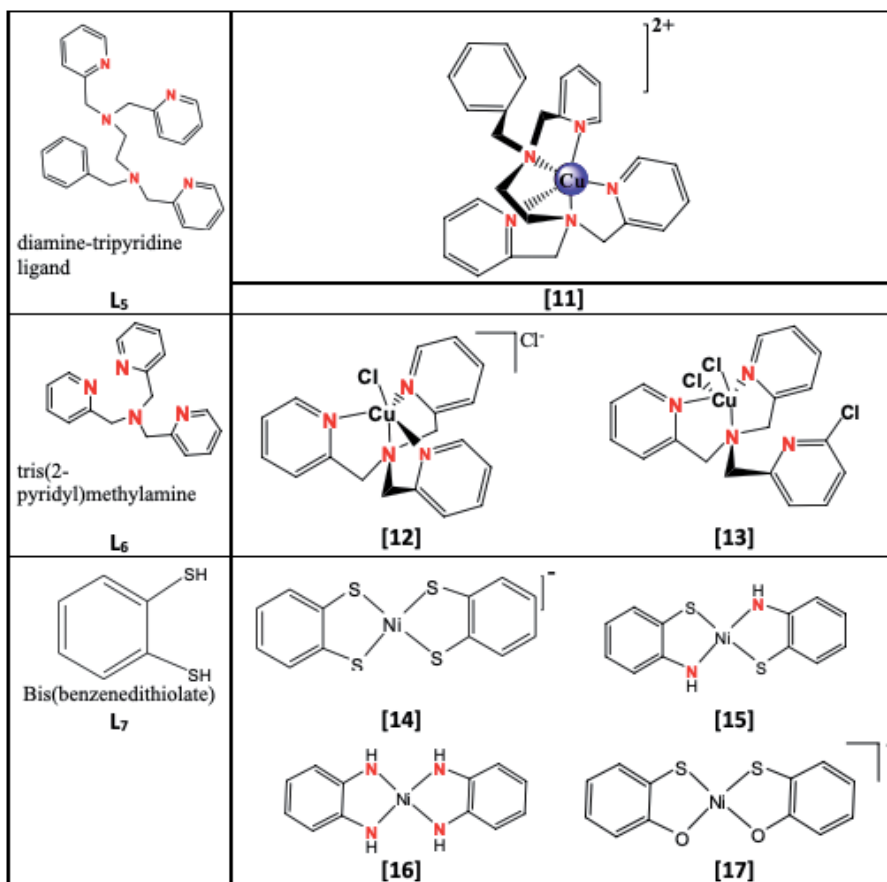


Table 1.
Structure of redox-active ligands, electrocatalysts, and photocatalysts.

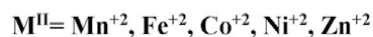
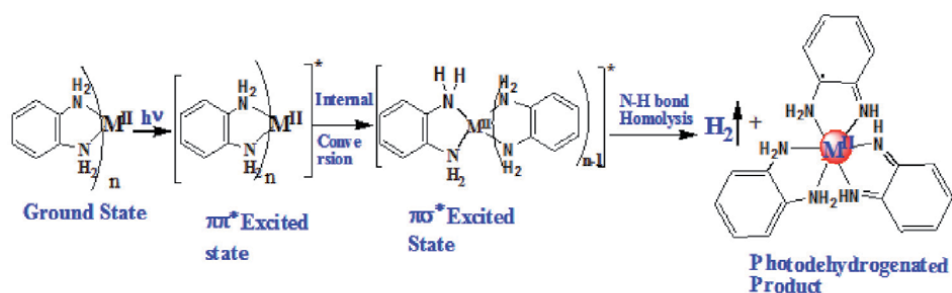


Figure 4.
Plausible mechanism for photochemical HER with $[M\text{-opda}]$ complexes.

2.2 Electrocatalytic cycle for H_2 evolution

In the electrocatalytic cycle, V. Artero and coworker observed that in acetonitrile medium, halide ligands are banished with reduced oxidation state from Co^{II} to Co^I . Upon reduction, the coordination in number decreases from six in Co^{II} state to

Catalysts	Redox-active organic ligands	Catalytic potential (Ep)	Solvent	TON(H ₂ mol cat ⁻¹)	Ref.
[1] ^a	<i>o</i> -Phenylenediamine	—	THF	5.5	[65]
[2]	<i>o</i> -Phenylenediamine	—	THF	2.9	[67]
[3]	<i>o</i> -Phenylenediamine	—	THF	0.99	[65]
[4]	<i>o</i> -Phenylenediamine	—	THF	0.51	[65]
[5]	<i>o</i> -Phenylenediamine	—	THF	0.73	[65]
[6] ^b	Diimine-dioxime	-0.68 V vs. Fc ⁺⁰	H ₂ O/CH ₃ CN	300	[70]
[7]	Diimine-dioxime	-0.96 V vs. Fc ⁺⁰	H ₂ O/CH ₃ CN	50	[70]
[8]	Bis(thiosemicarbazone)	-1.7 V vs. Fc/Fc ⁺	CH ₃ CN	37	[74]
[9]	Bis(thiosemicarbazone)	-1.7 V vs. Fc/Fc ⁺	CH ₃ CN	73	[75]
[10] ^c	Diamine-tripyridine	-0.90 V vs. Fc ⁺⁰	acidic-H ₂ O	1.4x 10 ⁴	[70]
[11] ^d	TMPA	-1.81 V vs. SCE	CH ₃ CN/H ₂ O	6180	[76]
[12]	Cl-TMPA	-1.72 V vs. SCE	CH ₃ CN/H ₂ O	10,014	[76]
[13]	Bis(benzenedithiolate)	-2.25 V vs. SCE	CH ₃ CN	0	[77]
[14]	<i>o</i> -Aminobenzenethiolate	-1.64 V vs. SCE	CH ₃ CN	6190	[77]
[15]	<i>o</i> -Aminobenzene	-2.03 V vs. SCE	CH ₃ CN	900	[77]
[16]	2-Mercaptophenolate	-1.62 V vs. SCE	CH ₃ CN	5600	[77]

a = photochemical H₂ production from [M-opda 1-5] (7.98 × 10⁻² mmol) with HQ (7.98 × 10⁻¹ mmol) in (4 mL) under an N₂ atmosphere at 20°C for 190 h in the presence of 4 AMS (irradiation with 300 W Xe lamp, 250–385 nm).

b = in light-driven condition of TEA and a cyclometalated iridium-based photosensitizer; CV was done in glassy carbon electrode (100 mVs⁻¹) in the presence of *p*-cyanoanilinium tetrafluoroborate. *c* = the controlled potential electrolysis of complex **11** was measured at pH 2.5 under N₂ atmosphere at a scan rate of 50 mVs⁻¹ in phosphate buffer, over 2 hours using a glassy carbon electrode. *d* = conditions, 0.1 M *n*-Bu₄NPF₆, scan rate 100 mVs, in Ar-saturated CH₃CN/H₂O.

Table 2. Electrochemical data and catalytic efficiency of metal complexes for water-splitting hydrogen evolution reaction.

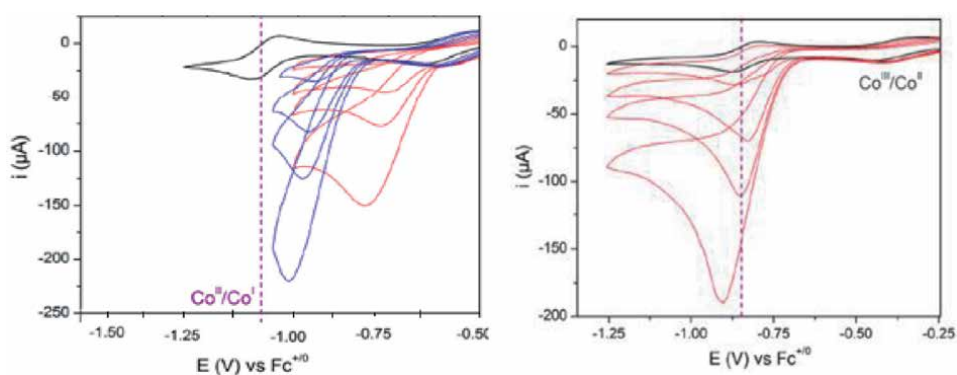


Figure 5. Cyclic voltammograms of (6) Br₂ and (7) Br₂ (1 mM, black traces) recorded in CH₃CN at a glassy carbon electrode at a speed of 100 mV·s⁻¹ (the figure is reproduced from Ref. [69], with permission from the publisher).

five in Co^I state; this characteristic was supported by DFT calculations [71]. In the catalytic cycle (Figure 6), the first step is the transfer of electron and proton by proton-coupled electron transfer (PCET) process. PCET is a chemical reaction that

involves the transfer of electron and proton in which the oxidation number changes by Co^{II} to Co^{I} . In the second steps, further electron and proton transfer takes place by PCET process, and the oxidation number changes from Co^{I} to Co^{II} . In the last step, H_2 is produced in dihydrogen bond through an intramolecular mechanism. The authors also confirmed cobalt diimine-dioxime catalysts **6** and **7** active for H_2 evolution under light-driven conditions in the presence of photosensitizers, associated with Ru, Ir, or Re derivatives. The photocatalytic activity of **6-Br₂** was observed in mixed $\text{H}_2\text{O}/\text{CH}_3\text{CN}$ solvent in the presence of TEA and cyclometalated iridium-based photosensitizer [72]. Turnover numbers (TON) determined after continuous 4 h UV-visible light irradiation **6-Br₂** showed 300 ($\text{H}_2 \text{ mol cat}^{-1}$), whereas **7-Br₂** complex shows only 50 ($\text{H}_2 \text{ mol cat}^{-1}$) as shown in Table 2.

Similarly, cobalt bis(iminopyridine) complex **8** was prepared for electrocatalytic water-splitting reaction [73]. The ligand-centered redox activity was observed during the cyclic voltammetry, suggesting the considerable role of redox-active ligand which is completely involved to stabilize the cobalt metal in higher oxidation state. The two reduction potentials were observed for the $\text{Co}^{\text{III}}/\text{Co}^{\text{II}}$ (quasi reversible) and $\text{Co}^{\text{II}}/\text{Co}^{\text{I}}$ (reversible) couples at -0.34 V and -0.86 V (vs. Ag/AgC), respectively. The improved water reduction was attributed to the assimilation of a redox-active-ligand to cobalt which facile reduction of $[\text{Co-H}]^{\text{n+}}$ species.

2.3 Zn^{II} and Cu^{II} complexes for HER

Grappnerhaus et al. [74] recently reported two homogeneous electrocatalysts for H_2 production. They derived bis(thiosemicarbazones) ligand from 1,2-diones, considered as a kind of multitalented redox non-innocent system. Tetra-coordinated N_2S_2 is able to bind with low-valent transition metals centered and formed to stable neutral complexes (**9**, **10**) (Table 1). Zn^{II} complex **9** containing a redox-active

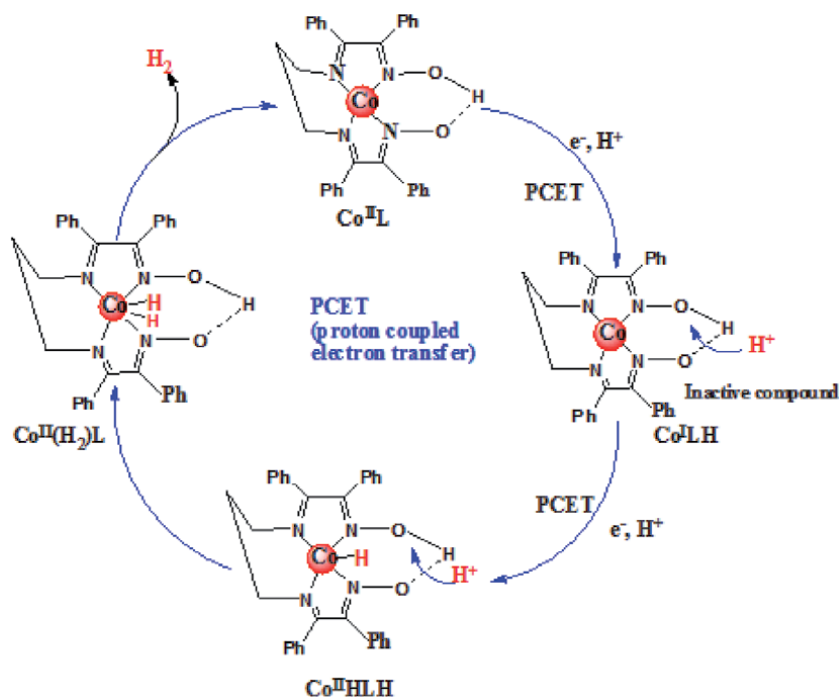


Figure 6. Possible pathway for catalytic hydrogen evolution, involving PCET processes.

moiety diacetyl-bis (N-4 methyl-3-thiosemicarbazide) exhibits the homogeneous catalysis of electro-driven H₂ evolution through proton reduction with a maximum of TOF 1170 s⁻¹ in CH₃OH and 11,700 s⁻¹ in CH₃CN at an overpotential of 0.756 V and 1.074 V, CH₃COOH used as proton source. Bulk electrolysis showed that the TON of H₂ evolution of Zn^{II} is 37 in over 2.5 h experiments. To make this more comparative, Grapperhaus and coworker synthesized another Cu^{II} complex with similar ligand diacetyl-bis(N-4-methyl-3-thiosemicarbazide) and examined H₂ evolution reaction. Cu^{II} complex **10** exhibits a maximum TOF of 10,000 s⁻¹ in CH₃CN and 5100 s⁻¹ in DMF at an overpotential of 0.80 and 0.76 V, respectively. Controlled potential electrolysis confirmed Cu^{II} complex act as an excellent electrocatalyst to produce H₂ with a minimum faradic efficiency of 81% and TON as high as 73 during experiment over 23 h. They examined HER mechanism of complex **10** through DFT computational studies. In the proposed mechanism, initially the protonation occurs at the hydrazino nitrogen ligand. This was followed by an electrochemical step as a formation of reduced Cu^I species [Cu^I(HL)]. The second protonolysis occurs at the opposite hydrazine nitrogen of the ligand to yield [Cu^I(H₂L)]⁺. Further one-electron reduction of [Cu^I(H₂L)]⁺ leads to the formation of the H₂ evolution illustrated in **Figure 7**. Hence, here it is worth to mention that the identity of metal ions at the active site affects the HER mechanism.

Professor Wang and group proposed [75] a significant homogeneous mononuclear copper electrocatalyst for H₂ production attributed to diamine-tripyridine ligand; complex **11** attains trigonal bipyramidal geometry. According to the author, this ionic copper complex [Cu(bztpen)]²⁺ with a five coordinating nitrogen atom shows a Jahn-Teller effect. Electrochemical and spectroscopic studies supported that the H₂ generation reaction takes place by two successive proton-coupled reduction processes. On the experimental observations of DPV, CV, UV-vis, and ¹H-NMR spectroscopic study, the authors proposed two possible pathways: path (A), protonation takes place at the Cu^I centered in the first step (Eqs. (4) and (5)), and path(B), protonation occurs at one of the nitrogen atoms of the ligand (Eqs. (6), (7), and (8)). H₂ generation reaction in path B takes place by two successive proton-coupled reduction processes. Protonation occurs at the ligand centered in the first reduction step, followed by the Cu^I centered in the second step. This provides [(bztpenH)Cu^{II}(H)]²⁺ copper hydride species, which release H₂ and regenerate Cu^{II} catalyst.

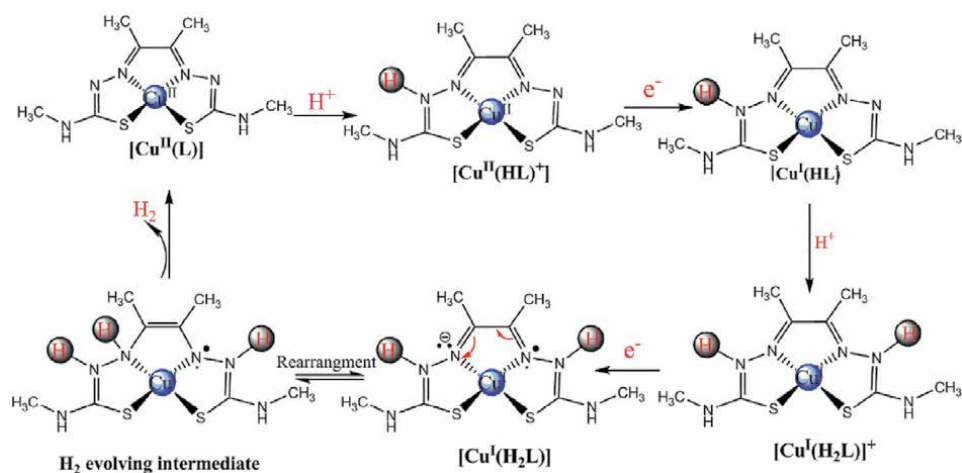
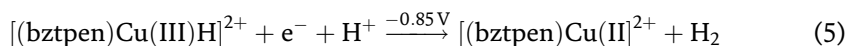
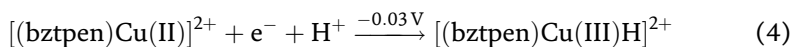
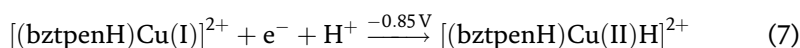
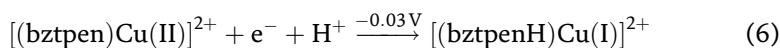


Figure 7.
Plausible mechanism for proton reduction in complex [CuL].

Path A:



Path B:



According to the author's studies on the mechanism of this process, the controlled potential electrolysis of complex **11** was measured at pH 2.5 in phosphate buffer at -0.90 V, over 2 h in a glassy carbon electrode. TON 1.4×10^4 mol H_2 (mol cat^{-1}) cm^{-2} was calculated on a faradic efficiency of approximately 96%, which corresponds to a TOF of 2.0 mol H_2 (mol cat^{-1}) $\text{s}^{-1}\text{cm}^{-2}$ of $[(\text{bztpen})\text{Cu}](\text{BF}_4)_2$.

Moreover, Wang et al. [76] fabricated and examined two Cu complexes with TMPA = tris(2-pyridyl)methylamine and Cl-TMPA 1-(6-chloropyridin-2-yl)methyl-*N,N*-bis(pyridin-2-ylmethyl)methaneamine for photocatalytic H_2 evolution behavior. They observed both in Cu(II) complexes $[\text{Cu}(\text{TMPA})\text{Cl}]\text{Cl}$ (**12**) and $[\text{Cu}(\text{Cl-TMPA})\text{Cl}_2]$ (**13**) that (**13**) is far efficient for photocatalytic H_2 production than (**12**), due to the presence of more labile Cl ligand with longer Cu-Cl bond length and a dangling Cl-substituted pyridyl unit in the second coordination sphere, which both contribute to a higher photocatalytic activity of complex (**13**). TMPA acts as a tetradentate ligand and coordinate with Cu(II) in a distorted trigonal manner; Cl-TMPA acts as a tridentate ligand coordinate to Cu(II) with two chloride ions in a distorted square pyramidal manner, leaving one Cl-substituted pyridyl group in the second coordination sphere structure which is given in **Table 1**. ESI-MS data favor the formation of Cu-hydride intermediate for hydrogen evolution. The authors investigated the photocatalytic H_2 production activities in the presence of a multicomponent $[\text{Ir}(\text{ppy})_2(\text{dtbpy})]\text{Cl}$ (ppy = 2-phenylpyridine, dtbpy = 4,4'-di-*tert*-butyl-2,2'-bipyridine) and triethylamine (TEA) photosystems as sacrificial reductant (SR) under optimal condition upon 6 h of irradiation of UV-visible light, the turnover number (TON) of which is calculated as 6108 for complex (**12**) and 10,014 for complex (**13**).

Based on the control potential electrolysis experimental data, the authors proposed photocatalytic hydrogen evolution mechanism. In the first step, excited PS system takes out one electron from TEA and donates to Cu^{II} center of complex (**13**). The protonated Cl-substituted pyridyl unit accepts that electron and kicks out the Cu-Cl center for the dissociation of Cl ligand which is substituted at the apical position which is more labile (longest bond length Cu-Cl). After that, the Cu^{I} species accept one e^{-} and one H^{+} from the reduced Cl-substituted pyridinium moiety; $\text{Cu}^{\text{II}}\text{-H}$ center is formed as a key intermediate which lead to H_2 evolution. This executive mechanism provides us guidelines to design more efficient Cu-based catalysts for WRCs in the near future (**Figure 8**).

2.4 Ni electrocatalysts for HER

Professor Richard Eisenberg and coworker [77] synthesized a sequence of nickel bis(chelate) complexes; all complexes attained square planar geometry and examined photocatalytic as well as electrocatalytic behavior for hydrogen evolution.

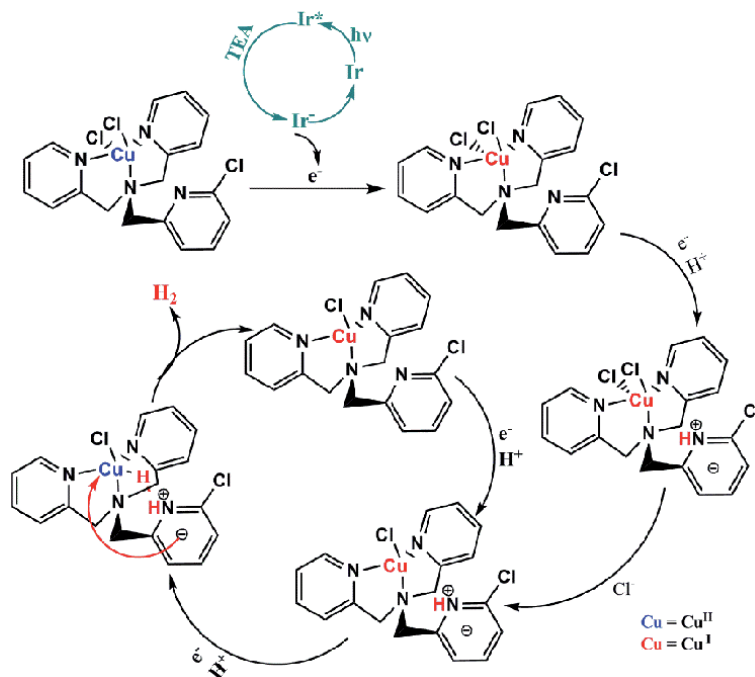


Figure 8.
 Photocatalytic H_2 evolution mechanism for complex $[Cu(Cl-TMPA)Cl_2]$ **12**.

Fluorescein (Fl) as the photosensitizer along with triethanolamine (TEOA) as the sacrificial electron donor was used in water under basic medium ($pH = 9.8$). Bis(chelate) complexes (**14–17**) contain bdt(bisdithiolate) and their derivatives having S, O, or N as donors for coordination to the Ni center. The photochemical study reveals that only complexes **15** and **17** exhibited similar activity of hydrogen production in terms of TON (6000 mol of H_2 per mole of catalyst in 100 h). In contrast, the TON for the sample complex **16** was much lower (~ 900). Complex **14** was observed to be inactive for hydrogen generation. To understand the better significant result, the authors pursued electrochemical experiments under a fixed potential to examine the catalytic activity of complexes. In the absence of acid, both monoanionic complexes **14** and **17** exhibit only one reversible redox couple at -0.56 and -0.45 V, respectively, which is attributed to the $[NiL_2]^-/[NiL_2]^{2-}$ ligand-based reductions. The neutral complexes **15** and **16** exhibit two reversible reduction waves at -0.11 and -0.94 V and at -0.89 and -1.53 V, respectively. However, on increasing the concentration of acetic acid to these solutions, more negative catalytic waves were observed in cyclic voltammetry study. Complex **14** shows much more negative reduction potential (-2.25) which suggested this system is inactive for H_2 generation (as we discussed earlier). As is the case for complex **14**, **complex 16** exhibits a catalytic wave potential at -2.03 V which showed poor activity for H_2 generation as a consequence of not favorable electron transfer step from Fl^- to the catalyst. Moreover, complexes **15** and **17** show activity for light-driven H_2 generation; these two complexes display electrocatalytic wave potential at significantly less negative at -1.64 and -1.62 V, respectively.

3. Concluding remarks and future scope

Here we present a recent development of molecular catalysts toward clean and renewable fuels using earth-abundant metals. We have highlighted a series of Co-,

Ni-, Cu-, Zn-based complexes for HER. We have recapitulated the fundamental principles of hydrogen and oxygen evolution reactions with molecular complexes. The designing and fabrication of the molecular complexes with redox-active ligands have been discussed in details; HER activity of the complexes strongly dependent on redox-active ligands as well the central metal ions are discussed in detail. A mechanistic approach and transfer of electron and proton during the homogeneous electrocatalyst and photocatalysts cycle are given in point. Although reasonable progress has been made in the development of metal complexes based electrocatalysts and chromospheres for photocatalytic hydrogen production, still several issues exist which need further improvement: (i) some photocatalytic systems suffer from low activities and short life times which is manifested in the instability of catalytic systems and so concern on the systems with modest water splitting activity and poor stability of the complexes. (ii) most of the complexes are not soluble in water leading to the use of organic solvent or mixture of organic-water solvent. From the future prospective, it is required to develop redox-active ligands with substituted functional group to increase the solubility of complexes in water. More experimental, spectroscopic, magnetic, and theoretical investigations is still needed to be carried out in order to understand the ligand- and metal-centered electron transfer processes. (iii) In addition, the overpotential requirements for most of the organic ligands are still very high, a chelating ligands giving much lower thermodynamic potentials and much smaller oxidation potential that should be utilized in future. (iv) In the regard of future growth in this field, with the need to design molecular complexes that can be immobilized on the surface of the electrode, for this purpose addition of suitable functional group in the ligand is necessity. These complexes can also be supported by the development of surface of the solid photocatalyst, like TiO_2 , BiVO_4 , etc. to demonstrate efficient photoelectrochemical cell.

Acknowledgements

The authors acknowledges the helps received from Ms. Priyadarshini Sahu and Mr. Abhineet Verma during the manuscript preparation.

Author details

Shipra Sagar¹, Ravi K. Kanaparthi², Manish K. Tiwari³ and Satyen Saha^{3*}


1 Department of Chemistry, Central University of Jharkhand, Ranchi, India

2 Department of Chemistry, Central University of Kerala, Kerala, India

3 Department of Chemistry, Institute of Science, Banaras Hindu University, Varanasi, India

*Address all correspondence to: satyen.saha@gmail.com

IntechOpen

© 2020 The Author(s). Licensee IntechOpen. This chapter is distributed under the terms of the Creative Commons Attribution License (<http://creativecommons.org/licenses/by/3.0>), which permits unrestricted use, distribution, and reproduction in any medium, provided the original work is properly cited. 

References

- [1] Lewis NS, Nocera DG. Powering the planet: Chemical challenges in solar energy utilization. *Proceedings of the National Academy of Sciences of the United States of America*. 2006;**103**: 15729-15735
- [2] Kim D, Sakimoto KK, Hong D, Yang P. Artificial photosynthesis for sustainable fuel and chemical production. *Angewandte Chemie, International Edition*. 2015;**54**: 3259-3266
- [3] Esswein AJ, Nocera DG. Hydrogen production by molecular photocatalysis. *Chemical Reviews*. 2007;**107**:4022-4047
- [4] Tollefson J. Green carbon as a bridge to renewable energy. *Nature*. 2010;**464**: 1262-1264
- [5] Pagliaro M, Konstandopoulos AG, Ciriminna R, Palmisano G. Solar hydrogen: Fuel of the near future. *Energy & Environmental Science*. 2010; **3**:279-287
- [6] Armaroli N, Balzani V. The hydrogen issue. *ChemSusChem*. 2011;**4**:21-36
- [7] Nocera DG. Solar fuels and solar chemicals industry. *Accounts of Chemical Research*. 2017;**50**:616-619
- [8] Stamenkovic VR, Strmcnik D, Lopes PP, Markovic NM. Energy and fuels from electrochemical interfaces. *Nature Materials*. 2017;**16**:57-69
- [9] Hwang J, Rao RR, Giordano L, Katayama Y, Yu Y, Shao-Horn Y. Perovskites in catalysis and electrocatalysis. *Science*. 2017;**358**: 751-756
- [10] Andreiadis ES, Chavarot-Kerlidou M, Fontecave M, Artero V. Artificial photosynthesis: From molecular catalysts for light-driven water splitting to photoelectrochemical cells. *Photochemistry and Photobiology*. 2011; **87**:946-964
- [11] Joya KS, Joya YF, Ocakoglu K, van de Krol R. Water-splitting catalysis and solar fuel devices: Artificial leaves on the move. *Angewandte Chemie, International Edition*. 2013;**52**: 10426-10437
- [12] Berardi S, Drouet S, Francis L, Gimbert-Surinach C, Guttentag M, Richmond C, et al. Visible light driven water splitting in a molecular device with unprecedentedly high photocurrent density. *Chemical Society Reviews*. 2014;**43**:7501-7519
- [13] Song W, Chen Z, Brennaman MK, Concepcion JJ, Patrocinio AOT, Iha NYM, et al. Making solar fuels by artificial photosynthesis. *Pure and Applied Chemistry*. 2011;**83**:749-768
- [14] Gust D, Moore TA, Moore AL. Solar fuels via artificial photosynthesis. *Accounts of Chemical Research*. 2009; **42**:1890-1898
- [15] Zou Z, Ye J, Sayama K, Arakawa H. Direct splitting of water under visible light irradiation with an oxide semiconductor photocatalyst. *Nature*. 2001;**414**:625-627
- [16] Hara M, Kondo T, Komoda M, Ikeda S, Shinohara K, Tanaka A, et al. Cu₂O as a photocatalyst for overall water splitting under visible light irradiation. *Chemical Communications*. 1998;**3**:357-358
- [17] Wang X, Xu Q, Li M, Shen S, Wang X, Wang Y, et al. Photocatalytic overall water splitting promoted by an α - β phase junction on Ga₂O₃. *Angewandte Chemie, International Edition*. 2012;**51**:13089-13092
- [18] Liao L, Zhang Q, Su Z, Zhao Z, Wang Y, Li Y, et al. Efficient solar

- water-splitting using a nanocrystalline Co-O photocatalyst. *Nature Nanotechnology*. 2014;**9**:69-73
- [19] Balat M. Potential importance of hydrogen as a future solution to environmental and transportation problems. *International Journal of Hydrogen Energy*. 2008;**33**: 4013-4029
- [20] Wang M, Wang Z, Gong X, Guo Z. The intensification technologies to water electrolysis for hydrogen production, a review. *Renewable and Sustainable Energy Reviews*. 2014;**29**: 573-588
- [21] Xu Y, Kraft M, Xu R. Metal-free carbonaceous electrocatalysts and photocatalysts for water splitting. *Chemical Society Reviews*. 2016;**45**: 3039-3052
- [22] Oshima T, Lu D, Ishitani O, Maeda K. Intercalation of highly dispersed metal nanoclusters into a layered metal oxide for photocatalytic overall water splitting. *Angewandte Chemie, International Edition*. 2015;**54**: 2698-2702
- [23] Chen X, Shen S, Guo L, Mao SS. Semiconductor-based photocatalytic hydrogen generation. *Chemical Reviews*. 2010;**110**:6503-6570
- [24] Rausch B, Symes MD, Chisholm G, Cronin L. Decoupled catalytic hydrogen evolution from a molecular metal oxide redox mediator in water splitting. *Science*. 2014;**345**:1326-1330
- [25] Symes MD, Cronin L. Decoupling hydrogen and oxygen evolution during electrolytic water splitting using an electron-coupled-proton buffer. *Nature Chemistry*. 2013;**5**:403-409
- [26] Rausch B, Symes MD, Cronin L. A bio-inspired, small molecule electron-coupled proton buffer for decoupling the half-reactions of electrolytic water splitting. *Journal of the American Chemical Society*. 2013; **135**:13656-13659
- [27] Zou Z, Ye J, Sayama K, Arakawa H. Direct splitting of water under visible light irradiation with an oxide semiconductor photocatalyst. *Nature*. 2001;**414**:625-627
- [28] Zhang P, Wang M, Li C, Li X, Dong J, Sun L. Photochemical H₂ production with noble-metal-free molecular devices comprising a porphyrin photosensitizer and a cobaloxime catalyst. *Chemical Communications*. 2010;**46**:8806-8809
- [29] Bartelmess J, Weare WW, Sommer RD. Synthesis, characterization and structural investigation of novel *meso*-pyridyl BODIPY-cobaloxime complexes. *Dalton Transactions*. 2013; **42**:14883-14891
- [30] Yuan YJ, Tu JR, Lu HW, Yu ZT, Fan XX, Zou ZG. Neutral nickel(II) phthalocyanine as a stable catalyst for visible-light-driven hydrogen evolution from water. *Dalton Transactions*. 2016; **45**:1359-1363
- [31] Karunadasa HI, Chang CJ, Long JR. A molecular molybdenum-oxo catalyst for generating hydrogen from water. *Nature*. 2010;**464**:1329-1333
- [32] Kok B, Forbush B, McGloin M. Cooperation of charges in photosynthetic O₂ evolution - I, a linear four step mechanism. *Photochemistry and Photobiology*. 1970; **11**:457-475
- [33] Askerka M, Brudvig GW, Batista VS. The O₂-evolving complex of photosystem II: recent insights from quantum mechanics/molecular mechanics (QM/MM), extended x-ray absorption fine structure (EXAFS), and femtosecond x-ray crystallography data. *Accounts of Chemical Research*. 2017; **50**:41-48

- [34] Morales-Guio CG, Stern L, Hu X. Nanostructured hydro treating catalysts for electrochemical hydrogen evolution. *Chemical Society Reviews*. 2014;**43**: 6555-6569
- [35] Laursen AB, Patraju KR, Whitaker MJ, Retuerto M, Sarkar T, Yao N, et al. Nanocrystalline Ni₅P₄: A hydrogen evolution electrocatalyst of exceptional efficiency in both alkaline and acidic media. *Energy & Environmental Science*. 2015;**8**: 1027-1034
- [36] Huang Z, Chen Z, Chen Z, Lv C, Meng H, Zhang C. Ni₁₂P₅ nanoparticles as an efficient catalyst for hydrogen generation via electrolysis and photoelectrolysis. *ACS Nano*. 2014;**8**: 8121-8129
- [37] Feng L, Vrubel H, Bensimon M, Hu X. Easily-prepared dinickel phosphide (Ni₂P) nanoparticles as an efficient and robust electrocatalyst for hydrogen evolution. *Physical Chemistry Chemical Physics*. 2014;**16**: 5917-5921
- [38] Li R, Li C. Chapter one- Photocatalytic water splitting on semiconductor-based Photocatalysts. *Advances in Catalysis*. 2017;**60**:1-57
- [39] Vozniuk O, Tanchoux N, Millet JM, Albonetti S, Di Renzo F, Cavani F. *Horizons in Sustainable Industrial Chemistry and Catalysis*. Vol. 178. Elsevier; 2019. pp. 281-302
- [40] Yuan Y-J, Yu Z-T, Chen D-Q, Zou Z-G. Metal-complex chromophores for solar hydrogen generation. *Chemical Society Reviews*. 2017;**46**:603-631
- [41] Tschierlei S, Karnahl M, Presselt M, Dietzek B, Guthmuller J, González L, et al. Photochemical fate: The first step determines efficiency of H₂ formation with a supramolecular photocatalysts. *Angewandte Chemie, International Edition*. 2010;**49**:3981-3984
- [42] Fukuzumi S, Kobayashi T, Suenobu T. Photocatalytic production of hydrogen by disproportionation of one-electron-reduced rhodium and iridium-ruthenium complexes in water. *Angewandte Chemie, International Edition*. 2011;**50**:728-731
- [43] Stoll T, Gennari M, Fortage J, Castillo CE, Rebarz M, Sliwa M, et al. An efficient Ru(II) -Rh(III) -Ru(II) polypyridyl photocatalyst for visible-light-driven hydrogen production in aqueous solution. *Angewandte Chemie, International Edition*. 2014;**53**:1654-1658
- [44] Khine Ma SS, Hisatomi T, Domen K. Hydrogen production by photocatalytic water splitting. *Journal of Japan Petroleum Institute*. 2013;**56**(5):280-287
- [45] Adams RE, Grusenmeyer TA, Griffith AL, Schmehl RH. Transition metal hydride complexes as mechanistic models for proton reduction catalysis. *Coordination Chemistry Reviews*. 2018; **362**:44-53
- [46] Berardi S, Drouet S, Franca L, Gimbert-Suriñach C, Guttentag M, Richmond C, et al. Molecular artificial photosynthesis. *Chemical Society Reviews*. 2014;**43**:7501-7519
- [47] Robinson SJC, Heinekey DM. Hydride & dihydrogen complexes of earth abundant metals: Structure, reactivity, and applications to catalysis. *Chemical Communications*. 2017;**53**: 669-676
- [48] Schilter D, Camara JM, Huynh MT, Hammes-Schiffer S, Rauchfuss TB. Hydrogenase enzymes and their synthetic models: The role of metal hydride. *Chemical Reviews*. 2016;**116**: 8693-8749
- [49] Gärtner F, Sundararaju B, Surkus AE, Boddien A, Loges B, Junge H, et al. Light-driven hydrogen generation: Efficient iron-based water reduction catalysis. *Angewandte*

- Chemie, International Edition. 2009;**48**: 9962-9965
- [50] Hollmann D, Gärtner F, Ludwig R, Barsch E, Junge H, Blug M, et al. Insights into the mechanism of photocatalytic water reduction by DFT supported in situ EPR/Raman spectroscopy. *Angewandte Chemie, International Edition*. 2011;**50**:10246-10250
- [51] Gärtner F, Boddien A, Barsch E, Fumino K, Losse S, Junge H, et al. Photocatalytic hydrogen generation from water with iron carbonyl phosphine complexes: Improved water reduction catalysts and mechanistic insights. *Chemistry - A European Journal*. 2011;**17**:6425-6436
- [52] Gartner F, Cozzula D, Losse S, Boddien A, Anilkumar G, Junge H, et al. Synthesis, characterisation and application of iridium(III) photosensitisers for catalytic water reduction. *Chemistry - A European Journal*. 2011;**17**:6998-7006
- [53] Yuan YJ, Yu ZT, Gao HL, Zou ZG, Zheng C, Huang W. Tricyclometalated iridium complexes as highly stable photosensitizers for light-induced hydrogen evolution. *Chemistry - A European Journal*. 2013;**19**:6340-6349
- [54] Lazarides T, Delor M, Sazanovich IV, McCormick TM, Georgakaki I, Charalambidis G, et al. Coutsolelos, Photocatalytic hydrogen production from a noble metal free system based on a water soluble porphyrin derivative and acobaloxime catalyst. *Chemical Communications*. 2014;**50**:521-523
- [55] Muckerman JT, Fujita E. Theoretical studies of the mechanism of catalytic hydrogen production by a cobaloxime. *Chemical Communications*. 2011;**47** (46):12456-12458
- [56] Nazeeruddin MK, Diau EWG, Yeh CY, Zakeeruddin SM, Gratzel M. Porphyrin-sensitized solar cells with cobalt (II/III)-based redox electrolyte exceed 12 percent efficiency. *Science*. 2011;**334**:629-634
- [57] Franco F, Cometto C, Nencini L, Barolo C, Sordello F, Minero C, et al. Local proton source in electrocatalytic CO₂ reduction with [Mn(bpy-R)(CO)₃Br] complexes. *Chemistry - A European Journal*. 2017;**23**:4782-4793
- [58] Luca OR, Crabtree RH. Redox active ligands in catalysis. *Chemical Society Reviews*. 2013;**42**:1440-1459
- [59] Lyaskovskyy V, de Bruin B. Redox non-innocent ligands: Versatile new tools to control catalytic reactions. *ACS Catalysis*. 2012;**22**:270-279
- [60] Thompson EJ, Berben LA. Electrocatalytic hydrogen production by an aluminium (III) complex: Ligand-based proton and electron transfer. *Angewandte Chemie, International Edition*. 2015;**54**:11642-11646
- [61] Solis BH, Maher AG, Dogutan DK, Nocera DG, Hammes-Schiffer S. Nickel phlorin intermediate formed by proton-coupled electron transfer in hydrogen evolution mechanism. *Proceedings of the National Academy of Sciences of the United States of America*. 2015;**113**: 485-492
- [62] Luo G-G, Zhang H-L, Tao Y-W, Wu Q-Y, Tian D, Zhang Q. Recent progress in ligand-centered homogeneous electrocatalysts for hydrogen evolution reaction. *Inorganic Chemistry Frontiers*. 2019;**6**:343-354
- [63] Ran J, Zhang J, Yu J, Jaroniec M, Qiao SZ. Earth-abundant cocatalysts for semiconductor-based photocatalytic water splitting. *Chemical Society Reviews*. 2014;**43**:7787-7812
- [64] Berardi S, Drouet S, Francas L, Gimbert-Surinach C, Guttentag M, Richmond C, et al. Molecular artificial

- photosynthesis. Chemical Society Reviews. 2014;**43**:7501-7519
- [65] Yoshida M, Ueno S, Okano Y, Usui A, Kobayashi A, Kato M. Photochemical hydrogen production from 3d transition-metal complexes bearing *o*-phenylenediamine ligands. Journal of Photochemistry and Photobiology A: Chemistry. 2015;**313**: 99-106
- [66] Konno Y, Matsushita N. pH-dependent color-change behavior of bis (*o*-phenylenediamine) platinum(II) complex and pH-dependent redox of bis (*o*-semibenzoquinonediimine)platinum (II) complex. Chemical Society of Japan. 2006;**79**:1046-1053
- [67] Matsumoto T, Chang HC, Wakizaka M, Ueno S, Kobayashi A, Nakayama A, et al. Nonprecious-metal-assisted photochemical hydrogen production from *ortho*-Phenylenediamine J. American Chemical Society. 2013;**135**:8646-8654
- [68] Roberts GM, Williams CA, Young JD, Ullrich S, Paterson MJ, Stavros VG. Unraveling ultrafast dynamics in photoexcited aniline. Journal of the American Chemical Society. 2012;**134**:12578-12589
- [69] Keffer N, Chavarot-Kerlidou M, Artero V. Hydrogen evolution catalyzed by cobaltdiimine-dioxime complexes Acc. Chemistry Research. 2015;**48**: 1286-1295
- [70] Giorgetti M, Berrettoni M, Ascone I, Zamponi S, Seeber R, Marassi R. X-ray absorption spectroscopy study on the electrochemical reduction of Co((DO) (DOH) pn)Br₂. Electrochimica Acta. 2000;**45**:4475-4482
- [71] Zhang P, Jacques PA, Chavarot-Kerlidou M, Wang M, Sun L, Fontecave M, et al. Phosphine coordination to a cobalt diimine-dioxime catalyst increases stability during light-driven H₂ production. Inorganic Chemistry. 2012;**51**:2115-2120
- [72] Haddad AZ, Garabato BD, Kozlowski PM, Buchanan RM, Grapperhaus CA. Beyond metal-hydrides: Non-transition-metal and metal-free ligand-centered electrocatalytic hydrogen evolution and hydrogen oxidation. Journal of the American Chemical Society. 2016;**138**: 7844-7847
- [73] Stubbert BD, Peters JC, Gray HB. Journal of the American Chemical Society. 2011;**133**:18070-18073
- [74] Haddad AZ, Cronin SP, Mashuta MS, Buchanan RM, Grapperhaus CA. Metal-assisted ligand centered electrocatalytic hydrogen evolution upon reduction of a bis (thiosemicarbazonato)Cu(II) complex. Inorganic Chemistry. 2017;**56**: 11254-11265
- [75] Zhang P, Wang M, Yang Y, Yao T, Sun L. A molecular copper catalyst for electrochemical water reduction with a large hydrogen-generation rate constant in aqueous solution. Angewandte Chemie, International Edition. 2014; **53**(50):13806-13807
- [76] Wang J, Li C, Zhou Q, Wang W, Hou Y, Zhang B, et al. Photocatalytic hydrogen evolution by Cu(II) complexes. Dalton Transactions. 2016; **45**:5439-5443
- [77] Das A, Han Z, Brennessel WW, Holland PL, Eisenberg R. Nickel complexes for robust light-driven and electrocatalytic hydrogen production from water. ACS Catalysis. 2015;**5**: 1397-1406

Arsenomolybdates for Photocatalytic Degradation of Organic Dyes

Zhi-Feng Zhao

Abstract

Polyoxometalates (POMs) have fascinating structures and promising properties. The arsenomolybdates, as an important branch of POMs, are outstanding photocatalysts for organic dyes. In this work, we selected organic dyes to evaluate the photocatalytic activity of arsenomolybdates under UV light, containing compared with photocatalytic activity of different structural arsenomolybdates, stability, and the photocatalytic reaction mechanism of arsenomolybdates as photocatalyst. The arsenomolybdates may be used to as environmental photocatalysts for the degrading of organic dyes and solving the problem of environmental pollution.

Keywords: arsenomolybdates, photocatalyst, photocatalytic activity, organic dyes, UV light

1. Introduction

POMs is one of the most outstanding materials in modern chemistry, as the metal-oxide clusters with abundant structures and interesting properties [1–6], which render them to potential applications in electrochemistry [7, 8], photochemistry [9, 10], catalytic fields [11, 12], and so on (**Figure 1**). Chalkley reported the photoredox conversion of $\text{H}_3[\text{PW}_{12}\text{O}_{40}]$ into a reduced POM by photoirradiation with UV light in the presence of 2-propanol as a reducing reagent in 1952 [13]. Hill et al. started systematic investigation of photoredox catalysis using POMs in the 1980s [14]. Accordingly, POMs photocatalysis has been applied to a wide range of reactions, including H_2 evolution, O_2 evolution, CO_2 reduction, metal reduction, and the degradation of organic pollutants and dyes [15–20].

POMs are subdivided into isopolyoxometalates, which feature addenda metal and oxygen atoms, and heteropolyoxometalates, where a central heteroatom provides added structural stabilization and enables reactivity tuning [21]. In recent years, the research of POMs is mainly focused on heteropolyoxometalates. The arsenomolybdates are essential member of the heteropolymolybdates family [22], because of the redox properties of Mo and As atoms. The discoveries of many excellent articles on arsenomolybdates for ferromagnetic, antitumor activity, electrocatalysis properties, and lithium-ion battery performance have been reported in the last years [23–26]. However, there is no stress and discuss on the progress of arsenomolybdates for degradation of organic dyes. Arsenomolybdates possess

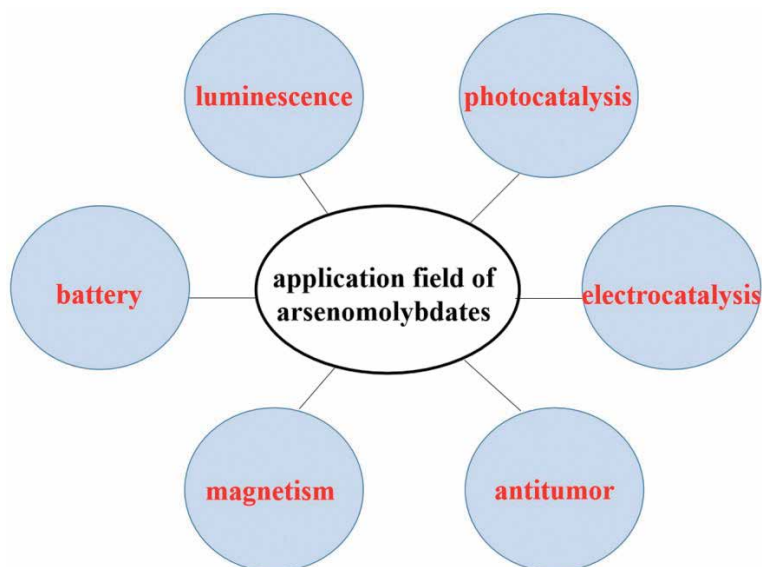


Figure 1.
The potential application field of arsenomolybdates.

high-efficient proton delivery, fast multi-electron transfer, strong solid acidity and excellent reversible redox activity [27], which may result to prominent photocatalytic activities. In particular, the integration of metal-organic frameworks (MOFs) into arsenomolybdates for photocatalysis has attracted widespread attention over the past decade, since MOFs combine porous structural and ultrahigh internal surface areas.

Based on these results, we provide a summary of recent works in the synthesis, structure, the photocatalytic activity, reaction kinetics and mechanism mechanisms of arsenomolybdates, which aim at finding the direction followed with the opportunities and challenges for the arsenomolybdates photocatalysis to accelerate the step to realize its practical application in degradation of organic dyes.

2. Syntheses and structure of arsenomolybdates

2.1 Syntheses of arsenomolybdates

Arsonomolybdates crystals reported were almost synthesized via self-assembly processes using hydrothermal method (**Figure 2**). Many factors in the synthetic process should be considered, such as reaction time and temperature, concentration of starting materials, compactness, pH values, and so on. The some experiments indicate that the temperatures are in the range of 110–180°C for srsonomolybdates synthesized, when the pH value of the mixture is adjusted to approximately 3–6.8, $[\text{H}_x\text{As}_2\text{Mo}_6\text{O}_{26}]^{(6-x)-}$ (abbreviated $\{\text{As}_2\text{Mo}_6\}$), $[(\text{MO}_6)(\text{As}_3\text{O}_3)_2\text{Mo}_6\text{O}_{18}]^{4-}$ (abbreviated $\{\text{As}_6\text{Mo}_6\}$) and $[\text{As}^{\text{III}}\text{As}^{\text{V}}\text{Mo}_9\text{O}_{34}]^{6-}$ (abbreviated $\{\text{As}_2\text{Mo}_9\}$) types were easy to formed, when the pH value is within the range of 2.5–5.5 and 2–4, $[\text{AsMo}_{12}\text{O}_{40}]^{3-}$ (abbreviated $\{\text{AsMo}_{12}\}$) and $[\text{As}_2\text{Mo}_{18}\text{O}_{62}]^{6-}$ (abbreviated $\{\text{As}_2\text{Mo}_{18}\}$) types were successfully synthesized. At the same time, the choice of transition metal, organic ligand, and molybdenic source have also affect for

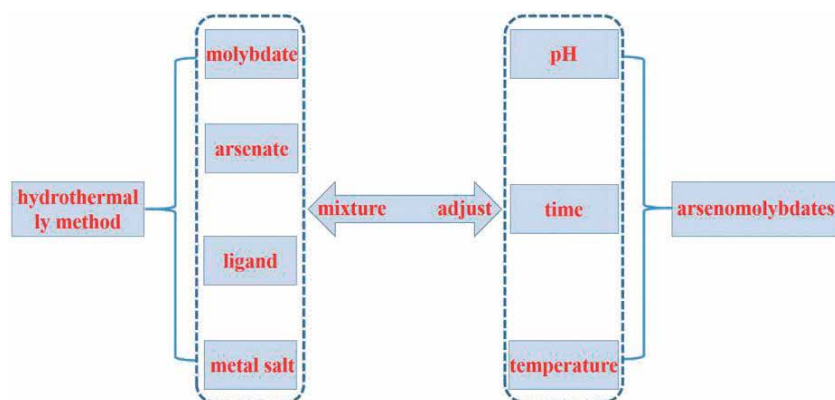


Figure 2.
 The synthesis chart of arsenomolybdates crystal.

arsenomolybdates crystals. Therefore, further exploration of synthetic conditions is necessary, which can provide more experimental data for arsenomolybdates.

2.2 Structure of classical arsenomolybdates

Up to now, various structures of arsenomolybdates were reported and discussed in detail. The following types are classical arsenomolybdates clusters: (i) $\{\text{As}_2\text{Mo}_6\}$ type, Pope's group reported the first $\{\text{As}_2\text{Mo}_6\}$ cluster [28], in which the Mo_6O_6 ring is constructed from six MoO_6 octahedra connected via an edge-sharing mode, the opposing faces have two capped AsO_4 tetrahedra. Then Zubieta's group and Ma's group reported $[\text{Mo}_x\text{O}_y\text{RAsO}_3]^{n-}$ ($\text{RAsO}_3 = \text{organoarsenic acid}$) and $[\text{Mo}_6\text{O}_{18}(\text{O}_3\text{AsPh})_2]^{4-}$ ($\text{Ph} = \text{PhAsO}_3\text{H}_2$) clusters [29, 30]. (ii) $\{\text{As}_6\text{Mo}_6\}$ type, which is derived from the A-type Anderson anion $[(\text{Mo}_6)\text{Mo}_6\text{O}_{18}]^{10-}$, the central $\{\text{Mo}_6\}$ octahedron is coordinated with six $\{\text{MoO}_6\}$ octahedra hexagonally arranged by sharing their edges in a plane. The cyclic As_3O_6 trimers are capped on opposite faces of Anderson-type anion plane. Each As_3O_6 group consists of three AsO_3 pyramids linked in a triangular arrangement by sharing corners and bonded to the central Mo_6 octahedron and two MoO_6 octahedra via μ_3 -oxo groups. Wang and co-workers reported the compound $(\text{C}_5\text{H}_5\text{NH})_2(\text{H}_3\text{O})_2[(\text{CuO}_6)\text{Mo}_6\text{O}_{18}(\text{As}_3\text{O}_3)_2]$ [31], Zhao groups synthesized the compound $[\text{Cu}(\text{arg})_2]_2[(\text{CuO}_6)\text{Mo}_6\text{O}_{18}(\text{As}_3\text{O}_3)_2] \cdot 4\text{H}_2\text{O}$ [32]. (iii) $\{\text{AsMo}_{12}\}$ type, has a AsO_4 tetrahedron at the center and 12 surrounding MoO_6 octahedra, such as $[\text{NBu}_4]_6[\text{Fe}(\text{C}_5\text{H}_5)_2][\text{HAsMo}_{12}\text{O}_{40}]_2$ [33]. $\{\text{As}_2\text{Mo}_9\}$ type, is derived from the trivacant Keggin moiety, which is capped by a triangular pyramidal $\{\text{AsO}_3\}$ group, e.g., $[\text{Cu}(\text{en})_2\text{H}_2\text{O}]_2\{[\text{Cu}(\text{en})_2][\text{Cu}(\text{en})_2\text{As}^{\text{III}}\text{As}^{\text{V}}\text{Mo}_9\text{O}_{34}]\} \cdot 2 \cdot 4\text{H}_2\text{O}$ and $[\text{Cu}(\text{en})_2(\text{H}_2\text{O})]_4[\text{Cu}(\text{en})_2(\text{H}_2\text{O})_2]\{[\text{Cu}(\text{phen})(\text{en})][\text{As}^{\text{III}}\text{As}^{\text{V}}\text{Mo}^{\text{VI}}_9\text{O}_{34}]_2\}$ [34, 35]. (iv) $\{\text{As}_2\text{Mo}_{18}\}$ type, as a classical Wells–Dawson cluster, can be described as two $[\text{AsMo}_9\text{O}_{34}]^{9-}$ units derived from an Keggin anion by the removal of a set of three corner-sharing MoO_6 octahedra, e.g., $[\text{Himi}]_6[\text{As}_2\text{Mo}_{18}\text{O}_{62}] \cdot 11\text{H}_2\text{O}$ [36].

In comparison with the classical arsenomolybdates, many nonclassical arsenomolybdates have also been prepared in the past of years, such as $\text{Ag}_{12.4}\text{Na}_{1.6}\text{Mo}_{18}\text{As}_4\text{O}_{71}$ [37], $(\text{NH}_4)_{11}[\text{AgAs}_2\text{Mo}_{15}\text{O}_{54}]_3 \cdot 6\text{H}_2\text{O} \cdot 2\text{CH}_3\text{CN}$ [38], $[\text{As}^{\text{III}}_2\text{Fe}^{\text{III}}_5\text{MMo}_{22}\text{O}_{85}(\text{H}_2\text{O})]^{n-}$ ($\text{M} = \text{Fe}^{3+}$, $n = 14$; $\text{M} = \text{Ni}^{2+}$ and Mn^{2+} , $n = 15$) [39], $\{\text{Cu}(2,2'\text{-bpy})\}_2\{\text{H}_2\text{As}_2\text{Mo}_2\text{O}_{14}\}$ [40], $\{[\text{Cu}(\text{imi})_2]_3\text{As}_3\text{Mo}_3\text{O}_{15}\} \cdot \text{H}_2\text{O}$ [41], and so on. The novel arsenomolybdate structure is gaining more and more attention.

3. Photocatalytic activity of arsenomolybdates

3.1 Photodegradation process

In recent years, POMs have attracted a lot of attention as photocatalysts for the decomposition of wastewater [42]. Organic dyes, such as methylene blue (MB), rhodamine B (RhB), azon phloxine (AP), and so on, is a typical organic pollutant in waste water. In this work, the photocatalytic activities of arsenomolybdates are investigated via the photodecomposition of organic dyes under UV light irradiation (**Figure 3**). The photocatalytic reactions were conducted using a common process [27]: arsenomolybdates and organic dyes solution were mixed and dispersed by ultrasonic. The suspension was stirred until reached the surface-adsorption equilibrium. Then, a high pressure Hg lamp was used as light source to irradiate the mixture, which was till stirred for keeping the mixture in suspension. At regular intervals, the sample was withdrawn from the vessel and arsenomolybdates was removed by several centrifugations, and the clear liquid was analyzed by using UV-Vis spectrophotometer.

3.2 Photocatalytic degradation of MB

The common arsenomolybdates photocatalysis are shown in **Figure 4**. The photocatalytic activities of arsenomolybdates are review via the photodecomposition of MB under UV light irradiation (**Figure 5**). Su groups reported six compounds with $[H_xAs_2Mo_6O_{26}]^{(6-x)-}$ clusters and copper-organic complexes. Six $\{As_2Mo_6\}$ compounds were irradiated for 135 min under, the photocatalytic decomposition rates are 94.5%, 93.0%, 92.1%, 92.2%, 93.6%, and 96.5%, respectively [43]. Then the $\{Co(btbb)(H_2O)_2\}_2\{H_2As_2Mo_6O_{26}\} \cdot 2H_2O$ exhibited better photocatalytic activity in the degradation of MB at the same process, the photocatalytic decomposition rate is 94.27% [44]. Su groups synthesized two $\{As_2Mo_6\}$ compounds with $[H_xAs_2Mo_6O_{26}]^{(6-x)-}$ clusters and free organic ligands, photocatalytic activities of they are detected, the conversion rate of MB is 91.8% and 92.2% when adding two $\{As_2Mo_6\}$ compounds as the catalyst 160 min later, respectively [45].

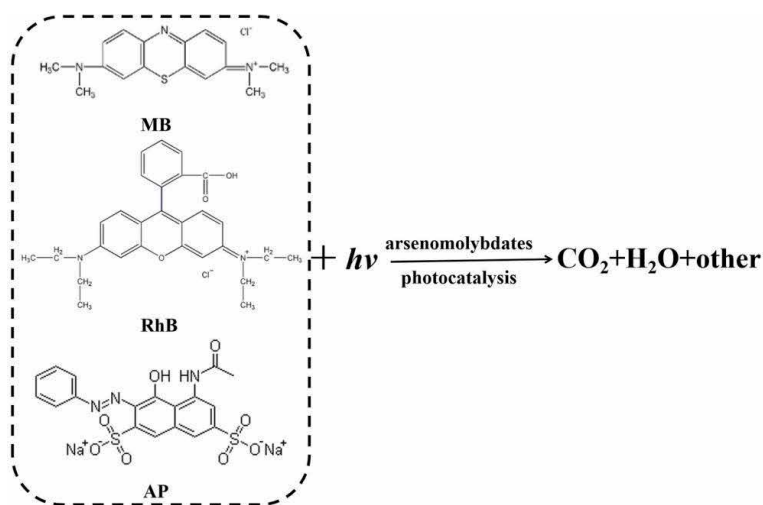


Figure 3.
The structure of dyes and photodecomposed product.

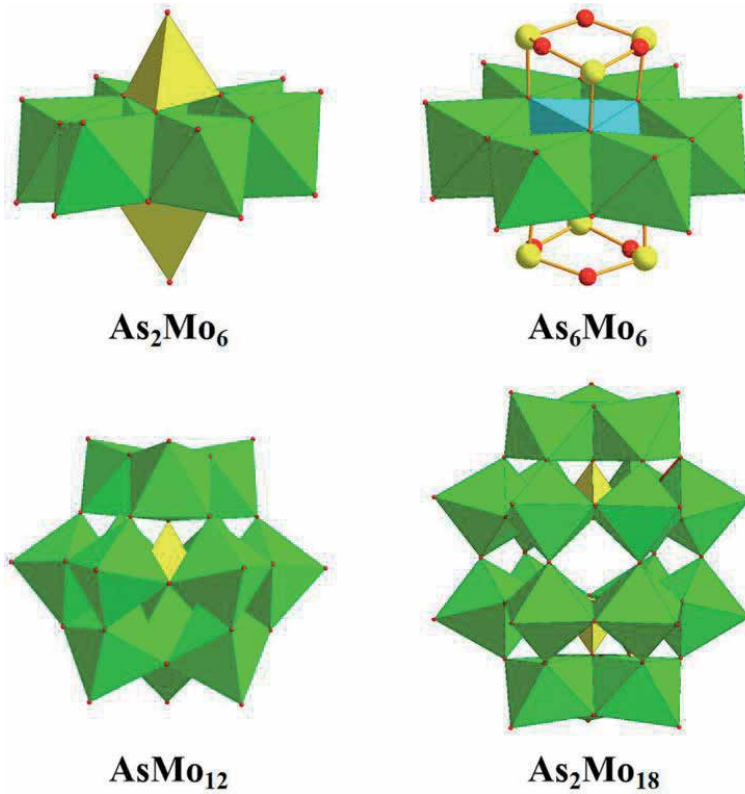


Figure 4.
 The common arsenomolybdates photocatalysis polyoxoanion.

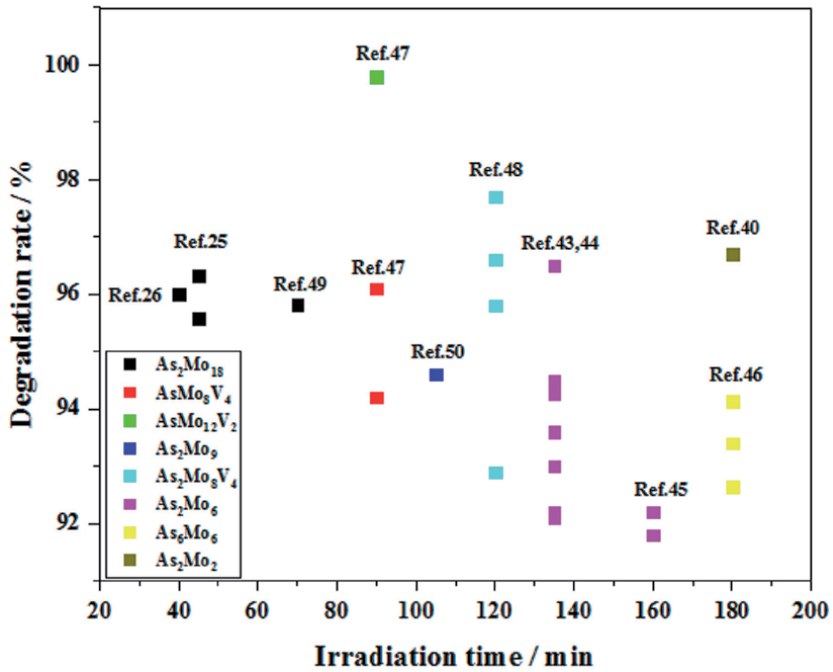


Figure 5.
 The arsenomolybdates photocatalytic decomposition rates of MB under UV irradiation.

The above data show that the photocatalytic activity of the compound composed of $[H_xAs_2Mo_6O_{26}]^{(6-x)-}$ clusters and metal-organic complexes is higher than supramolecular assemblies based on isomers $[H_xAs_2Mo_6O_{26}]^{(6-x)-}$ clusters in the degradation of MB under UV irradiation, which may be that the polyoxoanions can connect with transition metals in diverse modes, which enhanced the contact area between catalysts and substrates availing charge-transfer.

The three $\{As_6Mo_6\}$ compounds, $((phen)(H_2O)_4)_2[(CoO_6)(As_3O_3)_2Mo_6O_{18}] \cdot 2H_2O$, $\{[Co(phen)_2(H_2O)]_2[(CoO_6)(As_3O_3)_2Mo_6O_{18}]\} \cdot 4H_2O$ and $\{[Zn(biim)_2(H_2O)]_2[(ZnO_6)(As_3O_3)_2Mo_6O_{18}]\} \cdot 4H_2O$, as catalysts under UV light irradiation after 180 min [46], the photocatalytic decomposition rates of MB are about 92.64, 93.40, and 94.13%.

Yu groups prepared three Keggin arsenomolybdates, the photocatalytic decomposition rates of MB are 94.2% for $(Hbimb)(H_2bimb)[AsMo_8^{VI}V^V_4Co_2O_{40}]$, 96.1% for $(Hbimb)_2(H_2bimb)_{0.5}[AsMo_8^{VI}V^V_4Cu_2O_{40}] \cdot 1.5H_2O$, 99.8% for $[Cu^I(imi)_2][\{Cu^I(imi)_2\}_4\{AsMo_6^V Mo_6^{VI}O_{40}(V^{IV}_2O_2)\}]$ after 90 min irradiation, respectively [47].

Four biarsenate(III) capped Keggin arsenomolybdates with tetravanadium(IV) substituted were prepared, which exhibit excellent degradation activity for MB under UV light. The absorption peaks of MB reduced obviously after 120 min in the presence of four Keggin arsenomolybdates, the degradation rates for MB are 92.9%, 95.8%, 96.6%, and 97.7%, respectively [48].

The photocatalytic decomposition rate of MB is about 96% for $\{[Cu(btp)_2]_3[As_2Mo_{18}O_{62}]\}$ after 40 min [26], and the photocatalytic decomposition rates were 96.32% and 95.57% for $[Cu(pyr)_2]_6[As_2Mo_{18}O_{62}]$ and $[Ag(pyr)_2]_6[As_2Mo_{18}O_{62}]$ after irradiation for 45 min [25]. Yu reported that $(H_2bimyb)_3(As_2Mo_{18}O_{62})$ exhibits high-efficient degradation ability for MB under UV light. After UV light irradiation of $(H_2bimyb)_3(As_2Mo_{18}O_{62})$ for 70 min, the photocatalytic decomposition rate is 95.82% [49].

It is reported that the conversion rate of MB is 94.6% when adding compound $[Cu(imi)_2]_5Na[(AsO_4)Mo_9O_{27}(AsO_3)] \cdot 5H_2O$ as the photocatalyst after 105 min [50]. $\{Cu(2,2'-bpy)\}_2\{H_2As_2Mo_2O_{14}\}$ as photocatalyst was investigated via the photodecomposition of MB under UV light irradiation and the same conditions. The photocatalytic decomposition rate of MB that is 96.7% after 180 min [40].

3.3 Photocatalytic degradation of RhB

The photocatalytic activities of arsenomolybdates as photocatalysts are reviewed via the photodecomposition of RhB under UV light irradiation. The photocatalytic decomposition rates of RhB are about 96.34 and 95.7% for $\{Co(btb)(H_2O)_2\}_2\{H_2As_2Mo_6O_{26}\} \cdot 2H_2O$ and $\{[Cu(abi)\{H_4As^{III}As^V Mo_9O_{34}\}]\}_4[Cu(abi)_2] \cdot H_2O$ as photocatalysts under UV light irradiation after 135 and 140 min, respectively [27, 44]. $\{[Cu(btp)_2]_3[As_2Mo_{18}O_{62}]\}$ as photocatalyst was investigated decomposition rate of RhB after 40 min is about 96% [26]. The photocatalytic decomposition rates of RhB are 94.42 and 95.07% for $[M(pyr)_2]_6[As_2Mo_{18}O_{62}]$ ($M = Cu, Ag$) under UV light irradiation after 45 min [25].

The photocatalytic decomposition rates of RhB are 95.9% for $(Hbimb)(H_2bimb)[AsMo_8^{VI}V^V_4Co_2O_{40}]$, 94.3% for $(Hbimb)_2(H_2bimb)_{0.5}[AsMo_8^{VI}V^V_4Cu_2O_{40}] \cdot 1.5H_2O$, 95.8% for $[Cu^I(imi)_2][\{Cu^I(imi)_2\}_4\{AsMo_6^V Mo_6^{VI}O_{40}(V^{IV}_2O_2)\}]$ after 108 min irradiation, respectively [47].

3.4 Photocatalytic degradation of AP

AP, as one of the azo dyes, is relatively difficult to degrade, and so it was used as target molecules to evaluate the photocatalytic activity of arsenomolybdates under

UV irradiation. The photocatalytic activity of $\{\text{pyr}\}\{\text{Hbib}\}_2\{\text{As}^{\text{III}}_2(\text{OH})_2\text{As}^{\text{V}}_2\text{Mo}_{18}\text{O}_{62}\}$ was evaluated for the degradation of AP under UV irradiation [51], the degradation rate is 91.02% after UV light irradiation 90 min. In addition, the photocatalytic activity of noncapped OD analog $(\text{H}_2\text{bimy})_3(\text{As}_2\text{Mo}_{18}\text{O}_{62})$ was also studied under the same condition. Compared with $\{\text{pyr}\}\{\text{Hbib}\}_2\{\text{As}^{\text{III}}_2(\text{OH})_2\text{As}^{\text{V}}_2\text{Mo}_{18}\text{O}_{62}\}$, only 32.76% of AP was degraded by $(\text{H}_2\text{bimy})_3(\text{As}_2\text{Mo}_{18}\text{O}_{62})$ after 90 min [49], which indicates that the photocatalytic degradation effect of the bi-arsenic capped Dawson compound on AP is much better than that of noncapped analog. The 3D Dawson organic-inorganic hybrid arsenomolybdate, $\{\text{Ag}(\text{diz})_2\}_3[\{\text{Ag}(\text{diz})_2\}_3(\text{As}_2\text{Mo}_{18}\text{O}_{62})]\cdot\text{H}_2\text{O}$ exhibits merit photocatalytic properties for degradation of refractory dyes AP under UV light [52], the photocatalytic decomposition rate is 93.24% after 80 min.

The photocatalytic activities of $(\text{imi})_2[\{\text{Cu}^{\text{I}}(\text{imi})_2\}_2\{\text{Na}(\text{imi})_2\}\{\text{As}^{\text{III}}\text{As}_2^{\text{V}}\text{Mo}_{18}\text{O}_{62}\}]\cdot 2\text{H}_2\text{O}$ and $\{\text{Cu}^{\text{I}}_{0.5}(\text{trz})\}_6[\{\text{Cu}^{\text{I}}_{0.5}(\text{trz})\}_6(\text{As}_2\text{Mo}_{18}\text{O}_{62})]$ were evaluated for degradation of AP under UV irradiation. The photocatalytic decomposition rates are 89.06 and 96.38% after 80 min [53]. The photocatalytic decomposition rates are 92.49% of AP for $[\text{Cu}(\text{pyr})_2]_6[\text{As}_2\text{Mo}_{18}\text{O}_{62}]$ and 92.25% of AP for $[\text{Ag}(\text{pyr})_2]_6[\text{As}_2\text{Mo}_{18}\text{O}_{62}]$ after irradiation 135 min [25].

On the basis of the aforementioned points, $\{\text{As}_2\text{Mo}_{18}\}$ type arsenomolybdates with 3D networks possess the highest photocatalytic activities for photodecomposition of MB, RhB and AP under UV light irradiation. The following factors are maybe considered: First, quantity of Mo and O atoms in unit cell is a factor, which can increase the amount of charge-transfer from HOMO of O to LUMO of Mo, generating more electron-hole pairs. Second, the enhanced photocatalytic activity may have arisen from the 3D architecture, more extended 3D frameworks favor the migration of excited holes/electrons to the surfaces of $\{\text{As}_2\text{Mo}_{18}\}$ type to initiate the photocatalytic degradation reaction with organic dyes.

3.5 Reaction mechanisms of photocatalytic performance

Experimental and theoretical studies of arsenomolybdates photocatalysis have revealed that it typically proceeds based on the following mechanism [41, 42, 48, 52]: Irradiated of arsenomolybdates by UV light with energy equal to or greater than the E_g value of itself, which induces intramolecular charge-transfer from the HOMO of O to the LUMO of Mo, leading to the formation of photoexcited states, subsequently photogenerated electron-hole pairs were generated. The O_2 captures electron to form $\cdot\text{O}_2^-$ and the hole reacts with H_2O or OH^- ions to form $\cdot\text{OH}$. The $\cdot\text{O}_2^-$ and $\cdot\text{OH}$ radical decompose organic dyes' molecules into the final product, the detail of photocatalytic reaction is shown in Eqs. (1)–(4).



3.6 Stability

Some research data show that the samples were washed and dried after the arsenomolybdates as photocatalysis several cycles, and the infrared or X-ray diffraction test were carried out, the infrared spectra or X-ray diffraction data of arsenomolybdates demonstrate that there are almost unchanged before and after

photocatalytic reaction [44–48], which indicate that arsenomolybdates photocatalysis have excellent structural stability.

4. Conclusions

In this chapter, the arsenomolybdates are presented, and the attention is mainly focus on photocatalytic degradation of organic dyes. Various strategies are summarized and discussed based on the knowledge of synthesis, structure and photocatalytic properties for arsenomolybdates, which reflects the major directions of recent research in this field. There are vast research opportunities as new arsenomolybdates architectures are discovered in future; the great effort to promote the development of arsenomolybdates is needed to reduce the gap with commercial applications.

Acknowledgements

This work was supported by the Project of Introducing Talent of Guangdong University of Petrochemical Technology (2019rc052).

Conflict of interest

The authors declare no competing financial interest.

Abbreviations

arg	L-arginine
en	ethylenediamine
imi	imidazole
2,2'-bipy	2,2'-bipyridine
btb	1,4-bis(1,2,4-triazol-1-yl)butane)
phen	1,10'-phenanthroline
biim	biimidazole
bimb	1,4-Bis(imidazol-1-yl)butane
btp	1,3-bis(1,2,4-triazol-1-yl)propane
pyr	pyrazole
bib	1, 4-bis(1-imidazolyl)benzene
bimyb	1,4-Bis(imidazol-1-ylmethyl) benze
abi	2-aminobenzimidazole
bib	1,4-bis(1-imidazolyl)benzene
diz	1,2-diazole
trz	1,2,3-triazole

Author details

Zhi-Feng Zhao
College of Chemistry, Guangdong University of Petrochemical Technology,
Maoming, China

*Address all correspondence to: zhifengzhao1980@163.com

IntechOpen

© 2020 The Author(s). Licensee IntechOpen. This chapter is distributed under the terms of the Creative Commons Attribution License (<http://creativecommons.org/licenses/by/3.0>), which permits unrestricted use, distribution, and reproduction in any medium, provided the original work is properly cited. 

References

- [1] Sha JQ, Zhu PP, Yang XY, Li XN, Li X, Yue MB, et al. Polyoxometalates templated metal Ag–carbene frameworks anodic material for lithium-ion batteries. *Inorganic Chemistry*. 2017;**56**:11998-12002. DOI: 10.1021/acs.inorgchem.7b01962
- [2] Armatas NG, Ouellette W, Whitenack K, Pelcher J, Liu HX, Romaine E, et al. Construction of metal–organic oxides from molybdophosphonate clusters and copper-bipyrimidine building blocks. *Inorganic Chemistry*. 2009;**48**: 8897-8910. DOI: 10.1021/ic901133k
- [3] Azambuja FD, Parac-Vogt TN. Water-tolerant and atom economical amide bond formation by metal-substituted polyoxometalate catalysts. *ACS Catalysis*. 2019;**9**:10245-10252. DOI: 10.1021/acscatal.9b03415
- [4] Long DL, Tsunashima R, Cronin L. Polyoxometalates: Building blocks for functional nanoscale systems. *Angewandte Chemie, International Edition*. 2010;**49**(10):1736-1758. DOI: 10.1002/anie.200902483
- [5] Pang HJ, Yang M, Kang L, Ma HY, Liu B, Li SB, et al. An unusual 3D interdigitated architecture assembled from Keggin polyoxometalates and dinuclear copper(II) complexes. *Journal of Solid State Chemistry*. 2013;**198**: 440-444. DOI: 10.1016/j.jssc.2012.11.007
- [6] Hagrman PJ, Hagrman D, Zubieta J. Organic–inorganic hybrid materials: From “simple” coordination polymers to organodiamine-templated molybdenum oxides. *Angewandte Chemie International Edition*. 1999;**38**(18): 2638-2684. DOI: 10.1002/(SICI)1521-3773(19990917)38:18<2638::AID-ANIE2638>3.0.CO;2-4
- [7] Kim D, Seog JH, Kim MJ, Yang MH, Gillette E, Lee SB, et al. Polyoxometalate-mediated one-pot synthesis of Pd nanocrystals with controlled morphologies for efficient chemical and electrochemical catalysis. *Chemistry–A European Journal*. 2015;**21**: 5387-5394. DOI: 10.1002/chem.201406400
- [8] Walsh JJ, Bond AM, Forster RJ, Keyes TE. Hybrid polyoxometalate materials for photo(electro-) chemical applications. *Coordination Chemistry Reviews*. 2016;**306**:217-234. DOI: 10.1016/j.ccr.2015.06.016
- [9] Wang XL, Rong X, Lin HY, Cao JJ, Liu GC, Chang ZH. A novel Wells–Dawson polyoxometalate-based metal–organic framework constructed from the uncommon in-situ transformed bi (triazole) ligand and azo anion. *Inorganic Chemistry Communications*. 2016;**63**:30-34. DOI: 10.1016/j.inoche.2015.11.004
- [10] Sha JQ, Sun LJ, Zhu PP, Jiang JZ. The first two-fold interpenetrating polyoxometalate-based coordination polymer with helical channels: Structure and catalytic activities. *CrystEngComm*. 2016;**18**:283-289. DOI: 10.1039/C5CE02021B
- [11] Zhao ZF, Ding YZ, Bi JC, Su ZH, Cai QH, Gao LM, et al. Molybdenum arsenate crystal: A highly efficient and recyclable catalyst for hydrolysis of ethylene carbonate. *Applied Catalysis A: General*. 2014;**471**:50-55. DOI: 10.1016/j.apcata.2013.11.028
- [12] Peng G, Wang YH, Hu CW, Wang EB, Feng SH, Zhou YC, et al. Heteropolyoxometalates which are included in microporous silica, $Cs_xH_{3-x}PMo_{12}O_{40}/SiO_2$ and $Cs_yH_{5-y}PMo_{10}V_2O_{40}/SiO_2$, as insoluble solid bifunctional catalysts: Synthesis and selective oxidation of benzyl alcohol in liquid–solid systems. *Applied*

- Catalysis A: General. 2001;**218**:91-99. DOI: 10.1016/S0926-860X(01)00622-6
- [13] Chalkley L. The extent of the photochemical reduction of phosphotungstic acid. *The Journal of Physical Chemistry*. 1952;**56**(9): 1084-1086. DOI: 10.1021/j150501a012
- [14] Hill CL, Bouchard DA. Catalytic photochemical dehydrogenation of organic substrates by polyoxometalates. *Journal of the American Chemical Society*. 1985;**107**:5148-5157. DOI: 10.1021/ja00304a019
- [15] Tamimi M, Heravi MM, Mirzaei M, Zadsirjan V, Lotfian N, Eshtiagh-Hosseini H. $\text{Ag}_3[\text{PMo}_{12}\text{O}_{40}]$: An efficient and green catalyst for the synthesis of highly functionalized pyran-annulated heterocycles via multicomponent reaction. *Applied Organometallic Chemistry*. 2019;**33**: e5043-e5045. DOI: 10.1002/aoc.5043
- [16] Daraie M, Heravi MM, Mirzaei M, Lotfian N. Synthesis of Pyrazolo-[4,3,6]pyrido [2,3-d] pyrimidine-diones catalyzed by a nano-sized surface-grafted neodymium complex of the tungstosilicate via multicomponent reaction. *Applied Organometallic Chemistry*. 2019;**33**:e5058. DOI: 10.1002/aoc.5058
- [17] López X, Carbó JJ, Bo C, Poblet JM. Structure, properties and reactivity of polyoxometalates: A theoretical perspective. *Chemical Society Reviews*. 2012;**41**:7537-7571. DOI: 10.1039/C2CS35168D
- [18] Proust A, Thouvenot R, Gouzerh P. Functionalization of polyoxometalates: Towards advanced applications in catalysis and materials science. *Chemical Communications*. 2008;**16**: 1837-1852. DOI: 10.1039/B715502F
- [19] Song YF, Tsunashima R. Recent advances on polyoxometalate-based molecular and composite materials. *Chemical Society Reviews*. 2012;**41**: 7384-7402. DOI: 10.1039/C2CS35143A
- [20] Proust A, Matt B, Villanneau R, Guillemot G, Gouzerh P, Izzet G. Functionalization and post-functionalization: A step towards polyoxometalate-based materials. *Chemical Society Reviews*. 2012;**41**: 7605-7622. DOI: 10.1039/C2CS35119F
- [21] Pope MT, Müller A. Polyoxometalate chemistry: An old field with new dimensions in several disciplines. *Angewandte Chemie, International Edition*. 1991;**30**:34-48. DOI: 10.1002/anie.199100341
- [22] Chen CC, Wang Q, Lei PX, Song WJ, Ma WH, Zhao JC. Photodegradation of dye pollutants catalyzed by porous $\text{K}_3\text{PW}_{12}\text{O}_{40}$ under visible irradiation. *Environmental Science & Technology*. 2006;**40**: 3965-3970. DOI: 10.1021/es060146j
- [23] Wu PF, Zhang YP, Feng CT, Liu B, Hu HM, Xue GL. A large, X-shaped polyoxometalate $[\text{As}_6\text{Fe}_7\text{Mo}_{22}\text{O}_{98}]^{25-}$ assembled from $[\text{AsMo}_7\text{O}_{27}]^{9-}$ and $[\text{FeMo}_4\text{O}_{19}]^{11-}$ moieties. *Dalton Transactions*. 2018;**47**:15661-15665. DOI: 10.1039/C8DT02647E
- [24] Zhu TT, Wang J, Chen SH. Synthesis and anti-lung cancer activity of a novel arsenomolybdate compound. *Journal of Molecular Structure*. 2017; **1149**:766-770. DOI: 10.1016/j.molstruc.2017.08.032
- [25] Cong BW, Su ZH, Zhao ZF, Yu BY, Zhao WQ, Ma XJ. Two unusual 3D honeycomb networks based on Wells-Dawson arsenomolybdates with d^{10} transition-metal-pyrazole connectors. *Dalton Transactions*. 2017;**46**:7577-7583. DOI: 10.1039/c7dt01240c
- [26] Cong BW, Su ZH, Zhao ZF, Wang B. A novel 3D POMOF based on Wells-Dawson arsenomolybdates with excellent photocatalytic and lithium-ion

- battery performance. *CrystEngComm*. 2017;**19**:7154-7161. DOI: 10.1039/c7ce01734k
- [27] Zhao ZF, Su ZH, Cong BW, Gao W, Ma XJ. The new arsenomolybdate based on monocapped trivacant Keggin $\{H_4As^{III}As^VMo_9O_{34}\}$ cluster and Cu-abi complex: Synthesis, structure, photoluminescence and catalysis properties. *Journal of Cluster Science*. 2018;**29**:943-949. DOI: 10.1007/s10876-018-1390-6
- [28] Kwak W, Rajkovic LM, Stalick JK, Pope MT, Quicksall CO. Synthesis and structure of hexamolybdo bis (organoarsonates). *Inorganic Chemistry*. 1976;**15**(11):2778-2783. DOI: 10.1021/ic50165a042
- [29] Liu B, Yang J, Yang GC, Ma JF. Four new three-dimensional polyoxometalate-based metal-organic frameworks constructed from $[Mo_6O_{18}(O_3AsPh)_2]^{4-}$ polyoxoanions and copper(I)-organic fragments: Syntheses, structures, electrochemistry, and photocatalysis properties. *Inorganic Chemistry*. 2013;**52**:84-94. DOI: 10.1021/ic301257k
- [30] Burkholder E, Wright S, Golub V, O'Connor CJ, Zubieta J. Solid state coordination chemistry of oxomolybdenum organoarsenate materials. *Inorganic Chemistry*. 2003;**42**:7460-7471. DOI: 10.1021/ic030171f
- [31] He Q, Wang E. Hydrothermal synthesis and crystal structure of a new copper(II) molybdenum(VI) arsenate (III), $(C_5H_5NH)_2(H_3O)_2[(CuO_6)Mo_6O_{18}(As_3O_3)_2]$. *Inorganic Chemistry Communications*. 1999;**2**(9):399-402
- [32] Zhao JW, Zhang JL, Li YZ, Cao J, Chen LJ. Novel one-dimensional organic-inorganic polyoxometalate hybrids constructed from heteropolymolybdate units and copper-amino acid complexes. *Crystal Growth & Design*. 2014;**14**:1467-1475. DOI: 10.1021/cg500019g
- [33] Li ZF, Cui RR, Liu B, Xue GL, Hu HM, Fu F, et al. Structural and property characterization of two new charge-transfer salts based on Keggin ions and ferrocene. *Journal of Molecular Structure*. 2009;**920**:436-440. DOI: 10.1016/j.molstruc.2008.12.004
- [34] Han QX, Ma PT, Zhao JW, Wang ZL, Yang WH, Guo PH, et al. Three novel inorganic-organic hybrid Arsenomolybdate architectures constructed from Monocapped Trivacant $[As^{III}As^VMo_9O_{34}]^{6-}$ fragments with $[Cu(L)_2]^{2+}$ linkers: From dimer to two-dimensional framework. *Crystal Growth & Design*. 2011;**11**(2): 436-444. DOI: 10.1021/cg101125m
- [35] Niu JY, Hua JA, Ma X, Wang JP. Temperature-controlled assembly of a series of inorganic-organic hybrid arsenomolybdates. *CrystEngComm*. 2012;**14**:4060-4067. DOI: 10.1039/C2CE00030J
- [36] Yang YY, Xu L, Jia LP, Gao GG, Li FY, Qu XS, et al. Crystal structure and electrochemical properties of the supramolecular compound $[Himi]_6[As_2Mo_{18}O_{62}] \cdot 11H_2O$. *Crystal Research and Technology*. 2007;**42**(10): 1036-1040. DOI: 10.1002/crat.200710937
- [37] Hajji M, Zid MF. Synthesis, structure and ionic conductivity of the molybdenum arsenate: $Ag_{12.4}Na_{1.6}Mo_{18}As_4O_{71}$. *Solid State Sciences*. 2012;**14**(9):1349-1354. DOI: 10.1016/j.solidstatesciences.2012.07.021
- [38] Zhang YP, Li LL, Sun T, Hu HM, Xue GL. A cage-like polyanion with a Ag + enwrapped, $[AgAs_2Mo_{15}O_{54}]^{11-}$. *Inorganic Chemistry*. 2011;**50**: 2613-2618. DOI: 10.1021/ic102459r
- [39] Liu B, Li LL, Zhang YP, Ma Y, Hu HM, Xue GL. Three banana-shaped

arsenomolybdates encapsulating a hexanuclear transition-metal central magnetic cluster: $[\text{As}^{\text{III}}_2\text{Fe}^{\text{III}}_5\text{MMo}_{22}\text{O}_{85}(\text{H}_2\text{O})]^{n-}$ ($\text{M} = \text{Fe}^{3+}$, $n = 14$; $\text{M} = \text{Ni}^{2+}$ and Mn^{2+} , $n = 15$). *Inorganic Chemistry*. 2011;50:9172-9177. DOI: 10.1021/ic201418q

[40] Zhao WQ, Su ZH, Zhao ZF, Cong BW, Xia L, Zhou BB. The synthesis, structure and properties of a new compound with 1D linear chain arsenomolybdate anion building block. *Inorganic Chemistry Communications*. 2015;61:118-122. DOI: 10.1016/j.inoche.2015.09.008

[41] Zhao ZF, Zhou BB, Su ZH, Ma HY, Li CX. A new $[\text{As}_3\text{Mo}_3\text{O}_{15}]^{3-}$ fragment decorated with Cu(I)-Imi (Imi = imidazole) complexes: Synthesis, structure and electrochemical properties. *Inorganic Chemistry Communications*. 2008;11:648-651. DOI: 10.1016/j.inoche.2008.02.032

[42] Patel A, Patel K. Cs salt of dimanganese(II) substituted phosphotungstate: One pot synthesis, structural, spectroscopic characterization and solvent free liquid phase oxidation of styrene using different oxidants. *Polyhedron*. 2014; 69:110-118. DOI: 10.1016/j.poly.2013.11.033

[43] Cong BW, Su ZH, Zhao ZF, Yu BY, Zhao WQ, Xia L, et al. Assembly of six $[\text{H}_x\text{As}_2\text{Mo}_6\text{O}_{26}]^{(6-x)-}$ cluster-based hybrid materials from 1D chains to 3D framework with multiple Cu-N complexes. *CrystEngComm*. 2017;19:2739-2749. DOI: 10.1039/c7ce00319f

[44] Cong BW, Su ZH, Zhao ZF, Zhao WQ, Ma XJ, Zhou BB. A new rhombic 2D interpenetrated organic-inorganic hybrid material based on $[\text{H}_x\text{As}_2\text{Mo}_6\text{O}_{26}]^{(6-x)-}$ polyoxoanion and Co-btb complexes. *Inorganic Chemistry Communications*. 2017;83:11-15. DOI: 10.1016/j.inoche.2017.05.024

[45] Zhao ZF, Su ZH, Cong BW, Zhao WQ, Ma XJ. Organic-inorganic hybrid supramolecular assemblies based on isomers $[\text{H}_x\text{As}_2\text{Mo}_6\text{O}_{26}]^{(6-x)-}$ clusters. *Zeitschrift für Anorganische und Allgemeine Chemie*. 2017; 643:980-984. DOI: 10.1002/zaac.201700157

[46] Cong BW, Su ZH, Zhao ZF, Zhao WQ, Xia L, Zhou BB. The pH-controlled assembly of a series of inorganic-organic hybrid arsenomolybdates based on $[(\text{MO}_6)(\text{As}_3\text{O}_3)_2\text{Mo}_6\text{O}_{18}]^{4-}$ cluster. *Polyhedron*. 2017;127:489-495. DOI: 10.1016/j.poly.2016.10.035

[47] Li FR, Lv JH, Yu K, Zhang ML, Wang KP, Meng FX, et al. Effective photocatalytic and bifunctional electrocatalytic materials based on Keggin arsenomolybdate and different transition metal capped assemblies. *CrystEngComm*. 2018;20:3522-3534. DOI: 10.1039/C8CE00550H

[48] Zhao ZF, Cong BW, Su ZH, Li BR. Self-assembly of biarsenate capped Keggin arsenomolybdates with tetravanadium-substituted for photocatalytic degradation of organic dyes. *Crystal Growth & Design*. 2020; 20:2753-2760. DOI: 10.1021/acs.cgd.0c00123

[49] Cai HH, Lü JH, Yu K, Zhang H, Wang CM, Wang L, et al. Organic-inorganic hybrid supramolecular assembly through the highest connectivity of a Wells-Dawson molybdoarsenate. *Inorganic Chemistry Communications*. 2015;62:24-28. DOI: 10.1016/j.inoche.2015.10.006

[50] Zhao ZF, Su ZH, Zhao WQ, Gao W, Cong BW, Zhou BB. The hybrid organic-inorganic assemblies based on monocapped trivacant Keggin arsenomolybdate and CuI-organic units. *Journal of Cluster Science*. 2016; 27:1579-1590. DOI: 10.1007/s10876-016-1022-y

[51] Lv PJ, Yuan J, Yu K, Shen JH. An unusual bi-arsenic capped Well-Dawson arsenomolybdate hybrid supramolecular material with photocatalytic property and anticancer activity. *Journal of Inorganic and Organometallic Polymers and Materials*. 2018;**28**:899-905. DOI: 10.1007/s10904-017-0760-0

[52] Lv PJ, Cao WW, Yu K, Shen JH. A novel 2, 6-connected inorganic-organic 3-D open framework based on $\{\text{As}_2\text{Mo}_{18}\}$ with photocatalytic property and anticancer activity. *Inorganic Chemistry Communications*. 2017;**79**: 95-98. DOI: 10.1016/j.inoche.2017.03.028

[53] Li FR, Lv JH, Yu K, Zhang H, Wang CM, Wang CX, et al. Two extended Wells-Dawson arsenomolybdate architectures directed by Na(I) and/or Cu(I) organic complex linkers. *CrystEngComm*. 2017;**19**: 2320-2328. DOI: 10.1039/C6CE02539K

Visible-Light Photocatalysis of Aldehyde and Carbonyl Functionalities, an Innovative Domain

Alwar Ramani, Shobha Waghmode and Suresh Iyer

Abstract

The chemistry of aldehydes and resembling chromophores portrays a natural tendency to undergo chemical reactions through nucleophilic reagents, owing to the polarization arising from the electronegativity of oxygen atom, and they also can enolize as a result of the acidic nature of the α -hydrogen of the carbonyl functional group; thereby the C—C bond forming reactions can be attained either intra- or intermolecularly. Carbonyl addition reactions, enolate chemistry coupled with their capability to undergo [2+2] cycloaddition reactions, and the chemistry of carbonyl compounds are being mind-numbingly exploited in the design and process development of industrially, commercially, pharmacologically, and biologically value-added compounds. Ultimately abundant name reactions were registered, and many novel reactions endlessly appear; of late, prodigious development has been reported under the heading of visible-light photocatalysis (VLPC). Fascinatingly, VLPC has opened a new domain in the synthetic organic chemistry, and this domain paves the way to access broad spectrum of organic compounds with the ease of operations. In this chapter the chemistry of carbonyls by VLPC is briefly presented, which is comprising of not only functional group transformations but also asymmetric syntheses of complex organic compounds.

Keywords: aldehydes, VLPC, photosensitizers, asymmetric alkylation, enamines

1. Introduction

The periodic table comes to the mind when thinking of elements in chemistry, while organic chemistry brings to mind substances such as alcohol, aldehydes, ketones, aromatics, and other compounds based on the functional groups. Aldehydes, ketones, and carbonyl moieties are the most popular and routinely exploited functional groups in synthetic organic chemistry and in the design of organic synthesis since they render the desired synthetic manipulation and spring an easy access to complex molecular architecture. Not only in modern times but also from the times of alchemy, formaldehyde is very well utilized for embalming and preserving dead animal species by biologists; consequently, aldehyde class of compounds ranks to be the parent compounds for many other classes of compounds. Acetyl coenzyme derived from aldehyde functional group or acetaldehyde moiety is

responsible for the wide variety of natural products through biosynthesis, while toward the syntheses and manufacture of chemicals on the laboratory and in industries, also the aldehyde functional group is very well synthetically manipulated. They were not only converted into structurally complex compounds through enzymes, catalysts, and thermal process, but also photons convert aldehydes into other molecular architectures by means of eminent photochemical-chemical reactions such as Norrish-type photolysis, cyclobutanol formation through Yang reaction, and [2+2] cycloaddition with alkene (Paternó-Büchi reaction). Apart from conventional catalytic way, traditional synthesis uses name reactions and photochemistry; of late, visible light is being used [1]. Apparently, solar energy is a benign, benevolent, and renewable source of energy. Visible light emerging from the source of sun promotes chemical transformations through single-electron mechanism. Basically using visible light as energy source and in the presence of catalytic amount of metal photosensitizers or organocatalysts, the chemical reactions are carried out, and this process is termed as visible-light photocatalysis and abbreviated as VLPC [2, 3]. This opens a new chapter in the textbook of organic synthesis [4]. Photosensitizers are special molecules which support these light-induced molecular transformations by electron or energy transfer using its abundant light absorbance and redox property [5]. Aldehydes are subjected to VLPC conditions either protected as acetals or directly during the course of a reaction [6]. Further transformations such as oxidation to COOH are also essential reaction of aldehydes [7]. Aldol condensations and enamines are further variations in their reactions as building blocks in organic synthesis [4]. Thus, the application of aldehydes as building blocks is now elaborated with their VLPC reactions adding to its reaction repertoire. In this chapter we will discuss on the recent developments on VLPC of aldehydes.

VLPC is advantageous over the conventional catalysis since it employs the clean, renewable, and readily available visible light from our sun and this state-of-the-art protocol is convenient in its operation. Bench chemists are fascinated by VLPC due to the ease of recycling the heterogeneous catalytic material by simple filtration and because reactions are carried at ambient temperature and the work-up procedure is quite simple. Eventually, this field and phenomenon of synthetic organic chemistry have emerged as an innovative subdiscipline over the last decade; the scientists have made a step forward by carrying out the asymmetric induction [8]; with the advancement in modern analytical tools and the hard work of enthusiastic chemists, VLPC of aldehydes is emerging exponentially.

In the visible-light photocatalysis, the catalytic species is activated by the action of light, and the photocatalytic material is mostly a semiconducting material which in turn is capable of activating even the small molecules [5]. When the catalytic material is irradiated with light, it undergoes the absorption of photon, and the electron (e^-) is excited from the valence bond to the conduction band; consequently, a positive electron hole is generated in the semiconducting material (h^+), and this process is termed as *photoexcitation*. The excited electron then comes to the ground state through the mechanisms such as recombination and dissipates by means of non-radiative mechanism; in a sense, following the photoexcitation process, the catalytic material excited transfers the energy to the molecules in its close proximity through an orthodox redox mechanism in a pure chemistry sense, and the single-electron transfer (SET) occurs. For brevity, the mechanism is provided succinctly; in a nutshell, light source excites the catalytic material and transfers the energy to other molecules close by, and the chemical reaction occurs by means of electron transfer mechanism. This new discipline opened a new science of photophysics and photochemistry of transition metal coordination compounds. In this chapter a discussion of visible-light photocatalysis of aldehyde compounds is

presented; the discussion revolves around the recent developments on the chemistry of aldehydes in the domain of VLPC (**Figures 1 and 2**).

The polypyridyl complexes of Ru and Ir afford unique chemical reactivities due to their long-lived excited states when excited by visible light [5]. They are chemically robust and possess redox properties that are further fine-tunable by modifying the polypyridyl ancillary ligands. The Ru(bpy)₃Cl₂ is a widely known and commonly used photoredox molecule. The absorption of visible light leads to excited states that can function both as oxidants and reductants, which allows the generation of radical cations or radical anions under mild conditions. The amphoteric redox reactivity of the excited triplet state of Ru^{II}(bpy)₃²⁺, (³Ru^{II}(bpy)₃)²⁺, enables two distinct catalytic cycles, namely, the reductive quenching (RQC) and the oxidative quenching cycles (OQC). In RQC, (³Ru^{II}(bpy)₃)²⁺ first oxidizes a reductant into a radical cation and reduces into Ru^I(bpy)₃⁺ which subsequently reduces an oxidant into a radical anion species and converts itself into the ground-state catalyst. OQC starts with the oxidation of the complex (³Ru^{II}(bpy)₃)²⁺ to Ru^{III}(bpy)₃³⁺ followed by its reduction into Ru^{II}(bpy)₃²⁺.

Based on these viewpoints, cyclometallated Ir complexes have been rapidly developed due to their superior photophysical and photochemical properties. These photocatalysts are chemically robust and possess long-lived excited states. Their favorable redox properties allow redox-neutral reactions to be carried out as both reductants and oxidants that can be transiently generated during different stages in the catalytic process. This reactivity pattern thus is beneficial allowing exploration of

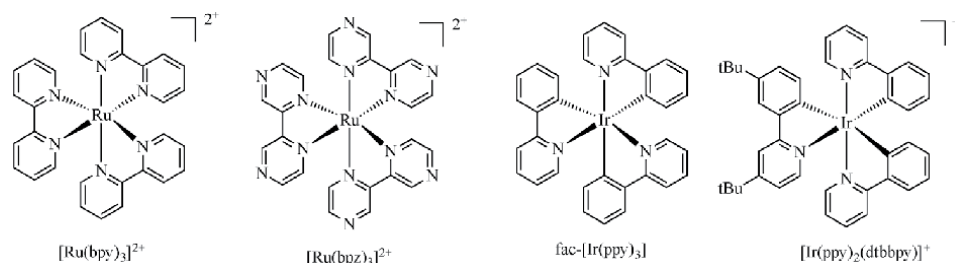


Figure 1. Photosensitizers: [Ru(bpy)₃]²⁺, [Ru(bpz)₃]²⁺, fac-[Ir(ppy)₃], [Ir(ppy)₂(dtbbpy)]⁺. Properties of [Ru(bpy)₃]²⁺ photocatalyst—[MLCT – λ = 452 nm].

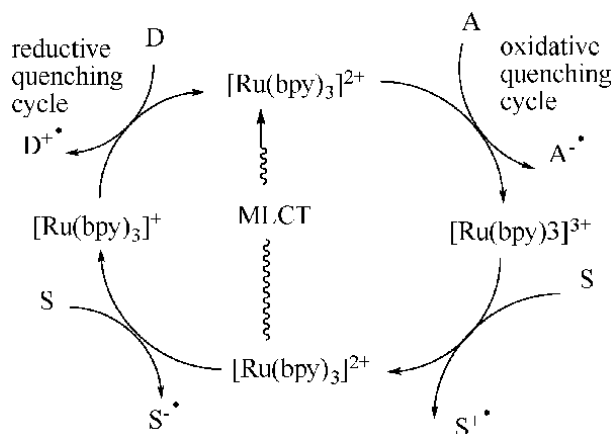


Figure 2. Ru redox cycle: A—sacrificial electron acceptor; D—sacrificial electron donor; S—substrate; bpy—2,2′-bipyridine; MLCT (metal to ligand charge transfer) – λ = 452 nm.

alternate reaction pathways under benign reaction conditions. They have thus been used as photoredox catalysts and serve as photosensitizers in organic synthesis [5].

2. Photoacetalization

Aldehydes are prone to oxidation and amenable to attack by nucleophiles and can enolize, and as a result the —CHO functional group needs to be protected while carrying out the complex molecular architecture. Protection, de-protection, and reversing the reactivity or polarity through umpolung are the rudimentary strategies in the realm of organic synthesis. For these important tactics, recently VLPC has contributed a protection methodology, and the authors have protected the —CHO group as acetal [6]. The advantage of this protocol is that it does not employ the strong mineral, Lewis, and other acidic conditions; consequently the VLPC strategy presented by the chemists ranks as green technology. The protection was carried out using an organic dye, Eosin Y, with the use of [light-emitting diode (LED)] irradiation to promote the reaction under a milder condition. Several aldehydes were catalyzed in very high yields under household irradiation to the corresponding acetals (**Figure 3**).

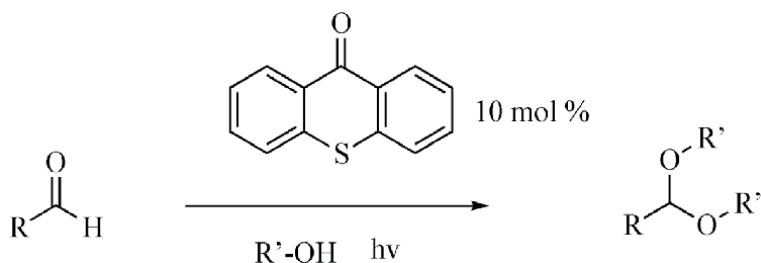


Figure 3.
Photocatalytic synthesis of acetals from aldehydes.

3. Photo-oxidation of aldehydes

The oxidation of organic compounds is being continuously explored since it is an important functional group modification, and the bench chemists are looking for environmental compatible and cost-effective methodologies for the same. By means of commercially affordable catalytic materials, several aldehydes were conveniently converted into their respective carboxylic acids where the $^1[\text{O}_2]$ is used as oxidant catalyzed by Ru and Ir catalytic materials. The reaction is notably chemoselective and does not distress other oxidizable functional groups assembled within the molecule. Among the photosensitizers studied, Ir(dFppy)₃ was the most efficient giving 99% yield of product from p-anisaldehyde. A wide range of aldehydes was studied with this catalyst and efficaciously oxidized under visible light [7] (**Figure 4**).

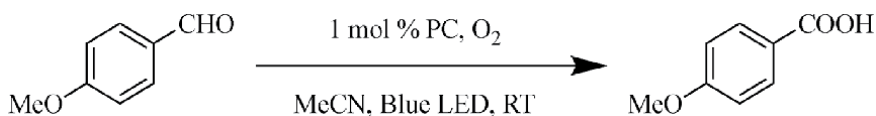


Figure 4.
Photocatalytic oxidation of aldehydes [7].

4. Direct C—H arylation and alkylation of aldehydes

Direct and catalytic C—H activation or functionalization comprising of arylation, alkenylation, alkylation, allylation, and annulation reaction is an important field in the synthetic organic chemistry in the manufacture and the process development of pharmacologically and biologically active ingredients. Knowing the importance of C—H activation, direct arylation of aldehydes has been achieved in a synergistic manner, where nickel catalyst was employed in combination with VLPC system. In this outstanding redox system, a hydrogen atom transfer (HAT) was achieved on the reactions in between commercially available aldehydes and aryl and alkyl bromides under milder conditions; it is interesting to note that the yields are excellent [9] (Figure 5).

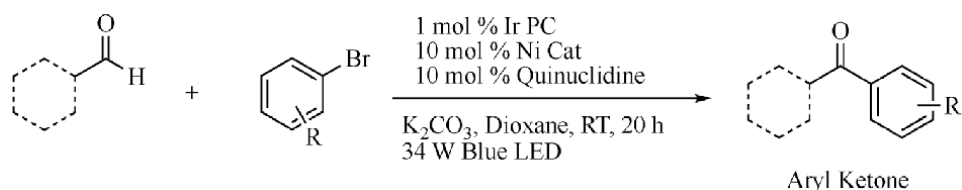


Figure 5.
Direct C—H arylation and alkylation of aldehydes [9].

The mechanism is based on the photoexcitation of the Ir photocatalyst which gives rise to the highly oxidizing species Ir* Ir[dF(CF₃)ppy]₂(dtbbpy) which oxidizes quinuclidine to form a cation radical. This radical cation then engages in a HAT event with any aldehyde to generate the acyl radical. Simultaneously oxidative addition of aryl bromide to LnNi (0) generates the aryl-Ni (II) species which is intercepted by the acyl radical to form the acyl-Ni complex. Both the Ni and the Ir photoredox catalysts then turn over in a critical reductive elimination step to the desired ketone product while regenerating the Ir and Ni catalysts. It is interesting to note that using this protocol, a pharmacologically active ingredient, namely, haloperidol, a typical antipsychotic drug, was synthesized [9] (Figure 6).

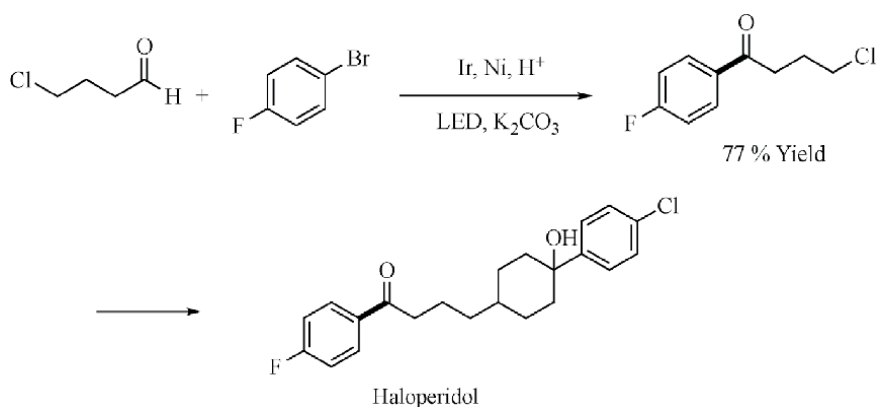


Figure 6.
Synthesis of haloperidol.

A two-step synthesis of haloperidol was achieved by this photoredox methodology. 1,4-Chlorobutanal was merged with 1-bromo-4-fluorobenzene using the

photoredox protocol to yield the ketone in high yield. Further exposure of this to the piperidine nucleophile thus gave haloperidol in short steps.

5. C—C bond formation enhanced by VPLC and alkylation of aldehydes through alkenes as alkylating agents

The α -alkylation of carbonyl compounds is a routine affair for synthetic chemists both for making substituents and also to synthesize pharmaceutically active ingredients (Figures 7 and 8). In the case of α -alkylation of aldehydes, the acidic methylenic (CH_2) hydrogen atoms are acidic in nature, and they can be removed; as a result an enol form is produced which directs the alkylating agents attached to the α -alkylation. A skillful execution of three catalytic materials together in a synergistic fashion enables an enantiomeric α -alkylation of aldehydes; mechanistically, the triple catalytic process is sequenced to deliver a hydrogen atom transfer, electron

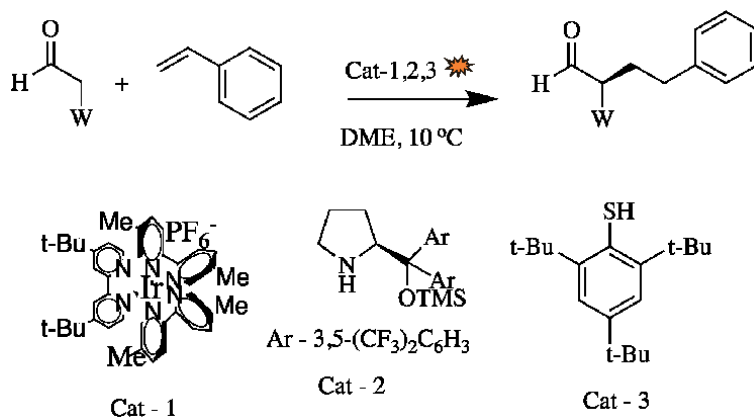


Figure 7.
Intermolecular alkylation with alkenes.

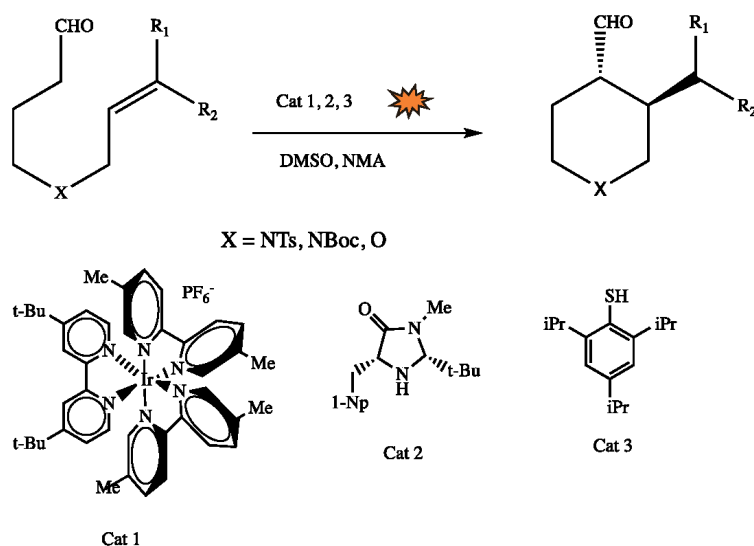


Figure 8.
Intramolecular alkylation.

borrowing tendency, and chirality induction through chiral imidazolidinones or prolinols with a thiophenol where the iridium catalyst transfers the activation of molecules by means of light energy (λ). The α -alkylation is carried out both by inter- and intramolecularly where the alkenes are alkylated at the α -position to the aldehyde functional group to furnish cyclic and acyclic products. The process is atom economical with a stereoselective process, allowing the production of value-added molecules from feedstock chemicals in a single step while consuming only one photon [10].

The mechanistic pathway is based on the excitation of Ir complex, and simultaneously the chiral reagent adds to the aldehyde compound through elimination of water and forms an enamine. The excited iridium complex oxidizes the enamine present in the reaction medium through a single-electron transfer mechanism; thus formed enaminy radical adds to the alkene substrate producing a carbon radical which is finally trapped by the hydrogen atom transfer catalyst. During the work-up procedure, the iminium ion is hydrolyzed to get the enantiomerically enriched product, and the organocatalyst is regenerated. Finally the reduction of the thiyl radical by the Ir(I) species regenerates the thiol catalyst as well as the Ir(III) catalyst to complete the redox cycle.

With the success in the α -alkylation protocol, its intramolecular version also achieved where an intramolecular cyclization with tethered alkenes was first attempted to determine the feasibility of enantioselective ring formation reaction. Interestingly, carbocycles and heterocycles were synthesized with high yield and enantiocontrol. Tosamide- or carbamate-protected N-tethered aldehydic alkenes gave rise to the corresponding piperidines, ether-linked systems provided trans-substituted tetrahydropyrans, and carbocycles were also attained. Pyrrolidines were also formed as well as seven-membered rings such as azepanes or cycloheptanes. High stereocontrol was obtained with trisubstituted alkenes, and where multiple alkenes were available, only proximal alkenes reacted to provide the corresponding cyclic molecule.

Following this successful reaction, intermolecular reactions with styrene was attempted. A variety of substituted aldehydes provided the alkylated products in high yields and selectivity. Terminal alkenes were suitable substrates though 1,1-disubstituted alkenes reacted with moderate efficiency.

6. Enantioselective α -trifluoromethylation and α -perfluoroalkylation of aldehydes

The fluorinated hydrocarbons possess unique physical properties and are so useful in dyes, polymers, agrochemicals, and drugs. In pharmaceuticals the perfluoroalkylated compounds which impart valuable physiological properties that enhance binding properties elevate lipophilicity and/or improved metabolic stability. The enantioselective incorporation of the CF_3 and perfluoroalkyl groups has thus been a challenging task for the synthetic chemists, and the enantioselective α -alkyl trifluoromethylation of ketones and aldehydes has been elusive. First the enantioselective and organocatalytic α -trifluoromethylation and α -perfluoroalkylation of aldehydes have been successfully achieved using a commercially available iridium photocatalyst and imidazolidinone catalyst. MacMillan et al. describe the enantioselective trifluoromethylation of aldehydes via the successful merger of enamine and photoredox catalysis [11]. Their reaction is based on the property of electrophilic radicals to combine with facially biased enamine intermediates (derived from aldehydes and chiral amines). The radicals are derived from the reduction of alkyl halides by a photoredox catalyst ($\text{Ir}(\text{ppy})_2(\text{dtbbpy})$). A broad

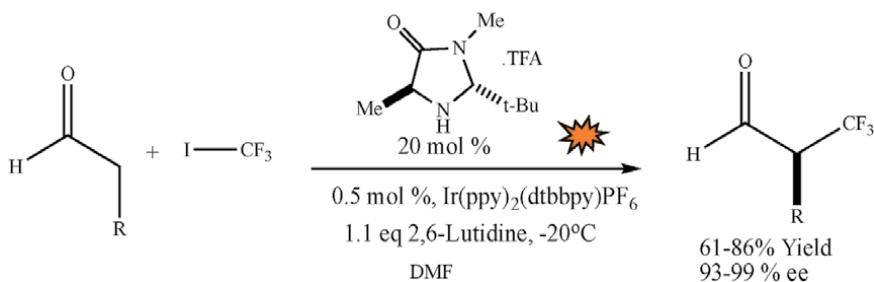


Figure 9.
 α -Trifluoromethylation of aldehydes [12].

range of perfluoroalkyl halides were found to participate in the enantioselective alkylation reaction. N-perfluoroalkyl substrates of varying chain length undergo successfully reductive radical formation and enamine addition with high yields and enantioselectivity (**Figure 9**).

The α -alkylation of carbonyl compounds is always an essential tool in the synthetic organic chemistry. It can be carried out both inter- and intramolecularly; the intramolecular version builds up the cyclic compounds with enhanced stereoselectivity. Among the α -alkylation reactions, of late, α -trifluoromethylation reactions are being much exploited since these compounds are of greater importance in agrochemical and pharmaceutical compounds. Iodotrifluoromethane is employed as a trifluoromethylating agent under a VLPC condition where the reaction and optical yields are highly appreciable. Mechanistically, the light excites the Ir complex, which oxidizes the enamine compound through a single-electron transfer mechanism; the enamine radical adds with the alkene substrate producing carbon-centered radical; thus series of reaction provides the desired compound, and the catalyst is regenerated [12].

7. Reaction of chiral enamine with α -bromocarbonyl compounds

Photoredox catalysis and organocatalysis are two powerful fields of molecule activation that have found widespread application in the areas of inorganic coordination and organic chemistry. The merger of these two fields is an important solution in asymmetric chemical synthesis. Specifically, the enantioselective intermolecular α -alkylation of aldehydes with α -bromocarbonyls has been accomplished using an activation pathway that combines both the photoredox catalyst Ru(bpy)₃Cl₂ (where bpy is 2,2'-bipyridine) and an imidazolidinone organocatalyst. This simple alkylation reaction, which was previously elusive, is now broadly applicable and highly enantioselective [11].

The initiation of the reaction requires quenching of the photocatalyst excited state ^{*}Ru(bpy)₃²⁺ by a sacrificial amount of enamine to provide the strongly reducing Ru(bpy)₃⁺. Electron transfer to the alkyl bromide induces fragmentation, affording bromide and the electron-deficient radical. Condensation of the aldehyde with the imidazolidinone organocatalyst furnishes chiral enamine. The C—C bond formation then occurs by the radical electrophile addition to the accessible *Si* face of the enamine and generates the α -amino radical. The two catalytic cycles then intersect with the single-electron oxidation of ^{*}Ru(bpy)₃²⁺ to yield Ru(bpy)₃⁺ and the iminium ion. Hydrolysis of the iminium releases the α -alkylated product and regenerates the organocatalyst (**Figures 10 and 11**).

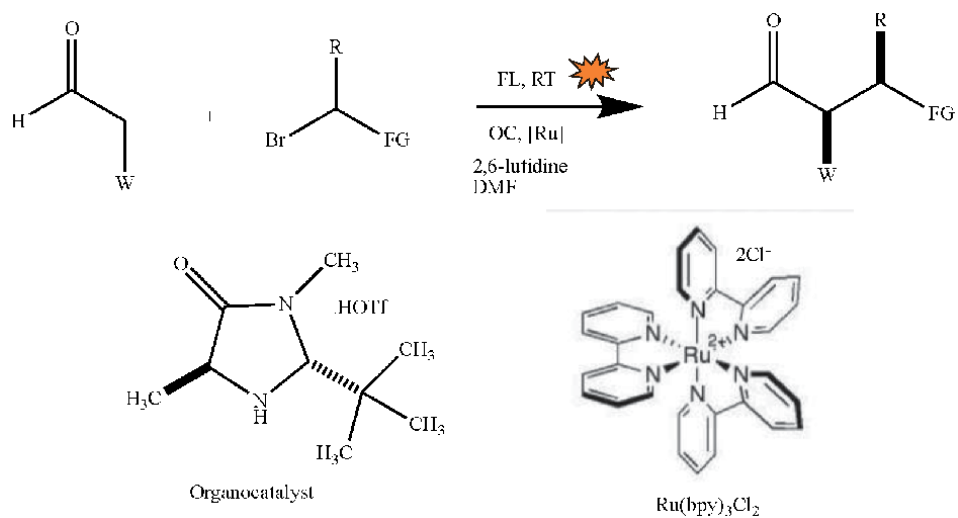


Figure 10.
 The direct asymmetric alkylation of aldehydes.

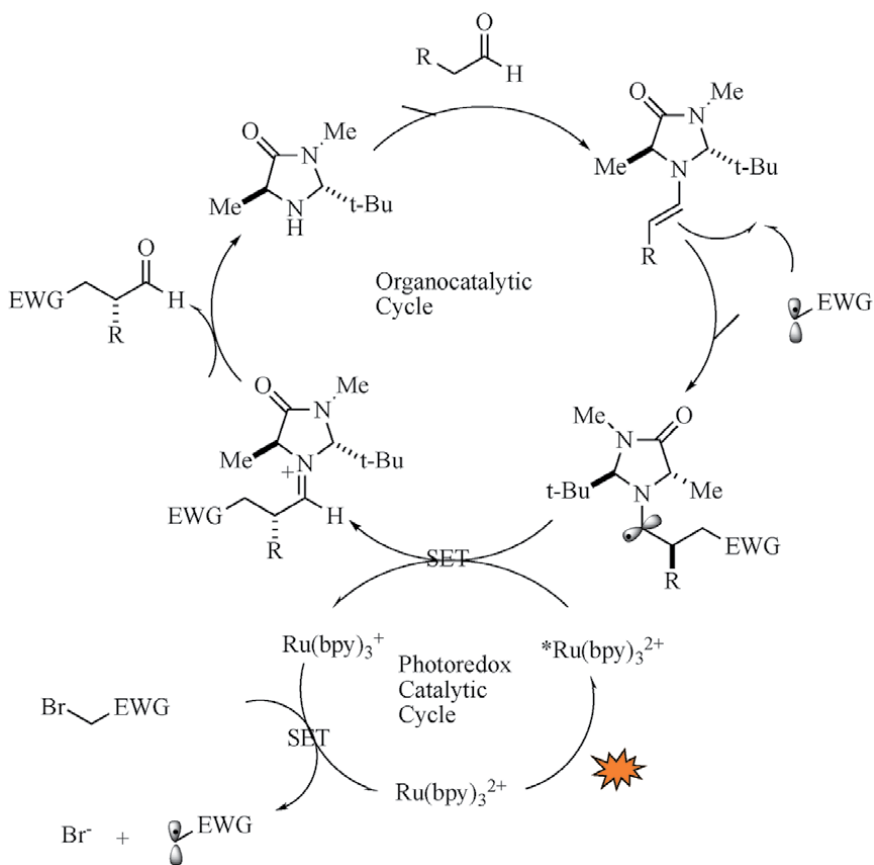


Figure 11.
 Catalytic cycle—the direct asymmetric alkylation of aldehyde.

8. Asymmetric α -amination of aldehydes by means of photoredox and organocatalysis

The synthetic design and developing methodology on the creation of C—N bonds within the complex molecular architecture in a stereospecific manner is a challenging task which is routinely needed in the process development of drug molecules. Consequently, α -amino aldehydes are the valuable structural motifs in the process development of drug molecules. However, asymmetric α -amination of aldehydes poses a plethora of potential challenges since the reaction medium contains reagents and chemicals that can racemize product molecule. In this context, a VLPC methodology has been demonstrated for α -amination of aldehydes in an enantioselective fashion using nitrogen-centered radicals which enables the synthesis stable to racemization, a tactful synthetic methodology. N-centered radicals are easily generated using dinitrosulfonyloxy groups (ODNS) which are capable of producing the requisite heteroatom-centered radical upon exposure to household light and in the presence of designed catalyst. The nitrogen-centered radical thus is produced when treated with a transient π -rich enamine (derived from the coupling of an imidazolidinone catalyst with the aldehyde); upon photonic excitation, single-electron transfer reaction produces nitrogen-centered radical. Then the reaction proceeds to yield an iminium ion, which up on hydrolysis gives rise to enantiomerically enriched α -amino aldehyde [13] (Figures 12 and 13).

This is an organocatalytic and photoredox-based approach to the asymmetric α -amination of aldehyde, where a functionalized nitrogen is directly coupled with a formyl precursor. This protocol provides a ready access to N-substituted α -amino aldehyde architecture without any racemization with more than 85% enantiomeric excess.

9. Catalytic α - and γ -alkylation of aldehydes and enals, a direct photoexcitation approach

The α - and γ -alkylations of aldehydes and enals, respectively, are an important C—C bond forming reaction and very important in the building complex molecular architecture. These alkylations were reported as a photo-organocatalytic reaction where the product is enantioselective. The procedure is executed utilizing the commercially available aminocatalyst and carried out under the illumination of fluorescent light bulb in the absence of photoredox catalyst. The authors have demonstrated a strategy in which photochemical activation of substrates provides reactive radical species by the action of visible-light active photoredox catalyst. In this system the catalyst is chiral that acts as a dual catalytic system and provides an

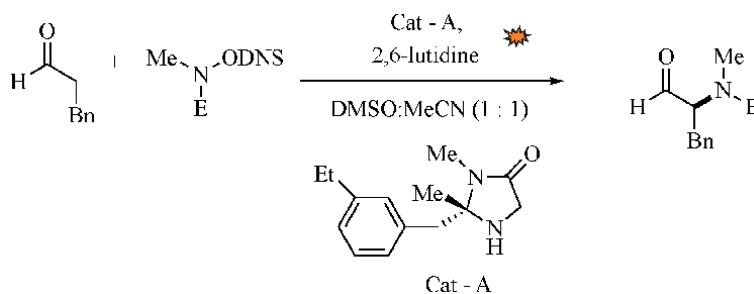


Figure 12.
 α -Amination of aldehydes.

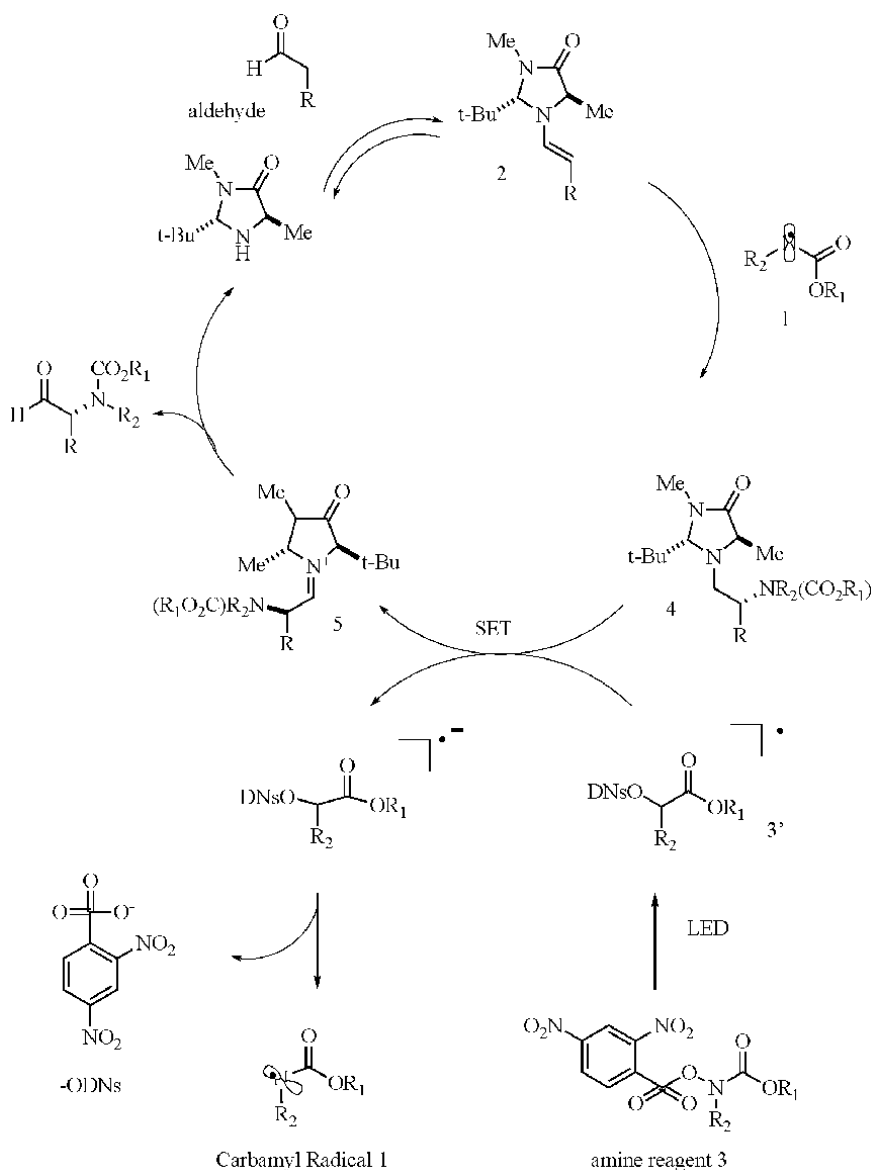


Figure 13.
 Catalytic cycle of α -amination.

easy access to chiral molecules as products in an asymmetric fashion. In a sense, in the reaction medium, the transiently generated enamines undergo electronic excitation by the action of light from reactive radical species from organic halides, which, in turn, provide an effective stereochemical induction to yield enantioselective alkylated products [14] (Figures 14 and 15).

10. Photoredox cross-dehydrogenative coupling (CDC) of aldehydes with xanthenes (chiral enamines with diaryl compounds)

Aldehydes under the treatment with visible light underwent catalytic asymmetric cross-dehydrogenative coupling reactions with xanthenes and thioxanthenes, and it is interesting to note that xanthenes are important candidates in the dye stuff

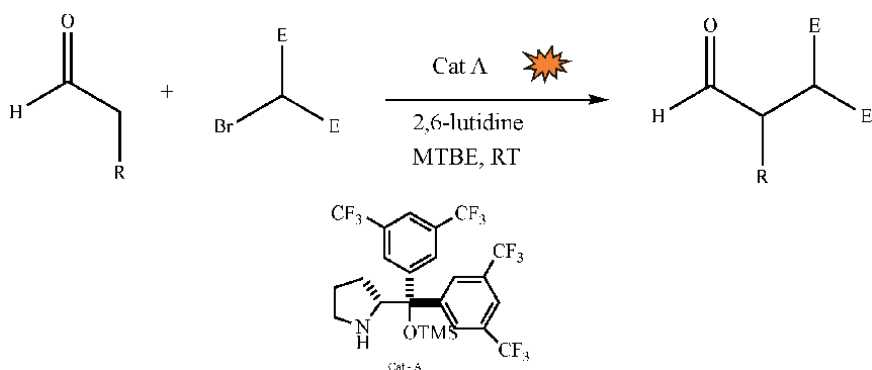


Figure 14.
α-Alkylation of aldehydes.

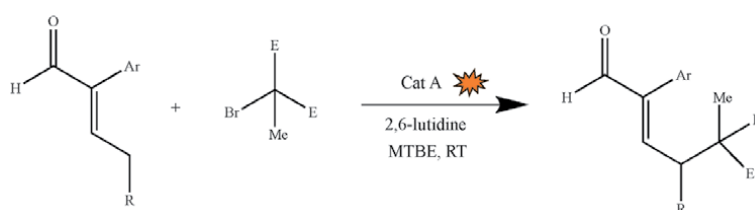


Figure 15.
γ-Alkylation of enals.

and drug industries. The coupling reactions are very highly enantioselective with good reaction and optical yields, and it was found to tolerate many functional groups under the reaction conditions that are described by the authors. They report that they were successful in their initial attempt itself on the symmetric cross-dehydrogenative coupling reaction between xanthene and pentanal employing Jørgensen's catalyst. With this protocol they developed the scope of enantioselective CDC of xanthenes with various aldehydes. Excellent product and optical yields were obtained with aliphatic aldehydes, while sterically hindered isobutyraldehyde gave poor yield but with excellent optical yield. Thioxanthenes too are tolerant under CDC reaction conditions [15] (**Figure 16**).

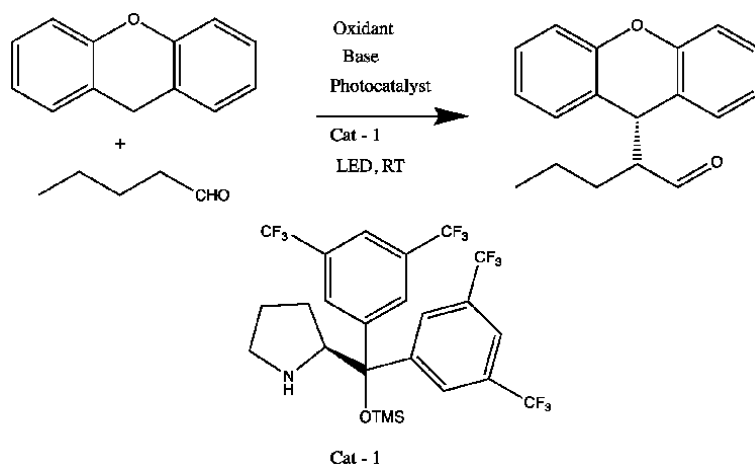


Figure 16.
Photoredox cross-dehydrogenative coupling of aldehydes with xanthenes.

11. Continuous flow α -arylation of N,N-dialkylhydrazones under visible-light photoredox catalysis

The α -arylation of aldehyde-derived N,N-dialkylhydrazones with electron-deficient aryl and heteroaryl cyanides gives rise to substituted products under visible-light conditions with the use of photoredox catalysts. These structural motifs hold interesting pharmacological activities, and by these novel technologies, α,α' -diaryl-N,N-cycloalkylhydrazones were obtained in moderate yields, and it is to be noted that conventional methods for the same are found to be non-cost-effective and time-consuming in nature. In this typical methodology, hydrazine and aryl or heteroaryl cyanides were subjected to 455 nm blue light-emitting diodes with 1 mol % of Ir(ppy)₃ as photocatalyst at 40 °C with LiOAc (2 equiv) as base and DMSO as solvent to get the desired product [16] (Figure 17).

The mechanism describes that single-electron transfer occurs from Ir(III) to cyanoarene, then the oxidized Ir(IV) undergoes a second electron transfer mechanism with hydrazine forming a radical cation, and the Ir is ready for the catalytic cycle. LiOAc deprotonates the proton from hydrazine system; then various steps of reactions yield the product. Ultimately, structurally complex α,α' -diaryl-N,N-cycloalkylhydrazones were obtained in moderate yields by the repetition of the direct arylation protocol. A continuous flow procedure for the preparation of α -aryl-N,N-dialkylhydrazones on a multigram scale has also been established.

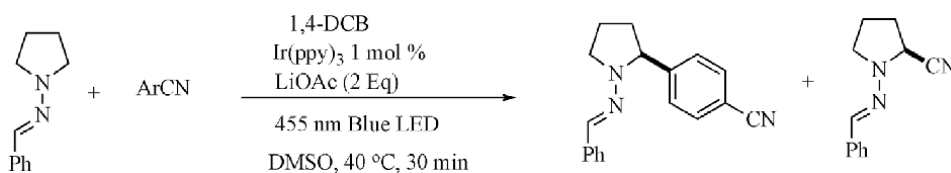


Figure 17.
 α -Arylation of hydrazones.

12. Rapid access to pharmacophore fragments from β -cyanoaldehydes

Realizing the importance of asymmetric synthesis of the late chemists, they are making use of photoredox and organocatalysis together, among which C—C bond forming reactions are very important in the construction of biologically active compounds in a stereoselective fashion. One of the C—C bond forming reactions which enable the alkylation of aldehydes with a reserved cyanide functional group in the new bond is useful for synthetic manipulations. The research article presented describes the generation of C—C bond by making use of α -bromocyanoalkylated compounds as reagents, and this reaction generated β -cyano alkyls in a single synthetic operation with stereoselectivity. In a typical experimental procedure, an aldehydic compound α -bromoacetonitrile, Ru(bpy)₃Cl₂, asymmetric organocatalyst, and an imidazolidinone catalyst reaction mixture is irradiated by a 26 W CFL light source. The results are highly appreciable with preparative yield and with excellent enantioselectivity. More interestingly, this useful methodology has also demonstrated a total synthesis of a lignin natural product, namely, (–) bursehernin [17].

13. Photocatalytic synthesis of piperazines from aldehydes and ketones

Piperazines are important class of compounds with important pharmacological properties such as anthelmintic, antiallergic, antibacterial, antihistaminic,

antiemetic, and antimigrainic activities, and hence developing a working technology for the syntheses of piperazine analogues is very important to arrive at structural activity relationship. To arrive at an array of piperazines, recently a research article is reported that utilizes silicon-based reagents, and they denote this as silicon amine protocol (SLAP); in this process a variety of aromatic, heteroaromatic, and aliphatic aldehydes and ketones were employed to produce an array of piperazines using iridium-based photoredox catalyst ($\text{Ir}[(\text{ppy})_2\text{dtbbpy}]\text{PF}_6$) and blue light radiation. The products obtained do not have any trace metal impurities since this protocol is tin-free alternative (SnAP—tin amine protocol). The reaction conditions enforced is mild and tolerates unprotected functional groups and steric hindrance and very importantly provides an access to wide array of piperazines without any trace metals for the SAR studies [18].

14. β -Arylation of aldehydes

The direct β -functionalization of carbonyl groups is very little known. MacMillan et al. first reported the combination of organocatalysis and photoredox catalysis for the direct β -C—H arylation of carbonyl compounds using benzonitrile as aryl donor (**Figure 18**). The proposed mechanistic rationale is shown in **Figure 19** and

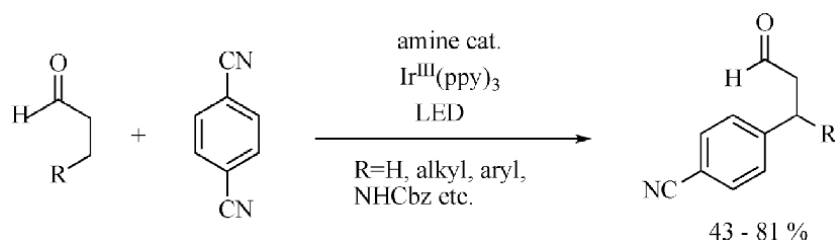


Figure 18.
 β -Arylation of aldehydes.

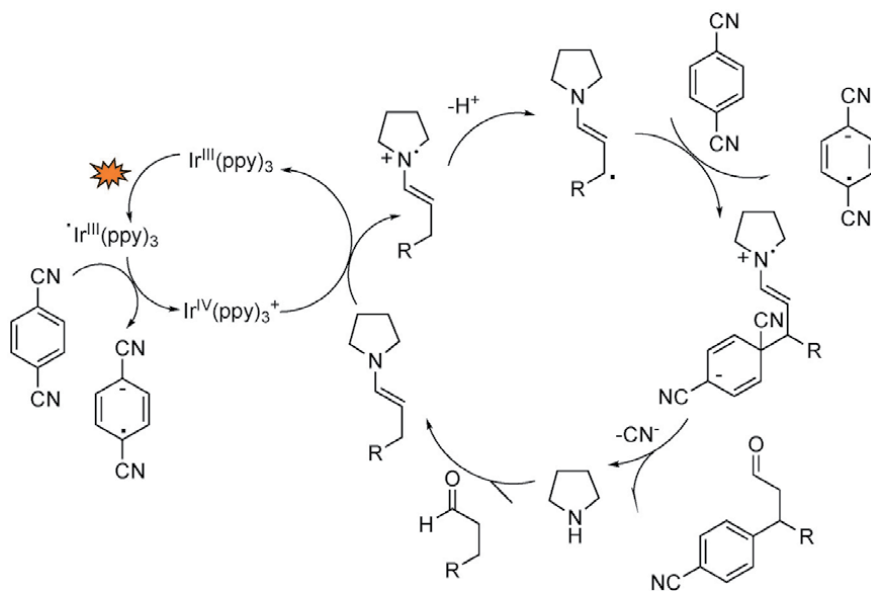


Figure 19.
 β -Arylation of aldehydes—organocatalytic cycle.

follows an oxidative quenching cycle pathway, starting with the formation of a cyclohexadienyl radical anion [19].

15. Enamine, direct β -alkylation

Saturated aldehydes can be alkylated at the beta position directly by a synergistic combination of photoredox catalysis and organocatalysis [20]. Enamine oxidation by visible-light LED provides an activated β -enaminy radical which readily combines with a wide range of Michael acceptors to produce β -alkyl aldehydes efficiently. Both inter- and intramolecular C—H functionalizations are possible in an atom economical redox-neutral process (Figure 20).

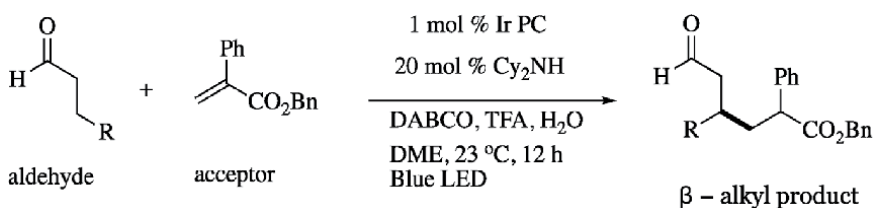


Figure 20.
Direct β -alkylation of enamines.

1,4-Diazabicyclo[2.2.2]octane (DABCO) as an organic base and DME as solvent were essential for the desired bond formation reaction. Thus a unique 5π -carbonyl activation utilizing the synergistic merger of organocatalysis and photoredox catalysis was used to accomplish the direct β -arylation of saturated ketones and aldehydes. A catalytically generated enaminy radical formed via oxidation and β -deprotonation of an enamine and a radical anion generated by photocatalytic reduction of cyanoarene couple to form the β -carbonyl products. The generality of the activation platform was further demonstrated by a β -aldol reaction of ketones with transiently generated aryl ketyl radicals to form γ -hydroxy ketone adducts. The reaction was then further extended to intramolecular cyclization via formation of cyclic molecules through both 6-exo and 5-exo cyclizations with useful efficiencies and diastereocontrol. This proves further that the critical step does not involve radical-radical coupling (Figure 21).

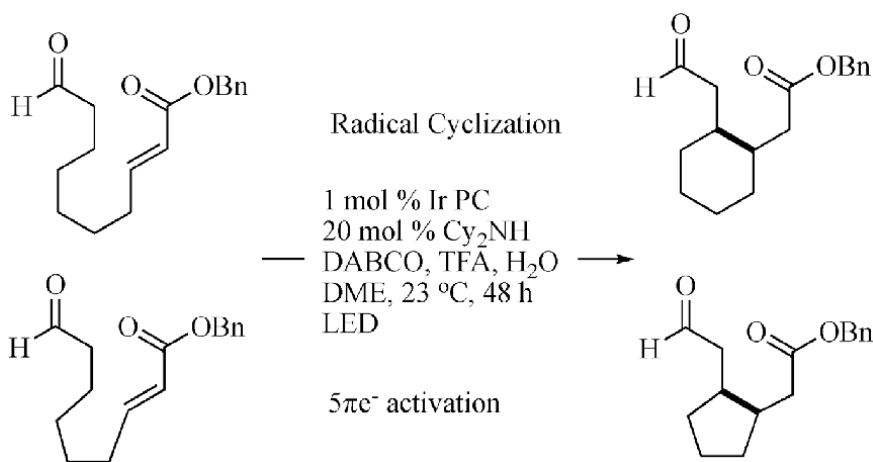


Figure 21.
 5π e⁻ activation, 6-exo to 5-exo.

16. Iminium and enamine catalysis in enantioselective photochemical reactions

Chiral iminium ion photochemistry is an emerging synthetic field; with the creativity of synthetic chemistry, they utilized [2+2] photocycloaddition to arrive at complex molecular architecture. In order to execute the [2+2] photocycloaddition, they have first synthesized an alkene tethered to a chiral iminium perchlorate salt, to procure the chiral product; the iminium salt is produced using a C2-symmetric chiral auxiliary. The bench chemists observed that (i) substituents at positions C2 and C5 of the pyrrolidine were crucial, (ii) the reaction process proceeds through single-electron transfer, (iii) the reaction takes place at the singlet hypersurface, (iv) this notable [2+2] cycloaddition reaction takes place via a concerted pathway resulting from the strong π to π^* absorption, and (v) the iminium salt absorbs light at 280 nm. The reward from this developed protocol was 82% ee and 40% chemical yield [21] (**Figure 22**).

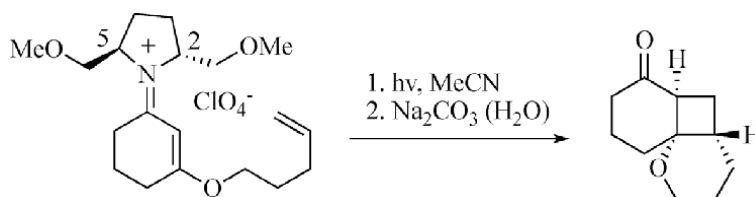


Figure 22.
Iminium catalysis: [2+2] photocycloaddition reaction of iminium salts.

17. Iminium catalysis: β -benzylation of enals and enones

The chemistry of ortho-quinodimethanes is very well exploited for the generation of six-membered carbocyclic frameworks by reacting with a diene and through an inter- or intramolecular [4+2] cycloaddition. Under VLPC condition, reports indicate that the photoexcitation of ortho-alkyl-substituted benzaldehydes and benzophenones generates the ortho-quinodimethanes, a diene intermediate, whereas instead of undergoing the [4+2] cycloaddition to yield the carbocyclic product, it gave solely the β -benzylated products through a Michael-type addition reaction. The secondary amine employed in this reaction is solely responsible for the Michael-type product (**Figure 23**).

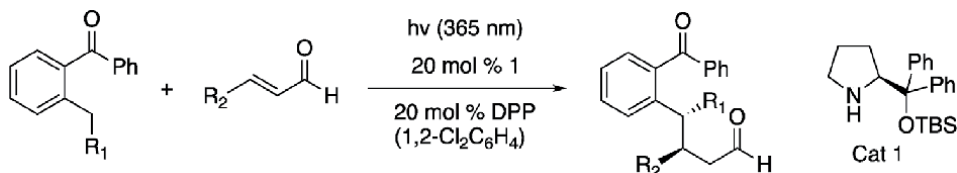


Figure 23.
 β -Benzylation of enals and enones.

The reaction mechanism is very interesting for the academic enthusiastic personalities; the chiral secondary amines react with the α,β -unsaturated compound that is used in the reaction medium. When the reaction mixture was irradiated with $\lambda = 365$ nm, the photons enolize the ortho-alkyl-substituted benzaldehyde or

benzophenone to (E)-enol and then the iminium salts in close proximity with the other reactants to deliver the Michael-type addition products rather than [4+2] cycloadducts. A density functional theory (DFT) computational study was carried out by the authors to shed some light on this unusual reactivity, and the results indicated that this transformation proceeds through a water-assisted proton shuttle mechanism. The optical yields are excellent, and it is worth mentioning that no photocatalyst was needed in this reaction.

18. Iminium catalysis: β -alkylation of enals and enones

A major breakthrough in the field of asymmetric radical chemistry was represented by Melchiorre group; they achieved the first enantioselective radical conjugate addition (RCA) to β,β -disubstituted cyclic enones by a combination of photoredox catalysis and iminium-based organocatalysis. The organocatalyst and the primary amine moiety react with a α,β -unsaturated enone forming a chiral iminium ion as the reactive intermediate; the 1,3-benzodioxole present in the reaction medium upon irradiation by means of an UV light-emitting diode and in the presence of tetrabutylammonium decatungstate (TBADT) generates a carbon-centered radical. Thus generated carbon-centered radical being short-lived and active, it reacts with the chiral iminium ion producing an α -iminyl radical cation. Then through an intramolecular SET process, the α -iminyl radical cation was reduced to enamine. A tautomerism reaction, that is, enamine-imine tautomerization, regenerates photocatalyst TBADT, and finally the work procedure gives rise to the product with excellent enantio- and diastereoselectivities, and the chiral amine is recovered [22] (Figure 24).

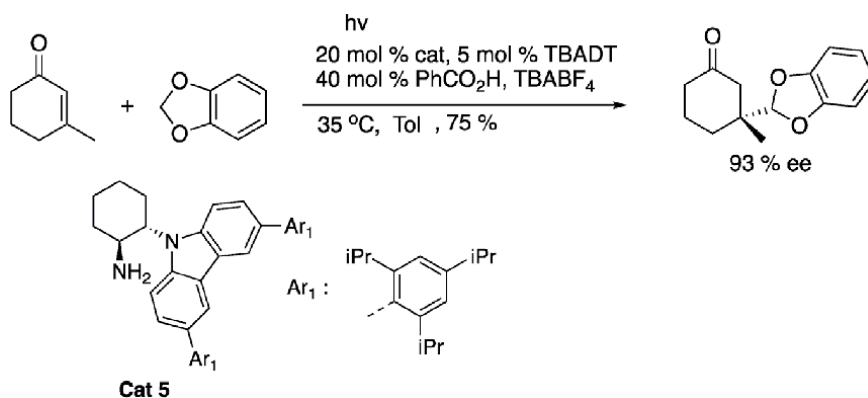


Figure 24.
Iminium catalysis: β -alkylation of enals and enones.

19. Enamine catalysis: β -alkylation of enals and enones

Following the footpaths of iminium catalysis, the twin brothers, namely, the photoredox catalysis and organocatalysis, fruitfully accomplished the enantioselective α -alkylation of aldehydes; the photoredox catalyst employed was 0.5 mol% of $\text{Ru}(\text{bpy})_3\text{Cl}_2$ (bpy = 2,20-bipyridine), and the photocatalyst utilized was 20 mol% of a chiral imidazolidinone. Under the reaction condition, the

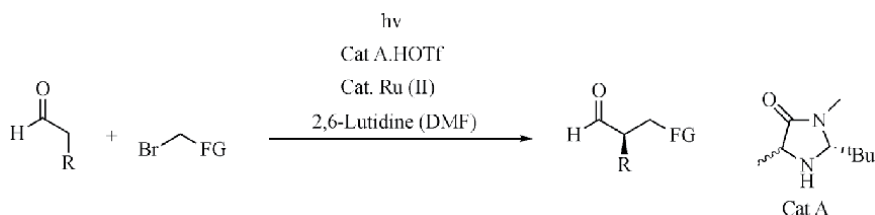


Figure 25.
Enamine catalysis.

substrate aldehydic compound reacts with a chiral enamine (organocatalyst) forming a chiral enamine intermediate; thereby the substrate is tuned to be nucleophilic in nature, and the nucleophilicity arises at the α -position to the aldehydic chromophore. Simultaneously, in the reaction medium, the photocatalyst is electronically excited by the visible light; once excited, it accepts a single electron from the chiral enamine, and the Ru [I] species then reduces the α -bromocarbonyl compound, and in this process the photocatalyst is regenerated. At the work-up the coupled product is released from the enamine with high stereoselectivity and in good yields (**Figure 25**).

20. Enamine catalysis: α -benzylation of aldehydes and ketones, α -hydroxylation, β -arylation

α -Benzylation and α -alkylation are thematically one and the same; however, much recent advances in α -benzylation of carbonyl compounds were reported with stereoselectivity (**Figure 26**).

A variety of electron-deficient aryl and heteroaryl methylene bromides were examined as the benzylating agents, and they were coupled with a range of aldehydes bearing different functional groups efficiently with excellent enantioselectivity. The benzylation reaction proceeds via an oxidative quenching cycle, in contrast to the reductive quenching cycle operation in the α -alkylation reaction. The hybrid organocatalytic cycle and photoredox catalytic cycle are similar to the reaction of aldehydes with alkyl halides described in **Figure 11**. The Ir photocatalyst fac-Ir(ppy)₃ and imidazolidinone organocatalyst generate the benzyl radical from electron-deficient benzyl halides. This benzyl radical then couples with the chiral enamine providing α -amino radical which is oxidized by the intermediate Ir(IV) species. Hydrolysis of the iminium ion releases the α -benzyl aldehyde. A range of electron-deficient heteroaromatics such as pyridines, pyrazines, pyrimidines, quinolines, and benzimidazoles undergo facile reaction (**Figure 27**).

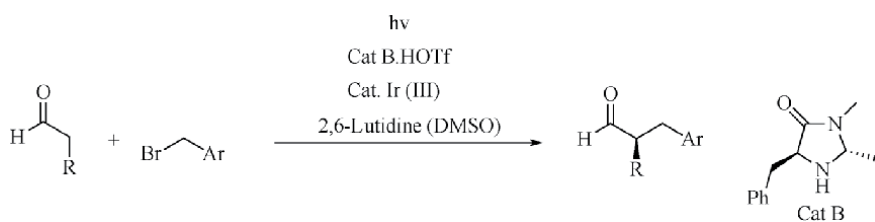


Figure 26.
Enamine benzylation.

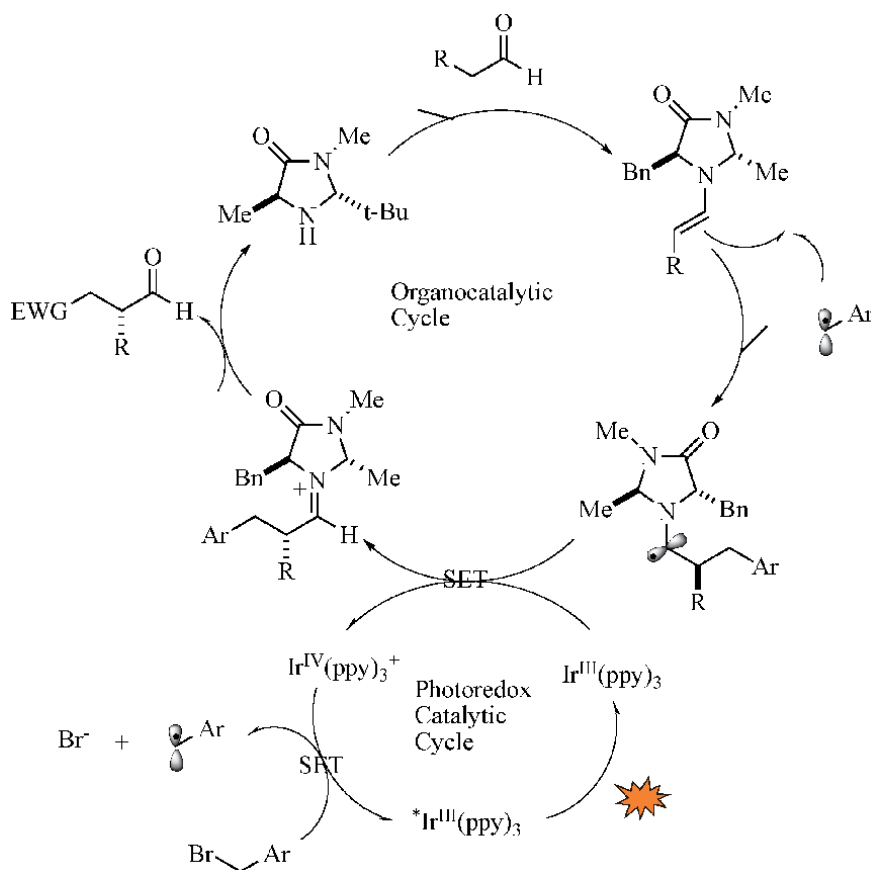


Figure 27.
 A catalytic cycle—enantioselective benzylation of aldehydes.

21. Enamine catalysis: α -hydroxylation of aldehydes and ketones

The α -hydroxylation of carbonyl compounds is a very important class of reaction in the design of drug molecules; mostly the hydroxylation is appended in a stereoselective fashion. Conveniently it is achieved by enolizing the carbonyl, and the oxidation is done by oxidizing agents such as epoxides, OsO_4 , and so on. Rarely the singlet oxygen is used for this functional group introduction. In this VLPC condition, the hardships related to the α -hydroxylation reactions are tackled with ease; an amine-catalyzed enantioselective α -hydroxylation of aldehydes under photochemical condition was achieved where (L)- α -Me proline-based organocatalyst was exploited and singlet oxygen is employed instead of explosive oxidizing agents. Mechanistically the amino acid-based organocatalyst activated the aldehyde, and

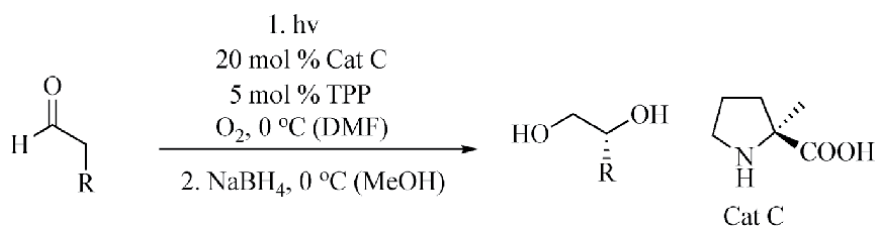


Figure 28.
 Enamine hydroxylation.

the α -position is ready for reactivity. Photosensitizer tetraphenylporphyrin (TPP) sensitizes $^3\text{O}_2$ to $^1\text{O}_2$ by the action of visible light, which then reacts with the substrate enamine through an ene-type reaction, forming α -hydroperoxide which is then reduced using NaBH_4 to get 1,2-diols. Later this methodology was extended to cyclic ketones and yielded appreciable enantioselectivity (**Figure 28**).

22. Enamine catalysis: β -arylation of ketones

The α -functionalization of carbonyl compounds is easily carried out, whereas functionalizing at the β -position is not easy and requires multiple synthetic operations. With creativity and with clear understanding of radical chemistry using a VLPC protocol, these authors have enolized the cyclic ketones; thereby a double bond is formed, and the radical chemistry created an allyl radical at the β -position. In the reaction medium, the iridium-based catalyst generated arene radical cation from cyanoarenes, which reacts with the allyl radical and forms the β -substituted ketones with the elimination of the cyanide group from the arene (**Figure 29**).

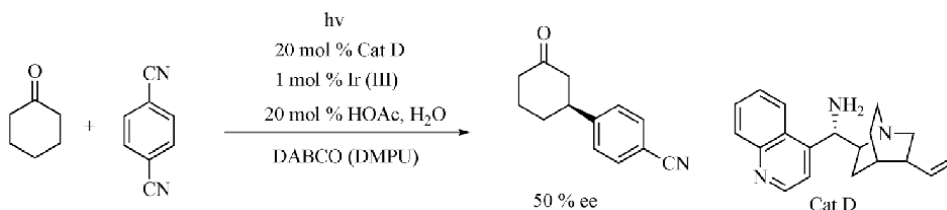


Figure 29.
Ketone β -arylation.

23. Relay visible-light photocatalysis

A relay visible-light photocatalysis strategy using formal 4+1 annulation and aromatization was achieved. Three successive photoredox cycles (one oxidative cycle and two reductive quenching cycles) were engaged in a reaction with one photocatalyst. Multiple quenching cycles could be demonstrated in a single reaction involving formal 4+1 annulation of hydrazone with 2-bromo diethylmalonate [23] (**Figure 30**).

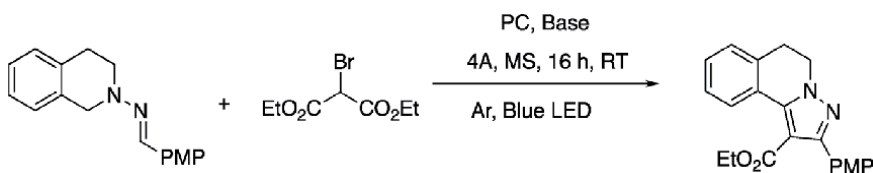


Figure 30.
Relay VLPC.

24. Conclusion

Photosynthesis has attracted biologists, physicists, and chemists for centuries; chemists by understanding how the plants synthesized chemicals using sunlight have been inspired, and that resulted in this new domain. Ultimately these new sets

of reactions under VLPC are photosynthesis mimic reactions, and the chemists brought the process into action at the laboratories.

VLPC strategies developed by chemists in recent years portrait the esthetic taste and the design of energy-saving and environmentally compatible and benign features in this innovative domain of organic synthesis.

Among all the subdisciplines of catalysis, the newly emerged gifted child, namely, visible-light photoredox catalysis, has grown rapidly and has made a great deal of interest in both academia and industry; in the near future, we will be witnessing the process development of drug molecules.

The twin catalysis comprising a chiral agent and the transition metal catalyst brought forward the asymmetric synthesis in a one-pot synthetic fashion in this neoteric protocol which portrays the highest level of creativity of synthetic chemists. Consequently, it can be construed that from the catalytic professionals, more VLPC protocols will emerge to attain pharmaceutically active ingredients through industrial manufacturing processes, especially in enantiomerically enriched forms.

In terms of kinetics, not much work is done, and such research articles are expected in the pipeline; much work has to be done on the recyclability and reusability of catalytic materials including the studies on leaching.

It is interesting to note that only in this domain the methodology quickly reached to the stage of asymmetric synthesis in a rapid way, implying the success in the process development of drug molecules; subsequently, more process developments are expected as the industrial process.

Author details

Alwar Ramani¹, Shobha Waghmode² and Suresh Iyer^{3*}


¹ Heriot-Watt University, United Kingdom

² Abasaheb Garware College, SPPU, Pune, Maharashtra, India

³ National Chemical Laboratory, Pashan, Pune, Maharashtra, India

*Address all correspondence to: s.iyer@ncl.res.in

IntechOpen

© 2020 The Author(s). Licensee IntechOpen. This chapter is distributed under the terms of the Creative Commons Attribution License (<http://creativecommons.org/licenses/by/3.0>), which permits unrestricted use, distribution, and reproduction in any medium, provided the original work is properly cited. 

References

- [1] Prier CK, Rankic AA, MacMillan DWC. Visible light photoredox catalysis with transition metal complexes; applications in organic synthesis. *Chemical Reviews*. 2013;**113**:5322-5363. DOI: 10.1021/cr300503r
- [2] Marzo L, Pagire SK, Reiser O, Kong B. Visible-light photocatalysis: Does it make a difference in organic synthesis? *Angewandte Chemie International Edition in English*. 2018; **57**:10034-10072. DOI: 10.1002/anie.201709766
- [3] Schultz DM, Yoon TP. Solar synthesis: Prospects in visible light photocatalysis. *Science*. 2014;**343**(6174): 1239176-1239176. DOI: 10.1126/science.1239176
- [4] Stephenson CRJ, Yoon TP, MacMillan DWC. *Visible Light Photocatalysis in Organic Chemistry*. Weinheim, Germany: Wiley-VCH Verlag GmbH & Co. KGaA; 2018. DOI: 10.1002/9783527674145. ISBN: 9783527335602
- [5] Karkas MD, Porco JA Jr, Stephenson CRJ. Photochemical approaches to complex chemotypes: Application in natural product synthesis. *Chemical Reviews*. 2016;**116**: 9683-9747. DOI: 10.1021/acs.chemrev.5b00760
- [6] Nikitas N, Triandafillidi I, Kokotos CG. Photoorganocatalytic synthesis of acetals from aldehydes. *Green Chemistry*. 2019;**21**:669-674. DOI: 10.1039/c8gc03605e
- [7] Iqbal N, Choi S, You Y, Cho EJ. Aerobic oxidation of aldehydes by visible light photocatalysis. *Tetrahedron Letters*. 2013;**54**(46):6222-6225. DOI: 10.1016/j.tetlet.2013.09.005
- [8] Narayanam JMR, Stephenson CRJ. Visible light photoredox catalysis: Applications in organic synthesis. *Chemical Society Reviews*. 2011;**40**(1): 102-113. DOI: 10.1039/b91388on
- [9] Zhang X, MacMillan DWC. Direct Aldehyde C-H arylation and alkylation via the combination of nickel, hydrogen atom transfer, and photoredox catalysis. *Journal of the American Chemical Society*. 2017;**139**(33):11353-11356. DOI: 10.1021/jacs.7b07078
- [10] Capacci AG, Malinowski JT, McAlpine NJ, Kuhne J, MacMillan DWC. Direct, enantioselective α -alkylation of aldehydes using simple olefins. *Nature Chemistry*. 2017;**9**(11):1073-1077. DOI: 10.1038/nchem.2797
- [11] Nicewicz DA, MacMillan DWC. Merging photoredox catalysis with organocatalysis: The direct asymmetric alkylation of aldehydes. *Science*. 2008; **322**(5898):77-80. DOI: 10.1126/science.1161976
- [12] Nagib DA, Scott ME, MacMillan DWC. Enantioselective α -trifluoromethylation of aldehydes via photoredox organocatalysis. *Journal of the American Chemical Society*. 2009; **131**(31):10875-10877. DOI: 10.1021/ja9053338
- [13] Cecere G, König CM, Alleva JL, MacMillan DWC. Enantioselective direct α -amination of aldehydes via a photoredox mechanism: A strategy for asymmetric amine fragment coupling. *Journal of the American Chemical Society*. 2013;**135**(31):11521-11524. DOI: 10.1021/ja406181e
- [14] Silvi M, Arceo E, Jurberg ID, Cassani C, Melchiorre P. Enantioselective organocatalytic alkylation of aldehydes and enals driven by the direct photoexcitation of enamines. *Journal of the American Chemical Society*. 2015;**137**:6120-6123. DOI: 10.1021/jacs.5b01662

- [15] Larionov E, Mastandrea MM, Pericàs MA. Asymmetric visible-light photoredox cross-dehydrogenative coupling of aldehydes with xanthenes. *ACS Catalysis*. 2017;**7**(10):7008-7013. DOI: 10.1021/acscatal.7b02659
- [16] Vega JA, Alonso JM, Méndez G, Ciordia M, Delgado F, Trabanco AA. Continuous flow α -arylation of N,N-dialkylhydrazones under visible-light photoredox catalysis. *Organic Letters*. 2017;**19**(4):938-941. DOI: 10.1021/acs.orglett.7b00117
- [17] Welin ER, Warkentin AA, Conrad JC, MacMillan DWC. Enantioselective α -alkylation of aldehydes by photoredox organocatalysis: Rapid access to pharmacophore fragments from β -cyanoaldehydes. *Angewandte Chemie International Edition in English*. 2015; **54**(33):9668-9672. DOI: 10.1002/anie.201503789
- [18] Hsieh S-Y, Bode JW. Silicon amine reagents for the photocatalytic synthesis of piperazines from aldehydes and ketones. *Organic Letters*. 2016;**18**(9): 2098-2101. DOI: 10.1021/acs.orglett.6b00722
- [19] Angnes RA, Li Z, Correia CRD, Hammond GB. Recent synthetic additions to the visible light photoredox catalysis toolbox. *Organic & Biomolecular Chemistry*. 2015;**13**(35): 9152-9167. DOI: 10.1039/c5ob01349f
- [20] Terrett JA, Clift MD, MacMillan DWC. Direct β -alkylation of aldehydes via photoredox organocatalysis. *Journal of the American Chemical Society*. 2014; **136**(19):6858-6861. DOI: 10.1021/ja502639e
- [21] Zou Y-Q, Hörmann FM, Bach T. Iminium and enamine catalysis in enantioselective photochemical reactions. *Chemical Society Reviews*. 2018;**47**(2): 278-290. DOI: 10.1039/c7cs00509a
- [22] Arceo E, Jurberg ID, Álvarez-Fernández A, Melchiorre P. Photochemical activity of a key donor-acceptor complex can drive stereoselective catalytic α -alkylation of aldehydes. *Nature Chemistry*. 2013; **5**(9):750-756. DOI: 10.1038/nchem.1727
- [23] Cheng J, Li W, Duan Y, Cheng Y, Yu S, Zhu C. Relay visible-light photoredox catalysis: Synthesis of pyrazole derivatives via formal [4 + 1] annulation and aromatization. *Organic Letters*. 2016;**19**(1):214-217. DOI: 10.1021/acs.orglett.6b03497

Supported-Metal Oxide Nanoparticles-Potential Photocatalysts

Vu T. Tan and La The Vinh

Abstract

Recently, nanosized metal oxides play an essential role in the photocatalytic system due to their ability to create charge carriers during the light irradiation. Metal oxide nanoparticles display excellent light absorption properties, outstanding charge transport characteristics, which are suitable in the photocatalytic system for the treatment of wastewater. Most of the photocatalysts found in the literature are in the form of powders. Only a few supported photocatalytic systems have been reported. The advantages of supported photocatalysts, such as that they produce a small pressure drop, have good mechanical stability and are easily separated from the reaction medium, make them superior to conventional powder photocatalysts. In this chapter, the definition of supported-metal oxide nanoparticles as the photocatalyst and their synthesis methodology are detailed discussed.

Keywords: photocatalysis, metal oxides, thin film, semiconductor, substrate

1. Introduction

1.1 General description about photocatalysis

Photocatalysis by semiconductors, such as those indicated above, is a well-established method for degrading organic contaminants in wastewaters. When the photon with energy greater than the band gap of the semiconductor is absorbed by the solid, an electron is excited from the valence band to the conduction band, resulting in an electron-hole pair. These exciting state conduction band electrons and valence band holes have several possible fates [1]:

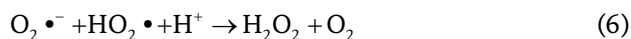
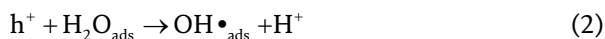
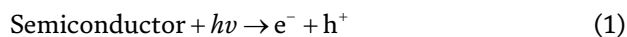
- a. they can combine and disperse the energy as heat while still in the bulk matrix of the crystal;
- b. they can become trapped in defect traps;
- c. they can migrate to the surface, where they recombine;
- d. they may take part in redox reactions with electron donors or acceptors adsorbed onto the surface, which is the desirable pathway if degradation of organic contaminants is to occur.

In aqueous systems, these adsorbed species will correspond to water molecules, hydroxide ions, and oxygen molecules.

It is clear to know that in semiconductors, the generation of electrons and holes depends on the position of the energy levels. Besides, the redox potential of a donor species on the surface of the photocatalyst needs to be more negative (higher in energy) than the valence band position of the semiconductor to fill the electron vacancies. Similarly, acceptor molecules must have a more positive redox potential (lower in energy) than the conduction band. In view of this, one of the advantages of TiO₂ and ZnO compared to other semiconductors is that their electronic structure is such that it allows both the reduction of protons and the oxidation of water [2]. This phenomenon can be appreciated in the redox potential diagram shown in **Figure 1**. Recently, the use of TiO₂ and ZnO as photocatalysts has been thoroughly investigated.

Numerous conditions of a photocatalyst are required to achieve high photocatalytic efficiency. Firstly, the bandgap of the semiconductor must be higher than the redox potential of the H₂O/OH[•] couple, and the material must be photo-stable. Secondly, the recombination of electron-hole pairs must be minimized. In other words, they need to be kept apart to allow time for the redox reactions to occur. Separation can be achieved by trapping electrons or holes in defects [4] or by using electrically conductive supports [5].

The holes in the photocatalyst valence band can oxidize the adsorbed water or hydroxide ions, while electrons in the conduction band can reduce molecular oxygen to superoxide anions [6]. These processes are summarized in the following equations:



The degradation of organic contaminants is commonly attributed to oxidation by hydroxyl radicals. This process is schematically described in **Figure 2**. This has led to the use of the term “Advanced Oxidation Processes,” although there is evidence that in some systems, reductive pathways also operate [7].

Among *Advanced Oxidation Processes*, the photocatalytic processes are focused on the conversion of highly toxic organic to either less toxic organic compounds or CO₂ and H₂O [8]. When the photocatalytic reaction is implemented in the presence of O₂, the catalyst plays two main roles: to scavenge the photogenerated electrons and to produce active oxygen species [9]. We already know that metal oxides can respond to both UV-light and visible light, depending on the energy band gap of the materials. Newly, the photocatalytic process used visible light is widely employed for environmental cleanup [10].

Recently, many metal oxides (TiO₂, ZnO, SnO₂, and WO₃) have been widely used for the photocatalysis process. This is due to their abundance in nature,

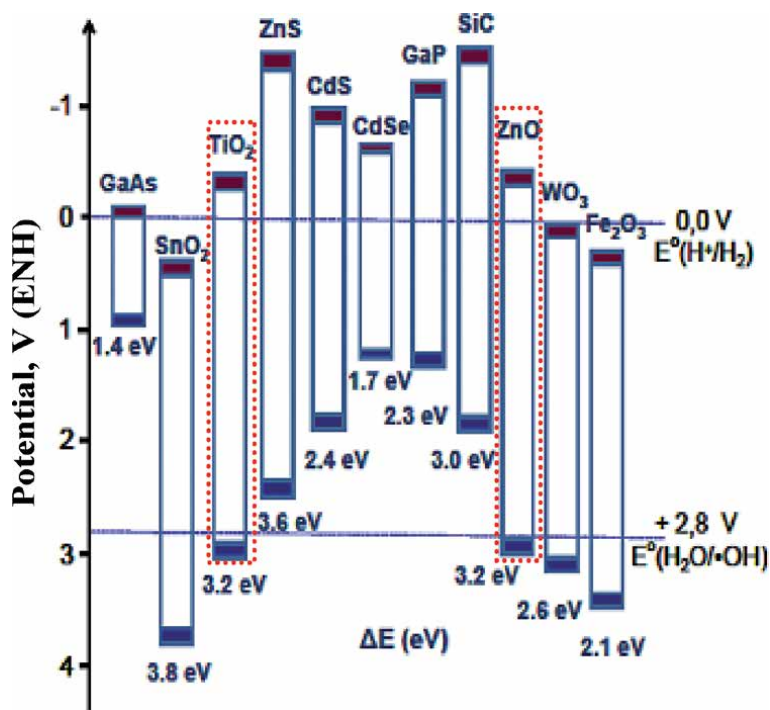


Figure 1. Band gaps (eV) and redox potentials for several semiconductors referred to the normal hydrogen electrode (NHE). Reproduced from Ania et al. [3].

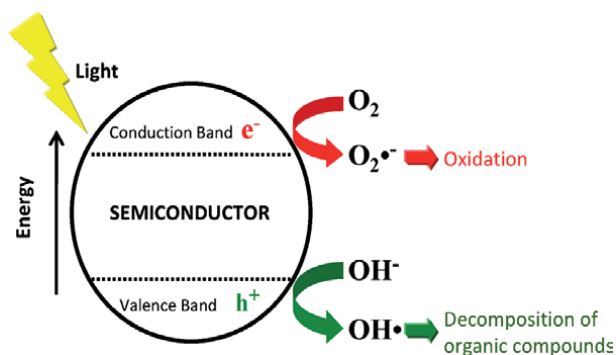


Figure 2. Schematic diagram showing the processes involved in semiconductor photocatalysis. Reproduced from Gratzel et al. [2].

stability in many conditions, and the capability to create charge carriers when they were exposed under UV or visible light. The advantageous combination of the electronic structure, light absorption capacities, and excited lifetimes of metal oxides have provided of metal oxides has provided them possible for their application as photocatalyst. The photocatalysis employing metal oxides such as TiO_2 , ZnO , SnO_2 , and WO_3 has demonstrated their efficiency in the degradation of various harmful pollutants into carbon dioxide and water.

The vast majority of the photocatalysts studied are in powder form with all the difficulties in handling and recovering that implies. Consequently, supported photocatalysts are nowadays an important research area.

2. Supported TiO₂ photocatalysts

When the light is irradiated to the surface of the semiconductor, its absorption of photons provokes the photocatalytic reaction at the surface of the catalyst. Among many semiconductor materials, titanium dioxide (TiO₂) nanoparticles have been widely studied for photocatalytic applications over the last two decades [11, 12]. TiO₂ is relatively inexpensive, insoluble in water, and non-toxic. It can provide photogenerated holes with high oxidizing power because of its wide bandgap (3.2 eV) [13].

The common mechanism of the photocatalytic process of TiO₂ material consists of the interfacial redox reactions of the generated holes and electrons when the TiO₂ materials are irradiated by light with appropriate energy (**Figure 3**) [14, 15].

Most of the photocatalysts found in the literature are in the form of powders. Only a few supported photocatalytic systems have been reported, even though they have clear advantages from a practical point of view [16–18]. The most important benefit is that the separation of the supported photocatalysts from the reaction medium is simple, which minimizes the power requirements. In addition, they can be adapted to operate in flow-type continuous reactors [19–21]. Most recently, research was described by Fernández et al. [21]. They reported two methods of deposition of TiO₂ powders on different substrates (glass, quartz, and stainless steel) and evaluated the photocatalytic activities of these supporting materials through the degradation of organic compounds (**Figure 4**).

The authors demonstrated the influence of coating methodology and photocatalytic activities. The results showed that titania deposited on quartz displays a similar photocatalytic activity to that of the powder form. Therefore, the result opens a new feature for a new advantage route to immobilize catalyst for flow reactor or batch reactor. Because filtration step to recover the catalyst always causes many drawbacks in water treatment.

Then some authors [22, 23] developed a new type of supported photocatalyst that consists of mixtures of noble metal nanoparticles and commercially available TiO₂ nanoparticles (P25, Degussa-Evonik) deposited by dip-coating procedure on quartz substrate. The photocatalytic activity of the immobilized catalyst was evaluated by the degradation of malic acid. A comparison of the photocatalytic activity between supported TiO₂ with the powder TiO₂ Degussa P-25 shows slightly lower catalytic activity. This phenomenon could be explained by the total surface exposed of the catalyst to the light during the irradiation. However,

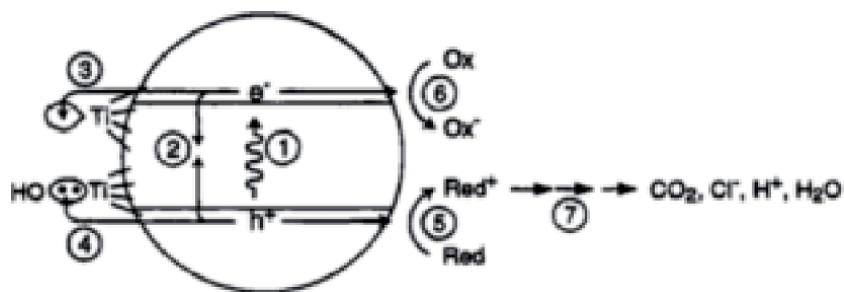


Figure 3.

The mechanism of photocatalysis process of TiO₂. Reproduced from Hoffman et al. [15]. (1) The formation of the electrons and holes by photon absorption. (2) The recombination of the generated electrons and holes. (3) The electron trapping of Ti (IV) at the conduction band to form Ti (III). (4) The hole trapping of titanol group at the valence band. (5) The oxidative pathways at the conduction band. (6) The reductive pathways at the valence band. (7) Photocatalytic oxidation reactions to form harmless compounds.

the result could be compensated by the advantage of eliminating the recovering catalyst after the treatment.

Lately, several works also reported the preparation of thin TiO_2 film on quartz substrates (**Figure 5**) by coating the TiO_2 sol using rotary evaporator [24], by dip-coating [25], by spin coating [26].

Recently, Borges et al. [27] supported commercial TiO_2 (Degussa P25) on glass spheres as a photocatalyst to treat the wastewater (**Figure 6**).

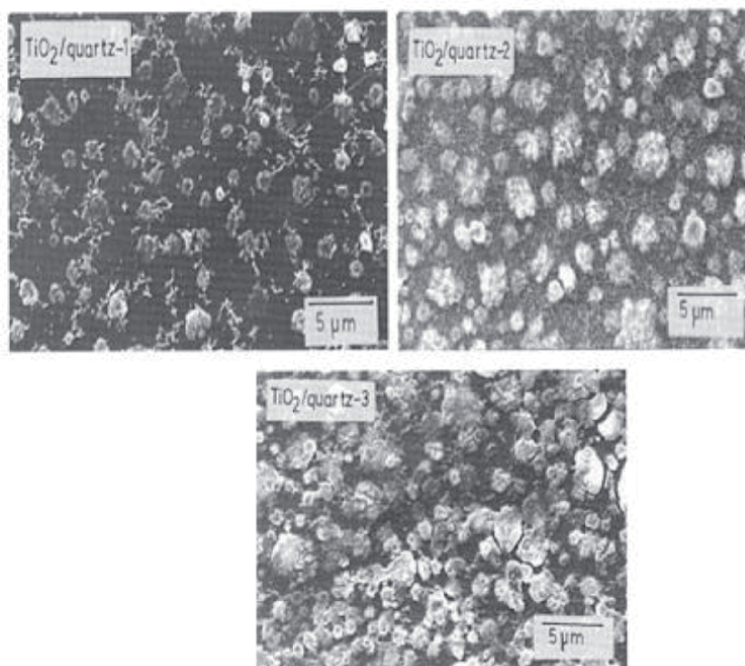


Figure 4. SEM micrographs for the three TiO_2 /quartz samples. Reproduced from Hoffman et al. [15].

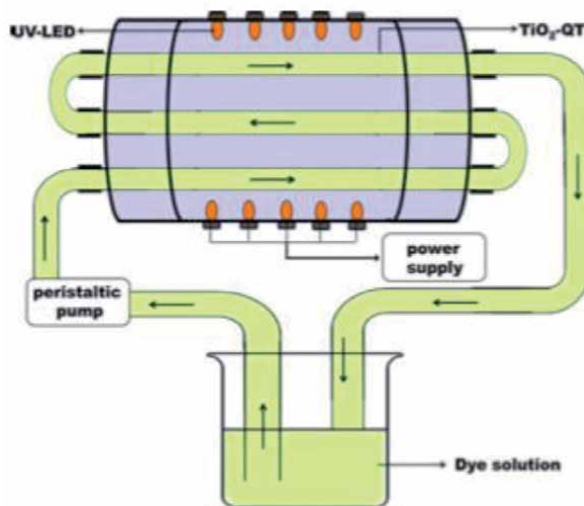


Figure 5. Schematic representation of photocatalytic reactor using TiO_2 supported on quartz. Reproduced by Natarajan et al. [25].

Figure 7 shows the surface morphology substrate of the glass spheres without TiO_2 particles. **Figure 7b** shows the TiO_2 supported on the substrate and the homogeneous distribution of TiO_2 on the surface of the glass sphere. The authors showed that photocatalytic treatment in photoreactor displays more advantages than in batch system for high volumes of industrial wastewater.

Later, several authors also used poly-vinylidene fluoride (PVDF) dual layer hollow fiber membrane as a support to immobilize TiO_2 to treat pharmaceutical compound in wastewater (**Figure 8**) [28, 29].

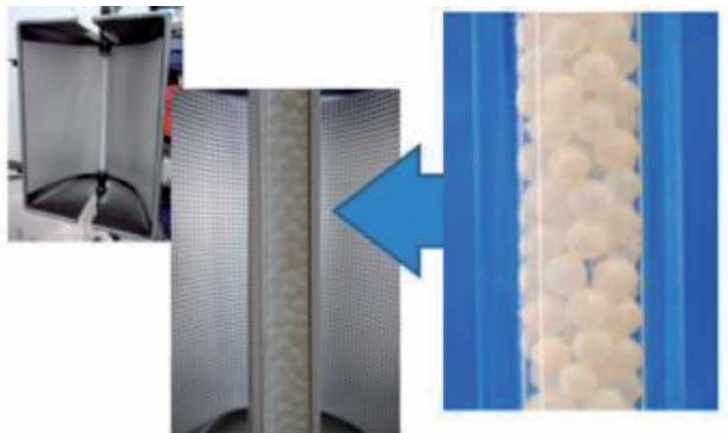


Figure 6. Packed-bed photoreactor system and glass spheres photocatalytic bed in photoreactor. Reproduced by Borges et al. [27].

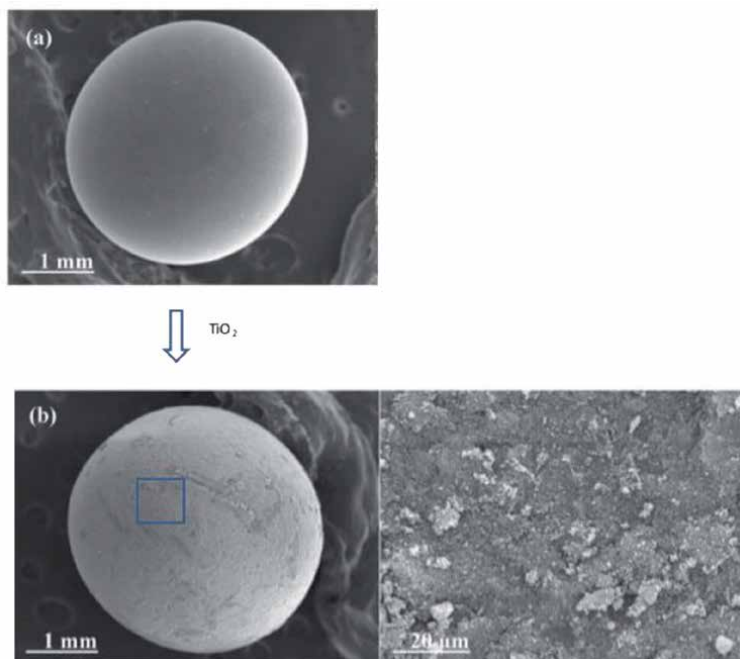


Figure 7. SEM image of the glass sphere (a), SEM image of TiO_2 supported on the glass sphere (b). Reproduced by Borges et al. [27].

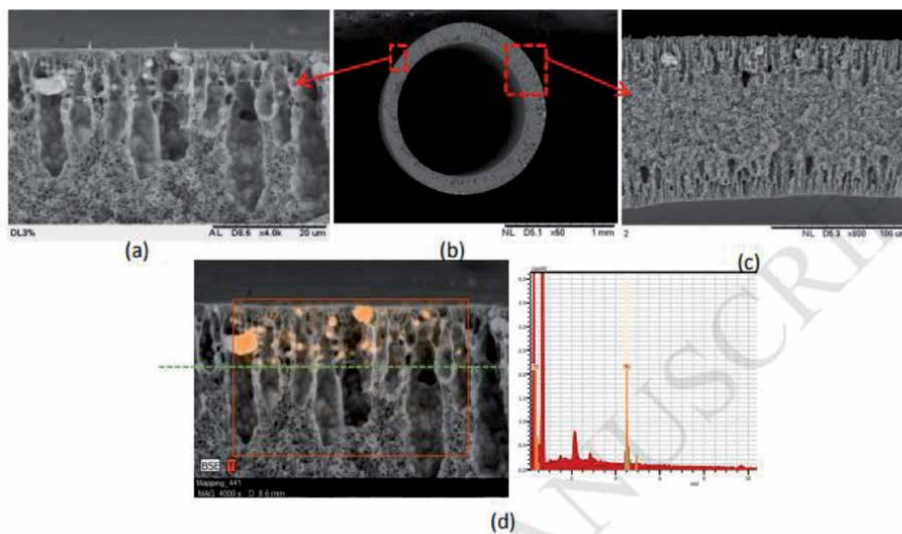


Figure 8. Images of the PVDF membranes: (a) outer surface, (b) full cross section, (c) partial cross section, and (d) EDX images of TiO_2 nanoparticles at the outer layer. Reproduced by Paredes et al. [29].

The author demonstrated that the TiO_2 supported catalyst on PVDF membranes improved the photo-transformation rate of wastewater compounds during the photocatalytic treatment. The author also claimed that the supported catalyst could be easily recycled without any separation systems or catalysis recovery technologies.

It is already to know that TiO_2 is used as a photocatalyst in the ultraviolet light region due to its wide bandgap. To improve its photocatalytic efficiency in the visible light, efforts have been made such as, doping TiO_2 with anionic species (Fluorine, Sulfur, Nitrogen), or combining TiO_2 with other metal oxides. The combination of TiO_2 with other metal oxides can reduce the recombination effect of the electron-hole before they migrate to the surface of the material [30]. In addition, the composite of TiO_2 with other metal oxides can be generated in the surface hydroxyl groups, which can trap holes after the irradiation process, which improve the separation of the electron-holes. In some cases, the composite of TiO_2 with other metal oxides can enhance the crystallinity degree of TiO_2 and increases the specific surface area of the composite which are two important properties for a photocatalyst.

Recently, TiO_2 is widely combined with other metal oxides, such as ZrO_2 , SnO_2 , WO_3 , CeO_2 , ZnO , to improve the photocatalytic activity of TiO_2 in the ultraviolet light and improving its photocatalytic efficiency in the visible region.

For example, the composite of mixed oxide ZrO_2 - TiO_2 material recently gains a great attention. By combining TiO_2 with ZrO_2 , the surface acidity of the composite can be increased, hence improved the reactivity compared to the TiO_2 [31]. In addition, the hydroxyl groups are located on the surface of the catalyst, where the holes are trapped which could improve the efficiency of the degradation of organic pollutant [32]. Therefore, the mixed oxide ZrO_2 - TiO_2 has been widely studied for the photodegradation of toxic organic compounds [31–35]. Many researchers also focused on the fabrication of ZrO_2 - TiO_2 composite thin film and study its photocatalytic efficiency under ultraviolet or visible irradiation [36–40].

Luo et al. has fabricated the ZrO_2 - TiO_2 composite thin film on glass substrate using micro-arc oxidation process and used it for the degradation of rhodamine

B under ultraviolet irradiation [40]. The $\text{ZrO}_2\text{-TiO}_2$ composite thin film consists of three compounds: anatase, rutile, and ZrO_2 phases, results that the generated electron can transfer from rutile to anatase. This phenomenon inhibits the recombination of the generated electron-hole pairs, thus improved the photocatalytic efficiency of the composite. The photodegradation of MB under UV light irradiation shows that the photocatalytic activity of $\text{ZrO}_2\text{-TiO}_2$ composite thin film is three times higher than that of the pure TiO_2 thin film.

Alotaibi et al. have reported the preparation of $\text{ZrO}_2\text{-TiO}_2$ composite thin film on glass substrate using aerosol-assisted chemical vapor deposition [32]. The photocatalytic activity of the fabricated composite thin film was evaluated through the photodegradation of resazurin redox dye under Ultraviolet light irradiation (Figure 9). The composite shows an enhancement of photocatalytic activity compared to a pure TiO_2 thin film fabricated by the same condition.

Tungsten oxide (WO_3) is a common dopant in heterogeneous photocatalysis. In the last decade, WO_3 was extensively combined with TiO_2 to improve the photocatalytic activity of TiO_2 in both UV and Visible light. Besides of using the catalyst in the powder form, the preparation of $\text{WO}_3\text{-TiO}_2$ film and its photocatalytic activity was extensively studied [41–44] due to its advantage of the recuperation way. The $\text{WO}_3\text{-TiO}_2$ film has been fabricated by several methodologies such as sol-gel and dip coating [45]; spin-coating [46]; solvothermal method combining magnetron sputtering [47]; or film on pyrex substrates by casting methodology [48].

For example, Fu et al. have fabricated the $\text{WO}_3\text{-TiO}_2$ film on quartz substrate by dip-coating synthesis [42]. The photocatalytic efficiency was evaluated by the degradation of 4-chlorophenol-4 CP, xenobiotic micropollutants, under the irradiation visible light. The result shows that by incorporation of WO_3 into TiO_2 , the $\text{WO}_3\text{-TiO}_2$ film can shift the absorption band from near UV region to the visible region. Under visible light, for the degradation of 4-CP, the prepared composite film demonstrated a higher photocatalytic activity for than that of pure TiO_2 film.

Recently, Adel et al. have prepared the $\text{WO}_3\text{-TiO}_2$ thin film on glass substrate by reactive chemical spraying and tested its photocatalytic activity under visible light. The results show that the photocatalytic thin film can degrade completely dye in textile, wastewater leading to cleaner processes [49].

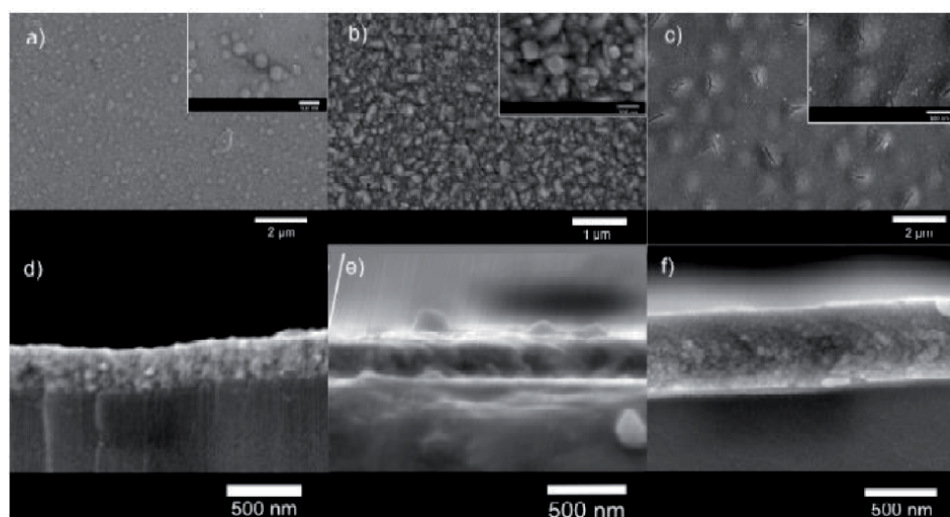


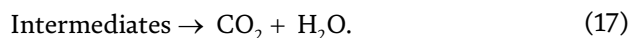
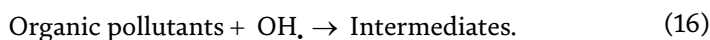
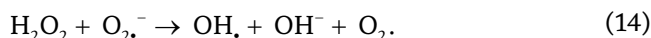
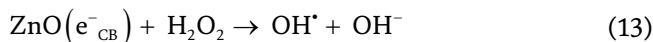
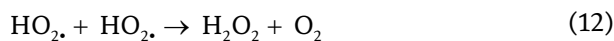
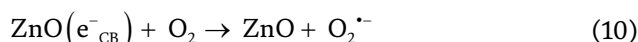
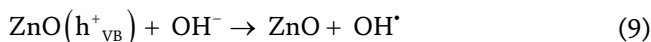
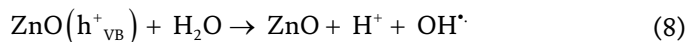
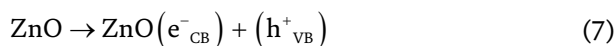
Figure 9. SEM images of the (a) ZrO_2 , (b) TiO_2 and (c) $\text{ZrO}_2\text{-TiO}_2$ composite films with the high magnification. The side on images—(d) ZrO_2 , (e) TiO_2 , and (f) $\text{ZrO}_2\text{-TiO}_2$ composite—shows the film thickness. Reproduced by Alotaibi et al. [32].

Spanu et al. have prepared Pt deposited on WO₃-TiO₂ nanotube arrays on Ti foil by sputtering method in order to improve the photocatalytic activity of the WO₃-TiO₂ system. The photocatalyst was used for the fabrication of H₂ by photocatalysis. The Pt deposited on WO₃-TiO₂ nanotube arrays show highly enhanced photocatalytic H₂ evolution efficiency comparing to other single-photocatalyst system such as (Pt-TiO₂ and WO₃-TiO₂) and pristine TiO₂ nanotubes [50].

3. Supported ZnO photocatalysts

ZnO is a metal oxide with a broad energy band gap (3.37 eV), which is one of the best semiconductors in the last decade. Recently, ZnO is extensively used as a photocatalyst under UV or Visible light irradiation due to its outstanding electrical, mechanical, optical, and non-toxic properties. In addition, the production cost of ZnO is low cost comparing to the fabrication of other semiconductors [51].

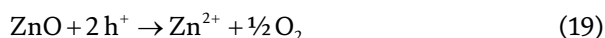
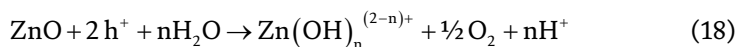
The mechanism of photocatalysis process of ZnO to degrade organic compounds under irradiation light can be summarized as follows [52]:



ZnO shares many similar properties with TiO₂, including a similar band gap (see **Figure 1**). There have even been several examples of ZnO displaying a higher photocatalytic activity than TiO₂ [53]. In addition, ZnO exhibits a better quantum efficiency because it can absorb a larger fraction of the solar spectrum than TiO₂ [54] and its price is even lower than that of TiO₂ [55]. Compared to TiO₂, ZnO can be easily supported on different types of substrates by means of low-temperature synthesis methods [56].

We already know that the photocatalytic efficiency of a photocatalyst is evaluated through the photogeneration of electron-hole pairs and their time-life. However, the main limitation of ZnO as a photocatalyst is the rapid recombination rate of photogenerated electron-hole pairs, which decreases the photocatalytic efficiency of ZnO. In addition, the use of ZnO as a photocatalyst is limited by the photocorrosion phenomenon. This process occurs because of the action of UV

radiation. As a consequence, the catalyst is partially dissolved, which gives rise to a dramatic decrease in catalytic activity [57]. The mechanism of this process is represented by the following self-oxidation reactions [58–60]:



where h^+ is the positive holes created by the action of UV radiation. Photocorrosion is the main obstacle to the use of ZnO as an effective photocatalyst. Therefore, significant efforts have been made to reduce the degradation of ZnO.

Beside TiO_2 using as a photocatalyst, Jung et al. [61] studied the synthesis and photocatalytic activity of CuO-ZnO nanowires supported on stainless steel wire meshes (SSWM). They showed that CuO-ZnO structures supported on SSWM exhibit an enhanced photocatalytic activity with respect to catalysts using other supports, such as ITO. This result they attributed to the efficient charge separation of the electron-hole pair favored by the SSWM support [61]. Another advantage of SSWM is its flexibility, which allows the mesh to be easily shaped to the desired configuration.

In general, the procedures used to achieve this involves the deposition onto the ZnO surface of: (a) silver nanoparticles [62–66]; (b) polyaniline monolayers [67], (c) graphitic carbon [68]; (d) Nafion films [69]; (e) AlSi nanoclays [70]; and (f) C_{60} fullerenes which become hybridized with ZnO [59].

Although the above modifications improve the photocatalytic stability of ZnO, some problems persist. For instance, Bessekhoud et al. [71] have reported that the photocatalytic activity of the doped materials is impaired by thermal instability and by an increase in the number of hole/electron recombination centers. Therefore, the development of novel methods that provide effective protection of the ZnO photocatalyst against photocorrosion is required.

An attempt must be made to increase catalytic activity under visible irradiation, since the solar spectrum contains a large fraction of visible light compared to UV radiation. Recently, the photocatalytic activity of ZnO in the visible region has been improved by various techniques, such as: (a) modification of the ZnO surface by non-metal element doping [72]; (b) transition metal doping [73, 74]; (c) the combination of ZnO with another semiconductor [75], etc. Of these methods, the coupling of different semiconductor photocatalysts offers great promise as it increases the charge separation of the electron-hole pairs, resulting in an increase in photocatalytic decolorization efficiency [76].

Recently, ZnO has been combined successfully with TiO_2 [77], CdO [78], CdS [79], and WO_3 [80]. CdO is a good candidate for coupling with ZnO due to its band gap, ~ 2.2 eV [78], so that $\text{Cd}_x\text{Zn}_{1-x}\text{O}$ nanostructures are active in the visible range. In addition, under visible light the excited electrons from the conduction band (CB) of ZnO can be easily transferred to the CB of CdO since the E_{CB} of CdO is lower than the E_{CB} of ZnO. These transferal processes increase the excess of electrons in the conduction band of CdO, which shifts in the Fermi level of CdO [81], increasing its photocatalytic efficiency. To the best of our knowledge, CdO-ZnO has been always synthesized in powder form. The use of CdO-ZnO supported on a target substrate (such as SSWM) as a photocatalyst for dye degradation processes in UV or visible has reported by Vu et al. [82]. They also attempt to demonstrate in parallel that coupling CdO and ZnO may be also an excellent method to avoid photocorrosion.

4. Supported WO₃ photocatalysts

Tungsten oxide (WO₃) is a high-ranking material in photocatalysis [83]. The WO₃ presents in several phases such as monoclinic, orthorhombic, triclinic, cubic, etc., but only the monoclinic phase exhibits the best photocatalytic efficiency. In addition, WO₃ is a material with many advantages, such as harmless, high stability in acidic and oxidative ambient, and its cost fabrication cost is very low compared with other photocatalysts [84].

It has been shown that the band gap energy of WO₃ is varied from 2.5 to 3.0 eV [85, 86], leading WO₃ can be used as a photocatalyst at the visible region. In recent times, there are many studies focused on the improvement strategies of the photocatalytic efficiency of WO₃ [84, 87].

Recently, the researchers have proposed many strategies for the fabrication of WO₃ thin film [88], such as sputtering deposition [89–92], aerosol-assisted chemical vapor deposition [93, 94], sol-gel spin-coating [95, 96], hydrothermal-assisted growth [97, 98], and surfactant-assisted spray pyrolysis [99, 100]. Many works focused on the photocatalytic efficiency of WO₃, especially the studying of WO₃ thin film as a photocatalyst in the visible region [84, 101].

For example, the author fabricated a WO₃ thin film with a thickness 500–600 nm deposited on a quartz substrate by DC reactive magnetron sputtering [102]. The fabricated film WO₃ used for the degradation of CH₃CHO (acetaldehyde) under ultraviolet, standard fluorescence, and visible light. The result shows that WO₃ film fabricated by sputtering can be a good photocatalyst under visible light region.

To improve the separation of photogenerated charged and to increase the photocatalytic activity, many researchers combined other elements with the WO₃ thin film. For example, Higashino et al. have fabricated a layer of WO₃ on the Al-W alloy coatings by selective solution and heat treatment (**Figure 10**). The formed thin film WO₃ exhibits photocatalytic self-cleaning properties under the visible light irradiation [103].

Takashima et al. have taken advantage of the multielectron reduction of Pt to improve the photocatalytic activity of WO₃ thin film on W foil. The author fabricated Pt loaded WO₃ thin film using a reactive DC magnetron sputtering technique or low damage reactive gas flow sputtering [104]. The formed Pt-WO₃ thin film was used to photodegrade CH₃CHO under visible light. The result shows that the fabricated thin film demonstrates excellent photodecomposition rates under visible light.

Another approach to improve the separation of photogenerated charged, C₃N₄ is combined with WO₃ film to form a heterojunction composite WO₃/C₃N₄. The

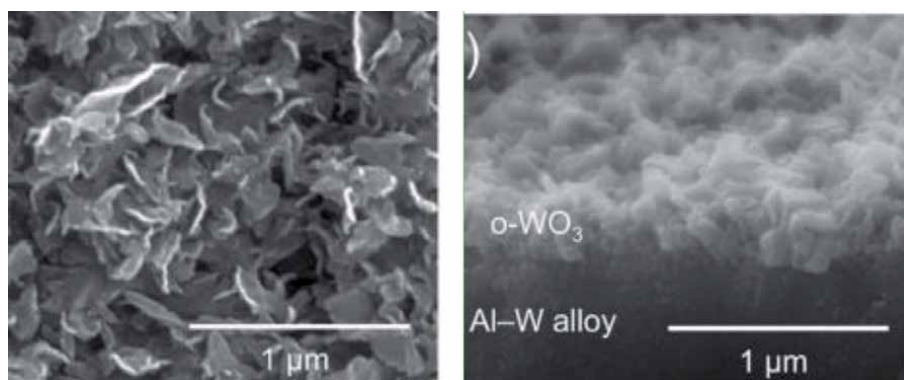


Figure 10. SEM images of the surface and cross-sectional of WO₃. Reproduced by Higashino et al. [103].

fabricated composite was deposited on fluorine-doped tin oxide (FTO) substrate [105]. The photocatalytic activity of the composite was tested by photocatalytic degradation of MB and Cr^{6+} in wastewater under UV illumination.

The supported $\text{WO}_3/\text{C}_3\text{N}_4$ composite presents higher photocatalytic activity on the decoloration of MB and the reduction of Cr^{6+} to Cr^{3+} , compared to the photocatalytic activity of WO_3 thin film.

5. Supported SnO_2 photocatalysts

SnO_2 is an inorganic compound that is exhibiting high optical transparency, excellent thermal and chemical stability, and strong oxidizing properties [106]. The band gap of SnO_2 is quite large, around 3.6 eV, which leads to SnO_2 being used as a photocatalyst in the UV region. This property makes SnO_2 an excellent photocatalyst for the degradation of many organic compounds.

Recently, SnO_2 played an important role in the photo-oxidation of pollutants and received a lot of attention despite the outstanding properties of this material. However, the vast number of researches used SnO_2 in the powder form as a photocatalyst for the degradation of the toxic organic compound, and the experiments are usually performed using SnO_2 in the powder form. There are only a few works describing the use of supported SnO_2 thin film as a photocatalyst.

In recent times, many methodologies have been applied for the fabrication of SnO_2 thin films such as, sol-gel [107], pulsed plasma deposition [108], pulsed laser deposition [109], reactive evaporation [110], and chemical bath deposition [111] methods.

For example, Jana et al. used the galvanic technique to fabricate SnO_2 thin film on transparent conducting oxide (TCO) [112].

Figure 11 shows the nanoporous flake-like structure, which allows more efficient transport of reactant molecules to the active interfaces and results in a higher photocatalytic activity for degrading methyl orange (MO) dye than that of P25 under UV light [112].

However, the SnO_2 in the powder form presents low photocatalytic activity comparing with other semiconductors due to its wide-band gap, 3.6 eV, and the rapid recombination of the photo-generated electron-hole pairs. Thus, the SnO_2 thin film could present lower photocatalytic efficiency comparing with SnO_2 in the bulk form. Therefore, the SnO_2 thin film is widely combined with other metal ions such as Ni, Co, Fe [113], Cr [114], Zn [115], Sb [116], W [117], or other semiconductors, such as ZnO [118], TiO_2 [119], etc.

For example, the W-doped SnO_2 thin films are fabricated on glass (ITO) substrate by simple chemical deposition techniques [120]. The result showed that the energy band gap is varied by the doping concentration of W, which is in the range of 3.46–3.35 eV. In addition, the UV-Visible absorption and Photoluminescence characterization results demonstrated that W-dopant SnO_2 could narrow the band gap, thus enhancing the photocatalytic efficiency of the W-doped SnO_2 in the visible light (**Figure 12**). The author used the fabricated W-doped SnO_2 for the degradation of Methylene Blue and Rhodamine (RHB) under the visible region. The W-doped SnO_2 thin film presents higher photocatalytic efficiency comparing to the pure SnO_2 thin film in the visible light irradiation.

In recent time, Sr-doped metal oxides have great attention in electronic and optoelectronic applications. Besides, when Sr is combined with SnO_2 , the crystal growth rate of SnO_2 is reduced, making the Sr-doped SnO_2 to have a higher specific surface area. Thus, the combination of Sr with SnO_2 can improve the photocatalytic activity of SnO_2 . For example, Haya et al. have prepared Sr-doped SnO_2 thin film

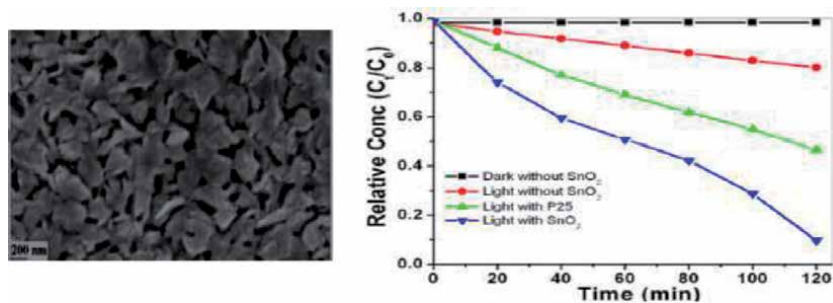


Figure 11. The SnO₂ thin film and the photocatalytic activity of SnO₂ thin film. Reproduced by Jana et al. [112].

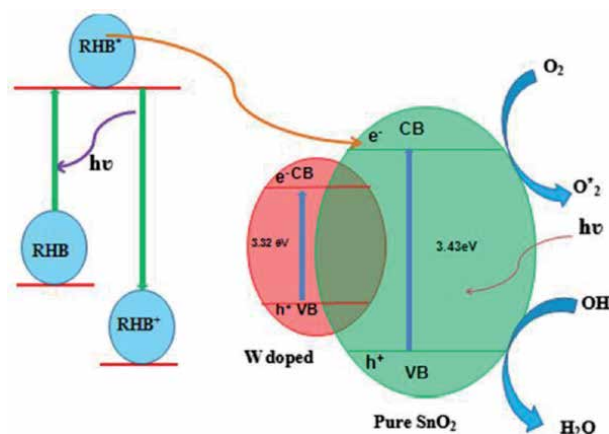


Figure 12. Schematic representation for photocatalytic mechanism of RHB in W-SnO₂ thin films. Reproduced by Vadivel et al. [120].

on glass substrate by simple sol-gel technique and study its photocatalytic activity under UV-irradiation [121]. The doping of Sr makes the SnO₂ thin film to decrease its degree of crystallinity, reducing the particle size and increasing the specific surface area of the thin film. The results show that the Sr-doped (8%) SnO₂ film has higher photocatalytic activity compared to undoped SnO₂ thin film.

In addition, many researchers also combined with other metal elements to improve the photocatalytic activity of SnO₂ thin film such as Cu-doped SnO₂ [122], Fe-doped SnO₂ [123], F- or Sr-doped [124], and Cl-doped SnO₂ [125] on glass substrate.

Recently, to improve the photocatalytic efficiency of SnO₂ thin film, B/Ag/F was doped with the SnO₂-ZnO composite film on glass by the sol-gel route. The fabricated composite thin film was used for the degradation of methyl green and formaldehyde under UV irradiation. The result showed that the synergy of ZnO and tri-doping B/Ag/F had improved the photocatalytic activity of SnO₂ thin film [126]. In addition, Kong et al. also prepared B/Fe co-doped SnO₂-ZnO thin film on glass substrates using the sol-gel technique. The prepared composite thin film improved the lifetime of the photogenerated charge carriers and optical absorption properties. The photocatalytic efficiency of the composite thin film was evaluated through the degradation of organic pollutants such as acid naphthol red and formaldehyde. The B/Fe co-doped SnO₂-ZnO film exhibits the highest photocatalytic activity compared with an undoped or only singly doped SnO₂ thin film [127].

6. Conclusion


In this chapter, an overview of the development of supported catalysts and their prospects from a scientific point of view is presented. We can see that the field has experienced major advances in the last 5 years, especially in the area of supported TiO₂, ZnO, WO₃, SnO₂, and mixed oxides on several types of substrates (SSWM, quartz, glass (ITO)). Based on the literature presented here, we believe that there is still quite a lot that can be achieved in improving the performance of supported catalysts for photocatalytic applications.

Author details

Vu T. Tan* and La The Vinh
School of Chemical Engineering, Hanoi University of Science and Technology,
Hanoi, Vietnam

*Address all correspondence to: tan.vuthi@hust.edu.vn

IntechOpen

© 2020 The Author(s). Licensee IntechOpen. This chapter is distributed under the terms of the Creative Commons Attribution License (<http://creativecommons.org/licenses/by/3.0>), which permits unrestricted use, distribution, and reproduction in any medium, provided the original work is properly cited. 

References

- [1] Philippopoulos CJ, Nikolaki MD. Photocatalytic Processes on the Oxidation of Organic Compounds in Water. Croatia: New Trends in Technologies; 2010. pp. 89-107. DOI: 10.5772/7588
- [2] Ania CO, Velasco LF, Valdés-Solís T. Photochemical behavior of carbon adsorbents. In: Novel Carbon Adsorbents. Oxford: Elsevier; 2012. pp. 521-547
- [3] Photoelectrochemical Cells. Nature. Available from: <https://www.nature.com/articles/35104607> [Accessed: 17 January 2020]
- [4] Zinc Oxide Nanoparticles with Defects—Ischenko—2005—Advanced Functional Materials—Wiley Online Library. 2005. Available from: <https://onlinelibrary.wiley.com/doi/10.1002/adfm.200500087> [Accessed: 17 January 2020]
- [5] Öztas M, Bedir M. Thickness dependence of structural, electrical and optical properties of sprayed ZnO:Cu films. Thin Solid Films. 2008;516(8):1703-1709. DOI: 10.1016/j.tsf.2007.05.018
- [6] Eslami A et al. Photocatalytic degradation of methyl tert-butyl ether (MTBE) in contaminated water by ZnO nanoparticles. Journal of Chemical Technology and Biotechnology. 2008;83(11):1447-1453. DOI: 10.1002/jctb.1919
- [7] Environmental Applications of Semiconductor Photocatalysis. Chemical Reviews. 1995;95(1):69-96. Available from: <https://pubs.acs.org/doi/abs/10.1021/cr00033a004> [Accessed: 17 January 2020]
- [8] Wang H et al. Semiconductor heterojunction photocatalysts: Design, construction, and photocatalytic performances. Chemical Society Reviews. 2014;43(15):5234-5244. DOI: 10.1039/C4CS00126E
- [9] Nosaka Y, Nosaka A. Generation and detection of reactive oxygen species in photocatalysis. Chemical Reviews. 2017;117:11302-11336. DOI: 10.1021/acs.chemrev.7b00161
- [10] Byrne C, Subramanian G, Pillai SC. Recent advances in photocatalysis for environmental applications. Journal of Environmental Chemical Engineering. 2018;6(3):3531-3555. DOI: 10.1016/j.jece.2017.07.080
- [11] Nakata K, Fujishima A. TiO₂ photocatalysis: Design and applications. Journal of Photochemistry and Photobiology C Photochemistry Reviews. 2012;13(3):169-189. DOI: 10.1016/j.jphotochemrev.2012.06.001
- [12] Fujishima A, Rao TN, Tryk DA. Titanium dioxide photocatalysis. Journal of Photochemistry and Photobiology C Photochemistry Reviews. 2000;1(1):1-21. DOI: 10.1016/S1389-5567(00)00002-2
- [13] Photocatalytic Degradation of Organic Dyes in the Presence of Titanium Dioxide under UV and Solar Light: Effect of Operational Parameters—Akbal—2005—Environmental Progress. 2005;24(3):317-322. Available from: <https://onlinelibrary.wiley.com/doi/abs/10.1002/ep.10092> [Accessed: 17 January 2020]
- [14] Schneider J et al. Understanding TiO₂ photocatalysis: Mechanisms and materials. Chemical Reviews. 2014;114(19):9919-9986. DOI: 10.1021/cr5001892
- [15] Hoffmann MR, Martin ST, Choi W, Bahnemann DW. Environmental applications of semiconductor photocatalysis. Chemical Reviews. 1995;95(1):69-96. DOI: 10.1021/cr00033a004

- [16] Taoda H. Development of TiO₂ photocatalysts suitable for practical use and their applications in environmental cleanup. *Research on Chemical Intermediates*. 2008;**34**(4):417-426. DOI: 10.1163/156856708784040579
- [17] Wang L, Wang X, Cui S, Fan X, Zu B, Wang C. TiO₂ supported on silica nanolayers derived from vermiculite for efficient photocatalysis. *Catalysis Today*. 2013;**216**:95-103. DOI: 10.1016/j.cattod.2013.06.026
- [18] Singh S, Mahalingam H, Singh PK. Polymer-supported titanium dioxide photocatalysts for environmental remediation: A review. *Applied Catalysis A: General*. 2013;**462-463**:178-195. DOI: 10.1016/j.apcata.2013.04.039
- [19] Enhancement of Photocatalytic Degradation of Methyl Orange by Supported Zinc Oxide Nanorods/ Zinc Stannate (ZnO/ZTO) on Porous Substrates. *Industrial & Engineering Chemistry Research*. 2013;**52**(38):13629-13636. Available from: <https://pubs.acs.org/doi/10.1021/ie4019726> [Accessed: 17 January 2020]
- [20] Photocatalytic Degradation Activity of Titanium Dioxide Sol–Gel Coatings on Stainless Steel Wire Meshes—Science Direct. *Materials Chemistry and Physics*. 2010;**124**(2):1225-1231. Available from: <https://www.sciencedirect.com/science/article/abs/pii/S025405841000684X> [Accessed: 17 January 2020]
- [21] Fernández A et al. Preparation and characterization of TiO₂ photocatalysts supported on various rigid supports (glass, quartz and stainless steel). Comparative studies of photocatalytic activity in water purification. *Applied Catalysis B: Environmental*. 1995;**7**(1):49-63. DOI: 10.1016/0926-3373(95)00026-7
- [22] Characterization and Photocatalytic Activity in Aqueous Medium of TiO₂ and Ag-TiO₂ Coatings on Quartz—Science Direct. *Applied Catalysis B: Environmental*. 1997;**13**:219-228. Available from: <https://www.sciencedirect.com/science/article/abs/pii/S0926337396001075> [Accessed: 17 January 2020]
- [23] Yu J, Xiong J, Cheng B, Liu S. Fabrication and characterization of Ag–TiO₂ multiphase nanocomposite thin films with enhanced photocatalytic activity. *Applied Catalysis B: Environmental*. 2005;**60**(3):211-221. DOI: 10.1016/j.apcatb.2005.03.009
- [24] Photocatalytic Degradation of Phenol in a Fluidized Bed Reactor Utilizing Immobilized TiO₂ Photocatalyst: Characterization and Process Studies—SciAlert Responsive Version. *Journal of Applied Sciences*. 2011;**11**(13). Available from: <https://scialert.net/fulltextmobile/?doi=jas.2011.2320.2326> [Accessed: 17 January 2020]
- [25] Photocatalytic Reactor Based on UV-LED/TiO₂ Coated Quartz Tube for Degradation of Dyes—Science Direct. *Chemical Engineering Journal*. 2011;**178**:40-49. Available from: <https://www.sciencedirect.com/science/article/pii/S1385894711012460> [Accessed: 17 January 2020]
- [26] Hanaor DAH, Triani G, Sorrell CC. Morphology and photocatalytic activity of highly oriented mixed phase titanium dioxide thin films. *Surface and Coating Technology*. 2011;**205**(12):3658-3664. DOI: 10.1016/j.surfcoat.2011.01.007
- [27] Borges ME, García DM, Hernández T, Ruiz-Morales JC, Esparza P. Supported photocatalyst for removal of emerging contaminants from wastewater in a continuous packed-bed photoreactor configuration. *Catalysts*. 2015;**5**(1):77-87. DOI: 10.3390/catal5010077
- [28] Borges ME, Sierra M, Esparza P. Solar photocatalysis at semi-pilot scale:

Wastewater decontamination in a packed-bed photocatalytic reactor system with a visible-solar-light-driven photocatalyst. *Clean Technologies and Environmental Policy*. 2017;**19**(4):1239-1245. DOI: 10.1007/s10098-016-1312-y

[29] Paredes L et al. Application of immobilized TiO₂ on PVDF dual layer hollow fibre membrane to improve the photocatalytic removal of pharmaceuticals in different water matrices. *Applied Catalysis B: Environmental*. 2019;**240**:9-18. DOI: 10.1016/j.apcatb.2018.08.067

[30] Sathasivam S et al. Combinatorial atmospheric pressure CVD of a composite TiO₂/SnO₂ thin film. *Chemical Vapor Deposition*. 2014;**20**:69-79. DOI: 10.1002/cvde.201307081

[31] Kambur A, Pozan G, Boz I. Preparation, characterization and photocatalytic activity of TiO₂-ZrO₂ binary oxide nanoparticles. *Applied Catalysis B: Environmental*. 2012;**s115-116**:149-158. DOI: 10.1016/j.apcatb.2011.12.012

[32] Alotaibi AM, Sathasivam S, Parkin IP. Aerosol assisted chemical vapour deposition of a ZrO₂-TiO₂ composite thin film with enhanced photocatalytic activity. *RSC Advances*. 2015;**5**(83):67944-67950. DOI: 10.1039/C5RA12340B

[33] Poliseti S, Deshpande PA, Madras G. Photocatalytic activity of combustion synthesized ZrO₂ and ZrO₂-TiO₂ mixed oxides. *Industrial and Engineering Chemistry Research*. 2011;**50**(23):12915-12924. DOI: 10.1021/ie200350f

[34] Wang X, Patel RL, Liang X. Significant improvement in TiO₂ photocatalytic activity through controllable ZrO₂ deposition. *RSC Advances*. 2018;**8**(45):25829-25834. DOI: 10.1039/C8RA03423K

[35] Koohestani H, Sadrnezhaad SK. Improvement in TiO₂ photocatalytic

performance by ZrO₂ nanocompositing and immobilizing. *Desalination and Water Treatment*. 2016;**57**(58):28450-28459. DOI: 10.1080/19443994.2016.1183233

[36] Maver K, Štangar UL, Černigoj U, Gross S, Korošec RC. Low-temperature synthesis and characterization of TiO₂ and TiO₂-ZrO₂ photocatalytically active thin films. *Photochemical & Photobiological Sciences*. 2009;**8**(5):657-662. DOI: 10.1039/B817475J

[37] Hernández-Alonso M, Tejedortejedor I, Coronado J, Soria J, Anderson M. Sol-gel preparation of TiO₂-ZrO₂ thin films supported on glass rings: Influence of phase composition on photocatalytic activity. *Thin Solid Films*. 2006;**502**:125-131. DOI: 10.1016/j.tsf.2005.07.256

[38] Linnik O et al. TiO₂/ZrO₂ thin films synthesized by PLD in low pressure N-, C- and/or O-containing gases: Structural, optical and photocatalytic properties. *Digest Journal of Nanomaterials and Biostructures*. 2012;**7**:1343-1352

[39] Hernández-Alonso MD, Tejedortejedor I, Coronado JM, Soria J, Anderson MA. Sol-gel preparation of TiO₂-ZrO₂ thin films supported on glass rings: Influence of phase composition on photocatalytic activity. *Thin Solid Films*. 2006;**502**:125-131. DOI: 10.1016/j.tsf.2005.07.256

[40] Luo Q et al. Preparation and characterization of ZrO₂/TiO₂ composite photocatalytic film by micro-arc oxidation. *Transactions of the Nonferrous Metals Society of China*. 2013;**23**(10):2945-2950. DOI: 10.1016/S1003-6326(13)62818-6

[41] Tatsuma T, Takeda S, Saitoh S, Ohko Y, Fujishima A. Bactericidal effect of energy storage TiO₂-WO₃ Photocatalysis in dark. *Electrochemistry Communications*. 2003;**5**:793-796. DOI: 10.1016/j.elecom.2003.07.003

- [42] Fu L, Cai W, Wang AW, Zheng YH, He L, Fu ZX. Synthesis and photocatalytic properties of TiO₂-WO₃ hybrid film. *Materials and Technologies*. 2015;**30**(5):264-268. DOI: 10.1179/1753555714Y.0000000256
- [43] Kim H-M, Kim D, Kim B. Photoinduced hydrophilicity of TiO₂/WO₃ double layer films. *Surface and Coating Technology*. 2015;**271**:18-21. DOI: 10.1016/j.surfcoat.2015.01.054
- [44] Chen G-S, Cheng C. Searching for the formation of TiO₂ mesoporous films with durable photoactivity by synergy of WO₃ and sodium using a simple sputtering and annealing process. *Applied Catalysis B: Environmental*. 2014;**150-151**:354-362. DOI: 10.1016/j.apcatb.2013.12.017
- [45] Rampaul A, Parkin IP, O'Neill SA, DeSouza J, Mills A, Elliott N. Titania and tungsten doped titania thin films on glass; active photocatalysts. *Polyhedron*. 2003;**22**(1):35-44. DOI: 10.1016/S0277-5387(02)01333-5
- [46] Tatsuma T, Takeda S, Saitoh S, Ohko Y, Fujishima A. Bactericidal effect of an energy storage TiO₂-WO₃ photocatalyst in dark. *Electrochemistry Communications*. 2003;**5**(9):793-796. DOI: 10.1016/j.elecom.2003.07.003
- [47] Tang K et al. Fabrication of WO₃/TiO₂ core-shell nanowire arrays: Structure design and high electrochromic performance. *Electrochimica Acta*. 2020;**330**:135189. DOI: 10.1016/j.electacta.2019.135189
- [48] Tae Kwon Y, Yong Song K, In Lee W, Jin Choi G, Rag Do Y. Photocatalytic behavior of WO₃-loaded TiO₂ in an oxidation reaction. *Journal of Catalysis*. 2000;**191**(1):192-199. DOI: 10.1006/jcat.1999.2776
- [49] Youssef AB, Laamari M, Bousselmi L. TiO₂ and WO₃/TiO₂ thin films for photocatalytic wastewater treatment. *International Journal of Environment and Waste Management*. 2019;**24**:151. DOI: 10.1504/IJEW.2019.10022371
- [50] Spanu D, Recchia S, Mohajernia S, Schmuki P, Altomare M. Site-selective Pt dewetting on WO₃-coated TiO₂ nanotube arrays: An electron transfer cascade-based H₂ evolution photocatalyst. *Applied Catalysis B: Environmental*. 2018;**237**:198-205. DOI: 10.1016/j.apcatb.2018.05.061
- [51] Ong CB, Ng LY, Mohammad AW. A review of ZnO nanoparticles as solar photocatalysts: Synthesis, mechanisms and applications. *Renewable and Sustainable Energy Reviews*. 2018;**81**:536-551. DOI: 10.1016/j.rser.2017.08.020
- [52] Rajamanickam D, Shanthi M. Photocatalytic degradation of an organic pollutant by zinc oxide-solar process. *Arabian Journal of Chemistry*. 2016;**9**:S1858-S1868. DOI: 10.1016/j.arabjc.2012.05.006
- [53] Lizama C, Freer J, Baeza J, Mansilla HD. Optimized photodegradation of reactive blue 19 on TiO₂ and ZnO suspensions. *Catalysis Today*. 2002;**76**(2):235-246. DOI: 10.1016/S0920-5861(02)00222-5
- [54] Sakthivel S, Neppolian B, Shankar MV, Arabindoo B, Palanichamy M, Murugesan V. Solar photocatalytic degradation of azo dye: Comparison of photocatalytic efficiency of ZnO and TiO₂. *Solar Energy Materials & Solar Cells*. 2003;**77**(1):65-82. DOI: 10.1016/S0927-0248(02)00255-6
- [55] Chiu WS et al. Photocatalytic study of two-dimensional ZnO nanopellets in the decomposition of methylene blue. *Chemical Engineering Journal*. 2010;**158**(2):345-352. DOI: 10.1016/j.cej.2010.01.052
- [56] Vu TT, del Río L, Valdés-Solís T, Marbán G. Tailoring the synthesis of

stainless steel wire mesh-supported ZnO. *Materials Research Bulletin*. 2012;**47**(6):1577-1586. DOI: 10.1016/j.materresbull.2012.02.017

[57] Kenanakis G, Giannakoudakis Z, Vernardou D, Savvakis C, Katsarakis N. Photocatalytic degradation of stearic acid by ZnO thin films and nanostructures deposited by different chemical routes. *Catalysis Today*. 2010;**151**(1):34-38. DOI: 10.1016/j.cattod.2010.02.054

[58] Neppolian B, Choi HC, Sakthivel S, Arabindoo B, Murugesan V. Solar/UV-induced photocatalytic degradation of three commercial textile dyes. *Journal of Hazardous Materials*. 2002;**89**(2):303-317. DOI: 10.1016/S0304-3894(01)00329-6

[59] Fu H, Xu T, Zhu S, Zhu Y. Photocorrosion inhibition and enhancement of photocatalytic activity for ZnO via hybridization with C60. *Environmental Science & Technology*. 2008;**42**(21):8064-8069. DOI: 10.1021/es801484x

[60] Photo-induced dissolution of zinc in alkaline solutions—Science Direct. Available from: <https://www.sciencedirect.com/science/article/pii/S0013468699003229> [Accessed: 17 January 2020]

[61] Fabrication of CuO-ZnO Nanowires on a Stainless Steel Mesh for Highly Efficient Photocatalytic Applications. Available from: https://www.researchgate.net/publication/49754945_Fabrication_of_CuO-ZnO_nanowires_on_a_stainless_steel_mesh_for_highly_efficient_photocatalytic_applications [Accessed: 17 January 2020]

[62] Ren C et al. Synthesis of Ag/ZnO nanorods array with enhanced photocatalytic performance. *Journal of Hazardous Materials*. 2010;**182**(1):123-129. DOI: 10.1016/j.jhazmat.2010.05.141

[63] Facile Synthesis of Ag/ZnO Heterostructures Assisted by UV Irradiation: Highly Photocatalytic Property and Enhanced Photostability—Science Direct. Available from: <https://www.sciencedirect.com/science/article/pii/S0025540811002741> [Accessed: 17 January 2020]

[64] Xie W, Li Y, Sun W, Huang J, Xie H, Zhao X. Surface modification of ZnO with Ag improves its photocatalytic efficiency and photostability. *Journal of Photochemistry and Photobiology A: Chemistry*. 2010;**216**(2):149-155. DOI: 10.1016/j.jphotochem.2010.06.032

[65] Tian C, Zhang Q, Jiang B, Tian G, Fu H. Glucose-mediated solution-solid route for easy synthesis of Ag/ZnO particles with superior photocatalytic activity and photostability. *Journal of Alloys and Compounds*. 2011;**509**(24):6935-6941. DOI: 10.1016/j.jallcom.2011.04.005

[66] Han Z, Ren L, Cui Z, Chen C, Pan H, Chen J. Ag/ZnO flower heterostructures as a visible-light driven photocatalyst via surface plasmon resonance. *Applied Catalysis B: Environmental*. 2012;**126**:298-305. DOI: 10.1016/j.apcatb.2012.07.002

[67] Photocorrosion Inhibition and Photoactivity Enhancement for Zinc Oxide via Hybridization with Monolayer Polyaniline. *The Journal of Physical Chemistry C*. Available from: <https://pubs.acs.org/doi/abs/10.1021/jp810748u> [Accessed: 17 January 2020]

[68] Photocorrosion Suppression of ZnO Nanoparticles via Hybridization with Graphite-like Carbon and Enhanced Photocatalytic Activity—Google Search. Available from: https://www.google.com/search?q=Photocorrosion+Suppression+of+ZnO+Nanoparticles+via+Hybridization+with+Graphite-like+Carbon+and+Enhanced+Photocatalytic+Activity&rlz=1C1GCEU_esES875ES875&oq=Ph

- otocorrosion+Suppression+of+ZnO+Na nanoparticles+via+Hybridization+with+Graphite-like+Carbon+and+Enhanced+Photocatalytic+Activity&aqs=chrome..69i57884j0j4&sourceid=chrome&ie=UTF-8 [Accessed: 17 January 2020]
- [69] Wang J, Liu P, Wang S, Han W, Wang X, Fu X. Nanocrystalline zinc oxide in perfluorinated ionomer membranes: Preparation, characterization, and photocatalytic properties. *Journal of Molecular Catalysis A: Chemical*. 2007;**273**(1):21-25. DOI: 10.1016/j.molcata.2007.03.062
- [70] Suchithra PS, Shadiya CP, Mohamed AP, Velusamy P, Ananthakumar S. One-pot microwave mediated growth of heterostructured ZnO@AlSi as a potential dual-function eco-catalyst for treating hazardous pollutants in water resources. *Applied Catalysis B: Environmental*. 2013;**130-131**:44-53. DOI: 10.1016/j.apcatb.2012.10.010
- [71] Bessekhouad Y, Robert D, Weber J-V, Chaoui N. Effect of alkaline-doped TiO₂ on photocatalytic efficiency. *Journal of Photochemistry and Photobiology A: Chemistry*. 2004;**167**(1):49-57. DOI: 10.1016/j.jphotochem.2003.12.001
- [72] Chen L-C, Tu Y-J, Wang Y-S, Kan R-S, Huang C-M. Characterization and photoreactivity of N-, S-, and C-doped ZnO under UV and visible light illumination. *Journal of Photochemistry and Photobiology A: Chemistry*. 2008;**199**(2):170-178. DOI: 10.1016/j.jphotochem.2008.05.022
- [73] Kaneva NV, Dimitrov DT, Dushkin CD. Effect of nickel doping on the photocatalytic activity of ZnO thin films under UV and visible light. *Applied Surface Science*. 2011;**257**(18):8113-8120. DOI: 10.1016/j.apsusc.2011.04.119
- [74] Cobalt-Doped Zinblend–Wurtzite Mixed-Phase ZnO Photocatalyst Nanoparticles with High Activity in Visible Spectrum—Science Direct. *Applied Catalysis B: Environmental*. 2014;**144**:435-441. Available from: <https://www.sciencedirect.com/science/article/abs/pii/S0926337313004670> [Accessed: 17 January 2020]
- [75] Zhu H-Y, Xiao L, Jiang R, Zeng G-M, Liu L. Efficient decolorization of azo dye solution by visible light-induced photocatalytic process using SnO₂/ZnO heterojunction immobilized in chitosan matrix. *Chemical Engineering Journal*. 2011;**172**(2):746-753. DOI: 10.1016/j.cej.2011.06.053
- [76] Tian H, Ma J, Li K, Li J. Photocatalytic degradation of methyl orange with W-doped TiO₂ synthesized by a hydrothermal method. *Materials Chemistry and Physics*. 2008;**112**(1):47-51. DOI: 10.1016/j.matchemphys.2008.05.005
- [77] Adsorption-Photodegradation of Humic Acid in Water by using ZnO Coupled TiO₂/Bamboo Charcoal Under Visible Light Irradiation—PubMed—NCBI. *Journal of Hazardous Materials*. 2013;**262**:16-24. Available from: <https://www.ncbi.nlm.nih.gov/pubmed/24004575> [Accessed: 17 January 2020]
- [78] ZnO/CdO Composite Nanorods for Photocatalytic Degradation of Methylene Blue under Visible Light—Science Direct. *Materials Chemistry and Physics*. 2011;**125**:277-280. Available from: <https://www.sciencedirect.com/science/article/abs/pii/S0254058410007571> [Accessed: 17 January 2020]
- [79] Pawar RC, Lee CS. Single-step sensitization of reduced graphene oxide sheets and CdS nanoparticles on ZnO nanorods as visible-light photocatalysts. *Applied Catalysis B: Environmental*. 2014;**144**:57-65. DOI: 10.1016/j.apcatb.2013.06.022

- [80] Li D, Haneda H, Ohashi N, Hishita S, Yoshikawa Y. Synthesis of nanosized nitrogen-containing $\text{MO}_x\text{-ZnO}$ ($M = \text{W, V, Fe}$) composite powders by spray pyrolysis and their visible-light-driven photocatalysis in gas-phase acetaldehyde decomposition. *Catalysis Today*. 2004;**93-95**:895-901. DOI: 10.1016/j.cattod.2004.06.099
- [81] Encapsulation of CdO/ZnO NPs in PU Electrospun Nanofibers as Novel Strategy for Effective Immobilization of the Photocatalysts—Science Direct. *Colloids and Surfaces A: Physicochemical and Engineering Aspects*. 2012;**401**:8-16. Available from: <https://www.sciencedirect.com/science/article/abs/pii/S0927775712001148> [Accessed: 17 January 2020]
- [82] Vu T, Rodil A, Marban G, Valdés-Solís T. Nanostructured stainless steel wire mesh-supported $\text{Cd}_x\text{Zn}_{1-x}\text{O}$: A stable photocatalyst under visible and ultraviolet irradiation. *Journal of Environmental Chemical Engineering*. 2014;**2**:1612-1620. DOI: 10.1016/j.jece.2014.06.018
- [83] Janáky C, Rajeshwar K, de Tacconi NR, Chanmanee W, Huda MN. Tungsten-based oxide semiconductors for solar hydrogen generation. *Catalysis Today*. 2013;**199**:53-64. DOI: 10.1016/j.cattod.2012.07.020
- [84] Dong P, Hou G, Xi X, Shao R, Dong F. WO_3 -based photocatalysts: Morphology control, activity enhancement and multifunctional applications. *Environmental Science. Nano*. 2017;**4**(3):539-557. DOI: 10.1039/C6EN00478D
- [85] Johansson M, Niklasson G, Osterlund L. Structural and optical properties of visible active photocatalytic WO_3 thin films prepared by reactive dc magnetron sputtering. *Journal of Materials Research*. 2012;**27**:3130-3140. DOI: 10.1557/jmr.2012.384
- [86] Wicaksana Y, Liu S, Scott J, Amal R. Tungsten trioxide as a visible light photocatalyst for volatile organic carbon removal. *Molecules*. 2014;**19**:17747-17762. DOI: 10.3390/molecules191117747
- [87] Tahir MB, Nabi G, Rafique M, Khalid NR. Nanostructured-based WO_3 photocatalysts: Recent development, activity enhancement, perspectives and applications for wastewater treatment. *International journal of Environmental Science and Technology*. 2017;**14**(11):2519-2542. DOI: 10.1007/s13762-017-1394-z
- [88] Formation of a Photocatalytic WO_3 Surface Layer on Electrodeposited Al-W Alloy Coatings by Selective Dissolution and Heat Treatment. *Scientific Reports*. 2019. Available from: <https://www.nature.com/articles/s41598-019-52178-6> [Accessed: 11 June 2020]
- [89] Valerini D, Hernández S, Di Benedetto F, Russo N, Saracco G, Rizzo A. Sputtered WO_3 films for water splitting applications. *Materials Science in Semiconductor Processing*. 2016;**42**:150-154. DOI: 10.1016/j.mssp.2015.09.013
- [90] Zheng H, Sadek AZ, Latham K, Kalantar-Zadeh K. Nanoporous WO_3 from anodized RF sputtered tungsten thin films. *Electrochemistry Communications*. 2009;**11**(4):768-771. DOI: 10.1016/j.elecom.2009.01.033
- [91] Khatko V et al. Tungsten trioxide sensing layers on highly ordered nanoporous alumina template. *Sensors and Actuators B: Chemical*. 2006;**118**(1):255-262. DOI: 10.1016/j.snb.2006.04.030
- [92] Visible-Light Active Thin-Film WO_3 Photocatalyst with Controlled High-Rate Deposition by Low-Damage Reactive-Gas-Flow Sputtering. *APL Materials*. 2010;**3**(10). Available from: <https://aip.scitation.org/>

doi/10.1063/1.4922942 [Accessed: 11 June 2020]

[93] Kim H, Bonsu RO, O'Donohue C, Korotkov RY, McElwee-White L, Anderson TJ. Aerosol-assisted chemical vapor deposition of tungsten oxide films and nanorods from oxo tungsten(VI) fluoroalkoxide precursors. *ACS Applied Materials & Interfaces*. 2015;7(4):2660-2667. DOI: 10.1021/am507706e

[94] Houweling ZS, Geus JW, Schropp REI. Hot-wire chemical vapor deposition of WO_{3-x} thin films of various oxygen contents. *Materials Chemistry and Physics*. 2013;140(1):89-96. DOI: 10.1016/j.matchemphys.2013.02.072

[95] Au BWC, Chan KY, Pang WL, Lee CL, Mustafa AH. Tungsten oxide (WO_3) films prepared by sol-gel spin-coating technique. *Solid State Phenomena*. 2018;280:71-75. Available from: /SSP.280.71 [Accessed: 11 June 2020]

[96] Kim K-W et al. Various coating methodologies of WO_3 according to the purpose for electrochromic devices. *Nanomaterials*. 2020;10:821-823. DOI: 10.3390/nano10050821

[97] Mathuri S, Margoni MM, Ramamurthi K, Babu RR, Ganesh V. Hydrothermal assisted growth of vertically aligned platelet like structures of WO_3 films on transparent conducting FTO substrate for electrochromic performance. *Applied Surface Science*. 2018;449:77-91. DOI: 10.1016/j.apsusc.2018.01.033

[98] Hydrothermal Formation of Tungsten Trioxide Nanowire Networks on Seed-Free Substrates and Their Properties in Electrochromic Device. Request PDF. Available from: https://www.researchgate.net/publication/262150728_Hydrothermal_Formation_of_Tungsten_Trioxide_Nanowire_Networks_on_Seed-Free_Substrates_and_Their_Properties_in_

Electrochromic_Device [Accessed: 11 June 2020]

[99] Bertus LM et al. Synthesis and characterization of WO_3 thin films by surfactant assisted spray pyrolysis for electrochromic applications. *Materials Chemistry and Physics*. 2013;140(1):49-59. DOI: 10.1016/j.matchemphys.2013.02.047

[100] Manceri L, Duta A. Synthesis of WO_3 thin films by surfactant mediated spray pyrolysis. *Ceramics International*. 2012;38:2873-2882. DOI: 10.1016/j.ceramint.2011.11.060

[101] Lai CW. WO_3 nanoplates film: Formation and photocatalytic oxidation studies. *Journal of Nanomaterials*. 2015;22:7. Available from: <https://www.hindawi.com/journals/jnm/2015/563587/> [Accessed: 11 June 2020]

[102] Visible Light-Induced Photocatalytic Properties of WO_3 Films Deposited by DC Reactive Magnetron Sputtering. *Journal of Vacuum Science & Technology A*. 2012;30:031503 Available from: <https://avs.scitation.org/doi/abs/10.1116/1.3696876?journalCode=jva> [Accessed: 11 June 2020]

[103] Higashino S, Miyake M, Ikenoue T, Hirato T. Formation of a photocatalytic WO_3 surface layer on electrodeposited Al-W alloy coatings by selective dissolution and heat treatment. *Scientific Reports*. 2019;9(1):16008. DOI: 10.1038/s41598-019-52178-6

[104] Takashima J, Oka N, Shigesato Y. Photocatalytic activity of WO_3 films crystallized by postannealing in air. *Japanese Journal of Applied Physics*. 2012;51(5R):055501. DOI: 10.1143/JJAP.51.055501

[105] Cui L et al. Facile preparation of Z-scheme $WO_3/g-C_3N_4$ composite photocatalyst with enhanced photocatalytic performance under visible light. *Applied Surface Science*.

2016;**391**:202-210. DOI: 10.1016/j.apusc.2016.07.055

[106] Bouras K et al. Optical and structural properties of Nd doped SnO₂ powder fabricated by the sol-gel method. *Journal of Materials Chemistry C*. 2014;**2**(39):8235-8243. DOI: 10.1039/C4TC01202J

[107] Huang Y, Li D, Feng J, Li G, Zhang Q. Transparent conductive tungsten-doped tin oxide thin films synthesized by sol-gel technique on quartz glass substrates. *Journal of Sol-Gel Science and Technology*. 2010;**54**(3):276-281. DOI: 10.1007/s10971-010-2182-0

[108] Huang Y, Zhang Q, Li G. Transparent conductive tungsten-doped tin oxide polycrystalline films prepared on quartz substrates. *Semiconductor Science and Technology*. 2008;**24**(1):015003. DOI: 10.1088/0268-1242/24/1/015003

[109] Nakao S, Yamada N, Hitosugi T, Hirose Y, Shimada T, Hasegawa T. Fabrication of transparent conductive W-doped SnO₂ thin films on glass substrates using anatase TiO₂ seed layers. *Physica Status Solidi C: Current Topics in Solid State Physics*. 2011;**8**(2):543-545. DOI: 10.1002/pssc.201000505

[110] Yadav JB, Patil RB, Puri RK, Puri V. Studies on undoped SnO₂ thin film deposited by chemical reactive evaporation method. *Materials Science and Engineering B*. 2007;**139**(1):69-73. DOI: 10.1016/j.mseb.2007.01.032

[111] Rifai A, Iqbal M, Tapran N, Nuruddin A, Suyatman S, Yulianto B. Synthesis and characterization of SnO₂ thin films by chemical bath deposition. *AIP Conf. Proc.* 2011;**1415**:231-233. DOI: 10.1063/1.3667263

[112] Jana S, Mitra B, Bera P, Sikdar M, Mondal A. Photocatalytic activity of galvanically synthesized nanostructure

SnO₂ thin films. *Journal of Alloys and Compounds*. 2014;**602**:42-48. DOI: 10.1016/j.jallcom.2014.02.182

[113] Soussi L et al. Effect of (Co, Fe, Ni) doping on structural, optical and electrical properties of sprayed SnO₂ thin film. *Surfaces and Interfaces*. 2020;**19**:100467. DOI: 10.1016/j.surfin.2020.100467

[114] Gandhi TI, Ramesh Babu R, Ramamurthi K. Structural, morphological, electrical and optical studies of Cr doped SnO₂ thin films deposited by the spray pyrolysis technique. *Materials Science in Semiconductor Processing*. 2013;**16**(2):472-479. DOI: 10.1016/j.mssp.2012.07.008

[115] Cho Y, Parmar NS, Nahm S, Choi J-W. Full range optical and electrical properties of Zn-doped SnO₂ and oxide/metal/oxide multilayer thin films deposited on flexible PET substrate. *Journal of Alloys and Compounds*. 2017;**694**:217-222. DOI: 10.1016/j.jallcom.2016.09.293

[116] Gupta S, Yadav BC, Dwivedi PK, Das B. Microstructural, optical and electrical investigations of Sb-SnO₂ thin films deposited by spray pyrolysis. *Materials Research Bulletin*. 2013;**48**(9):3315-3322. DOI: 10.1016/j.materresbull.2013.05.001

[117] Wang M et al. Transparent and conductive W-doped SnO₂ thin films fabricated by an aqueous solution process. *Thin Solid Films*. 2013;**544**:419-426. DOI: 10.1016/j.tsf.2013.02.088

[118] Ynineb F et al. Influence of Sn content on properties of ZnO:SnO₂ thin films deposited by ultrasonic spray pyrolysis. *Materials Science in Semiconductor Processing*. 2013;**16**:2021-2027. DOI: 10.1016/j.mssp.2013.07.023

- [119] Medjalidi F, Bouabellou A, Bouachiba Y, Taabouche A, Bouatia K, Serrar H. Study of TiO₂, SnO₂ and nanocomposites TiO₂:SnO₂ thin films prepared by sol-gel method: Successful elaboration of variable-refractive index systems. *Materials Research Express*. 2020;7(1):016439. DOI: 10.1088/2053-1591/ab6c0c
- [120] Vadivel S, Rajarajan G. Effect of W doping on structural, optical and photocatalytic activity of SnO₂ nanostructure thin films. *Journal of Materials Science: Materials in Electronics*. 2015;26(9):7127-7133. DOI: 10.1007/s10854-015-3335-2
- [121] Haya S, Brahmia O, Halimi O, Sebais M, Boudine B. Sol-gel synthesis of Sr-doped SnO₂ thin films and their photocatalytic properties. *Materials Research Express*. 2017;4(10):106406. DOI: 10.1088/2053-1591/aa8deb
- [122] Influence of Cu Doping on Structural, Optical and Photocatalytic Activity of SnO₂ Nanostructure Thin Films. *Materials Chemistry and Physics*. 148(3):528-532. Available from: <https://www.springerprofessional.de/en/influence-of-cu-doping-on-structural-optical-and-photocatalytic-/3559896> [Accessed: 13 June 2020]
- [123] Nassiri C, Hadri A, Chafi F, Rouchdi M, Fares B, Mzerd A. Structural, optical and electrical properties of Fe doped SnO₂ prepared by spray pyrolysis. *Journal of Materials and Environmental Sciences*. 2017;8:420-425
- [124] Thangaraju B. Structural and electrical studies on highly conducting spray deposited fluorine and antimony doped SnO₂ thin films from SnCl₂ precursor. *Thin Solid Films*. 2002;402(1):71-78. DOI: 10.1016/S0040-6090(01)01667-4
- [125] Abass AK. Electrical and optical properties of chlorine doped SnO₂ coatings. *Solid State Communications*. 1987;61(8):507-510. DOI: 10.1016/0038-1098(87)90502-3
- [126] Han K, Peng X-L, Li F, Yao M-M. SnO₂ composite films for enhanced photocatalytic activities. *Catalysts*. 2018;8(10):453. DOI: 10.3390/catal8100453
- [127] Kong X, Li F, Qi Z, Qi L, Yao M. SnO₂-based thin films with excellent photocatalytic performance. *Journal of Materials Science: Materials in Electronics*. 2017;28:1-8. DOI: 10.1007/s10854-017-6459-8

Ferrocenes as One-Electron Donors in Unimolecular Rectifiers

Robert Melville Metzger

Abstract

Ferrocene is a good electron donor, and as such has been used to test asymmetric conduction (rectification) in molecules that contain ferrocene. Of the five ferrocene-containing molecules that rectify (structures 11, 15, 19, 20, and 22), the last (22) exhibits a record rectification ratio, which should be a dramatic incentive for searching for more high-efficiency rectifiers.

Keywords: ferrocene, unimolecular electronics, rectification ratio, highest occupied molecular orbital, Aviram-Ratner proposal of 1974

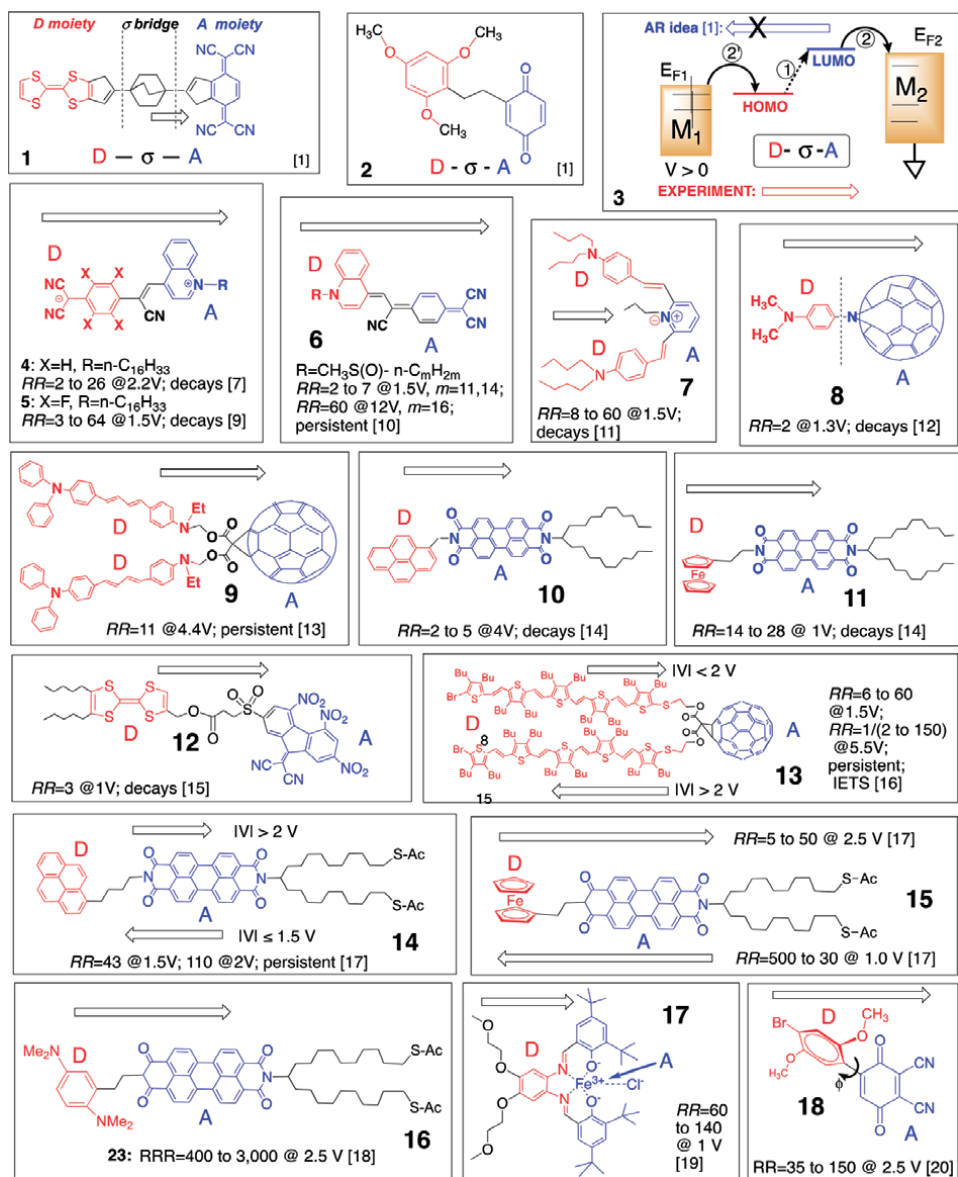
1. Introduction

“Unimolecular electronics” (UME) [1] was born in 1974 with a theoretical proposal by Arieh Aviram and Mark Ratner (AR) for a one-molecule rectifier (or diode) of electrical current donor-bridge-acceptor (D- σ -A) [1] (**Figure 1**, structures 1 and 2): within that molecule D represents a π -electron-rich one-electron donor (D) moiety, σ is a short and saturated bridge of sp^3 -hybridized C atoms (between two and maybe eight C atoms long), and A is the electron-poor moiety that can act a one-electron acceptor. One small correction, AR had suggested that the first mechanistic step would move electron and hole from metal electrodes to the highest occupied molecular orbital (HOMO) and lowest unoccupied molecular orbital (LUMO) and the second step would involve the relaxation of the excited-state zwitterion [1]. The experimental direction of rectification for D- σ -A molecules has been shown to be “anti-AR” (**Figure 1** structure 3): in step (1), under applied electric field, the neutral ground-state molecule D- σ -A forms an excited-state zwitterion $D^+-\sigma-A^-$; in step (2) the electron and hole are transferred to the metal electrodes [2].

The first rectifier (4 in **Figure 1**) was measured in 1990–1993 as a Langmuir-Blodgett (LB) multilayer between dissimilar metal electrodes by J. Roy Sambles (University of Exeter) and Geoffrey J. Ashwell (Cranfield University) [3, 4]. The asymmetric electrical current was confirmed at the University of Alabama (UA) as a LB monolayer of 4 between Al electrodes in 1997 [5] and then between oxide-free Au electrodes in 2001 [6, 7].

As of 2015, 53 unimolecular rectifiers had been measured worldwide [8], 15 of which at the UA (**Figure 1**, structures 4–18 [7–20]). Also, 169 molecular wires were measured around the world [8]. Several more rectifiers have been published worldwide since and many review articles on this subject have appeared [21–32].

The present article focuses on the use of one particular powerful one-electron donor in rectifiers: ferrocene.


Figure 1.

The Aviram-Ratner proposal of unimolecular rectification [1] with two specific molecules suggested (1, 2). Structure 3 shows the rectification direction (direction of larger and favored electron flow) seen (i) experimentally (bottom arrow from left to right, see Ref. [16]) and (ii) the rectification direction predicted by Aviram and Ratner (top arrow from right to left crossed out). Structures 4–18 are the unimolecular rectifiers studied at the University of Alabama (1997–2018) [7–20]: listed are the direction of enhanced current (hollow arrow), the rectification ratio $RR = -I(V_{max})/I(-V_{max})$, and the maximum bias V_{max} (Volts) measured; the word “decays” means that RR decreases monotonically as the measurement is repeated, while “persistent” means that RR does not decrease. The electron donor regions are shown in red, and the electron acceptor regions are shown in blue.

2. Results

In the 1980s, UME had hoped to develop useful molecular-scale ($\sim 2 \text{ nm}^3$) devices for ultrahigh-density and high-speed industrial electronics. To interrogate such molecules (or monolayers of molecules), metal electrodes or nanoelectrodes (Al, Ag, Au, etc.) are used: this is sketched below and explained in detail in many

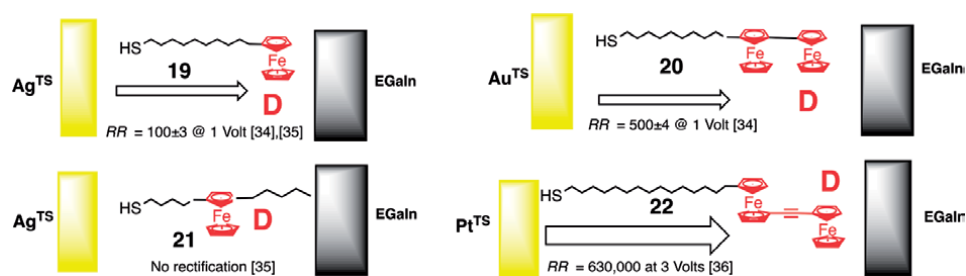


Figure 2.

Ferrocene-containing unimolecular rectifiers studied by the groups of Whitesides [33–35] and Nijhuis [36]: all are “asymmetry-type A” rectifiers; the hollow arrow denotes the preferred direction of electron flow through the “metal | molecule | metal” sandwich (from electrode far from the electron donor part to the nearest electrode). **Corrigenda for Ref. [8]:** (i) the arrows for **19** (i.e., “molecule 193”) and **20** (i.e., “molecule 196”) are drawn in the wrong direction: they would apply to D- σ -A rectifiers; (ii) for **20** (i.e., “molecule 196”), the reference in Ref. [8] should be [124] instead of [122], [123]; and (iii) for **21** (i.e., “molecule 197”), the reference in Ref. [8] should be [125] instead of [122], [123].

review articles [8, 21–32]. UME learned how inorganic metals couple (associate with or bond to) single organic molecules and how one can reliably exchange electrons and photons with these molecules.

In the meantime the much wealthier and commercially driven electronic industry has made gigantic strides and has developed high-speed almost-nanoscale electronic circuits using inorganic semiconductors (Si, Ge, and GaAs). Therefore the original hope and promise of UME have been defeated. Nevertheless, UME has learned to interrogate and control individual molecules, and its present challenge is how to combine and exploit electronic, photonic, and spintronic functions in new ways.

The present review looks at how ferrocene-containing molecules have contributed valid and promising and most recently also very dramatic UME rectifiers: in particular molecules **11** [14] and **15** [17] already mentioned in **Figure 1** and four other molecules shown in **Figure 2**, **19** [33, 34], **20** [33, 34], and **21** [33, 34] studied by the Whitesides group at Harvard University and **22** [36] studied by the Nijhuis group at Singapore National University. As discussed below, molecule **21** should not, and does not, rectify.

Electrical measurements of rectifiers. Rectification can be measured with some difficulty at the single-molecule level, but more conveniently as a monolayer between macroscopic metal electrodes as a “metal | molecule | metal” sandwich [32]. All molecules discussed here were studied either as a Langmuir-Blodgett monolayer (**11** [14]) or as self-assembled monolayers (SAMs) with thiol terminations that could be bound covalently to either super-flat “template-stripped” Ag^{TS} or A^{TS} electrodes (**15** [17], **19** [33, 34], and **20** [34]) or Pt^{TS} electrodes (**22** [37]). Most (but not all) rectifier measurements have been done with direct current [8, 32].

Candidate unimolecular rectifiers can be (i) electron donor molecules, (ii) electron acceptor molecules, or (iii) D- σ -A molecules [8, 32]. The search for organic rectifiers started in the era of quasi-one-dimensional organic metals with an enduring synthetic emphasis toward strong (easily oxidized) donor moieties D and strong (easily reduced) acceptor moieties A, connected by a covalently saturated and electrically insulating “sigma” (σ) bridge, forming a D- σ -A molecule. For instance, the proposed tetrathiafulvalene (TTF)- σ -tetracyanoquinodimethane molecule (**Figure 1**, structure **1**) would have a presumed low barrier to form the corresponding excited zwitterion D⁺- σ -A⁻. Yet in 1974, a (weak donor)- σ -(weak acceptor) molecule (**Figure 1**, structure **2**) was also proposed [1]. Surprisingly, the recently studied (and dimensionally very tiny) molecule **18** (that resembles molecule **2**) incorporates a weak electron donor D and a moderate electron acceptor

Molecule	I_D (g)	A_A (g)
Benzene	9.24	-1.15 ^a
Pyrene	7.37	0.56
Perylene	6.90	0.97
Pc	6.41	—
TMPD	6.20	—
TTF	6.83	—
Fc = Cp ₂ Fe	6.81 ^b	—
1,4-benzoquinone	9.99	1.91
TCNQ	9.50	3.30
PBI	—	3.93 ^c

^aFrom Ref. [42].
^bFrom Ref. [43].
^cCalculated from Ref. [18].

Table 1. Gas-phase ionization potentials I_D (eV) and gas-phase electron affinities A_A (eV), updated from [8], except where noted.

A, yet is an excellent rectifier [20]. We have also seen that a strong, easily oxidized donor like tetramethyl-*para*-phenylenediamine in molecule **16** blocks the current across the monolayer between -0.5 and +0.5 Volts (Coulomb blockade) [18].

Table 1 shows some relevant gas-phase ionization potentials I_D for electron donors D and gas-phase electron affinities A_A for electron acceptors A [8]. It should be noted that ferrocene (Fc or Cp₂Fe, where Cp is cyclopentadienyl) is as good an electron donor (i.e., has a relatively small I_D value) as tetrathiafulvalene TTF, but not as good as N,N,N',N'-tetramethyl-*para*-phenylenediamine (TMPD). Perylenebisimide (PBI) is as good an electron acceptor (i.e., has a similarly large A_A value) as 7,7,8,8-tetracyanoquinodimethane (TCNQ).

Four mechanisms for rectification. Four potential mechanisms for electrical rectification in molecules have been discussed [38–40]:

1. Schottky barriers (“S” rectifier) [38, 40].
2. Asymmetric placement of the electrophore in the electrode gap (“A” rectifier) [38].
3. Unimolecular processes depending on molecular energy levels (“U” rectifier) [38].
4. A recent fourth mechanism for rectification is asymmetric polarization (“AP” rectifier), when highly polar solvents can induce an asymmetric conductance of a symmetrical molecule between very asymmetric electrodes in a scanning break junction (SBJ) [41].

Purists would prefer pure-“U” rectifiers, requiring “S” = 0 and “A” = 0. For many molecules, for reasons of assembly, “U” and “A” effects are combined [39] (e.g., **Figure 1** for structures **4**, **5**, **6**, **10**, **11**, **14**, **15**, **16**). For molecules **19**, **20**, and **22** in **Figure 2**, only the “A” effect is operative: the chromophore donor moiety (indicated as “D” and shown in red) yields rectifiers because it is **asymmetrically placed** within the “metal | monolayer | metal” sandwich. When the D moiety is in the middle of molecule **21**, there can be and is no rectification [33, 34], as predicted [38].

Reversal of rectification: “Janus effect.” The molecules studied routinely at the UA rectify in the “anti-AR” direction, that is, intramolecular electron flow occurs from D to A (e.g., **Figure 1** structure 3) [2, 8]. However, D- σ -A rectifiers **13**, **14**, **15**, and **16** also show an additional “Janus effect”: at lower bias they rectify one way, and at higher bias (e.g., at ± 2.5 V), they rectify the other way [17, 18]! At lower bias, AR rectification may involve only one energy level (e.g., LUMO); at higher bias, anti-AR rectification may involve both HOMO and LUMO. Such bias-switchable rectifiers may be useful!

Rectification ratio. The asymmetry in electrical current I is quantified by the rectification ratio:

$$RR(V_{\max}) \equiv -I(V_{\max})/I(-V_{\max}) \quad (1)$$

where V is the applied bias or voltage. Typical RR values span several orders of magnitude; for the rectifiers **4–18** studied at the UA, $RR(V_{\max})$ is reported in **Figure 1**. The first rectifier, **4**, had $RR = 26$ [7]; **16** has a large $RR = 3000$ [19]. Why is the RR typically seen for unimolecular rectifiers ($RR \leq 10^3$) [8] so much smaller than the RR for commercial inorganic pn junction devices ($RR = 10^5$ – 10^6) [8]? If low RR s were intrinsic to UME rectifiers, then traditional Ge, Si, and Ga As semiconductor physicists could safely look down at UME as a harmless curiosity, not as a competitor. But, as discussed next, a huge increase in RR s was imminent.

We next discuss rectifier **16**, in which the electron donor moiety is the powerful electron donor TMPD instead of ferrocene (**Figure 5**). **Figure 6** shows a surprisingly large room temperature Coulomb blockade [18]: too much of a good thing, the

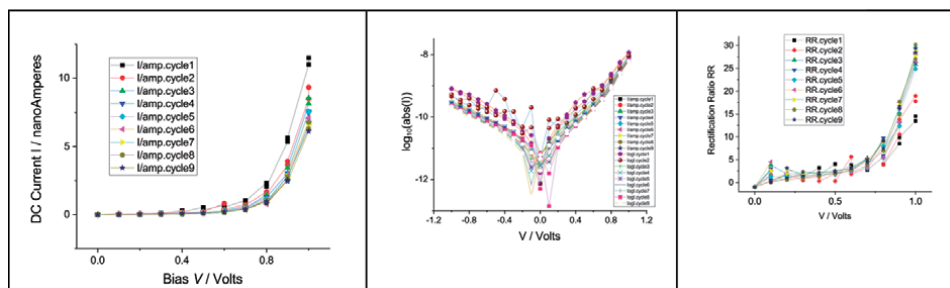


Figure 3. IV scans for a “Au | LB \rightarrow SAM of **15** | Cold Au | Ga₂O₃ | EGaIn” sandwich in the bias range from -1.0 to $+1.0$ Volts for the bias V increasing: (left) I (ampères) vs. V (Volts). (Center) $\log_{10}|I|$ vs. V . (Right) $RR(V) = -I(V)/I(-V)$ vs. V : (the average $\langle RR \rangle = 96.3 \pm 36.7$). The horizontal arrows indicate the scan direction; the vertical hollow arrows show how the ordinate values evolved with repeated scans [18].

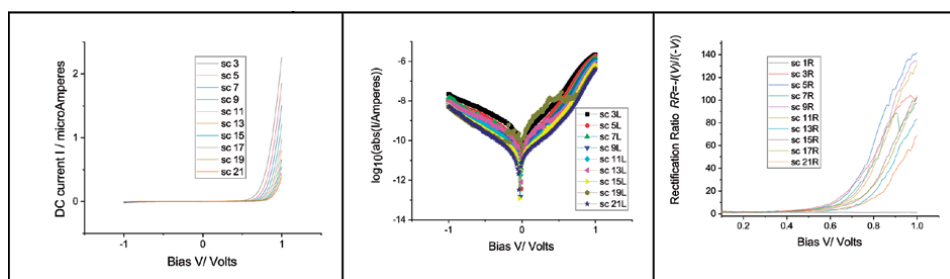
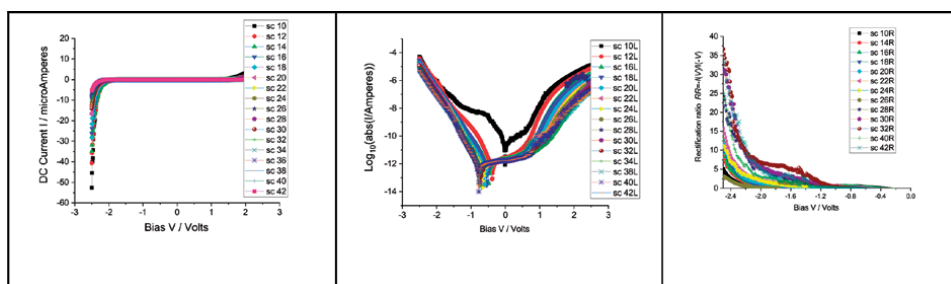
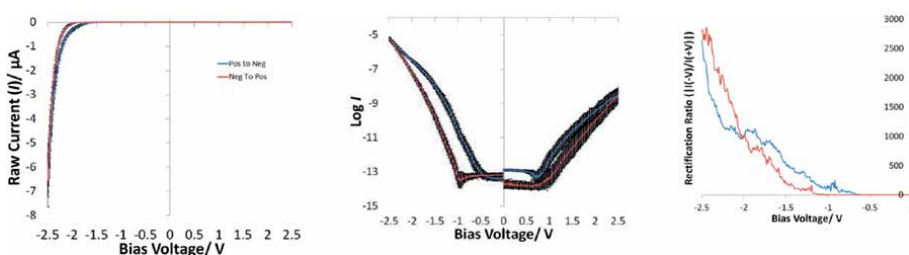


Figure 4. Current-voltage (IV) curves (I /ampères vs. V /Volts) for a “EGaIn | Ga₂O₃ | Au | Z-type LB monolayer of **11** | Cold Au | Ga₂O₃ | EGaIn” sandwich. (left) I vs. V . (Center) $\log_{10}|I|$ vs. V . (Right) $RR = 14$ – 28 vs. V . RR persists for up to 40 measurement cycles, with a minimal decrease in the currents (which are relatively small). Rectification was even seen for biases up to ± 2 Volts [14].


Figure 5.

IV scans for a “EGaIn | Au | LB → SAM of **15** | Cold Au | EGaIn” sandwich in the bias range from -2.5 to $+2.5$ Volts for the bias V increasing: (left) I (ampères) vs. V (Volts). (Center) $\log_{10}I$ vs. V . Note that the position of minimum current, which for normal tunneling curves of this type should occur at zero volt bias, as in Figures 3 (center) and 4 (center) shown above, is displaced here very significantly to the left by about 0.8 Volts: This is **incipient Coulomb blockade**. (Right) $RR(V)^{\circ} = I(V)/I(-V)$ vs. V [18].


Figure 6.

IV scans for a “EGaIn | Au | LB → SAM of **16** | Cold Au | EGaIn” sandwich in the bias range from -2.5 to $+2.5$ Volts for the bias V increasing: (left) I (ampères) vs. V (Volts) (average of 50 scans). (Center) $\log_{10}I$ vs. V . **True Coulomb blockade**. (C) $RR(V)^{\circ} = I(V)/I(-V)$ vs. V . (right) RR vs. V [18].

TMPD oxidizes too easily and prevents current from flowing for a large bias range [18]! Beyond where the Coulomb blockade was operative, a relatively impressive $RR \approx 3000$ is reached.

The Whitesides group (including Nijhuis) studied the rectification of self-assembled monolayers of thiol-containing molecules **19** and **20** and the non-rectification of the symmetric **22** [35], in sandwich “Au | SAM | Ga₂O₃ | GaIn” with a thorough effort to isolate the potential influence of the disordered Ga₂O₃ oxide that forms at the surface of the GaIn eutectic (without completely covering it) [33–35] (Figure 7).

Recent huge rectification ratio. A very dramatic result was published recently for the (“A-type”) rectifying monolayer sandwich “Pt^{TS}-S-C₁₅H₃₀-Fc-C≡C-Fc | EGaIn” (Figure 2, structure 22) consisting of a diad of ferrocene (Fc) donors (linked by an alkynyl-C≡C-), with a pentadecanethiol “tail” [36]. This sandwich was studied between a bottom template-stripped electrode M^{TS} (=Pt^{TS}, Au^{TS}, or Ag^{TS}) and an EGaIn droplet top electrode. The new record is a very dramatic $RR = 6.3 \times 10^5$ at ± 3 Volts for Pt^{TS} (but much less for Au^{TS} or Ag^{TS}) (Figure 8) [36]. Also, the conductance “plateaued” around -2 Volts when the Ag^{TS} electrode was used [36].

The key improvements in [36] were (i) using Pt as the “bottom” electrode, because Pt^{TS} tolerates a larger bias range than Au^{TS} or Ag^{TS}, (ii) a presumed efficient van der Waals contact between Fc-C≡C-Fc and EGaIn, and (iii) a “long enough alkyl tail” to get a very small reverse-bias current [38].

Also, light emission was measured (with blinking) for **22**, with a broad peak at 1.7 eV ($\lambda_{\max} = 730$ nm), but only at the large negative bias V that corresponds

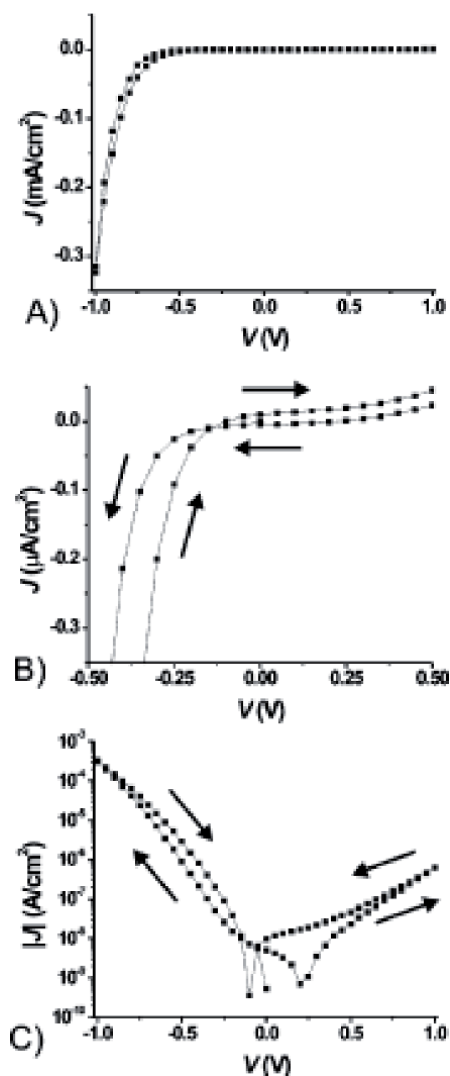


Figure 7. JV scans for “ $\text{Ag}^{\text{TS}}/\text{SAM of alkanethiol CH}_3(\text{CH}_2)_{11}\text{SH}/\text{Ga}_2\text{O}_3/\text{EGaIn}$ ” sandwich in the bias range from -1.0 to $+1.0$ Volts, (A) J vs. V (B) detail of (A) showing hysteresis (C) $\log_{10}J$ vs. V . $\text{RR} \approx 100$. From Ref. [33, 34].

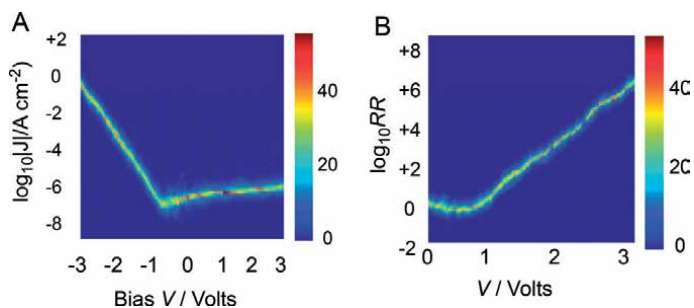


Figure 8. IV data for “ $\text{Pt}^{\text{TS}}/\text{SAM of 22}/\text{Ga}_2\text{O}_3/\text{EGaIn}$ ” sandwich: (A) $\log_{10}J$ vs. V and (B) rectification ratio $\text{RR}(V)$ vs. V . the current densities $J = I/A$ are calculated from the measured currents I and the estimated areas A of the EGaIn drops. The “heat map” shows in false color the number of times that any point in the xy plot was recorded (see color code on the right of each xy plot) From Ref. [36].

to rectification: this emission was attributed to surface plasma polaritons excited distally within the Pt electrode after tunneling. Thus, the electrical excitation at large negative bias may have accessed the HOMO and HOMO-1 of Fc, but the energy is emitted neither directly (electroluminescence from Fc⁺ with an expected narrow energy distribution) nor indirectly (as lattice phonons), but indirectly and effectively, as surface plasma polaritons with a wide spectral distribution [36].

3. Conclusion

The frustrating issue of historically low measured *RRs* [8] has thus been resolved experimentally [36]: organic monolayer rectifiers may finally challenge the *RR* of inorganic *pn* junction rectifiers.

However, the measured *RRs* for alkanethiols are hundreds of times smaller than expected from careful theoretical simulations [42]: this puzzle must be solved, so that measurements are not victims of unforeseen inefficiencies in the “metal | molecule” interface. The number of measured unimolecular rectifiers has grown dramatically, but their preselection as candidate rectifiers has been somewhat haphazard. Once the “metal | molecule” interface is brought under experimental control, better measurements may provide valid physical organic criteria to guide the design of the better unimolecular rectifiers of tomorrow.

There has also been a recent brief review on this exact topic [43]; for the sake of brevity, we refer the reader to the papers cited for other significant rectifiers containing the donor ferrocene [43–49].


Author details

Robert Melville Metzger

Laboratory for Molecular Electronics, Department of Chemistry and Biochemistry,
University of Alabama, Tuscaloosa, AL, USA

*Address all correspondence to: rmetzger@ua.edu

IntechOpen

© 2019 The Author(s). Licensee IntechOpen. This chapter is distributed under the terms of the Creative Commons Attribution License (<http://creativecommons.org/licenses/by/3.0>), which permits unrestricted use, distribution, and reproduction in any medium, provided the original work is properly cited. 

References

- [1] Aviram A, Ratner MA. Molecular rectifiers. *Chemical Physics Letters*. 1974;**29**:277-283
- [2] Metzger RM, Mattern DL. Unimolecular electronic devices. In: Metzger RM, editor. *Unimolecular and Supramolecular Electronics II: Chemistry and Physics Meet at the Metal-Molecule Interface*. Vol. 313. Heidelberg, Dordrecht, London, New York: Springer Topics in Current Chemistry; 2012. pp. 39-84
- [3] Ashwell GJ, Sambles JR, Martin AS, Parker WG, Szablewski M. Rectifying characteristics of Mg | (C₁₆H₃₃-Q3CNQ LB film) | Pt structures. *Journal of the Chemical Society, Chemical Communications*. 1990:1374-1376
- [4] Martin AS, Sambles JR, Ashwell GJ. Molecular rectifier. *Physical Review Letters*. 1993;**70**:218-221
- [5] Metzger RM, Chen B, Höpfner U, Lakshmikantham MV, Vuillaume D, Kawai T, et al. Unimolecular electrical rectification in hexadecyl-quinolinium tricyanoquinodimethanide. *Journal of the American Chemical Society*. 1997;**119**:10455-10466
- [6] Xu T, Peterson IR, Lakshmikantham MV, Metzger RM. Rectification by a monolayer of hexadecylquinolinium tricyanoquinodimethanide between gold electrodes. *Angewandte Chemie International Edition*. 2001;**40**:1749-1752
- [7] Metzger RM, Xu T, Peterson IR. Electrical rectification by a monolayer of hexadecylquinolinium tricyanoquinodimethanide measured between macroscopic gold electrodes. *The Journal of Physical Chemistry. B*. 2001;**105**:7280-7290
- [8] Metzger RM. Unimolecular electronics. *Chemical Reviews*. 2015;**115**:5056-5115
- [9] Honciuc A, Otsuka A, Wang Y-H, McElwee SK, Woski SA, Saito G, et al. Polarization of charge-transfer bands and rectification in hexadecylquinolinium 7,7,8-tricyanoquinodimethanide and its tetrafluoro analog. *The Journal of Physical Chemistry. B*. 2006;**110**:15085-15093
- [10] Jaiswal A, Rajagopal D, Lakshmikantham MV, Cava MP, Metzger RM. Unimolecular rectification and other properties of CH₃C(O)S-C₁₄H₂₈Q⁺-3CNQ⁻ and CH₃C(O)S-C₁₆H₃₂Q⁺-3CNQ⁻ organized by self-assembly, Langmuir-Blodgett, and Langmuir-Schaefer techniques. *Physical Chemistry Chemical Physics*. 2007;**9**:4007-4017
- [11] Baldwin JW, Amaresh RR, Peterson IR, Shumate WJ, Cava MP, Amiri MA, et al. Rectification and nonlinear optical properties of a Langmuir-Blodgett monolayer of a pyridinium dye. *The Journal of Physical Chemistry. B*. 2002;**106**:12158-12164
- [12] Metzger RM, Baldwin JW, Shumate WJ, Peterson IR, Mani P, Mankey GJ, et al. Large current asymmetries and potential device properties of a Langmuir-Blodgett monolayer of dimethylanilinoaza fullerene sandwiched between gold electrodes. *The Journal of Physical Chemistry. B*. 2003;**107**:1021-1027
- [13] Honciuc A, Jaiswal A, Gong A, Ashworth K, Spangler CW, Peterson IR, et al. Current rectification in a Langmuir-Schaefer monolayer of fullerene-bis-[4-diphenylamino-4"-(N-ethyl-N-2"-ethyl)amino-1,4-diphenyl-1,3-butadiene] malonate between Au electrodes. *The Journal of Physical Chemistry. B*. 2005;**109**:857-871
- [14] Shumate WJ, Mattern DL, Jaiswal A, Burgess J, Dixon DA, White TR, et al. Spectroscopic and rectification studies of three donor sigma-acceptor

- compounds, consisting of a one-electron donor (pyrene or ferrocene), a one-electron acceptor (perylenebisimide), and a C₁₉ swallowtail. *The Journal of Physical Chemistry. B.* 2006;**2006**(110):11146-11159
- [15] Shumate WJ. Ph. D. Dissertation, University of Alabama; 2007
- [16] Honciuc A, Metzger RM, Gong A, Spangler CW. Elastic and inelastic electron tunneling spectroscopy of a new rectifying monolayer. *Journal of the American Chemical Society.* 2007;**129**:8310-8319
- [17] Johnson MS, Kota R, Mattern DL, Hill CM, Vasiliu M, Dixon DA, et al. A two-faced "Janus" unimolecular rectifier exhibits rectification reversal. *Journal of Materials Chemistry C.* 2014;**2**:9892-9902
- [18] Johnson MS, Kota R, Mattern DL, Metzger RM. Janus reversal and coulomb blockade in ferrocene-perylenebisimide and N,N,N',N'-tetramethyl-para-phenylene-diamine-perylenebisimide D- σ -A rectifiers. *Langmuir.* 2016;**32**:6851-6859
- [19] Johnson MS, Wickramasinghe L, Verani C, Metzger RM. Confirmation of the rectifying behavior in a pentacoordinate [N₂O₃] iron(III) surfactant using a eutectic Ga-In | LB monolayer | Au assembly. *Journal of Physical Chemistry C.* 2016;**2016**(120):10578-10583
- [20] Meany JE, Johnson MS, Woski SA, Metzger RM. Surprisingly big rectification ratios for a very small unimolecular rectifier. *ChemPlusChem.* 2016;**81**:1152-1155
- [21] Tour JM, Kozaki M, Seminario JM. Molecular-scale electronics: A synthetic/computational approach to digital computing. *Journal of the American Chemical Society.* 1998;**120**:8486-8493
- [22] Love JC, Estroff LA, Kriebel JK, Nuzzo RG, Whitesides GM. Self-assembled monolayers of thiolates on metals as a form of nanotechnology. *Chemical Reviews.* 2005;**105**:1103-1169
- [23] Aradhya SV, Venkataraman L. Single-molecule junctions beyond electronic transport. *Nature Nanotechnology.* 2013;**8**:399-409
- [24] Sun L, Diaz-Fernandez YA, Gschneidner TA, Westerlund F, Lara-Avila S, Moth-Poulsen K. Single-molecule electronics: From chemical design to functional devices. *Chemical Society Reviews.* 2014;**43**:7378-7411
- [25] Nichols RJ, Higgins SJ. Single-molecule electronics: Chemical and analytical perspectives. *Annual Review of Analytical Chemistry.* 2015;**8**:389-417
- [26] Lambert CJ. Basic concepts of quantum interference and electron transport in single-molecule electronics. *Chemical Society Reviews.* 2015;**44**:875-888
- [27] Xiang D, Wang X, Jia C, Lee T, Guo X. Molecular-scale electronics: From concept to function. *Chemical Reviews.* 2016;**116**:4318-4440
- [28] Su TA, Neupane M, Steigerwald ML, Venkataraman L, Nuckolls C. Chemical principles of single-molecule electronics. *Nature Reviews Materials.* 2016;**1**:16002
- [29] Vilan A, Aswal D, Cahen D. Large-area, ensemble molecular electronics: Motivation and challenges. *Chemical Reviews.* 2017;**117**:4248-4286
- [30] Vilan A, Cahen D. Chemical modification of semiconductor surfaces for molecular electronics. *Chemical Reviews.* 2017;**117**:4624-4666
- [31] Cuevas JC, Scheer E. *Molecular Electronics.* Second ed. Singapore: World Scientific; 2017

- [32] Metzger RM. Quo Vadis unimolecular electronics? *Nanoscale*. 2018;**10**:10316-10332
- [33] Nijhuis CA, Reus WF, Whitesides GM. Molecular rectification in metal-SAM-metal oxide-metal junctions. *Journal of the American Chemical Society*. 2009;**131**:17814-17827
- [34] Nijhuis C, Reus WF, Barber JR, Dickey MD, Whitesides GM. Charge transport and rectification in arrays of SAM-based tunneling junctions. *Nano Letters*. 2010;**10**:3611-3619
- [35] Nijhuis C, Reus WF, Siegel AC, George M, Whitesides. A molecular half-wave rectifier. *Journal of the American Chemical Society*. 2011;**133**:15397-15411
- [36] Reus WF, Thuo MM, Shapiro ND, Nijhuis CA, Whitesides GM. The SAM, not the electrodes, dominates charge transport in metal-monolayer//Ga₂O₃/gallium-indium eutectic junctions. *ACS Nano*. 2012;**6**:4806-4822
- [37] Chen X, Roemer M, Yuan L, Du W, Thompson D, del Barco E, et al. Molecular diodes with rectification ratios exceeding 10⁵ driven by electrostatic interactions. *Nature Nanotechnology*. 2017;**12**:797-803
- [38] Krzeminski C, Delerue C, Allan G, Vuillaume D, Metzger RM. Theory of rectification in a molecular monolayer. *Physics Review*. 2001;**B64**:085405
- [39] Mujica V, Ratner MA, Nitzan A. Molecular rectification: Why is it so rare? *Chemical Physics*. 2002;**281**:147-150
- [40] Van Dyck C, Ratner M. Molecular rectifiers: A new design based on asymmetric anchoring moieties. *Nano Letters*. 2015;**15**:1577-1584
- [41] Capozzi B, Xia J, Adak O, Dell EJ, Liu Z-F, Taylor JC, et al. Single-molecule diodes with high rectification ratios through environmental control. *Nature Nanotechnology*. 2015;**10**:522-527
- [42] Xie Z, Baldea I, Frisbie CD. Why one can expect large rectification in molecular junctions based on alkane monothiols and why rectification is so modest. *Chemical Science*. 2018;**9**:4456-4467
- [43] Welker ME. Ferrocenes as building blocks in molecular rectifiers and diodes. *Molecules*. 2018;**23**:1551
- [44] Wimbush KS, Reus WF, van der Wiel WG, Reinhoudt DN, Whitesides GM, Nijhuis CA, et al. Control over rectification in supramolecular tunneling junctions. *Angewandte Chemie, International Edition*. 2010;**49**:10176-10180
- [45] Song J, Vancso GJ. Responsive organometallic polymer grafts: Electrochemical switching of surface properties and current mediation behavior. *Langmuir*. 2011;**27**:6822-6829
- [46] Mentovich ED, Rosenberg-Shraga N, Kalifa I, Gozin M, Mujica V, Hansen T, et al. Gated-controlled rectification of a self-assembled monolayer-based transistor. *Journal of Physical Chemistry C*. 2011;**117**:8468-8474
- [47] Park S, Park JH, Hwang S, Kwak J. Programmable electrochemical rectifier based on a thin-layer cell. *ACS Applied Materials & Interfaces*. 2017;**9**:20955-20962
- [48] Broadnax AD, Lamport ZA, Scharmann B, Jurchescu OD, Welker ME. Ferrocenealkylsilane molecular rectifiers. *Journal of Organometallic Chemistry*. 2018;**856**:23-26
- [49] Zhang G-P, Mu YQ, Wei MZ, Wang S, Huang H, Hu GC, et al. Designing molecular rectifiers and spin valves using metallocene-functionalized undecanethiolates: One transition metal Atom matters. *Journal of Materials Chemistry C*. 2018;**6**:2105-2112

Section 3

Substitution Reactions

Correlation between HSAB Principle and Substitution Reactions in Bioinorganic Reactions

Tanja Soldatović

Abstract

Substitution reactions are a type of reactions where one functional group or ligand is substituted by another. They could be electrophilic or nucleophilic, depending upon whether the reagent is involved. Complex compounds could be involved in a number of substitution reactions such as ligand exchange, solvent exchange, complexation or anation reactions, solvolysis, acid and base hydrolysis, inter- and intramolecular isomerization, racemization, and metal ion reaction. Hard-soft acid–base principle (HSAB) contributes to better understanding of the mechanism of nucleophilic substitution reactions of transition metal complexes. Metal–ligand bonds in transition metal compounds are closely related to the HSAB nature of metals and their preferred ligands. Also, the principle is qualitatively useful to predict the preference of the metal for the ligand in bioinorganic reactions.

Keywords: substitution, complexes, hard-soft acid–base principle, metal–ligand bonds, bioinorganic reactions

1. Introduction

The aim of this chapter is to present connection between hard-soft acid–base principle with bioinorganic substitution reactions. Bioinorganic chemistry is an interdisciplinary field which connects inorganic chemistry with different types of chemistries, physics, medicine, biology, physiology, etc. This field includes studies of kinetic and thermodynamic of substitution reactions of transition metal ion coordination compounds and biomolecules such as enzymes, nucleic acids, proteins, peptides, amino acids, and others.

Ligand substitution reactions are the most fundamental type of chemical reaction that can occur when a metal complex is dissolved in solution in the presence of other nucleophiles. Acid–base properties of central metal ions and ligands are very important for understanding the mechanism of interactions between metal ions (Lewis acids) and various biomolecules (Lewis bases) with different donor atoms. HSAB principle is qualitatively useful to predict the preference of the metal for the ligand and to predict the stability of M–L bonds. Hard-hard or soft-soft bonds of acid and base contribute to the stabilization and strength of the bonds between donor and acceptor. These factors also include the charges and sizes of the cation and donor atom, their electronegativities, and the orbital's overlap between them.

2. Hard and soft metal centers and ligands

From the theory we know that Lewis acid is an electron acceptor and a Lewis base is an electron donor. In coordination chemistry, we consider the central metal ions as a Lewis acid which are coordinated (bonded) by one or more molecules or ions (ligands) which act as Lewis bases. The formed coordinated bonds between the central atom or ion with ligands have covalent character, which are known under the name coordinate covalent bond or simple coordinate bond. The acceptor properties of metal ions toward ligands could be divided into two classes. These two classes are “hard” acids or class (a) cations and “soft” acids or class (b) cations. Similar patterns were found for other donor atoms: ligands with O- and N-donors form more stable complexes with class (a) cations, while those with S- and P-donors form more stable complexes with class (b) cations.

The terms “hard” and “soft” acids arise from a description of the polarizabilities of the metal ions. Hard acids are typically either small monocations with a relatively high charge density or are highly charged, again with a high charge density. These ions are not very polarizable and show a preference for donor atoms that are also not very polarizable, e.g., O. Such ligands are called hard bases. Soft acids tend to be large monocations with a low charge density, e.g., Pd^{2+} , and are very polarizable. Soft metal ions prefer to form coordinate bonds with donor atoms that are also highly polarizable, e.g., P. Such ligands are called soft bases. Pearson's classification of hard and soft acids comes from a consideration of a series of donor atoms placed in order of electronegativity:



A hard acid is one that forms the most stable complexes with ligands containing donor atoms from the left side of the series. The reverse is true for a soft acid. This classification is listed in **Table 1**.

The applications of the HSAB principle are useful to predict thermodynamically stable M-L bonds. For example:

- Fe(III) belongs to a class of hard acids and prefers the hard bases, e.g., O. Thus, it is understandable why the concentration of Fe(III) ions in the body is controlled by OH^- , O^{2-} , and RO^- species. In ferritin protein that stores iron and releases it in a controlled fashion, Fe(III) ions are bound by the phenolate group $-\text{OPh}$.

Hard (acids)	Intermediate (acids)	Soft (acids)
Li^+ , Na^+ , K^+ , Rb^+ , Be^{2+} , Mg^{2+} , Ca^{2+} , Sr^{2+} , Sn^{2+} , Mn^{2+} , Al^{3+} , Ga^{3+} , In^{3+} , Sc^{3+} , Cr^{3+} , Fe^{3+} , Co^{3+} , Y^{3+} , Th^{4+} , Pu^{4+} , Ti^{4+} , Zr^{4+} , $[\text{VO}]^{2+}$, $[\text{VO}_2]^+$	Pb^{2+} , Fe^{2+} , Co^{2+} , Ni^{2+} , Cu^{2+} , Zn^{2+} , Os^{2+} , Ru^{3+} , Rh^{3+} , Ir^{2+}	Zero oxidation state metal centers, Tl^+ , Cu^+ , Ag^+ , Au^+ , $[\text{Hg}_2]^{2+}$, Hg^{2+} , Cd^{2+} , Pd^{2+} , Pt^{2+} , Ru^{2+} , Tl^{3+}
Hard (bases)	Intermediate (bases)	Soft (bases)
F^- , Cl^- , H_2O , ROH , R_2O , $[\text{OH}]^-$, $[\text{RO}]^-$, $[\text{RCO}_2]^-$, $[\text{CO}_3]^{2-}$, $[\text{NO}_3]^-$, $[\text{PO}_4]^{3-}$, $[\text{SO}_4]^{2-}$, $[\text{ClO}_4]^-$, $[\text{ox}]^{2-}$, NH_3 , RNH_2	Br^- , $[\text{N}_3]^-$, py, $[\text{SCN}]^-$ (N-bound), ArNH_2 , $[\text{NO}_2]^-$, $[\text{SO}_3]^{2-}$	I^- , H^- , R^- , $[\text{CN}]^-$ (C-bound), CO (C-bound), RNC , RSH , R_2S , $[\text{RS}]^-$, $[\text{SCN}]^-$ (S-bound), R_3P , R_3As , R_3Sb , alkenes, arene

Table 1. Selected hard and soft metal centers (Lewis acids) and ligands (Lewis bases) and those that exhibit intermediate behavior.

- Pt(II) a soft acid prefers soft bases S-donor instead of N-donor ligands. Antitumor activity of platinum(II)-based drugs is explained by the assumption that they firstly react with S-donor biomolecules, which is kinetically more favorable and then comes to form thermodynamically more stable Pt-DNA adducts.

Ligands with hard N- or O-donor atoms form more stable complexes with s- and p-block metal cations (e.g., Na⁺, Mg²⁺), early d-block metal cations (e.g., Co³⁺, Cr³⁺), and f-block metal ions (e.g., Th⁴⁺). On the other hand, ligands with soft P- or S-donors have a preference for heavier p-block metal ions (e.g., Tl⁺) and later d-block metal ions (e.g., Pd²⁺, Ag⁺).

Complex formation involves ligand substitution. If we suppose that metal ion is a hard acid, the hard-hard bond with ligands is favorable. If ligand is a soft base, ligand substitution will not be favorable. If metal ion is a soft acid and ligand is a soft base, soft-soft interaction is favorable.

Although successful, the HSAB principle initially lacked a satisfactory quantitative basis. Today it is possible to use DFT theory to derive electronic chemical potential values (electronic chemical potential) and chemical hardness values [1].

3. Substitution reactions in transition metal coordination chemistry

Substitution reactions of complexes are divided on electrophilic (S_E) or nucleophilic (S_N) depending on the replacement of either central metal ion or ligand. If the metal ion is substituted during the reaction, i.e., electrophile, the reactions are electrophilic substitution (Eq. (1)); otherwise if a ligand is replaced, that is nucleophilic substitution reaction (Eq. (2)) [2, 3]:



Ligand substitution reactions in metal complexes can occur in two ways, either by a combination of solvolysis and substitution by ligand or simple exchange in which there is a replacement of one ligand by another without the direct inclusion of solvent. The direct substitution is more relevant for the square-planar complexes with regard to octahedral complexes. For other complex geometries, both routes are used [4].

Nucleophilic substitution reactions, according to Langford and Gray, are carried out in three different mechanisms: dissociative (D), associative (A), or interchange mechanism (I) (**Figure 1**) [2].

In the dissociative mechanism (D), the first step of the reaction is dissociation of the one ligand L from the inner coordination sphere, whereby an intermediate with a decreased coordination number forms. In the next step, the entering ligand X binds to the central metal ion. Since the first step of the reaction is slower, it determines the overall rate of the substitution reaction.

In the associative mechanism (A), in the first step, the entering ligand X binds to the central metal ion, forming an intermediate with an increased coordination number, and then, in the second step, the leaving ligand L leaves the coordination sphere of the complex. The formation of an intermediate with an increased coordination number is slower, and it determines the rates of this substitution process.

When an intermediate cannot be detected by kinetic, stereochemical, or product distribution studies, the so-called interchange mechanisms (I) are invoked. Associative interchange mechanisms (I_A) have rates dependent on the nature of the

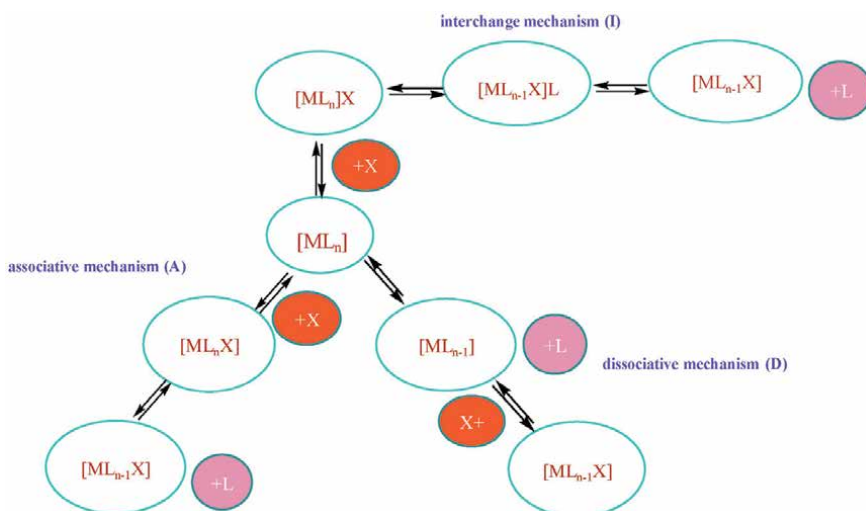


Figure 1.
Schematic representation of the mechanisms for substitution reactions.

entering group, whereas dissociative interchange (I_D) mechanisms do not. If the process of breaking the bond between the central metal ion and the outgoing ligand L has a greater impact on the rate of reaction, the mechanism is I_D , and if forming a new bond between the central metal ion and the entering ligand X has a greater impact on the chemical reaction rate, the mechanism is marked with I_A [2, 3].

The associative mechanism is well-known and preferred for four-coordinated square-planar complexes. Dissociative mechanisms are more common for six-coordinated octahedral complexes. Five-coordinated complexes could react in both mechanisms [4]. For investigations of complex-ligand substitution reactions, experimental techniques such as spectroscopic techniques (UV–Vis, NMR, Mössbauer, IR, Raman, EPR spectroscopy, MS), rapid cryogenic X-ray structure determinations of reactive intermediates, matrix isolation of reactive intermediates, fast kinetic techniques, low-temperature kinetics, high-pressure kinetic and thermodynamic techniques to construct volume profiles as compared to energy profiles, and theoretical methods to analyze and predict reaction mechanisms are widely used [2–4].

3.1 Bioinorganic reactions

Under the classification of bioinorganic reactions, we consider the interactions of metal ions with biomolecules under physiological conditions. Ligand affinity and possible coordination geometries of the metal center are important bioinorganic principles. Metal–ligand bonds are closely related to the HSAB nature of metals and their preferred ligands. Many factors could affect metal–ligand complex formation including the formation of competing equilibria-solubility products, complexation, and/or acid–base equilibrium constants—sometimes referred to as “metal ion speciation” which all affect the complex formation. Ion size and charge, preferred metal coordination geometry, and ligand chelation effects all affect metal uptake. In biological systems, as in all others, metal ions exist in an inner coordination sphere with ligands binding directly to the metal. The bioinorganic reaction mechanism includes investigation of all processes which occur during applications of metal-based drugs. Thus, the determination of mechanism helps to clarify what will happen after administrations of the drugs and helps to improve medical characteristics of them.

4. Substitution reactions of platinum(II) and zinc(II) complexes with biomolecules in correlation with HSAB principle

4.1 Substitution reactions of platinum(II) complexes

Platinum complexes are in medical use worldwide. Cisplatin or *cis*-diamminedichloridoplatinum(II), *cis*-DDP is the first generation of antitumor metal-based complex. Many years of research indicated that preference platinum(II) as soft acid toward soft bases is responsible for the negative side effect of this drug. From the moment of injection of the drugs in the body to their binding to DNA molecules, a large number of secondary processes happen that are responsible for the occurrence of toxic effects [5, 6]. Thus, platinum(II) possesses high affinity for the sulfur and in the blood plasma itself reacts immediately with albumin or other biomolecules that contain sulfur (proteins or peptides in which L-cysteine or L-methionine). Considering that the concentration of thiol, including L-cysteine and glutathione, in intracellular fluid is about 10 mM, it is presumed that the platinum(II)-based antitumor reagents first react with sulfur donor nucleophiles, which is kinetically favored and after that form thermodynamically more stable Pt-DNA compounds.

The monofunctional complexes represent a good model for investigations of platinum(II) interactions with various biomolecules which contains sulfur and nitrogens. The structures of complexes disable the bifunctional coordination to the DNA, because of that, they do not exhibit antitumor properties, but simplify investigation of substitution reactions of these complexes.

The most studied monofunctional complexes are $[\text{PtCl}(\text{terpy})]^+$ and $[\text{PtCl}(\text{dien})]^+$ and their aqua analog in different reaction conditions. *Dien* (diethylenetriamine or 1,5-diamino-3-azapentane) or *terpy* (2,2':6',2''-terpyridine) are tridentate ligands, while the fourth coordination place is occupied with labile ligand, mostly chlorido ligand. *Terpy* ligand affects nucleophilic substitution reactions which are controlled by strong π -acceptor ability of the tridentate chelate 2,2':6',2''-terpyridine. The electronic communication between three pyridine rings causes a decrease in electronic density on the platinum center due to additional formation of π -back bond and makes it more electrophilic and more reactive.

Considering that platinum as soft acid prefers soft bases such as sulfur-coordinated biomolecules, we have studied kinetics for the complex formation of $[\text{PtCl}(\text{terpy})]^+$ with guanosine-5'-monophosphate (5'-GMP) in the presence and absence of glutathione (GSH) at pH ca. 6, with concentration $[\text{Pt}(\text{terpy})\text{Cl}]^+:\text{GSH}:5'\text{-GMP}$ ratio of 1:2:10 [7].

The observed pseudo-first-order rate constants, k_{obs} , as a function of the total concentration of nucleophile are described by Eq. (3):

$$k_{\text{obs}} = k_1 + k_2 [\text{nucleophile}] \quad (3)$$

A least-squares fit of the data according to Eq. (3) resulted in values for the forward anation rate constants, k_2 , and the reverse equation rate constant, k_1 [2]. The substitution reactions are characterized by almost zero values for k_1 . Thus, the complex formation reaction for the GSH goes almost to completion. Linear plots of the observed *pseudo*-first-order rate constants k_{obs} versus the total concentration of the GSH pass almost through the origin (**Figure 2**).

The intercept is very small within the experimental error limits (**Figure 2**), illustrating that the solvent cannot effectively displace the coordinated nucleophile. Thus, no significant solvent or reverse reaction path was observed in the present systems, such that direct nucleophilic substitution is the major observed reaction pathway under the selected conditions. The following rate law can be formulated:

$$k_{\text{obsd}} = k_2 [\text{nucleophile}] \quad (4)$$

where k_2 is a *second-order* rate constant for the forward reaction. The rate law indicates that the reactions proceed via a direct nucleophilic substitution pathway. The second-order rate constants are obtained from the linear least-squares analysis of the kinetic data.

Obtained data clearly point to a kinetic preference $[\text{PtCl}(\text{terpy})]^+$ toward the GSH at pH *ca.* 6. 5'-GMP is also a very good nucleophile for Pt(II) complexes but at neutral pH cannot compete with GSH. The second-order rate constant for GSH is 10^2 times higher for GSH than for the 5'-GMP. This is also reflected in the competition reactions utilizing mixtures of the GSH and GMP. Also, proton and ^{195}Pt NMR data did not show any N7 coordination of GMP, in spite of its excess, in the presence of thiols [8].

However, at or near neutral pH, although less than 10% of thiols are deprotonated, the N-bonding bases cannot compete with the thiol-containing amino acids and peptides [8, 9]. Therefore, binding primarily takes place through the sulfur donor sites.

According to the HSAB principle, the platinum prefers sulfur donor biomolecules as soft base, but with nitrogen donors, biomolecules (intermediate) build thermodynamically very stable complexes. The interactions of anticancer platinum-based drugs with sulfur thioether biomolecules are more favorable. According to this we have investigated the competitive reactions of $[\text{PtCl}(\text{dien})]^+$ (10 mM) with L-methionine 5'-GMP in a molar ratio: $[\text{PtCl}(\text{dien})]^+:\text{L-methionine}:5'\text{-GMP} = 1:1:3$ [10, 11]. In the initial stage of the reactions (<40 h), ^1H NMR peak for the free L-methionine (δ 2.142 ppm) decreases in intensity, and new peak of the $[\text{Pt}(\text{dien})(\text{S-meth})]^{2+}$ appeared in the spectrum (δ 2.544 ppm), whereas a little of the 5'-GMP reacted. In the later stages (72 h), the peaks for the bounded L-methionine and free 5'-GMP (δ 8.208 ppm) decreased in intensity, whereas those for free L-methionine increased in intensity, as did those assignable to bound 5'-GMP in $[\text{Pt}(\text{dien})(\text{N7-GMP})]^{2+}$ (δ 8.624 ppm) as shown in **Figure 3** [10].

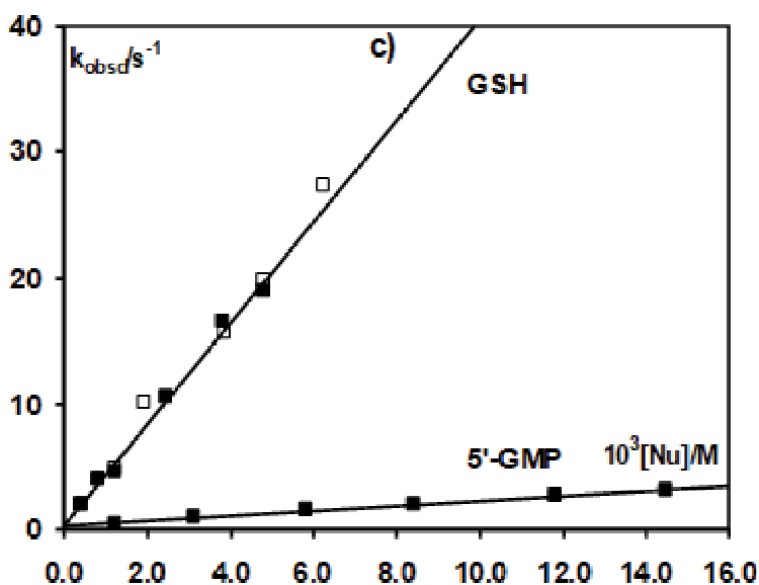


Figure 2. Observed pseudo-first-order rate constants, k_{obs} as a function of nucleophile concentration at 37°C for 5'-GMP and GSH without 5'-GMP (open square) and in the presence of excess of 5'-GMP (full square) [7].

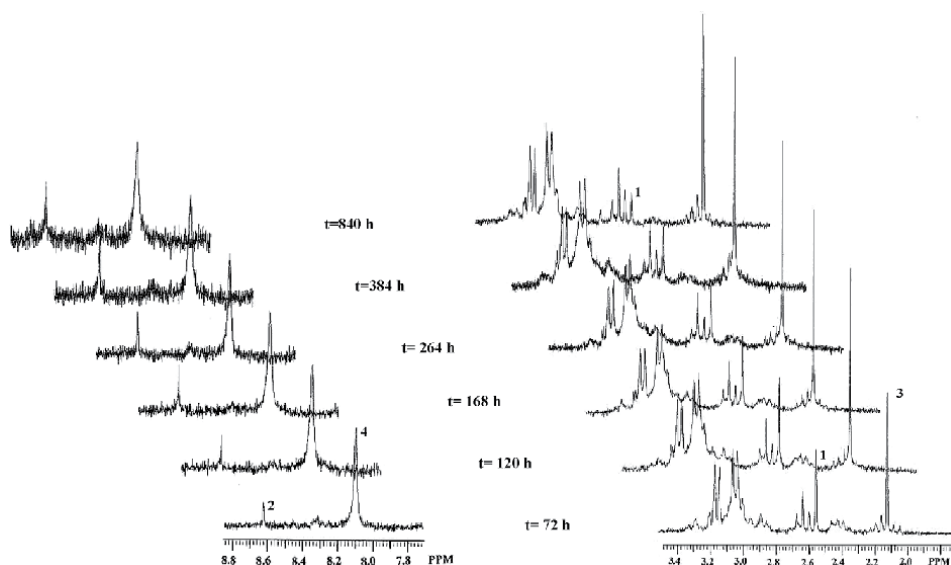


Figure 3. ^1H NMR spectra of the reactions of $[\text{PtCl}(\text{dien})]^+$ (10 mM) with mixture of L-methionine and 5'-GMP in the ratio 1:1:3 (where **1** is the signal for the $[\text{Pt}(\text{dien})(\text{S-meth})]^{2+}$, **2** is the signal for the $[\text{Pt}(\text{dien})(\text{N7-GMP})]^{2+}$, **3** is the signal for the free L-methionine, and **4** is the signal for the free 5'-GMP [10]).

In separated experiments we confirmed that the reactions of $[\text{PtCl}(\text{dien})]^+$ with L-methionine is relatively fast, and the complex $[\text{Pt}(\text{dien})(\text{N7-GMP})]^{2+}$ can be formed from $[\text{Pt}(\text{dien})(\text{S-meth})]^{2+}$ in direct displacement of coordinated L-methionine by 5'-GMP. Moreover, the 5'-GMP proton signals of the end product are identical to those belonging to $[\text{Pt}(\text{dien})(\text{N7-GMP})]^{2+}$ formed by direct reactions of 5'-GMP and $[\text{PtCl}(\text{dien})]^+$ complex [10].

As could be seen, initially there is rapid formation of $[\text{Pt}(\text{dien})(\text{S-meth})]^{2+}$ followed by displacement of L-methionine by 5'-GMP (**Figure 4**). In the later stages, the concentration of $[\text{Pt}(\text{dien})(\text{N7-GMP})]^{2+}$ is predominant [10].

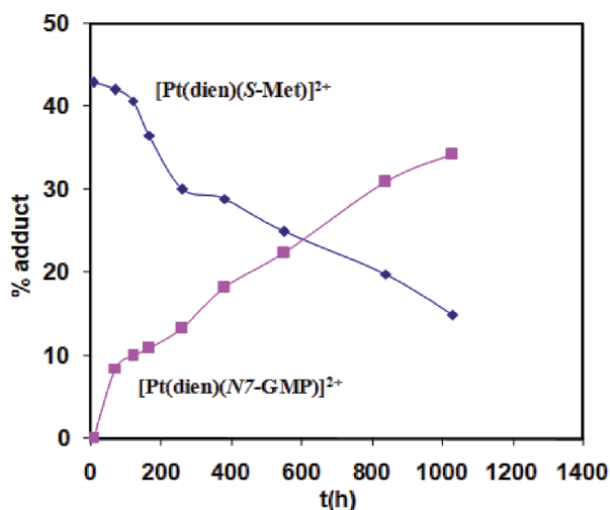


Figure 4. Observed product formation during the competition reaction of $[\text{PtCl}(\text{dien})]^+$ with L-methionine and 5'-GMP in molar ratio $[\text{PtCl}(\text{dien})]^+ : \text{L-methionine} : 5'-\text{GMP} = 1:1:3$ [10].

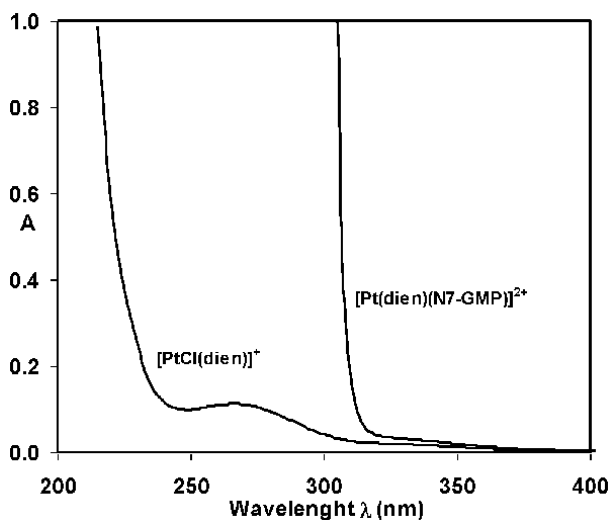


Figure 5. Electronic spectra for the starting complex, $[\text{PtCl}(\text{dien})]^+$, and for the final product, $[\text{Pt}(\text{dien})(\text{N7-GMP})]^{2+}$ [10].

The spectra of the starting complex, $[\text{PtCl}(\text{dien})]^+$ and the final reaction product is presented in **Figure 5** [11].

In these experiments we confirmed that the mechanism of interactions of platinum(II) complexes as soft acid with soft sulfur bases originating from thiols and thioethers differs in the presence of an excess intermediate nitrogen bases (e.g., DNA constituent), depending on biomolecules that will react. If sulfur is from the thioether molecule, the resulting Pt-S(thioether) bond may be interrupted in the presence of the DNA molecule, i.e., the N7 atom from the guanosine-5'-monophosphate may substitute the molecule of thioether from the resulting complex. Also, the thiol molecule may substitute the thioether from compound. However, the bond between the platinum complex and the molecule containing the thiol group is not favorable. The compounds are extremely stable and nonselective. The Pt-S(thioether) products are "platinum reservoirs" in the organism; they are suitable intermediates in platinum complex(II) and DNA molecule reactions, while Pt-S(thiol) compounds completely deactivate complexes forming the compounds responsible for toxic effects.

4.2 Substitution reactions of zinc(II) complexes

Transition metal compounds play crucial roles in bioinorganic reactions as cofactors in metalloproteins; they act mainly as a Lewis acid. The electronic properties of Zn(II), such as intermediate Lewis acidity, redox inertness, and flexible coordination geometry, render it a suitable cofactor in several proteins that perform essential biological functions. Zinc(II) ions are essential cellular components involved in several biochemical processes.

Zinc is a good Lewis acid, especially in complexes with lower coordination numbers; it lowers the pK_a of coordinated water and is kinetically labile, and the inter conversion among its four-, five-, and six-coordinate states is fast [12]. The utilization of zinc(II) for synthesis of novel antitumor non-platinum drugs could be beneficial. The non-platinum antitumor complexes could be alternatives to platinum-based drugs due to their better characteristics and less negative side effects.

We investigated the kinetics and mechanism of ligand substitution reactions between $[\text{ZnCl}_2(\text{terpy})]$ and biomolecules [13, 14].

Kinetics and mechanism of the substitution processes of $[\text{ZnCl}_2(\text{terpy})]$ complex with tripeptide GSH were investigated under *pseudo*-first-order conditions with respect to the complex concentration. Whatever system is considered, the absorbance always shows an exponential growth or downtrend versus time indicating the first-order kinetics with respect to the nucleophile ($v = -d[\text{Nu}]/dt = k_{\text{obsd}}[\text{Nu}]$) [2]. The kinetics traces showed two reaction steps, but different reaction mechanism for substitution reactions between $[\text{ZnCl}_2(\text{terpy})]$ complex and glutathione has been obtained (**Figure 6**).

For the substitution reactions between $[\text{ZnCl}_2(\text{terpy})]$ and glutathione, *first-order* linear dependence, k_{obs1} , on the complex concentration at low concentration was observed. At higher concentration, saturation kinetics was obtained. These could be explained by considering that the first step is a very fast pre-equilibrium formation of intermediate (*pseudo*-octahedral complex), followed by rearrangement to final complex, whereas one chloride is substituted by GSH (**Figure 7**) [13].

The value of rate second-order constant k_2 which described the substitution of the one chloride and pre-equilibrium constant K_1 could be determinate using Eq. (5).

$$k_{\text{obs1}} = \frac{k_2 K_1 [\text{Zn}^{\text{II}}]}{1 + K_1 [\text{Zn}^{\text{II}}]} \quad (5)$$

The value of pre-equilibrium constant was found to be $K_1 = 1831 \text{ mol}^{-1} \text{ L}$. The second substitution step is independent of glutathione concentration $k_{\text{obs2}} = k_2$, which indicates that chelation process takes place (**Figures 6** and **7**). At pH 7.38 GSH is deprotonated [15], the formation of five-membered chelate ring is possible via O-carboxylate and N-ammine group from γ -glutamyl residue [16]. Five-coordinate metal centers Zn(II) according hard-soft acid nature of metals prefer O-carboxylate bioligands [17, 18].

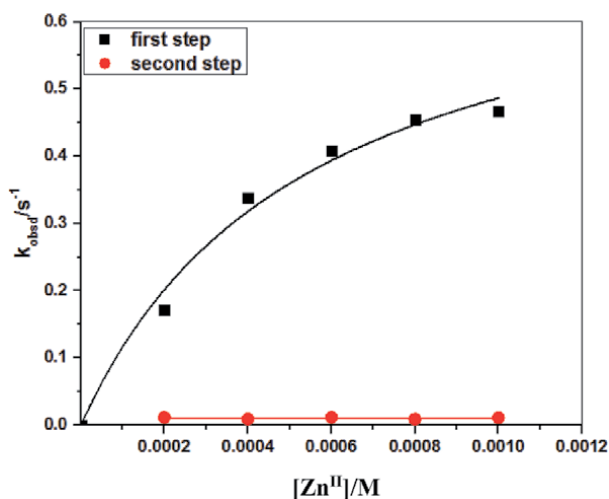


Figure 6. Pseudo-first-order rate constants as a function of complex concentration for the first and second substitution reactions of the $[\text{ZnCl}_2(\text{terpy})]$ and complex with glutathione at pH 7.38 (0.005 M phosphate buffer) in the addition of 0.010 M NaCl at 22 °C [13].

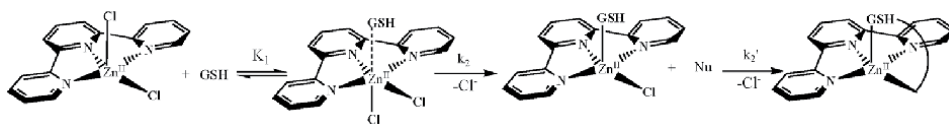


Figure 7.

The proposed reaction pathways for the reaction of $[ZnCl_2(terpy)]$ complex and glutathione [13].

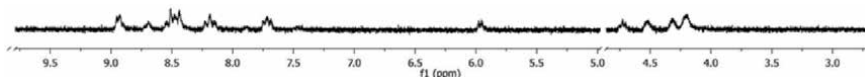


Figure 8.

NMR spectra of the reaction between $[ZnCl_2(terpy)]$ and 5'-GMP at 295 K, pD 4.5 in D_2O after 1 minute [14].

The nature of the ligand in inner coordination sphere is expected to play an important role in the binding of the metal complexes to biomolecules and in their cytotoxic effect. We have made an attempt to the mechanism of substitution between DNA constituent 5'-GMP and square-pyramidal $[ZnCl_2(terpy)]$ complex by 1H NMR method [14]. The reaction reached completion for less than 1 min, which was visible in NMR tube. The color of the solution after addition of 5'-GMP in molar ratio 1:1 turns white. 1H NMR spectra were recorded after 24, 48 h, and during several weeks, but changes in spectrum have not been observed (**Figure 6**).

The singlet of H8 proton of the coordinated 5'-GMP appeared at 8.70 ppm, while the doublet of the H1' proton was at 5.97 ppm. Corresponding to terpy ligand in the spectrum, six proton patterns have been observed. The doublet of 6,6'' appeared at 8.95 ppm, the multiplet formed by covered signals of 3',5' protons, from middle pyridine; 4,4'' protons appeared in the range 8.49–8.42 ppm, the triplets of 4' proton from middle pyridine ring; and 5,5'' protons were at 8.19 and 7.71 ppm, respectively. The doublet of 3,3'' protons seems to be at the same position as H8 proton of 5'-GMP (the signal was broadened) (**Figure 8**) [17]. The protons in the aromatic region of the spectra all correspond to signals from known terpy ligand coordinated to metal ions as is expected [19, 20].

As mentioned before, $[ZnCl_2(terpy)]$ reacted immediately with DNA constituent; the rate of nucleophilic substitution reaction is controlled by strong π -acceptor ability of the tridentate chelate 2,2':6',2''-terpyridine. The electronic communication between three pyridine rings causes a decrease in electronic density on the zinc center due additional formation of π -back bonding and makes it more electrophilic and more reactive. The final product $[ZnCl(terpy)(N7-GMP)]$ is also characterized by DFT calculation in combination with experimental NMR technique. The results are in good agreement; it confirmed coordination via N7 donor (intermediate Lewis base) [14].

In order to confirm the geometry around the coordinated center, structural index τ [21] was calculated for both $[ZnCl(terpy)(N7-GMP)]$ and $[ZnCl(en)(N7-GMP)]$ complexes. For five-coordinated Zn(II) complex, the structural index $\tau_5 = (\beta - \alpha)/60^\circ$ (α and β are the two largest angles around the central atom) [21], which represents the relative amount of trigonality (square-pyramid, $\tau_5 = 0$; trigonal-bipyramid, $\tau_5 = 1$) is 0.32. The coordination geometry around zinc ion could be best described as somewhat between square-pyramidal and trigonal-bipyramidal, more like leaned toward distorted square-pyramidal geometry. Reported structures of three ZnN_3S_2 complexes, namely, $[Zn(terpy)(iPrO)_2PS_2]_2$ [22], $[Zn(BMIP)]$ [23], and $[Zn(BMAP)]$ [24], have similar position of the donor atoms in the ligands resulting in distorted trigonal-bipyramidal geometry of complex with minor distortion due to the bulky groups.

5. Conclusions

The theory of hard and soft acids and bases (HSAB) has proven to be a useful tool in predicting the outcome of bioinorganic substitution reactions. According to this principle, electrophile such as complex compounds of transition metal ions reacts preferentially with donor atoms of biologically relevant nucleophiles of similar hardness or softness. Strong bonds are forming between hard acids and hard bases, soft acids and soft bases or borderline acids with borderline. Thus, platinum (II) belong to soft acid, and prefer soft bases. Kinetically are preferred reactions with sulfur donor biomolecules but more thermodynamically stable are Pt-N products. On other hand zinc(II) is borderline hard/soft ions and readily complexes with ligands containing a range of donor atoms, e.g., hard O-, intermediate N- and soft S-donors according to coordination numbers.

Acknowledgements

The author gratefully acknowledges the financial support from the State University of Novi Pazar and the Ministry of Education, Science and Technological Development, Republic of Serbia (Projects No. 172011).

Conflict of interest

The author declares no conflict of interest.

Author details

Tanja Soldatović
Department of Chemical-Technological Sciences, State University of Novi Pazar,
Novi Pazar, Serbia

*Address all correspondence to: tsoldatovic@np.ac.rs

IntechOpen

© 2020 The Author(s). Licensee IntechOpen. This chapter is distributed under the terms of the Creative Commons Attribution License (<http://creativecommons.org/licenses/by/3.0>), which permits unrestricted use, distribution, and reproduction in any medium, provided the original work is properly cited. 

References

- [1] Housecroft CE, Sharpe AG. *Inorganic Chemistry*. 4th Ed. Harlow, England; New York: Pearson; 2012. p. 1213. ISBN-13: 978-0273742753
- [2] Tobe ML, Burgess J, editors. *Inorganic Reaction Mechanism*. England: Longman; 1999. p. 688. ISBN-13: 978-0582236776
- [3] Langford CH, Gray HB. *Ligand Substitution Processes*. 2nd ed. New York: Benjamin; 1974. p. 103
- [4] Wilkins RG. *Kinetics and Mechanism of Reactions of Transition Metal Complexes*. 2nd thoroughly revised ed. New York, Weinheim: Wiley-VCH Verlag GmbH; 2002. p. 465. ISBN: 3-527-28389-7
- [5] Lippert B, editor. *Cisplatin, Chemistry and Biochemistry of Leading Antitumor Drugs*. Zurich: Wiley-VCH; 1999. p. 563. ISBN: 3906390209
- [6] Reedijk J. Why does cisplatin reach guanine-N7 with competing S-donor ligands available in the cell? *Chemical Reviews*. 1999;99:2499-2510. DOI: 10.1021/cr980422f
- [7] Bugarčić ŽD, Soldatović T, Jelić R, Algueró B, Grandas A. Equilibrium, kinetic and HPLC study of the reactions between platinum(II) complexes and DNA constituents in the presence and absence of glutathione. *Dalton Transactions*. 2004;22:3869-3877. DOI: 10.1039/B411168K
- [8] Teuben JM, Rodrigez i Zubiri M, Reedijk J. Glutathione readily replaces the thioether on platinum in the reaction with $[\text{Pt}(\text{dien})(\text{GSMe})]^{2+}$ (GSMe = S-methylated glutathione); a model study for cisplatin-protein interactions. *Journal of the Chemical Society Dalton Transactions*. 2000;3: 369-372. DOI: 10.1039/A908135F
- [9] Bugarčić ŽD, Heinemann FW, van Eldik R. Substitution reactions of $[\text{Pt}(\text{terpy})\text{X}]^{2+}$ with some biologically relevant ligands. Synthesis and crystal structure of $[\text{Pt}(\text{terpy})(\text{cyst-S})](\text{ClO}_4)_2 \cdot 0.5\text{H}_2\text{O}$ and $[\text{Pt}(\text{terpy})(\text{guo-N}^7)](\text{ClO}_4)_2 \cdot 0.5\text{guo} \cdot 1.5\text{H}_2\text{O}$. *Dalton Transactions*. 2004;2:279-286. DOI: 10.1039/B311056G
- [10] Soldatović T, Bugarčić ŽD. Study of the reactions between platinum(II) complexes and L-methionine in the presence and absence of 5'-GMP. *Journal of Inorganic Biochemistry*. 2005;99(7):1472-1479. DOI: 10.1016/j.jinorgbio.2005.04.005
- [11] Soldatović T, Čanović P, Čanović D, Bugarčić ŽD. Competitive reactions of L-methionine and 5'-GMP towards platinum(II) complexes. *Medicinal Chemistry*. 2005;1(6):547-561. DOI: 10.2174/157340605774598117
- [12] Williams RJP. Bio-inorganic chemistry: Its conceptual evolution. *Coordination Chemistry Reviews*. 1990; 100:573-610. DOI: 10.1016/0010-8545(90)85020-S
- [13] Selimović E, Jeremić S, Ličina B, Soldatović T. Kinetics, DFT study and antibacterial activity of zinc(II) and copper(II) terpyridine complexes. *Journal of the Mexican Chemical Society*. 2018;62:1-21
- [14] Soldatović T, Selimović E, Šmit B, Ašanin D, Planojević N, Marković S, et al. Interactions of zinc(II) complexes with 5'-GMP and their cytotoxic activity. *Journal of Coordination Chemistry*. 2019;72(4):690-706. DOI: 10.1080/00958972.2019.1569229
- [15] Smith RM, Martel AE. *Critical Stability Constants*. 2nd Suppl. Vol. 6. New York, NY: Plenum Press; 1989. p. 20. ISBN: 978-1-4615-6764-6
- [16] Wiseman DA, Sharma S, Black SM. Elevated zinc induces endothelial

- apoptosis via disruption of glutathione metabolism: Role of the ADP translocator. *Biometals*. 2010;**23**:19-30. DOI: 10.1007/s10534-009-9263-y
- [17] Bertini I, Gray HB, Stiefel EI, Valentine JS. *Biological Inorganic Chemistry. Structure and Reactivity*. Sausalito, CA: University Science Books; 2007. p. 739. ISBN-13: 978-1891389436
- [18] Roat-Malone RM. *Bioinorganic Chemistry: A Short Course*. Hoboken, NJ: John Wiley & Sons Inc.; 2002. p. 348. ISBN: 0-471-15976-X
- [19] Cummings SD. Platinum complexes of terpyridine: Interaction and reactivity with biomolecules. *Coordination Chemistry Reviews*. 2009;**253**: 1495-1516. DOI: 10.1016/j.ccr.2008.12.009
- [20] Manikandamathavan VM, Weyhermüller T, Parameswari RP, Sathishkumar M, Subramaniana V, Balachandran UN. DNA/protein interaction and cytotoxic activity of imidazole terpyridine derived Cu (II)/Zn(II) metal complexes. *Dalton Transactions*. 2014;**43**:13018-13031. DOI: 10.1039/C4DT01378F
- [21] Uhlenbrock S, Wagner R, Krebs B. Syntheses and characterization of novel tri- and hexa-nuclear zinc complexes with biomimetic chelate ligands. *Journal of the Chemical Society Dalton Transactions*. 1996;**18**:3731-3736. DOI: 10.1039/DT9960003731
- [22] Harrison PG, Begley MJ, Kikabhai T, Killer F. Zinc(II) bis(*O,O'*-dialkyl dithiophosphates): Complexation behaviour with pyridine and other multidentate nitrogen donor molecules. The crystal and molecular structures of the 1:1 complexes of bis(*O,O'*-diisopropyl dithiophosphato)zinc(II) with pyridine, 2,2'-bipyridine, and 2,2' : 6',2''-terpyridine and of (1,11-diamino-3,6,9-triazaundecane)zinc(II) bis(*O,O'*-diethyl dithiophosphate). *Journal of the Chemical Society Dalton Transactions*. 1986;**5**:929-938. DOI: 10.1039/DT9860000929
- [23] Lindoy LF, Busch DH, Goedken V. Helical co-ordination: Five-co-ordinate zinc and cadmium complexes formed by metal-ion-induced ligand reactions. *Journal of the Chemical Society, Chemical Communications*. 1972;**11**: 683-684. DOI: 10.1039/C39720000683
- [24] Brand U, Burth R, Vahrenkamp H. Design of trigonal-bipyramidal ZnN₃S₂ complexes. *Inorganic Chemistry*. 1996;**35**(4):1083-1086. DOI: 10.1021/ic950731d

Protic Reaction Media for Nucleophilic Substitution Reactions

Sandip S. Shinde

Abstract

This chapter deals with the unusual substitution reactions in non-aprotic solvent. Selective protic solvents that are widely being accepted for nucleophilic substitution reactions not only enhance the reaction rate but also give desire for selectivity of substituted product. Protic solvents such as *tert*-alcohol, primary alcohol, ionic liquids with *tert*-alcohol and primary alcohol functionality, and bis-cationic ionic liquid with protic functionality were shown best result in substitution reactions. Aliphatic nucleophilic substitution significantly developed in protic reaction medium due to the hydrogen bonding interaction with leaving groups and nucleophile. The development of substitution reactions from past two decades are summarised in this book chapter.

Keywords: substitution reactions, nucleophilic, alcohol solvents, phase transfer catalyst

1. Introduction

Substitution reaction is one of the important classes of organic reactions. The term substitution itself indicates that the organic reaction process in which the one moiety/functional group will be replaced by other new group/moiety. Generally, there are two types of substitution reactions: one is bimolecular substitution reaction and the other is unimolecular substitution (S_N1) reaction. The bimolecular reaction is a reaction in which the replacing group generates partially a positive charge on a substrate and a new electron-rich group occupies the position of the replacing group as shown in **Figure 1**. In short, it is referred as bimolecular nucleophilic substitution reactions (S_N2) [1]. Aliphatic nucleophilic substitution reaction is generally performed in a non-protic solvent so that the nucleophile will be free

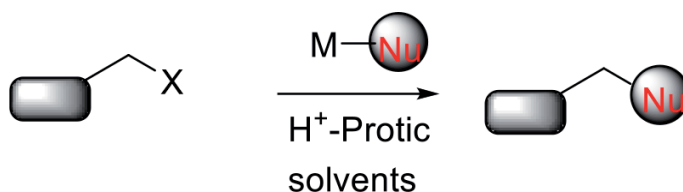


Figure 1. Substitution reactions with metal nucleophile (MNu) in protic solvent.

and flexible to replace the leaving group. In case of a protic solvent, the electron-rich species of nucleophile forms the hydrogen bond; thus, it reduces the efficiency of nucleophile, decreases nucleophilicity, and reduces the reaction rate. By contrast, some reactive nucleophiles, which show dual characters, may act as a base as well as a nucleophile; in such case, the possibility to form other side products are more. To improve the selectivity of the product, hydrogen bonding with reactive nucleophile will play a key role. Thus, a number of nucleophilic substitution reactions are performed in protic solvents such as *tert*-butanol, alcohol-functionalized ionic liquids, ammonium ionic liquids, or polyethylene glycols. In this book chapter, the recent development of S_N2 reactions in protic solvent to improve the selectivity of substituted product is covered [2].

2. Protic solvent substitutions

2.1 Alcohol-mediated substitution reactions

Chi et al. developed the nucleophilic substitution reactions using *tert*-alcohol solvents such as *tert*-butanol, *tert*-amyl alcohol, etc [3]. Nucleophiles such as fluorine gave promising results and an excellent desire for the selectivity of fluorinated product with low formation of corresponding by-product alkene. **Figure 1** shows the alkyl sulfonate leaving group replaced by fluorine efficiently in the *tert*-amyl alcohol-mediated reaction conditions. The extreme effect of protic solvent-mediated fluorination with alkali metal fluoride was demonstrated.

They observed that the alcohol solvent particularly nonpolar such as *tert*-alcohol enhances the nucleophilicity of the electron-rich nucleophilic ion, radically in lack of any type of promoter or phase-transfer catalyst, which significantly enhances the rate of the nucleophilic substitutions and reduces the generation of corresponding side products, i.e. alcohols, ethers and alkene, compared with substitution reactions in dipolar aprotic medium. The importance of this reaction method is that it is useful in radiopharmaceuticals for the synthesis of fluorine-18-labelled imaging agents for positron emission tomography (PET) [4]. They demonstrated the application of protic-mediated reactions for radiolabelling of important molecular imaging agents in good yield and quality in shorter time compared to aprotic-mediated reaction conditions of nucleophilic substitution reactions [5]. They further studied the influence of the *tert*-alcohol solvent conditions for nucleophilic substitutions with series of alkali metal fluorides. The possible hydrogen bonding interaction of nucleophile fluorine and the sulfonyloxy substrate promote the rate of reaction [6]. Mechanistically, the hydrogen bonding between alkali metal fluoride and aprotic solvent, the generation of protic alcohol-solvated ion and the hydrogen bonding between the leaving group sulfonate and the alcohol solvent seem to favour the enhancement in the rate of nucleophilic substitutions without PTC. They found that the fluorination with specific substrates with *tert*-butylammonium fluoride in alcohol solvent affords the corresponding fluoroproducts in high yield than that obtained by the conventional methods using dipolar aprotic solvents. The protic medium also suppresses the formation of by-products, such as alkenes, ethers and cyclic adducts.

2.2 *Tert*-alcohol-functionalized ionic liquid

Shinde et al. exhibited the synergistic effect of *tert*-alcohol and ionic liquids in substitution reactions [7]. They merged the two solvents, ionic liquid (IL) and *tert*-alcohols, into one molecule for nucleophilic substitution as shown in

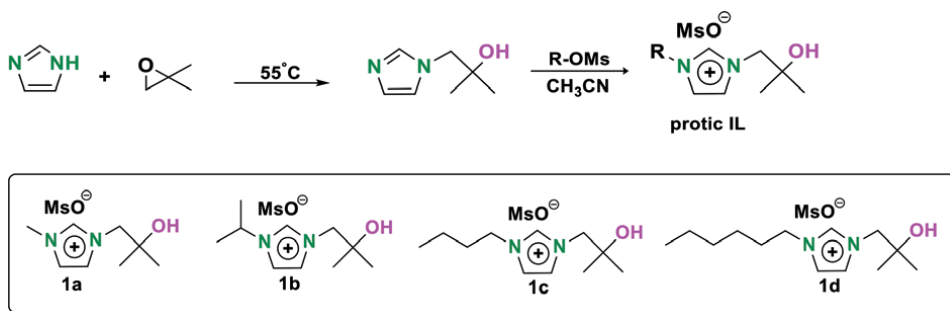


Figure 2.
Synthesis of tert-alcohol-functionalized ionic liquid for substitution reactions.

Figure 2. These hybridised ILs not only increase the nucleophilic reactivity of the fluoride anion but also reduce the olefin by-product. The preparation of novel imidazolium salts with counter anion [8]. Imidazole reacted with isobutylene oxide without or free solvents to give quantitatively yield N-tert-alcohol-substituted imidazole. N-tert-alcohol-substituted imidazole reacted with methyl, isopropyl, n-butyl, n-hexyl methane sulphonate in acetonitrile at 90°C gave the corresponding N₁-alkyl-N₃-tert-alcohol substituted imidazolium salts (ILs) **1a–1d**. All of these imidazolium mesylates are liquids at room temperature.

In the development of the fluorination process, ILs play both roles, i.e. reaction media and phase-transfer catalysts. They found that nucleophilic fluorination is accelerated in **1a** and that tert-alcohol solvents show good performance in nucleophilic fluorination, thereby side reactions are remarkably suppressed via a weak F–H hydrogen bond, which maintains the inherent nucleophilicity and reduces the basicity of the fluoride anion. The new hybridization of ILs and tert-alcohol functionality would provide dual advantages of reaction acceleration and minimization of side reactions.

Figure 3 depicted the use of protic ionic liquid in nucleophilic fluorination. The reaction of the primary triflate of R-D-galactopyranose in the presence of **1a** as a protic catalyst yielded the fluorinated product (**6a**) in almost quantitative yield with no by-products [7].

The reaction of the secondary mesylate, which could easily be eliminated to the corresponding olefin, showed a similar trend. Such superior reactivity and selectivity were obviously due to the previously mentioned synergistic effect of tert-alcohol functionality and imidazolium salts (**Figure 4**) [9].

2.3 Protic ethylammonium nitrate

Crosio et al. developed a new protic ionic liquid (IL) ethylammonium nitrate (EAN) inside toluene/benzyl-n-hexadecyldimethylammonium chloride (BHDC) as shown in **Figure 5** and studied its application on reverse micelles affects [10]. They found the Cl⁻ ion nucleophilicity on the bimolecular nucleophilic substitution (S_N2) reaction between this anion and dimethyl-4-nitrophenylsulfonium trifluoromethanesulfonate. It was the first study where the polar EAN was used as a suitable reaction medium for toluene-BHDC reverse micelles as a nanoreactor for performing the kinetic studies. The light scattering experiment discloses the formation of RMs containing the protic EAN ionic liquid component. Their experiments demonstrate that the homogeneous reaction medium is low effective compared to EAN-mediated S_N2 reaction conditions. The protic ionic liquid EAN acts as an aprotic medium once it is entrapped in BHDC RMs by hydrogen bonding

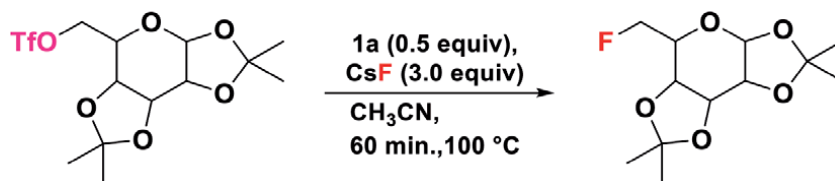


Figure 3.
Nucleophilic fluorination by protic ionic liquid **1a**.



Figure 4.
Nucleophilic fluorination on secondary mesylate by using CsF and **1a**.

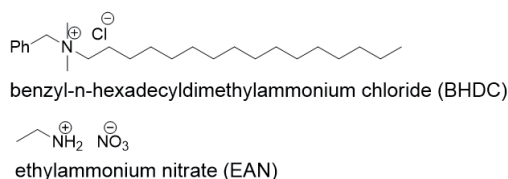


Figure 5.
Structures of ethylammonium nitrate (EAN).

interactions; as a result, nucleophilicity of chloride increases dramatically. Thus, the protic EAN is found as a suitable reaction solvent for nucleophilic bimolecular substitution reactions. These experiments demonstrate the flexibility of this kind of nanoreactor system to alter the polar protic solvent trapping and its impact on the rate of the reaction.

2.4 Polar protic solvent glycol

Song et al. observed that the alcohol contained polyethylene glycol as good reaction media for various nucleophilic substitution reactions [10]. Achiral polyether derivatives have shown dramatic acceleration in the S_N2 reactions by the simultaneous activation of both the nucleophile and electrophile sites of the leaving group. They also studied desilylation and found that bis-terminal $-OH$ group plays a key role that the desilylation kinetic resolution is successively done of the silyl ethers of racemic secondary alcohols.

2.5 Primary alcohol-functionalized ionic liquid

Further, polyethylene glycol was used for functionalization of imidazolium-based ionic liquid and studied for S_N2 reactions. Kim et al. [11] synthesised hexaethylene glycol *chain* ILs [hexaethylene glycol-im][OMs] and [dihexaethylene glycol-im][OMs] (hexaethylene glycol-im = 1-hexaethylene glycolic 3-methylimidazolium cation; dihexaethylene glycol-im = 1,3-dihexaethylene glycolic imidazolium cation; OMs = mesylate anion) by using simple organic reaction process as shown in **Figure 6** [12]. Synthesized various lengths of oligoether have better chelation efficiency with metal cation due to presence of oxygen atoms interaction from both side of imidazolium IL.

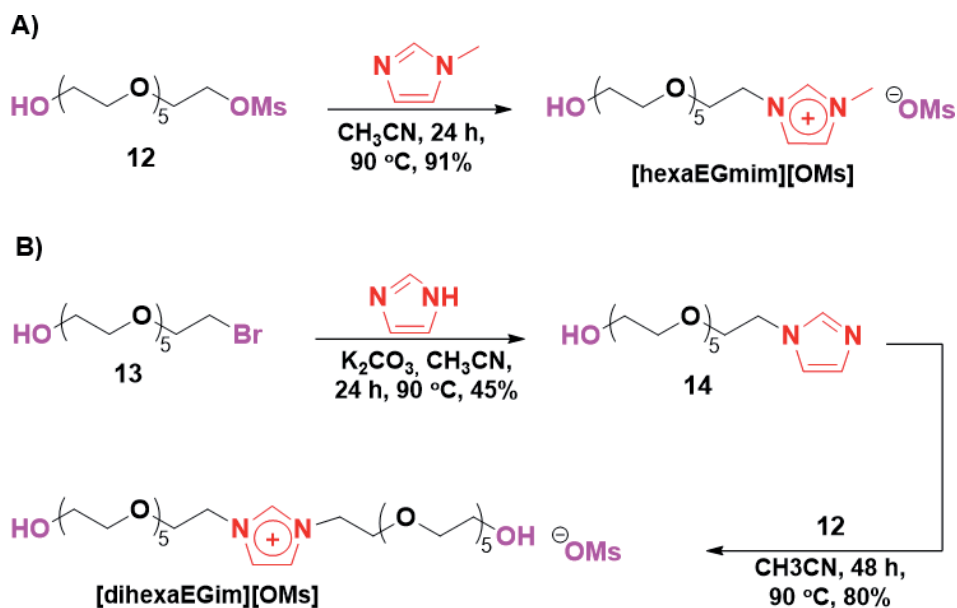
The author described the role of all functional moieties of ionic liquid in nucleophilic fluorination by using salts of metal nucleophiles (Figure 7).

The application of di-functional polyether chain-substituted imidazolium ionic liquids in the synthesis of various bioactive molecules such as fluoro-flumazenil, fluoropropyl ciprofloxacin, etc., which are useful in molecular probes for PET, is synthesised using a protic ionic liquid as shown in Figure 8.

2.6 Di-*tert*-alcohol-functionalized dicationic ionic liquid

The same research group developed another dicationic protic ionic liquid for substitution reactions. A task-specific hexaethylene glycol bridged bis-cationic ionic liquid (BFIL) such as bis(2-hydroxy-2-methyl-n-propylimidazolium) dimesylate (hexaethylene glycol chain-D⁺OHIM) was prepared, and its role in nucleophilic substitution reactions using an alkali metal nucleophiles was investigated [13]. They also compared their activities with a variety of mono-cationic ILs and found that the hexaethylene glycol chain-functionalized IL more effectively enhanced the reactivity of KX compared with the *tert*-alcohol-functionalized IL hexaethylene glycol chain-D⁺OHIM (Figure 9).

The use of bis-functionalized ionic liquid (BFIL) enhances the substitution reaction rate compared to conventional ionic liquid as well as mono-functionalized protic ionic liquid due to the higher activity of BFIL by the additional dicationic moieties compared with the mono-cationic ionic liquid methods. The author found that the hexaethylene glycol moiety of these hexaethylene glycol chain-functionalized ILs enhances the reactivity of alkali metal fluorides by two effects; one is chelation effect with alkali metal cations, allowing the fluoride to become necked, and the other is the flexible fluoride influence by flexible H-bonding between the hydroxyl groups of BFIL, *t*-alcohol medium and nucleophile. In the case of *t*-alcohol-functionalized BFIL, the *t*-alcohol moiety showed selectively flexible H-bonding in the process. Subsequently,



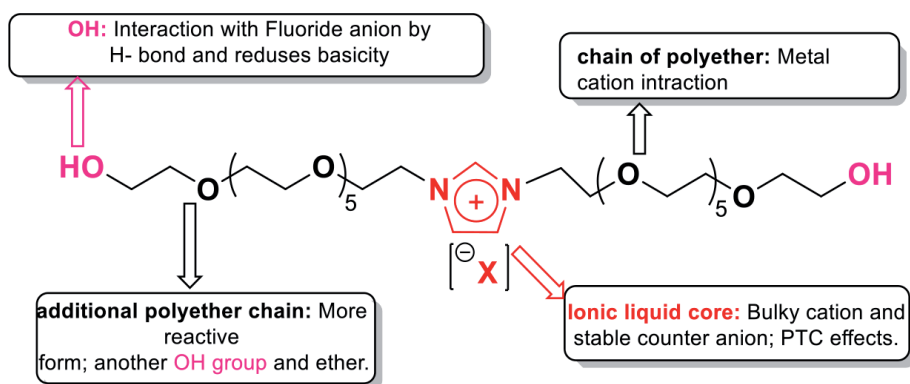


Figure 7.
Di-functional polyether chain-substituted imidazolium IL.

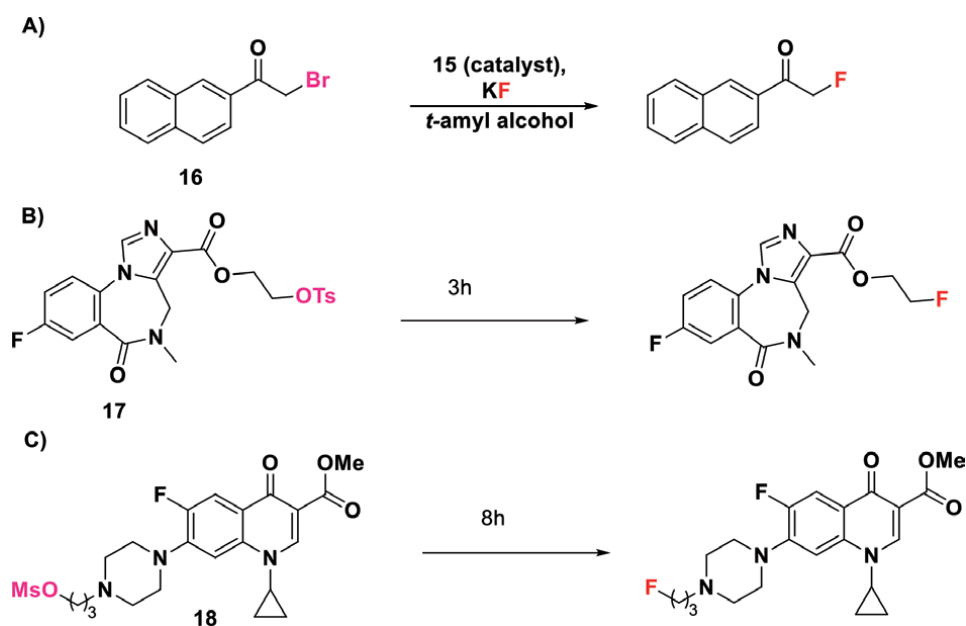


Figure 8.
Fluorination reaction by using bis-glycol substituted ILs catalyst with various leaving groups. A) acyl bromide B) tosylate C) mesylate substrates.

bi-alcohol-functionalized BFIL, having two imidazolium cations functionalized by ethylene glycol chain, showed the excellent catalytic increases in the reactivity of metal fluoride in the nucleophilic substitution among the mono-cationic convention ionic liquids. *Tert*-alcohol-funtionlaized ionic liquid not only enhances the nucleophilicity of ion but also reduces the formation of by-products alkene and ether.

The reaction of fluorination on another base-sensitive substrate of secondary alkyl tosylate using hexaethylene glycol chain-DHIM with KF in *t*-amyl alcohol at 80°C got a better yield of the secondary fluoro-product (**Figure 10**).

2.7 Protic amine tri-*tert*-butanolamine

Shinde et al. developed novel series of protic amines, i.e. tri-*tert*-butanol amine, which can be used as catalyst or media for substitution reactions [14].

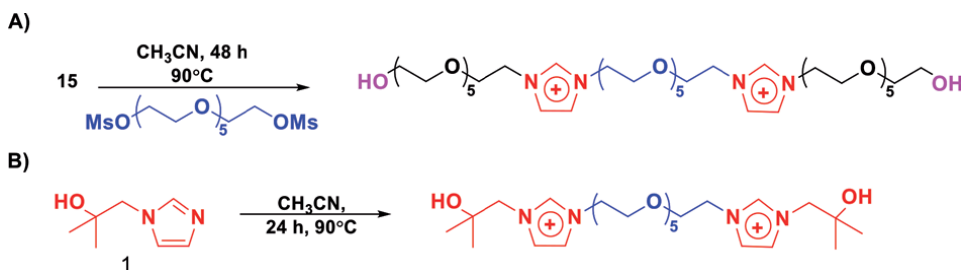


Figure 9. Synthesis of novel bis-functionalized protic ionic liquids: (A) bis(3-hexaethylene glycol chainyl imidazolium) dimesylate (hexaethylene glycol-DHIM) and (B) bis(2-hydroxy-2-methyl-n-propylimidazolium) dimesylate (hexaethylene glycol-D'OHIM).



Figure 10. Fluorination on secondary tosylate using KF with hexaethylene glycol chain-DHIM.

Tert-butanol-functionalized amines were prepared as shown in **Figure 11**. The easy synthesis of this amine was solvent-free reaction of isobutylene oxide with respective amines to afford corresponding tri-*tert*-butanolamine [(tri-*t*BuOH)A], 1-[Ethyl(2-hydroxy-2-methylpropyl)amino]-2-methylpropan-2-ol [(di-*t*BuOH)EtA] and 1-(diethylamino)-2-methyl-2-propanol [(mono-*t*BuOH)Et₂A]. These protic amines act as promoters with alkali metal salts in the nucleophilic fluorination of alkylsulfonates. It significantly enhances the reactivity of alkali metal salts with the minimum formation of side products (alkene, ether and alcohol) compared to conventional phase-transfer catalyst. The synergism of *tert*-alcohol and amine moiety plays a pivotal role in fluorination.

Fluorination reactions on the secondary leaving group of natural steroid substrate, cholesterol that was successfully converted into 2-fluoro-cholesterol in reasonable good yield (**Figure 12**).

The reaction of OTf-containing substrate in the presence of promoter *t*-butanolamine was much faster in giving the desired fluoro-product. It gave good substitution reactions with other leaving groups such as O-tosylate and O-nosylate as shown in **Figure 13**.

Substitution reactions with reactive substrate such as bromoacetophenone to fluoro acetophenone gave poor conversion of corresponding fluorinated product, **Figure 14**. It may be due to the *tert*-butanolamine that may react with acyl bromide and form the corresponding quaternary salts.

The reaction could be conducted in acetonitrile on a wide variety of substrates with little alkene formation observed. Further, Lee et al. studied the quantum chemical calculations of these substitution reactions and suggested that tris-*tert*-butanolamine complexed the fluoride ion through multiple

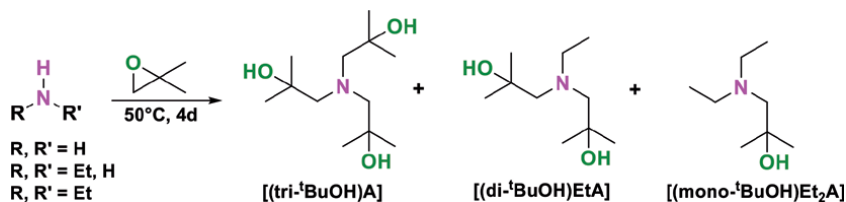


Figure 11. Synthesis of various *tert*-butanol amines.

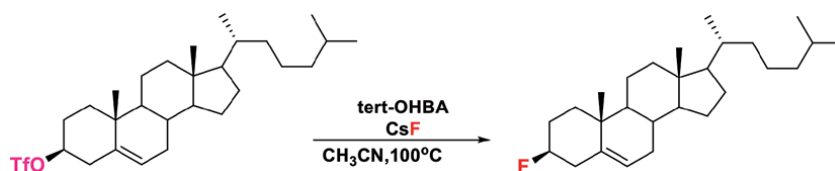


Figure 12. Nucleophilic fluorination on secondary substrate with metal salts using *t*-butanolamine.

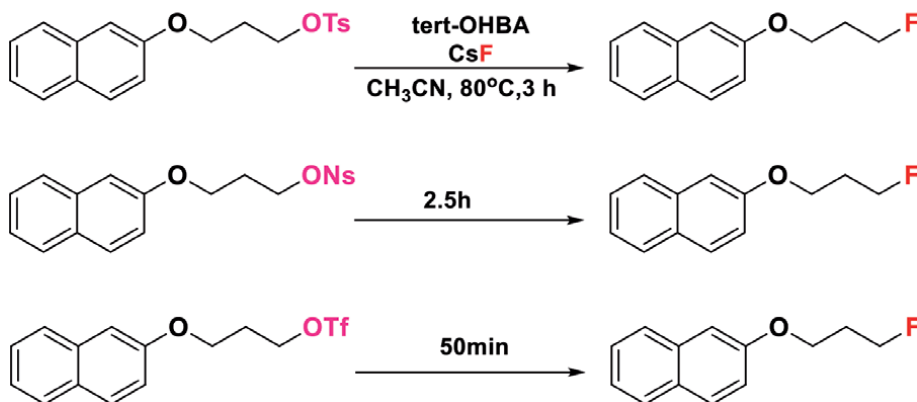


Figure 13. Fluorination on primary substrate in the presence of *t*-BuOH-amine.



Figure 14. Acyl bromide substitution reactions in presence of *tert*-butanol amine.

O–H...nucleophile–hydrogen bonds during the nucleophilic substitution reaction [15]. The formation of such complex did not have an effect on the reactivity of nucleophilicity and gave a selective substituted product.

3. Conclusion remark

In conclusion, the book chapter covers the recent development of protic solvents as reaction media of various substitution reactions. Aliphatic nucleophilic substitution reactions were extensively investigated in protic reaction medium and were found to be better reaction media compared to conventional aprotic solvents conditions. The protic solvents such as *tert*-amyl alcohol, *tert*-butanol, *tert*-alcohol-functionalized ionic liquid and amine are being widely used in fluorination reactions. These solvents are adopted by radiopharmaceuticals for the synthesis of value-added imaging agents for PET. The use of protic solvents is easy access and easy handling due to high-boiling points; they can be easily separated from the product because most of them are water soluble. The primary alcohol and *tert*-alcohol ionic liquids are not only used as solvents but also as promoters in various substitution reactions. These protic ionic liquids are ecofriendly and easy to synthesize and recover it after reactions.

Author details

Sandip S. Shinde
Fredric-Alexander University, Erlangen, Germany

*Address all correspondence to: shinde88@gmail.com

IntechOpen

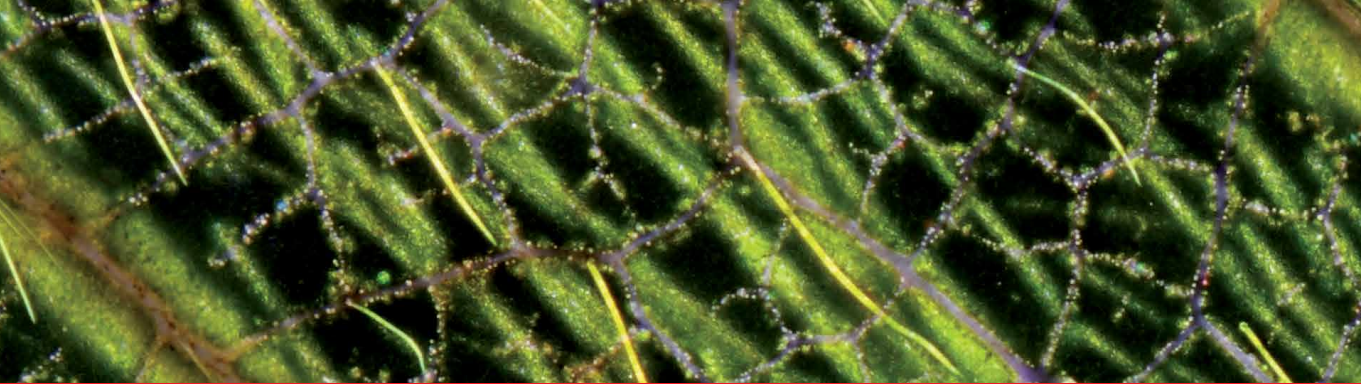
© 2020 The Author(s). Licensee IntechOpen. This chapter is distributed under the terms of the Creative Commons Attribution License (<http://creativecommons.org/licenses/by/3.0>), which permits unrestricted use, distribution, and reproduction in any medium, provided the original work is properly cited. 

References

- [1] Shinde SS, Patil SN, Thore SN, Pawar RP, Ametha KL. Synthesis of fluorinated heterocyclic molecule via multicomponent reactions. In: *Multicomponent Reactions. Synthesis of Bioactive Heterocycles*. Taylor and Francis Group, CRC Press; 2017. Chap. 7
- [2] Lee J-W, Oliveira MT, Jang HB, Lee S, Chi DY, Kim DW, et al. Hydrogen-bond promoted nucleophilic fluorination: Concept, mechanism and applications in positron emission tomography. *Chemical Society Reviews*. 2016;**45**:4638-4650
- [3] Kim DW, Song CE, Chi DY. New method of fluorination using potassium fluoride in ionic liquid: Significantly enhanced reactivity of fluoride and improved selectivity. *Journal of the American Chemical Society*. 2002;**124**:10278-10279
- [4] Kim DW, Song CE, Chi DY. Significantly enhanced reactivities of the nucleophilic substitution reactions in ionic liquid. *The Journal of Organic Chemistry*. 2003;**68**:4281-4285
- [5] Kim DW, Ahn D-S, Y-Ho O, Lee S, Kil HS, Oh SJ, et al. A new class of SN2 reactions catalyzed by protic solvents: Facile fluorination for isotopic labeling of diagnostic molecules. *Journal of the American Chemical Society*. 2006;**128**:16394-16397
- [6] Kim DW, Jeong ST, Lim M-H, Sohn JA, Katzenellenbogen DYC. Facile nucleophilic fluorination reactions using tert-alcohols as a reaction medium: Significantly enhanced reactivity of alkali metal fluorides and improved selectivity. *The Journal of Organic Chemistry*. 2008;**73**:957-962
- [7] Shinde SS, Lee BS, Chi DY. Synergistic effect of two solvents, tert-alcohol and ionic liquid, in one molecule in nucleophilic fluorination. *Organic Letters*. 2008;**10**:733-735
- [8] Shinde SS, Chi HM, Lee BS, Chi DY. tert-Alcohol-functionalized imidazolium ionic liquid: Catalyst for mild nucleophilic substitution reactions at room temperature. *Tetrahedron Letters*. 2009;**50**:6654-6657
- [9] Shinde SS, Patil SN, Ghatge A, Kumar P. Nucleophilic fluorination using imidazolium based ionic liquid bearing tert-alcohol moiety. *New Journal of Chemistry*. 2015;**39**:4368-4374
- [10] Crosio MA, Correa NM, Silber JJ, Falcone RD. A protic ionic liquid, when entrapped in cationic reverse micelles, can be used as a suitable solvent for a bimolecular nucleophilic substitution reaction. *Organic & Biomolecular Chemistry*. 2016;**14**:3170-3177
- [11] Jadhav VH, Jeong H-J, Lim ST, Sohn M-H, Kim DW. Tailor-made hexaethylene glycolic ionic liquids as organic catalysts for specific chemical reactions. *Organic Letters*. 2011;**13**:2502-2505
- [12] Lee JW, Hyeong HY, Hong BJ, Kim K, Park S-W, Lee S, et al. Bis-terminal hydroxy polyethers as all-purpose, multifunctional organic promoters: A mechanistic investigation and applications. *Angewandte Chemie, International Edition*. 2009;**48**:7683-7686
- [13] Jadhav VH, Kim JG, Park SH, Kim DW. Task-specific hexaethylene glycol bridged di-cationic ionic liquids as catalysts for nucleophilic fluorination using potassium fluoride. *Chemical Engineering Journal*. 2017;**308**:664-668
- [14] Shinde SS, Khonde NS, Kumar P. Tri-tert-butanolamine as an organic

promoter in nucleophilic fluorination.
ChemistrySelect. 2017;2:118-122

[15] Lee S-S, Jung H-K, Shinde SS,
Lee S. Mechanistic study of nucleophilic
fluorination promoted by tri-tert-
butanolamine. Journal of Fluorine
Chemistry. 2017;197:80-86



*Edited by Satyen Saha,
Ravi Kumar Kanaparthi and Tanja V. Soldatović*

This book represents a unique blend of topics covering photon-initiated reactions to substitution reactions. Additionally, several fantastic chapters on the photophysics of popular dyes and their applications make the book interesting for researchers working on photon-initiated physical and chemical processes.

Published in London, UK
© 2021 IntechOpen
© buccaneership / iStock

IntechOpen

